Finanziato dall'Unione europea - NextGenerationEU - DM 351 - CUP: I61I22000270007 - CB: 38-411-41-DOT1341413-2056

Università Degli Studi Di Napoli "Parthenope"

Dipartimento di Ingegneria

Doctoral (PhD) Course

in

Information and Communication Technology and Engineering

XXXVIII Cycle

November 2022 – October 2025

SSD: IINF-01/A

Highly sensitive and tunable fiber optic biosensors exploiting localized surface plasmon resonance of gold nanostars

Supervisor **Prof. Agostino Iadicicco** *Candidate:* **Amin Moslemi**

Coordinator: **Prof. Agostino Iadicicco**

Abstract

The main objective of this thesis is the design and fabrication of fiber optic biosensors based on Localized Surface Plasmon Resonance (LSPR) using gold nanostructures. When a noble metallic nanostructure is illuminated by an electromagnetic wave, the free electrons within the nanostructure begin to oscillate collectively with the incident EM field. The oscillation domain extends beyond the nanostructure dimensions, leading to the accumulation of charge at its surface and generating a strong localized electric field known as surface plasmon resonance (SPR). In nanostructures smaller than the wavelength of the incident light, this effect becomes localized referred to as LSPR. As a result, a portion of the incident electromagnetic spectrum is absorbed by the nanostructure. For noble metals such as gold and silver, this resonance typically occurs in the visible range. The position and intensity of the LSPR absorption band depend strongly on the size, shape, and material composition of the nanostructure, as well as on the surrounding refractive index (SRI).

The SRI sensitivity of LSPR is a crucial property for biosensing applications. When biological components are immobilized onto the sensing surface, they alter the local refractive index near the nanostructure. This change leads to a measurable shift in the LSPR resonance wavelength or intensity, providing a label-free means of detection. Due to their excellent SRI sensitivity and chemical compatibility, gold nanostructures are particularly suitable for bioconjugation with antibodies, enabling the development of highly specific and selective biosensors for a variety of biological and chemical targets.

In parallel, optical fibers offer a powerful platform for sensing applications because of their flexibility, compactness, and immunity to electromagnetic interference. They operate with low-power light sources and can be easily integrated into different environments. These features, combined with the high signal-to-noise ratio of optical measurements, allow fiber optic sensors to achieve an ultra-low limit of detection (LOD) and high sensitivity. Therefore, the integration of gold nanostructures with optical fibers represents a promising approach for developing advanced LSPR-based fiber optic biosensors.

In this context, the thesis presents a comprehensive study on the design, simulation, fabrication, and characterization of fiber optic LSPR sensors optimized for biological detection. The initial chapters provide the theoretical background of both SPR and LSPR, along with examples of their implementation in bulk and fiber-optic configurations. Following this, numerical simulations were conducted to study the effect of the SRI on the resonance band of spherical nanoparticles (NPs) and to evaluate their SRI sensitivity. Further investigations were performed to examine the influence of particle size, shape, and aggregation state on the plasmonic response. For optimization purposes, gold nanostars (NSs) were also simulated to explore how geometrical parameters affect the LSPR resonance band and sensitivity.

The next part of the work focuses on the experimental design of the fiber optic transducer. An uncladded multimode optical fiber was used to achieve evanescent wave interaction between the guided light and the surrounding medium. NPs and NSs were synthesized and deposited onto the functionalized fiber surface. The LSPR bands of these transducers were characterized in reflection mode and compared with the UV-Vis spectra of nanoparticles in solution, as well as with SEM and TEM images to confirm morphology and size distribution. The SRI sensitivity of the sensor was then calculated and analyzed.

As a preliminary step toward biosensing applications, Thiram pesticide, which is a chemical compound known to interact naturally with gold nanostructures, was selected as a model analyte. The corresponding sensitivity and LOD were evaluated to estimate the biosensing performance of the proposed transducer.

Subsequently, the sensing platform was biofunctionalized with specific antibodies for cortisol and ochratoxin A (OTA) to achieve selective and specific biosensing capabilities. These experiments were conducted at the University of Aveiro during a research exchange period, which significantly broadened my knowledge and experimental skills in the field of fiber optic biosensing.

Finally, an additional study was carried out to enhance the SRI and biosensing sensitivity of Tilted Fiber Bragg Grating (TFBG) sensors through the incorporation of gold nanostructures. The modified TFBG sensors were applied for the detection of glyphosate, demonstrating good selectivity, repeatability, and potential for environmental monitoring applications.

Overall, this thesis provides both theoretical and experimental insights into the development of plasmonic fiber optic biosensors. By combining the optical advantages of fiber platforms with the plasmonic properties of gold nanostructures, the presented work contributes to advancing high-performance, label-free sensors for biological and chemical detection, with promising applications in environmental monitoring, medical diagnostics, and food safety.

Acknowledgements

I would like to express my sincere gratitude to **Professor Agostino Iadicicco**, my supervisor and PhD coordinator, for his invaluable guidance, continuous support, and trust throughout my doctoral studies. His confidence in my abilities has been a source of great motivation, and I truly hope to have met his expectations and made him proud.

My deepest appreciation is extended to **Professor Stefania Campopiano** for her constant understanding and dedication to supporting international students. Her efforts in creating a welcoming and comfortable academic environment have greatly alleviated the challenges of studying away from home.

I wish to express my heartfelt thanks to **Dr. Flavio Esposito**, my co-supervisor, for his insightful scientific guidance, valuable advice, and encouragement. His mentorship has significantly contributed to my professional growth, and I am deeply grateful for the friendly and collaborative relationship we have shared.

I would also like to acknowledge **Dr. Lucia Sansone** and **Dr. Michele Giordano** from the **CNR-IPCB** group for their scientific collaboration, technical assistance, and for providing access to laboratory facilities essential to this work.

My sincere thanks go to **Professor Carlos Marques** and his research group at the **University of Aveiro**, in particular **Thais de Andrade Silva** and **Simone Soares**, for their kind support and collaboration during my exchange period.

I am also grateful to my colleagues and friends, **Attena, Elena, Anubhav, Sidrish, Marika, Pegah, Aida, Mojgan and Andrea**, for their helpful discussions, cooperation, and the pleasant working atmosphere in the laboratory.

Finally, I acknowledge with gratitude the **financial support provided by the Italian Government under the PNRR program**.

This PhD journey has been an unforgettable experience, one filled with challenges, growth, and invaluable lessons that I will carry with me throughout my life.

" And at last but not least, I want to thank me for believing in me, I want to thank me for doing all this hard work. I wanna thank me for having no days off. I wanna thank me for never quitting. I wanna thank me for always being a giver and trying to give more than I receive. I wanna thank me for trying to do more right than wrong. I wanna thank me for being with myself at all times."

Amin Moslemi

Acronyms

APTES	(3-aminopropyl) triethoxysilane	**OF**	Optical Fiber
BEM	Boundary Element Method	**OTA**	Ochratoxin A
BRE	Biological Recognition Element	**OTB**	OchraToxin B
BSA	Bovine Serum Albumin	**PBS**	Phosphate-Buffered Saline
DCF	Double-Clad Optical Fiber	**PCF**	Photonic Crystal Fiber
DDA	Discrete Dipole Approximation	**PMMA**	Poly(methyl methacrylate)
DSL	Dynamic Light Scattering	**PML**	Perfectly Matched Layer
EDC	Ethyl-Di-Carbodiimide	**POF**	Plastic Optical Fiber
EEFM	Excitation-Emission Fluorescence Matrix	**SAM**	Self-Assembled Monolayer
ELISA	Enzyme-Linked Immunosorbent Assay	**SD**	Standard Deviation
FDTD	Finite Difference Time Domain	**SEM**	Scanning Electron Microscopy
FEM	Finite Element Method	**SERS**	Surface-Enhanced Raman Spectroscopy
FOM	Figure Of Merit	**SH**	sulfhydryl
FOS	Fiber Optic Sensors	**SMF**	Single-Mode Fiber
FWHM	Full Width at Half Maximum	**SRI**	Surrounding Refractive Index
GO	Graphene Oxide	**SPR**	Surface Plasmon Resonance
ITO	Indium Tin Oxide	**TE**	Transverse Electric
LOD	Limit of Detection	**TEM**	Transmission Electron Microscopy
LSPR	Localized Surface Plasmon Resonance	**TFBG**	Tilted Fiber Bragg Grating
MMF	Multi-Mode Fiber	**TIR**	Total Internal Reflection
MPTES	(3-mercaptopropyl) trimethoxysilane	**Thiram**	Tetramethyl Thiuram Disulfide
NHS	N-Hydroxysuccinimide	**UV-Vis**	Ultraviolet-Visible
NP	Nanoparticle	**TIR**	Total Internal Reflection
NS	Nanostar	**ZP**	Zeta Potential

List of Publications

1. Moslemi, T. de Andrade Silva, F. Esposito, N. Santos, S. Campopiano, L. Sansone, M. Giordano, J. Nedoma, J.P. de Oliveira, A. Iadicicco, C. Marques, Cortisol detection via fiber optic biosensor based on localized surface plasmon resonance of gold nanostars, Photonics Res (2025). https://doi.org/10.1364/PRJ.571026.
2. A. Moslemi, L. Sansone, F. Esposito, C. Marques, S. Campopiano, M. Giordano, A. Iadicicco, Highly sensitive gold nanostar based optical fiber sensor with tunable plasmonic resonance, Sensors and Actuators Reports (2025) 100326. https://doi.org/10.1016/j.snr.2025.100326.
3. A. Moslemi, L. Sansone, F. Esposito, S. Campopiano, M. Giordano, A. Iadicicco, Optical fiber probe based on LSPR for the detection of pesticide Thiram, Opt Laser Technol 175 (2024) 110882. https://doi.org/10.1016/j.optlastec.2024.110882.
4. A. Moslemi, L. Sansone, F. Esposito, C. Marques, S. Campopiano, M. Giordano, A. Iadicicco, Optical Fiber Probe Based on Localized Surface Plasmon Resonance of Gold Nanostructures for Chemical Sensing, in: Proceedings of the 13th International Conference on Photonics, Optics and Laser Technology, SCITEPRESS - Science and Technology Publications, 2025: pp. 157–162. https://doi.org/10.5220/0013395000003902.
5. A. Moslemi, L. Sansone, F. Esposito, C. Marques, S. Campopiano, M. Giordano, A. Iadicicco, Comparative evaluation of Thiram detection by LSPR-based fiber optic probes with different nanostructures, in: 29th International Conference on Optical Fiber Sensors, SPIE, 2025: pp. 1297–1300.
6. A. Moslemi, L. Sansone, F. Esposito, S. Campopiano, M. Giordano, A. Iadicicco, Localized Surface Plasmon Resonance on Optical Fiber Surface for Chemical Sensing, in: Proceedings of the 12th International Conference on Photonics, Optics and Laser Technology, SCITEPRESS - Science and Technology Publications, 2024: pp. 110–117. https://doi.org/10.5220/0012593500003651.
7. A. Moslemi, L. Sansone, F. Esposito, S. Campopiano, M. Giordano, A. Iadicicco, Fiber Optic Probes Exploiting Localized Surface Plasmon Resonance for Chemical Detection, in: Annual Meeting of the Italian Electronics Society, Springer, 2024: pp. 335–340.

Table of Contents

List of Figures

In the case of dimers, Figure 3-7(A) illustrates a configuration where two nanoparticles are aligned along the x-axis within the xy-plane, while light propagates perpendicular to their alignment along the z-axis. The polarization of incident light remains unchanged, simulating a scenario where two nanoparticles aggregate side-by-side in a linear arrangement orthogonal to the propagation direction. The corresponding absorption spectrum, shown in Figure 3-7(B) as a black curve, exhibits a single peak at 560 nm, closely resembling the spectrum of an isolated AuNP, as seen in Figure 3-7(A). Further investigations explore the spectral response under rotational variations of the dimer. Figure 3-7(B) presents absorption spectra for rotation angles of 30°, 45°, 60°, and 90° about the y-axis. As the rotation angle increases, the effective aggregate dimension along the light propagation axis (z-axis) changes, leading to a notable spectral shift. Specifically, two distinct absorption peaks emerge: the shorter-wavelength peak corresponds to the individual NP response, while the longer-wavelength peak arises due to the increased effective size of the dimer along the z-axis upon rotation. Since experimental

List of Tables

1. Chapter 1
Introduction

This chapter provides an overview of the research context underpinning the work presented in this thesis. Key activities and contributions are summarized, followed by an explanation of the thesis's organizational structure.

1.1. Scientific scenario and motivations

In recent decades, optical biosensors have emerged as one of the most powerful and versatile analytical tools for the detection and quantification of biological and chemical species. Their operation is based on the interaction between light and matter, where specific biological recognition events induce measurable optical changes. Optical biosensors are attracting increasing attention in a wide range of fields, spanning from medical diagnostics and drug development to food safety and environmental monitoring, due to their high sensitivity, real-time detection capability, and potential for label-free operation. The possibility of detecting biomolecular interactions without the need for fluorescent or enzymatic labels represents a significant advantage in terms of simplicity, cost-effectiveness, and preservation of the biological activity of the analyte.

Among optical biosensing technologies, fiber-optic sensors represent a particularly attractive platform thanks to their unique advantages, including compactness, mechanical robustness, and immunity to electromagnetic interference. Optical fibers can operate in harsh or remote environments, and their small diameter enables minimally invasive measurements, making them especially suitable for in situ and in vivo applications. Moreover, the vast design flexibility of optical fibers allows the integration of various sensing mechanisms and functional coatings, enabling the realization of highly tailored sensing architectures.

Within this context, plasmonic biosensors have gained considerable interest due to their ability to exploit the excitation of surface plasmons, coherent oscillations of free electrons at the surface of metallic nanostructures, upon interaction with light. In particular, the phenomenon known as Localized Surface Plasmon Resonance (LSPR), which occurs in metallic nanoparticles of dimensions comparable to or smaller than the wavelength of light, provides a powerful mechanism for refractive index sensing. Small variations in the local dielectric environment surrounding the nanoparticles result in significant shifts in the LSPR spectral response, thus enabling highly sensitive detection of molecular binding events occurring at the nanoparticle surface.

Gold nanostructures have emerged as materials of choice for LSPR-based sensing due to their excellent chemical stability, biocompatibility, and tunable optical properties. Among them, gold nanostars (NSs) have attracted growing attention because of their distinctive morphology characterized by sharp tips and multiple branches, which give rise to intense local electromagnetic field enhancements, so-called “hot spots”, and a tunable plasmonic response across the visible and near-infrared spectrum. These features make NSs ideal candidates for developing biosensors with enhanced sensitivity and spectral tunability.

The central motivation of this research is to combine the advantages of fiber-optic technology with the remarkable plasmonic properties of gold nanostars to develop a new generation of highly sensitive and tunable fiber-optic biosensors. The integration of LSPR-active nanostructures onto optical fiber platforms represents a promising strategy to achieve compact, robust, and efficient sensing devices capable of real-time and label-free detection of biomolecular interactions in complex environments.

1.2. Optical fiber sensors technology

An optical fiber (OF) is a cylindrical dielectric structure with a diameter of hundreds of micrometers, functioning as a waveguide to transmit light. In principle, an optical fiber consists of a core at its center, surrounded by a cladding with a lower refractive index than the core. The entire structure is encased in a protective polymer jacket to prevent mechanical damage. Optical fibers can be fabricated from various materials, including silica, plastic, or hybrid compositions, with the core and cladding either in pure form or doped with other elements. This doping allows precise control of the refractive index, which is essential for efficient light propagation [1], [2], [3], [4].

The operating principle of an optical fiber is based on Total Internal Reflection (TIR). When light is coupled into the core of the fiber at a specific angle (respect to the normal at the boundary) , it travels forward until it reaches the core-cladding boundary. Due to the difference in refractive indices between the core and cladding, the light is reflected back into the core, allowing it to propagate along the fiber. For TIR to occur, two conditions must be satisfied, The refractive index of the core (n_1) must be greater than that of the cladding (n_2). The angle of incidence (θ) at the core-cladding boundary must exceed the critical angle (θ_c). If the incident angle is greater than θ_c, the light undergoes complete reflection and

remains confined within the core. If the angle is smaller than θ_c, the light refracts (bends) into the cladding, leading to signal loss. Figure 1.1 illustrates a visual example of TIR using a laser and a polymer block, demonstrating how light behaves at different incidence angles [2].

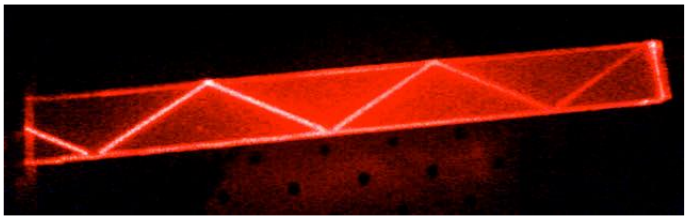

Fig. 1.1. TIR of laser beam in polymeric block.

Optical fibers were initially developed and utilized for communication purposes. Over time, fiber optics emerged as a promising tool for sensing applications. In the past few decades, significant advancements in fiber optics have led to increased production and widespread adoption of fiber optic sensors (FOS). Their usage has grown exponentially due to several advantages, including remote sensing capabilities and applicability in harsh environments, such as high-temperature or highly corrosive conditions [5], [6].

FOSs have gained remarkable attention in recent years, particularly in biomedical and biochemical sensing applications, due to their outstanding performance and unique structural advantages. Their inherent characteristics, such as compact size, low weight, immunity to electromagnetic interference, and high flexibility, make them suitable for integration into a wide range of environments, including harsh or remote conditions. From a sensing perspective, FOSs provide excellent sensitivity and an enhanced signal-to-noise ratio, allowing for precise detection of minute physical, chemical, or biological changes [7], [8],[9].

Since variations in target parameters are encoded in the optical signals transmitted through the fiber, optical fiber sensor systems are inherently sensitive to environmental factors such as light, temperature, and humidity. However, these interferences can be minimized through careful sensor design and configuration. Additionally, the performance of an optical fiber sensor system is influenced by the availability and specifications of its components, such as the bandwidth of the light source and the response time of the photodetector. The selection of these components is not solely based on their technical specifications but also on cost considerations and the overall system performance requirements [10].

While the optical fiber shields light from the external medium, most chemical and biosensors are based on customized configurations that enable the interaction of light with the surrounding environment. This dependency enables FOSs to detect even subtle environmental variations, including molecular interactions and changes in analyte concentration, with exceptional accuracy. Beyond biomedical applications, these sensors are increasingly employed in environmental monitoring,

industrial process control, and structural health diagnostics, offering real-time and label-free measurement capabilities. Their fabrication versatility, coupled with cost-effective deployment, continues to expand their potential for next-generation sensing technologies, where compactness, reliability, and high precision are essential [11], [12].

Fiber optic sensors can detect a wide range of physical and chemical parameters, such as temperature, strain, humidity, and [8], [13], [14], [15], [16], [17], [18], [19], [20], [21], [22], [23]. They are generally classified into two major types: intrinsic and extrinsic optical fiber sensors. In extrinsic sensors, the optical fiber acts merely as a waveguide, while the actual sensing occurs outside the fiber itself [4]. Conversely, in intrinsic sensors, the fiber functions as both the sensor and the waveguide, as seen in Fiber Bragg Gratings (FBG) and Long Period Gratings (LPG) [24], [25], [26], [27], [28].

Plasmonic biosensors are advanced optical sensing platforms that harness the collective oscillations of free electrons at the interface between a metal and a dielectric medium, a phenomenon known as SPR. These sensors translate subtle refractive index changes occurring near the metal surface, typically induced by biomolecular interactions, into measurable optical signals. This property enables label-free, highly sensitive detection of a variety of biological analytes. When light interacts with metallic nanostructures, commonly composed of gold or silver, it excites electron oscillations that enhance the local electromagnetic field intensity. This enhanced sensitivity allows plasmonic biosensors to detect minute changes in the refractive index caused by molecular binding events, making them effective for identifying biomolecules such as proteins, nucleic acids, and toxins [29], [30].

A particularly powerful mechanism within this field is LSPR, which occurs in metallic nanoparticles or nanostructures where conduction electrons oscillate collectively in resonance with incident light. The resonance wavelength depends on parameters such as particle size, shape, composition, and the refractive index of the surrounding medium. The advantage of LSPR respect to SPR is polarization independence and easier to excite. When biomolecules attach to the nanoparticle surface, they cause measurable shifts in the LSPR peak, providing information about the binding event within a few nanometers of the plasmonic surface. This extreme sensitivity enables extra low limit of detection with rapid response times and high spatial resolution. Owing to their miniaturization capability, tunability, and compatibility with diverse nanomaterials, including gold, silver, titanium nitride, and graphene-based hybrids.

LSPR-based plasmonic biosensors are increasingly integrated into fiber-optic systems, microfluidic chips, and wearable diagnostic platforms. Their applications span biomedical diagnostics, environmental monitoring, and food safety testing, where they offer precise, portable, and real-time analytical capabilities. By amplifying light–matter interactions at the nanoscale, plasmonic biosensors bridge the fields of nanophotonics and biosensing, paving the way for next-generation detection technologies with exceptional sensitivity and versatility [30], [31], [32], [33].

Among the various configurations of FOSs as extrinsic sensors, those incorporating SPR and, more notably, LSPR mechanisms have attracted growing attention for biosensing applications [34], [35] As

a result, integrating LSPR into fiber optics has opened new possibilities for compact, label-free, and real-time biosensing platforms that combine the advantages of nanoplasmonics with the robustness and flexibility of optical fiber technology [36], [37], [38], [39], [40],[41], [42].

Recent years, numerous studies have explored the integration of spherical metallic nanoparticles with FOSs to improve their sensitivity and overall sensing performance [28], [33], [43], [44], [45], [46], [47]. Most of these investigations have relied on wavelength shift and intensity interrogation techniques, where changes in LSPR peak position or amplitude serve as indicators of variations in the Surrounding Refractive Index (SRI) or the presence of target analytes. These approaches have successfully demonstrated the potential of nanoparticle-based FOSs for biosensing, environmental monitoring, and chemical detection applications. However, despite their advantages, spherical nanoparticles exhibit certain limitations, particularly in terms of their tunability and electromagnetic field enhancement. The uniform shape of nanospheres confines the plasmonic response to a narrow spectral region, which restricts their ability to achieve broad and tunable LSPR bands required for advanced sensing applications.

In contrast, the use of more complex plasmonic nanostructures, such as gold NSs, offers a promising alternative due to their unique morphological features [48]. NSs offer exceptional potential for plasmonic sensing due to their unique multibranched geometry, which provides a high surface-to-volume ratio and generates strong electromagnetic “hot spots” at their sharp tips. These features make them highly sensitive to refractive index variations, allowing detection of analytes at extremely low concentrations. Their optical response is also tunable across the visible to near-infrared range by adjusting morphological parameters such as spike length and tip sharpness. Moreover, strong plasmonic coupling between branches further enhances the sensing performance compared to simpler nanoparticle shapes. Despite these advantages, the integration of nanostars into fiber-optic platforms remains relatively unexplored, presenting a promising opportunity for developing compact, highly sensitive LSPR-based biosensors [49], [50], [51], [52], [53], [54], [55]. For example, Cennamo et al. [56] demonstrated that the use of NSs on a plastic optical fiber (POF) platform improved the sensor’s SRI response, showing that the strong plasmonic coupling associated with the star-shaped geometry could be effectively utilized in optical fiber sensing. This finding highlights the potential of nanostar-based LSPR systems in developing next-generation, highly sensitive biosensing devices.

Building upon these advances, our recent work has further investigated the impact of replacing conventional spherical nanoparticles with nanostars on fiber platforms. We have shown that by transitioning from NPs to NSs, it is possible to achieve a noticeable red-shift of the LSPR attenuation band toward higher wavelengths. This shift arises from the elongated spikes and anisotropic geometry of the NSs, which modify the local electromagnetic field distribution and extend the resonance into the near-infrared region. Such a spectral tunability not only enhances the sensitivity of the fiber sensor but also improves its compatibility with low-cost, commercially available optical components typically optimized for near-infrared operation. These findings demonstrate that nanostar-functionalized optical

fibers hold great promise for developing advanced plasmonic sensors that combine strong field enhancement, tunable spectral response, and practical integration with existing fiber-optic systems for real-world biomedical and environmental applications [57], [58].

1.3. Overview of LSPR sensing technologies

The development of LSPR-based biosensors has progressed through three main technological platforms like planar, colloidal, and on-chip systems, each contributing unique advantages while also presenting inherent limitations that have motivated the emergence of fiber-optic LSPR systems. Traditional LSPR biosensors operate on the principle of light interaction with metallic nanostructures, most commonly gold or silver, which support localized plasmonic oscillations sensitive to refractive index variations near their surfaces [47], [59].

Planar LSPR sensors generally employ substrate with different metallic patterns like nanoparticle self-assembled deposition or nanohole arrays fabricated through lithographic techniques, offering robust, reusable platforms that are particularly well suited for analytical and laboratory applications. For instance, Chen et al. [60] designed a sensing chip consisting of an optical waveguide slide glass combined with a microfluidic poly(methyl methacrylate) (PMMA) substrate. The surface of the waveguide glass was modified with gold nanoparticles integrated with graphene oxide, enabling enhanced plasmonic response and improved sensing performance. Similarly, in other planer LSPR sensor, Xiang et al. [61] fabricated large-scale gold nanohole arrays on glass substrates using nanosphere lithography (NSL), extending the sensing area. They demonstrated that the LSPR sensitivity of these nanoholes to local refractive index changes could be effectively utilized for the detection of biomolecular interactions such as bovine serum albumin (BSA) binding and biotin–streptavidin immunoassays. These examples highlight the strong analytical potential of planar LSPR sensors while also underscoring the need for more compact, flexible, and integrable platforms an objective that fiber-optic LSPR technologies are increasingly addressing.

Colloidal LSPR systems rely on dispersed metallic nanoparticles suspended in solution, offering a simple and cost-effective approach for plasmonic sensing [62], [63]. These systems enable straightforward synthesis and allow for label-free detection, making them attractive for rapid and accessible measurements. However, their performance is often limited by issues such as poor reusability and nanoparticle aggregation, which can compromise signal stability and accuracy. For example, Rohit et al. [64] demonstrated a sensing method by mixing a biological target, specifically the pesticide Thiram, which naturally interacts with silver, with a colloidal silver nanoparticle solution. By monitoring changes in the UV–visible spectrum of the colloid, they were able to identify the target analyte. Nevertheless, this approach suffered from spectral deformation caused by nanoparticle aggregation, leading to reduced measurement precision and a relatively high Limit of Detection (LOD).

Such challenges highlight the practical constraints of colloidal LSPR systems and emphasize the need for more stable and reproducible plasmonic platforms.

On-chip LSPR biosensors represent an advanced class of plasmonic sensing systems that integrate metallic nanostructures within microfluidic platforms, enabling high-throughput, real-time detection in compact and portable formats ideal for point-of-care diagnostics. For instance, Terada et al. [65] developed a single-cell secretion detection chip composed of microwells designed to trap individual cells, each surrounded by gold nanopillars capable of supporting LSPR measurements. Using a combination of microfabrication and nanofabrication techniques, both the nanopillar arrays and microwell structures were precisely fabricated on a cyclic olefin polymer (COP) film, allowing the system to monitor cellular secretions with remarkable sensitivity. Although such on-chip configurations can achieve detection limits in the nanomolar to picomolar range, they still face challenges related to large-scale fabrication, optical alignment, and integration consistency, which limit their widespread application despite their strong potential for biomedical sensing and diagnostic technologies [66].

Integrating metallic nanostructures such as gold nanoparticles, thin films, or nanocomposites directly onto optical fibers creates a powerful hybrid platform that unites the high refractive index sensitivity of plasmonic systems with the compactness, flexibility, and remote accessibility of fiber technology. In these systems, the evanescent field of guided light within the fiber interacts with metallic nanostructures coated on regions such as the unclad surface, fiber tip, or tapered section, efficiently exciting localized surface plasmons. This interaction allows for real-time, label-free biosensing in complex media such as biological fluids or tissues, offering a compact and robust platform for remote diagnostics. Recent developments in this field include the incorporation of nanostructures like gold nanostars, nanorods, and hybrid metallic layers fabricated through self-assembly, sputtering, or laser-assisted deposition methods. These innovations have significantly improved nanostructure adhesion, uniformity, and spectral reproducibility, resulting in tunable plasmonic resonances extending from the visible to near-infrared regions and enabling the detection of analytes such as cortisol, environmental toxins, and viral biomarkers with exceptional sensitivity.

Despite these advances, fiber-integrated LSPR biosensors still face several key challenges that hinder their widespread application. One of the major issues is stability, as metallic nanoparticles can detach or aggregate when exposed to harsh chemical environments or temperature fluctuations, degrading sensor performance over time. Reproducibility remains another concern, since random nanoparticle distribution and inconsistent surface functionalization can lead to variations in spectral response between different probes. Additionally, achieving precise control over sensitivity and optical response requires optimizing the plasmonic coupling between the fiber's guided modes and the nanostructures, an aspect that is highly dependent on their morphology, spacing, and deposition uniformity. Even minor fabrication deviations can result in unwanted spectral shifts or broadened resonance peaks, reducing measurement precision [29], [66].

To overcome these limitations, recent research has focused on improving fabrication accuracy through advanced techniques such as laser nano-printing, lithographic patterning on fiber tips, and the use of hybrid coatings with dielectric spacers that enhance both stability and field confinement. Furthermore, machine-learning-based calibration methods are being explored to dynamically correct spectral variations in real time, improving measurement reliability. In summary, the central scientific challenge now lies in achieving stable, reproducible, and tunable integration of plasmonic nanostructures, particularly gold-based materials, into optical fiber systems, paving the way for next-generation LSPR biosensors that are ultra-sensitive, compact, and reliable for biomedical and environmental applications.

1.4. Thesis objectives and structure

This thesis focuses on advancing the field of fiber-optic sensing through the excitation of LSPR by evanescent waves, enabling the detection of biological targets with high sensitivity and selectivity. The research addresses a key scientific gap in the practical integration of gold nanostructures, particularly gold NSs, onto optical fibers while maintaining precise control over plasmon resonance tunability and ensuring compatibility with cost-effective, widely available optical hardware.

The fundamental objective is to design a multimode optical fiber-based plasmonic biosensor that bridges the gap between nanophotonic tunability and fiber-optic practicality. The process begins with an in-depth study of the interaction between noble metallic nanostructures and light, both individually and in coupled configurations. Particular attention is given to understanding how nanostructure morphology, including spike length, core size, and tip angle, affects the absorption and scattering spectra and, consequently, the LSPR resonance condition.

A major challenge in this context lies in achieving stable, uniform, and repeatable coupling of gold nanostructures on optical fiber surfaces. Conventional fabrication techniques, such as electron-beam lithography or focused ion beam milling, offer high precision but are costly, time-consuming, and difficult to scale, often resulting in limited reproducibility. Furthermore, although gold NSs exhibit remarkable plasmonic enhancement in colloidal or planar substrates, their integration onto curved fiber surfaces remains complex due to issues like nanoparticle aggregation, uneven surface coverage, and low colloidal concentration, which hinder uniform LSPR excitation and reduce sensing reliability [67], [68].

To overcome these challenges, this work proposes a simplified and scalable integration approach for immobilizing NSs onto multimode optical fibers. The strategy involves chemical surface functionalization and low-temperature coating methods to ensure uniform NSs coverage while preserving strong plasmonic activity. The resulting transducer design maintains mechanical robustness, optical alignment, and plug-and-play compatibility with commercial spectrometers, connectors, and

low-cost readout systems. Such compatibility ensures the device's adaptability to existing optical infrastructure, enabling large-scale and low-cost deployment.

Once LSPR excitation is successfully achieved, the fiber transducer is characterized through refractometry to measure the SRI sensitivity and to benchmark its performance against existing plasmonic sensors. Subsequently, the sensor is applied to biological detection, both with and without a Biological Recognition Element (BRE). The research also explores how nanostructure morphology and plasmonic coupling effects influence the LSPR resonance band, SRI sensitivity, and LOD. Additional studies focus on improving selectivity, thermal stability, and reproducibility under varying environmental conditions.

The developed LSPR fiber transducer, when functionalized with specific antibodies, demonstrates successful detection of multiple biological targets, including Thiram pesticide, Cortisol, and Ochratoxin A (OTA). Parallel investigations are also conducted on enhancing the surface sensitivity of a Tilted Fiber Bragg Grating (TFBG) by depositing gold nanostructures on its surface. This complementary device aims at the sensitive detection of glyphosate, broadening the scope of plasmonic fiber sensors for environmental and biochemical monitoring.

Overall, this thesis presents a comprehensive framework for developing reproducible, tunable, and scalable plasmonic fiber-optic biosensors. By merging simplified nanostructure deposition techniques with geometry-dependent spectral tuning, the work contributes a practical pathway toward portable, low-cost, and high-performance LSPR-based diagnostic systems that combine laboratory-level sensitivity with real-world usability.

This Thesis is divided into chapters as in following:

Chapter 2 provides the theoretical background on the working principles of SPR and LSPR, along with their sensing mechanisms. It also includes examples to illustrate their applications in various sensing technologies.

Chapter 3 presents a numerical analysis of the LSPR effect on NPs and NSs, exploring their optical properties, resonance behavior, sensitivity to environmental changes, as well as the effects of aggregation and morphology.

Chapter 4 presents the synthesis protocols for NPs and NSs, the preparation of the transducer, nanostructure deposition, and a detailed explanation of the experimental setup. compares different transducers deposited with NPs and NSs in terms of attenuation band and SRI sensitivity and an estimation of bio-sensitivity with Thiram pesticide, referencing the simulation results.

Chapter 5 and 6 explore the detection of various biological components at very low concentrations, including Cortisol and OTA using LSPR based fiber optic sensors based on different nanostructures.

Chapter 7 focuses on enhancing the surface sensitivity of a TFBG sensor. The goal is to detect the biological target glyphosate and is achieved by depositing gold nanostructures onto the grating.

Finally, Chapter 8 reports the conclusions of the thesis and perspectives.

Chapter 8 Conclusion and Future work.

1.5. Original contributions of the thesis

The originality of this thesis can be summarized in the following points.

First here we propose simple configuration to merge the advantages of optical fiber technology and the spectral features of LSPR for chemical- and bio-sensing applications. While gold NSs have been explored in colloidal or planar configurations, their use in fiber-optic platforms, particularly for biological sensing, remains extremely limited. This work represents studies to experimentally implement NSs on optical fibers and to systematically investigate the influence of their morphology on both the LSPR spectral position and the SRI sensitivity and how to control these two important parameter chemically during synthesis.

In additional, the thesis introduces a comprehensive numerical–experimental comparison that validates the simulation results with experimental data, showing strong agreement between the predicted and measured resonance wavelength shifts as a function of the refractive index. Importantly, the numerical section is not only intended as a theoretical validation, but also serves as a powerful design tool for optimizing sensor configurations prior to fabrication. By establishing direct correlations between morphology, local field distribution, and sensitivity, the simulation framework provides valuable predictive insight for the rational design of next-generation LSPR-based fiber sensors.

Overall, this thesis advances the state of the art by demonstrating a simple and reproducible fabrication route for fiber-optic LSPR sensors, which represents a crucial step toward their practical deployment in real-world biosensing scenarios. The combination of experimental innovation, numerical modelling, and chemical control strategies presented here contributes to the development of highly sensitive, tuneable, and scalable fiber-based plasmonic platforms, paving the way for their integration in medical diagnostics, environmental monitoring, and industrial sensing applications.

1.6. References

[1] B. S. Finn, “City of Light: The Story of Fiber Optics (review),” Technol Cult, vol. 43, no. 1, pp. 194–196, Jan. 2002, doi: 10.1353/tech.2002.0013.

[2] J. M. Senior and M. Y. Jamro, Optical fiber communications: principles and practice. Pearson Education, 2009.

[3] L. Thevenaz, Advanced fiber optics. EPFL press, 2011.

[4] H. Kadhum Hisham, “Optical Fiber Sensing Technology: Basics, Classifications and Applications,” American Journal of Remote Sensing, vol. 6, no. 1, p. 1, 2018, doi: 10.11648/j.ajrs.20180601.11.

[5] M. Elsherif et al., “Optical fiber sensors: Working principle, applications, and limitations,” Adv Photonics Res, vol. 3, no. 11, p. 2100371, 2022.

[6] B. D. Gupta, Fiber optic sensors: principles and applications. New India Publishing, 2006.

[7] S. Choudhary, F. Esposito, L. Sansone, M. Giordano, S. Campopiano, and A. Iadicicco, “Polyphenylene oxide based lossy mode resonance fiber sensor for the detection of volatile organic and inorganic compounds,” Opt Laser Technol, vol. 180, p. 111519, Jan. 2025, doi: 10.1016/j.optlastec.2024.111519.

[8] S. Ma et al., “Optical Fiber Sensors for High-Temperature Monitoring: A Review,” Sensors, vol. 22, no. 15, p. 5722, Jul. 2022, doi: 10.3390/s22155722.

[9] A. Ricciardi et al., “Lab-on-fiber technology: a new vision for chemical and biological sensing,” Analyst, vol. 140, no. 24, pp. 8068–8079, 2015, doi: 10.1039/C5AN01241D.

[10] J. Peatross and M. Ware, “Physics of Light and Optics: A Free Online Textbook,” in Frontiers in Optics 2010/Laser Science XXVI, Washington, D.C.: OSA, 2010, p. JWA64. doi: 10.1364/FIO.2010.JWA64.

[11] L. Zu et al., “Ultrasensitive and Multiple Biomarker Discrimination for Alzheimer’s Disease via Plasmonic & Microfluidic Sensing Technologies,” Advanced Science, vol. 11, no. 24, Jun. 2024, doi: 10.1002/advs.202308783.

[12] F. Chiavaioli et al., “Ultrahigh Sensitive Detection of Tau Protein as Alzheimer’s Biomarker via Microfluidics and Nanofunctionalized Optical Fiber Sensors,” Adv Photonics Res, vol. 3, no. 11, Nov. 2022, doi: 10.1002/adpr.202200044.

[13] P. Roriz, S. Silva, O. Frazão, and S. Novais, “Optical Fiber Temperature Sensors and Their Biomedical Applications,” Sensors, vol. 20, no. 7, p. 2113, Apr. 2020, doi: 10.3390/s20072113.

[14] I. Hernandez-Romano, D. Monzon-Hernandez, C. Moreno-Hernandez, D. Moreno-Hernandez, and J. Villatoro, “Highly Sensitive Temperature Sensor Based on a Polymer-Coated Microfiber Interferometer,” IEEE Photonics Technology Letters, vol. 27, no. 24, pp. 2591–2594, Dec. 2015, doi: 10.1109/LPT.2015.2478790.

[15] L. P. Kollar and R. J. Van Steenkiste, “Calculation of the Stresses and Strains in Embedded Fiber Optic Sensors,” J Compos Mater, vol. 32, no. 18, pp. 1647–1679, Sep. 1998, doi: 10.1177/002199839803201802.

[16] C. M. Lawrence, D. V. Nelson, E. Udd, and T. Bennett, “A fiber optic sensor for transverse strain measurement,” Exp Mech, vol. 39, no. 3, pp. 202–209, Sep. 1999, doi: 10.1007/BF02323553.

[17] C.-C. Zhang, H.-H. Zhu, S.-P. Liu, B. Shi, and D. Zhang, “A kinematic method for calculating shear displacements of landslides using distributed fiber optic strain measurements,” Eng Geol, vol. 234, pp. 83–96, Feb. 2018, doi: 10.1016/j.enggeo.2018.01.002.

[18] M. Batumalay, S. W. Harun, N. Irawati, H. Ahmad, and H. Arof, “A study of relative humidity fiber-optic sensors,” IEEE Sens J, vol. 15, no. 3, pp. 1945–1950, 2014.

[19] J. Ascorbe, J. M. Corres, F. J. Arregui, and I. R. Matias, “Recent developments in fiber optics humidity sensors,” Sensors, vol. 17, no. 4, p. 893, 2017.

[20] Q. Zhou, M. R. Shahriari, D. Kritz, and G. H. Sigel, “Porous fiber-optic sensor for high-sensitivity humidity measurements,” Anal Chem, vol. 60, no. 20, pp. 2317–2320, 1988.

[21] E. Vorathin, Z. M. Hafizi, N. Ismail, and M. Loman, “Review of high sensitivity fibre-optic pressure sensors for low pressure sensing,” Opt Laser Technol, vol. 121, p. 105841, Jan. 2020, doi: 10.1016/j.optlastec.2019.105841.

[22] Z. F. Zhang, X. M. Tao, H. P. Zhang, and B. Zhu, “Soft Fiber Optic Sensors for Precision Measurement of Shear Stress and Pressure,” IEEE Sens J, vol. 13, no. 5, pp. 1478–1482, May 2013, doi: 10.1109/JSEN.2012.2237393.
[23] J. Lu et al., “High-performance temperature and pressure dual-parameter sensor based on a polymer-coated tapered optical fiber,” Opt Express, vol. 30, no. 6, p. 9714, Mar. 2022, doi: 10.1364/OE.452355.
[24] C. A. F. Marques, G.-D. Peng, and D. J. Webb, “Highly sensitive liquid level monitoring system utilizing polymer fiber Bragg gratings,” Opt Express, vol. 23, no. 5, p. 6058, Mar. 2015, doi: 10.1364/OE.23.006058.
[25] K. Liu et al., “Interferometer-Based Distributed Optical Fiber Sensors in Long-Distance Vibration Detection: A Review,” IEEE Sens J, vol. 22, no. 22, pp. 21428–21444, Nov. 2022, doi: 10.1109/JSEN.2022.3213036.
[26] F. Esposito, “(INVITED)Chemical sensors based on long period fiber gratings: A review,” Results in Optics, vol. 5, p. 100196, Dec. 2021, doi: 10.1016/j.rio.2021.100196.
[27] F. Esposito, A. Srivastava, L. Sansone, M. Giordano, S. Campopiano, and A. Iadicicco, “Label-Free Biosensors Based on Long Period Fiber Gratings: A Review,” IEEE Sens J, vol. 21, no. 11, pp. 12692–12705, Jun. 2021, doi: 10.1109/JSEN.2020.3025488.
[28] X. Liu et al., “Advanced fiber optic sensors for quantitative nitrite detection: Comparative analysis of plasmonic tilted fiber Bragg gratings and fiber optic tips with ion-imprinted polymers,” Sensors and Actuators Reports, vol. 8, p. 100233, Dec. 2024, doi: 10.1016/j.snr.2024.100233.
[29] S. Verma, A. K. Pathak, and B. M. A. Rahman, “Review of Biosensors Based on Plasmonic-Enhanced Processes in the Metallic and Meta-Material-Supported Nanostructures,” Micromachines (Basel), vol. 15, no. 4, p. 502, Apr. 2024, doi: 10.3390/mi15040502.
[30] A. Negm et al., “Materials Perspectives of Integrated Plasmonic Biosensors,” Materials, vol. 15, no. 20, p. 7289, Oct. 2022, doi: 10.3390/ma15207289.
[31] E. Ferrari, “Gold Nanoparticle-Based Plasmonic Biosensors,” Biosensors (Basel), vol. 13, no. 3, p. 411, Mar. 2023, doi: 10.3390/bios13030411.
[32] Q. Duan, Y. Liu, S. Chang, H. Chen, and J. Chen, “Surface Plasmonic Sensors: Sensing Mechanism and Recent Applications,” Sensors, vol. 21, no. 16, p. 5262, Aug. 2021, doi: 10.3390/s21165262.
[33] M. E. Hamza, M. A. Othman, and M. A. Swillam, “Plasmonic Biosensors: Review,” Biology (Basel), vol. 11, no. 5, p. 621, Apr. 2022, doi: 10.3390/biology11050621.
[34] Q. Wang et al., “Research advances on surface plasmon resonance biosensors,” Nanoscale, vol. 14, no. 3, pp. 564–591, 2022, doi: 10.1039/D1NR05400G.
[35] V. S. Chaudhary, D. Kumar, and S. Kumar, “Gold-Immobilized Photonic Crystal Fiber-Based SPR Biosensor for Detection of Malaria Disease in Human Body,” IEEE Sens J, vol. 21, no. 16, pp. 17800–17807, Aug. 2021, doi: 10.1109/JSEN.2021.3085829.
[36] V. Juvé et al., “Size-Dependent Surface Plasmon Resonance Broadening in Nonspherical Nanoparticles: Single Gold Nanorods,” Nano Lett, vol. 13, no. 5, pp. 2234–2240, May 2013, doi: 10.1021/nl400777y.
[37] Y. Sun and Y. Xia, “Gold and silver nanoparticles: A class of chromophores with colors tunable in the range from 400 to 750 nm,” Analyst, vol. 128, no. 6, p. 686, 2003, doi: 10.1039/b212437h.
[38] L. Rodríguez-Lorenzo, J. M. Romo-Herrera, J. Pérez-Juste, R. A. Alvarez-Puebla, and L. M. Liz-Marzán, “Reshaping and LSPR tuning of Au nanostars in the presence of CTAB,” J Mater Chem, vol. 21, no. 31, p. 11544, 2011, doi: 10.1039/c1jm10603a.
[39] F. Reyes Gómez et al., “Surface Plasmon Resonances in Silver Nanostars,” Sensors, vol. 18, no. 11, p. 3821, Nov. 2018, doi: 10.3390/s18113821.
[40] H. Bin Jeon, P. V. Tsalu, and J. W. Ha, “Shape Effect on the Refractive Index Sensitivity at Localized Surface Plasmon Resonance Inflection Points of Single Gold Nanocubes with Vertices,” Sci Rep, vol. 9, no. 1, p. 13635, Sep. 2019, doi: 10.1038/s41598-019-50032-3.
[41] Y. Il Park, H. Im, R. Weissleder, and H. Lee, “Nanostar Clustering Improves the Sensitivity of Plasmonic Assays,” Bioconjug Chem, vol. 26, no. 8, pp. 1470–1474, Aug. 2015, doi: 10.1021/acs.bioconjchem.5b00343.

[42] S. K. Dondapati, T. K. Sau, C. Hrelescu, T. A. Klar, F. D. Stefani, and J. Feldmann, "Label-free Biosensing Based on Single Gold Nanostars as Plasmonic Transducers," ACS Nano, vol. 4, no. 11, pp. 6318–6322, Nov. 2010, doi: 10.1021/nn100760f.
[43] L. Li, X. Zhang, Y. Liang, J. Guang, and W. Peng, "Dual-channel fiber surface plasmon resonance biological sensor based on a hybrid interrogation of intensity and wavelength modulation," J Biomed Opt, vol. 21, no. 12, p. 127001, Dec. 2016, doi: 10.1117/1.JBO.21.12.127001.
[44] P. Sharma, V. Semwal, and B. D. Gupta, "A highly selective LSPR biosensor for the detection of taurine realized on optical fiber substrate and gold nanoparticles," Optical Fiber Technology, vol. 52, p. 101962, Nov. 2019, doi: 10.1016/j.yofte.2019.101962.
[45] I. Del Villar et al., "Nano-Photonic Crystal D-Shaped Fiber Devices for Label-Free Biosensing at the Attomolar Limit of Detection," Advanced Science, Jul. 2024, doi: 10.1002/advs.202310118.
[46] B. Kaur, S. Kumar, J. Nedoma, R. Martinek, and C. Marques, "Advancements in optical biosensing techniques: From fundamentals to future prospects," APL Photonics, vol. 9, no. 9, Sep. 2024, doi: 10.1063/5.0216621.
[47] H. Wang et al., "Plasmonic Nanostructure Biosensors: A Review," Sensors, vol. 23, no. 19, p. 8156, Sep. 2023, doi: 10.3390/s23198156.
[48] H. Yuan, C. G. Khoury, H. Hwang, C. M. Wilson, G. A. Grant, and T. Vo-Dinh, "Gold nanostars: surfactant-free synthesis, 3D modelling, and two-photon photoluminescence imaging," Nanotechnology, vol. 23, no. 7, p. 075102, Feb. 2012, doi: 10.1088/0957-4484/23/7/075102.
[49] F. Zhang, L. Xu, Y. Wang, and P. Wang, "Engineering plasmonic Au nanostars: Enhanced plasmonic properties, preparation and biomedical application," Mater Today Bio, vol. 33, p. 102022, Aug. 2025, doi: 10.1016/j.mtbio.2025.102022.
[50] Y. Liu, H. Yuan, F. Kersey, J. Register, M. Parrott, and T. Vo-Dinh, "Plasmonic Gold Nanostars for Multi-Modality Sensing and Diagnostics," Sensors, vol. 15, no. 2, pp. 3706–3720, Feb. 2015, doi: 10.3390/s150203706.
[51] Y. Li, J. Ma, and Z. Ma, "Synthesis of gold nanostars with tunable morphology and their electrochemical application for hydrogen peroxide sensing," Electrochim Acta, vol. 108, pp. 435–440, Oct. 2013, doi: 10.1016/j.electacta.2013.06.141.
[52] M. Kahraman, E. R. Mullen, A. Korkmaz, and S. Wachsmann-Hogiu, "Fundamentals and applications of SERS-based bioanalytical sensing," Nanophotonics, vol. 6, no. 5, pp. 831–852, Aug. 2017, doi: 10.1515/nanoph-2016-0174.
[53] G. M. Das, S. Managò, M. Mangini, and A. C. De Luca, "Biosensing Using SERS Active Gold Nanostructures," Nanomaterials, vol. 11, no. 10, p. 2679, Oct. 2021, doi: 10.3390/nano11102679.
[54] C. M. Muntean et al., "Gold vs. Silver Colloidal Nanoparticle Films for Optimized SERS Detection of Propranolol and Electrochemical-SERS Analyses," Biosensors (Basel), vol. 13, no. 5, p. 530, May 2023, doi: 10.3390/bios13050530.
[55] B. Khlebtsov, E. Panfilova, V. Khanadeev, and N. Khlebtsov, "Improved size-tunable synthesis and SERS properties of Au nanostars," Journal of Nanoparticle Research, vol. 16, no. 10, p. 2623, Oct. 2014, doi: 10.1007/s11051-014-2623-8.
[56] N. Cennamo et al., "Localized Surface Plasmon Resonance with Five-Branched Gold Nanostars in a Plastic Optical Fiber for Bio-Chemical Sensor Implementation," Sensors, vol. 13, no. 11, pp. 14676–14686, Oct. 2013, doi: 10.3390/s131114676.
[57] N. Pazos-Perez, L. Guerrini, and R. A. Alvarez-Puebla, "Plasmon tunability of gold nanostars at the tip apexes," ACS Omega, vol. 3, no. 12, pp. 17173–17179, 2018.
[58] N. Cennamo et al., "Sensitive detection of 2,4,6-trinitrotoluene by tridimensional monitoring of molecularly imprinted polymer with optical fiber and five-branched gold nanostars," Sens Actuators B Chem, vol. 208, pp. 291–298, Mar. 2015, doi: 10.1016/j.snb.2014.10.079.
[59] D. M. Kim, J. S. Park, S.-W. Jung, J. Yeom, and S. M. Yoo, "Biosensing Applications Using Nanostructure-Based Localized Surface Plasmon Resonance Sensors," Sensors, vol. 21, no. 9, p. 3191, May 2021, doi: 10.3390/s21093191.

[60] C.-H. Chen and C.-Y. Chiang, “Determination of the Highly Sensitive Carboxyl-Graphene Oxide-Based Planar Optical Waveguide Localized Surface Plasmon Resonance Biosensor,” Nanomaterials, vol. 12, no. 13, p. 2146, Jun. 2022, doi: 10.3390/nano12132146.
[61] G. Xiang, N. Zhang, and X. Zhou, “Localized Surface Plasmon Resonance Biosensing with Large Area of Gold Nanoholes Fabricated by Nanosphere Lithography,” Nanoscale Res Lett, vol. 5, no. 5, pp. 818–822, May 2010, doi: 10.1007/s11671-010-9566-5.
[62] Y. Hong, Y.-M. Huh, D. S. Yoon, and J. Yang, “Nanobiosensors Based on Localized Surface Plasmon Resonance for Biomarker Detection,” J Nanomater, vol. 2012, no. 1, Jan. 2012, doi: 10.1155/2012/759830.
[63] H.-H. Jeong et al., “Dispersion and shape engineered plasmonic nanosensors,” Nat Commun, vol. 7, no. 1, p. 11331, Apr. 2016, doi: 10.1038/ncomms11331.
[64] J. V. Rohit and S. K. Kailasa, “Cyclen dithiocarbamate-functionalized silver nanoparticles as a probe for colorimetric sensing of thiram and paraquat pesticides via host–guest chemistry,” Journal of Nanoparticle Research, vol. 16, no. 11, p. 2585, Nov. 2014, doi: 10.1007/s11051-014-2585-x.
[65] Y. Terada et al., “Development of Nano–Micro Fused LSPR Chip for In Situ Single-Cell Secretion Analysis,” Micromachines (Basel), vol. 14, no. 7, p. 1404, Jul. 2023, doi: 10.3390/mi14071404.
[66] N. Bhalla and A. Q. Shen, “Localized Surface Plasmon Resonance Sensing and its Interplay with Fluidics,” Langmuir, vol. 40, no. 19, pp. 9842–9854, May 2024, doi: 10.1021/acs.langmuir.4c00374.
[67] L.-L. Lai, P.-H. Huang, G. Stemme, F. Niklaus, and K. B. Gylfason, “3D Printing of Glass Micro-Optics with Subwavelength Features on Optical Fiber Tips,” ACS Nano, vol. 18, no. 16, pp. 10788–10797, Apr. 2024, doi: 10.1021/acsnano.3c11030.
[68] M. E. Martínez-Hernández, J. Goicoechea, P. J. Rivero, and F. J. Arregui, “In Situ Synthesis of Gold Nanoparticles in Layer-by-Layer Polymeric Coatings for the Fabrication of Optical Fiber Sensors,” Polymers (Basel), vol. 14, no. 4, p. 776, Feb. 2022, doi: 10.3390/polym14040776.

2. Chapter 2
Fundamental theory of Surface Plasmon Resonance (SPR) and Localized SPR (LSPR) with examples

This chapter explores the fundamental principles of Surface Plasmon Resonance (SPR) and Localized Surface Plasmon Resonance (LSPR), which represent the basic mechanisms underlying plasmonic biosensing. In addition, the chapter provides an overview of the current state of the art in fiber-optic biosensors that exploit SPR and LSPR effects for high-sensitivity detection of biological analytes.

2.1. Theoretical principles of SPR

Surface Plasmon Resonance is a fundamental optical phenomenon that occurs at the interface of a metal and a dielectric medium. It is widely exploited in various scientific and technological applications, particularly in sensing, due to its high sensitivity to refractive index variations near the metal surface. This chapter provides an in-depth discussion of SPR, covering its theoretical foundations, excitation methods, and applications, with a special focus on its relevance to fiber optic biological sensors based on the LSPR effect.

Both SPR and LSPR rely on the plasmonic effect, but their underlying sensing mechanisms differ. SPR, first discovered by Wood in 1902 [1], involves the collective oscillation of free electrons propagating along a metal-dielectric interface. When incident light interacts with this interface, photons

couple with free electrons, transferring energy to create surface plasmons (SPs) [2]. Resonance occurs only when the photon frequency matches the natural oscillation frequency of the free electrons, satisfying strict momentum-matching conditions.

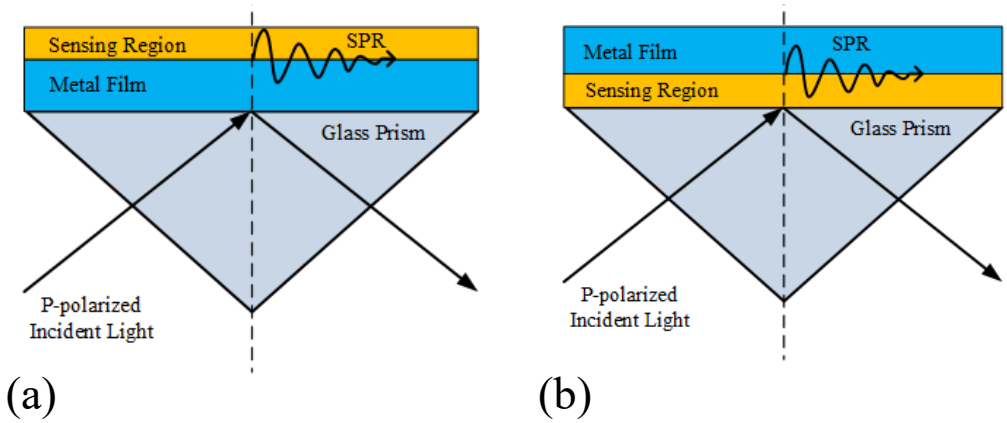

Figure 2-1 (A) Krestchmann and (B) Otto configurations for SPR effect. Adapted from [3].

The two most common SPR excitation configurations are the Kretschmann and Otto geometries (Fig. 2-1), the Kretschmann and Otto geometries. The Kretschmann configuration is more common and involves a thin metal layer, typically gold, deposited directly onto the surface of a glass prism. When light undergoes total internal reflection (TIR) within the prism, the resulting evanescent wave extends into the gold layer. This evanescent wave then couples with and excites surface plasmons at the outer gold-dielectric interface. This setup is particularly useful for biosensing because the outer gold surface can be easily modified to bind to specific biomolecules. In contrast, the Otto configuration places a small gap of air or another dielectric between the prism and the metal layer. In this arrangement, the evanescent wave from the prism must "tunnel" across this gap to reach and excite the surface plasmons on the metal. While the Otto configuration is less frequently used in biosensing than the Kretschmann, it offers a way to study plasmonic interactions in a highly controlled environment without direct physical contact between the prism and the metal film.

[4]The propagation of surface plasmons (SPs) is characterized by the propagation constant β_{sp}, given by:

$$\beta_{sp} = \frac{\omega}{c} n_{ef} = \frac{\omega}{c} \sqrt{\frac{\varepsilon_m n_D^2}{\varepsilon_m + n_D^2}} \qquad (2\text{-}1)$$

where ω is the angular frequency, c is the speed of light in vacuum, ε_m is permittivity of the metal and n_D is the refractive index of the dielectric. This equation shows that SPR is highly sensitive to changes in the dielectric's refractive index (n_D) and the metal's permittivity (ε_m), making it an excellent tool for detecting molecular interactions. Since the evanescent field is confined to a narrow region (150–400 nm from the surface) [4], even minute changes at the metal-dielectric interface (e.g., biomolecule binding) induce significant shifts in the plasmonic response.

For SPR excitation, the incident light must be Transverse Magnetic (TM) polarized, meaning the magnetic field is perpendicular to the plane of incidence, and the electric field has components along both the normal and tangential directions to the interface. This is necessary because surface plasmons involve oscillating charge distributions along the interface, requiring an electric field component normal to the surface [2].

In contrast, Transverse Electric (TE) polarized light, where the electric field is entirely perpendicular to the plane of incidence, cannot excite surface plasmons. This is because the required charge oscillations along the interface do not develop under TE polarization, and no surface-bound wave can be generated [2].

Based on the characteristics of the SPR effect, three primary sensing strategies, modulation of wavelength, angle, or intensity, are commonly employed to meet various sensing requirements [4]. These strategies are illustrated in Figure 2-2.

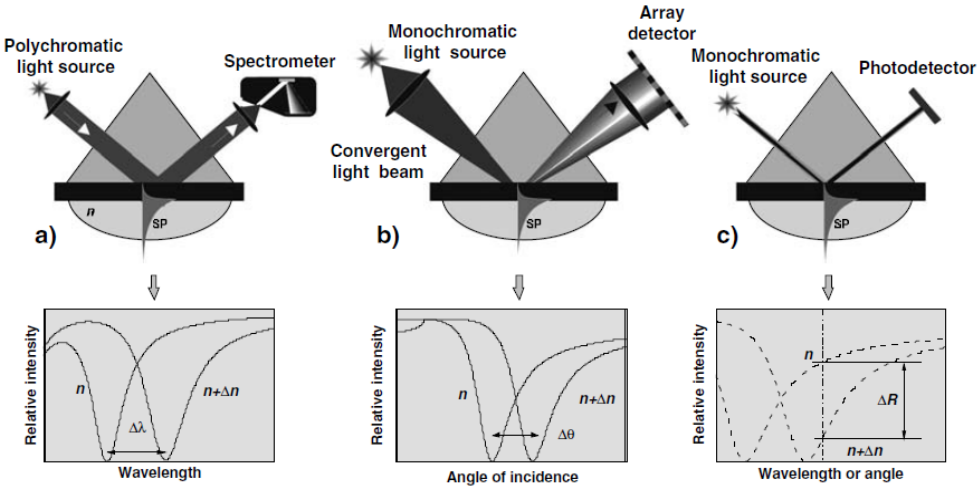

Figure 2-2. SPR sensing strategies based on modulation of a) wavelength, b) angle of incidence and c) light intensity. Adapted from [4].

In wavelength-based modulation (see Figure 2-2(a)), a broadband, polychromatic light source is directed at a fixed incident angle onto the sensor surface. The evanescent field is excited, and the reflected light is then analyzed by a spectrometer. The sensor's output is determined by detecting shifts in the plasmonic resonance wavelength. Any change in the refractive index of the surrounding medium, such as the binding of a target molecule, will cause a corresponding shift in this wavelength, which is then measured to quantify the interaction.

For angle-based modulation (see Figure 2-2(b)), a monochromatic light source with a fixed wavelength is used. Instead of changing the light's wavelength, the angle of the incident beam is varied. The sensor's output is determined by the shift in the resonance angle at which plasmons are excited. When the surrounding refractive index changes, the angle required to achieve resonance also shifts, and this change in angle is used as the sensing signal.

Intensity-based modulation (see Figure 2-2(c)) is the simplest of the three methods. Both the incident light's wavelength and its angle are kept fixed. In this configuration, changes in the surrounding refractive index directly affect the intensity of the reflected light. The output signal is simply the change in the intensity of the reflected beam, which makes this method straightforward but generally less sensitive than the other two

2.1.1. SPR sensing strategies based on modulation of wavelength

SPR sensing strategies based on wavelength modulation involve varying the incident light's wavelength to excite surface plasmons at the sensor-metal interface, with the resonance condition occurring at a specific wavelength where the light couples most efficiently with the plasmons. As the refractive index near the sensor surface changes due to analyte binding, the resonant wavelength shifts, allowing precise detection of biomolecular interactions in real-time. This approach offers high sensitivity and label-free detection, making it valuable for applications like biosensing, environmental monitoring, and medical diagnostics. By tracking the wavelength shift, researchers can quantify binding kinetics and analyte concentrations without requiring fluorescent or radioactive labels.

2.1.2. SPR sensing strategies based on modulation of angle of incidence

SPR sensing strategies based on the modulation of the angle of incidence involve varying the angle at which light interacts with a thin metal layer to excite surface plasmons. In this approach, a polarized light beam is directed onto the metal-dielectric interface at different angles, and the resonance condition is identified by detecting the angle where maximum energy transfer to the surface plasmons occurs, leading to a sharp dip in the reflected light intensity. This angle is highly sensitive to changes in the refractive index of the surrounding medium, making it effective for detecting biomolecular interactions, chemical concentrations, and environmental changes. By precisely monitoring shifts in the resonance angle, high-sensitivity and label-free sensing can be achieved, which is widely used in biosensing, medical diagnostics, and chemical analysis.

The sensor's operation relies on the phase-matching condition between the incident light and surface plasmon waves, described by Equation below

$$\theta = \sin^{-1}\left(\frac{1}{n_r}\sqrt{\frac{\varepsilon_{eff} n_1^2}{n_1^2 + \varepsilon_{eff}}}\right) \quad (2\text{-}2)$$

- θ: Resonance angle (dependent on refractive index changes).
- n_r: Refractive index of the prism (BK7 glass, n_r =1.39).
- ε_{eff}: Effective permittivity of the metal-dielectric interface.
- n_1: Refractive index of the sensing medium (e.g., water, n_1 =1.33–1).

When the incident light's wave vector matches the surface plasmon wave vector, resonance occurs, causing a sharp dip in reflectivity. The metasurface structure comprises a BK7 prism, a gold nano-layer (43–51 nm thick), and a silver layer (8–12 nm thick) featuring a symmetrical triangular pattern with a narrow gap (8–12 nm) along the *y*-axis [5].

2.1.3. SPR sensing strategies based on modulation of light intensity

SPR sensing strategies based on modulation of light intensity rely on detecting changes in the intensity of light reflected from a metal surface upon interaction with a target substance. In this approach, a laser or light source is directed at the metal surface at a specific angle, creating surface plasmon waves that are highly sensitive to changes in the refractive index near the surface. When a target molecule binds to the sensor surface, it alters the local refractive index, shifting the resonance condition and, consequently, modifying the intensity of the reflected light. By monitoring this change in intensity, the presence and concentration of the analyte can be determined with high sensitivity, making this technique particularly useful for real-time biosensing applications.

2.2. Effect of attenuation band of SPR on SRI sensitivity

The SRI sensitivity describes the shift in the attenuation band wavelength (Δλ) per unit change in the surrounding refractive index (Δn). To analyze the dependence of the attenuation band spectral position on SRI sensitivity, we start from the resonance condition in Equation (2-1). At resonance, the incident wavevector (k_{inc}) must match the surface plasmon wavevector (β_{sp}):

$$k_{inc} = \beta_{sp} \tag{2-3}$$

$$\frac{2\pi}{\lambda} n_{eff} = \frac{2\pi}{\lambda_{res}} \sqrt{\frac{\varepsilon_M n_D^2}{\varepsilon_M + n_D^2}} \tag{2-4}$$

where n_{eff} is the effective refractive index of the excitation mode. SRI sensitivity (S) is fundamentally defined as the derivative of the wavelength (λ) with respect to the refractive index of the dielectric environment (n_D)

$$S = \frac{\delta\lambda}{\delta n_D} = \frac{\lambda_{res}}{2} \cdot \frac{\varepsilon_m^2 n_D}{(\varepsilon_m + n_D^2)^2} \cdot \frac{1}{\sqrt{\frac{\varepsilon_m n_D^2}{\varepsilon_m + n_D^2}}} \tag{2-5}$$

According to Equations (2–5), the SRI sensitivity depends on the resonance wavelength, indicating higher sensitivity at longer wavelengths. Additionally, the sensitivity is influenced by the optical properties of the surface plasmon-active metal layer, particularly its permittivity (ε_m), with higher ε_m leading to greater sensitivity [6].

Both fiber-optic and prism-based SPR sensors exploit the SPR effect to detect refractive index changes but differ significantly in their configurations and applications. As discussed before, in prism-based SPR systems (e.g., the Kretschmann configuration), light passes through a high-refractive-index prism and strikes a thin metal film at a specific angle, exciting surface plasmons. The resonance condition depends on the analyte's refractive index, and the resulting shift is detected by monitoring changes in reflected light intensity. Prism-based SPR offers high stability, precise angular interrogation, and is widely used in laboratory biosensing applications, such as in Biacore instruments, due to its accuracy and reproducibility.

Fiber-optic SPR sensors consist of an optical fiber with a section with manipulation in structure to achieve evanescent wave, then coated with a thin metal layer (typically gold or silver). As light propagates through the fiber, the evanescent wave couples with the metal surface, exciting surface plasmons. When an analyte interacts with the metal coating, the local refractive index changes, altering the resonance condition and modulating the transmitted or reflected light. Fiber-optic SPR sensors are highly compact, flexible, and well-suited for remote and in-situ sensing, making them ideal for biomedical, environmental, and industrial applications.

The two sensing platforms differ fundamentally in their configuration, interrogation methods, and practical applications.

Prism-based SPR systems use a prism to generate total internal reflection (TIR), which excites surface plasmons. These systems typically rely on angular interrogation, where a shift in the resonance angle is measured. In contrast, fiber-optic SPR sensors use waveguiding through an optical fiber with a section of its cladding removed and coated with a metal film. This approach often utilizes wavelength or intensity modulation for signal detection.

Prism-based sensors are bulky and less portable, requiring precise optical alignment, which makes them best suited for controlled laboratory environments for high-precision biosensing tasks like drug discovery. Conversely, fiber-optic sensors are compact, lightweight, and flexible. Their design makes them ideal for real-time, in-situ monitoring in diverse settings, including medical diagnostics and environmental sensing, where their small size and resistance to electromagnetic interference (EMI) are advantageous. They are also generally more cost-effective and easier to integrate into portable devices.

While prism-based SPR remains the gold standard for lab-based, high-accuracy measurements, fiber-optic SPR offers superior portability, flexibility, and cost-effectiveness for real-world applications. The choice between the two depends on the specific requirements of sensitivity, stability, and deployment environment [7], [8], [9], [10], [11].

2.3. Selected studies of SPR based sensors

In this section, a few representative studies on the use of SPR phenomena for sensing applications will be discussed, with the aim of highlighting both their performance and the growing interest of the scientific community in novel sensing technologies.

In 2017, Zeng et al [12]. developed a SPR imaging sensor that uses a wavelength-scanning approach (WS-SPR). This system, which integrates an Acousto-Optic Tunable Filter (AOTF) and a white light laser (WLL), monitors the SPR resonance by varying the wavelength of the incident light while keeping the angle fixed. This method avoids moving parts, which enhances stability and repeatability. The system's performance was validated by detecting changes in refractive index using glycerol-water solutions, showing a sensitivity of 2000 nm/RIU and LOD of 1×10^{-6} RIU. Figure 2-3 (A) illustrates the feedback loop operation, while Figure 2-3 (B) depicts the experimental setup. Figures 2-3 (C) and (D) show the sensor's ability to track molecular interactions, including the SPR dip shift with changing salt concentrations and the real-time binding of an antigen-antibody pair 12].

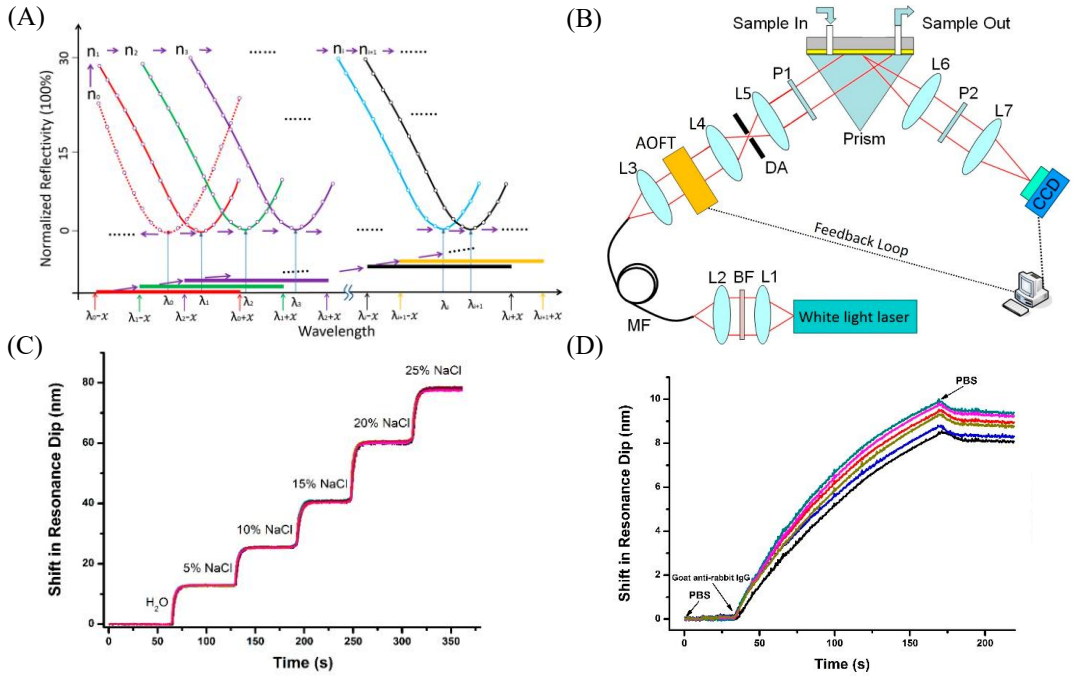

Figure 2-3 (A) Schematic of SPR dip tracking using a feedback loop technique. (B) Schematic of the SPR imaging (SPRi) system in the Kretschmann configuration. (C) SPR dip shift as a function of salt concentration in water. (D) Real-time wavelength response monitoring antigen-antibody binding between goat anti-rabbit IgG and rabbit IgG. Adapted from [12].

Alternatively, in Ref [5] the authors discuss a high-sensitivity biosensor based on an SPR structure, where the excitation is achieved through the modulation of incident angle. The sensor features a symmetrical triangular meta surface made of gold and silver layers, enhancing sensitivity to refractive index changes via angle modulation. At an operating wavelength of 632.8 nm, it achieves a peak

sensitivity of 364°/RIU, which is 1.7 times higher than traditional gold-layer sensors (135°/RIU) and 4.6 times higher than standard SPR configurations.

The design focuses the electric field to intensities up to 9×10^{10} V/m, boosting the light-analyte interaction. While this leads to a broader FWHM and a quality factor of 22.3, the sensor maintains a linear response (R = 0.99). Figures 2-4(A) illustrate the setup and the triangular meta surface's unit structure, and Figures 2-4(C) show the relationship between reflectivity and resonance angle [5].

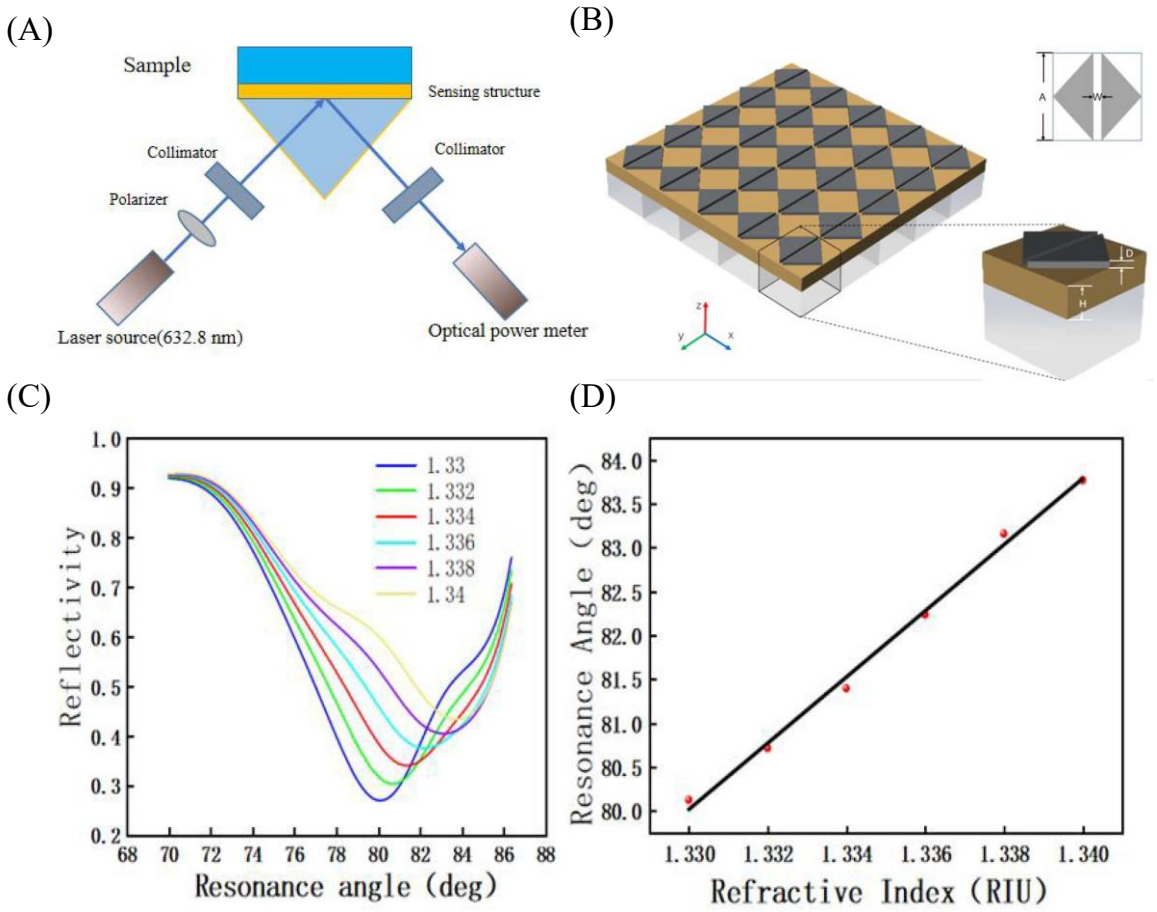

Figure 2-4. Sensor characterization: (A) Prism-based experimental schematic; (B) Metasurface unit structure with gold (H=43-51nm) and silver (D=8-12nm) layers featuring y-axis openings (W=8-12nm); (C) Reflectance curves for Δn=0.002; (D) Linear fitting of resonance angle vs refractive index. Adapted from [5].

SPR sensing strategies that utilize modulation of light intensity can be seen in Figure 2-5(A) as an example., where a 780 nm laser diode emits a 45° linearly polarized beam. Upon reflection from a gold-coated prism in contact with the analyte, the beam undergoes SPR. A photoelastic modulator (PEM), operating at 42 kHz, modulates the beam, and the reflected light's polarization state is analyzed using a lock-in amplifier to extract the 2nd and 3rd harmonic components of the modulated signal. The *s*-polarized component serves as a reference, while the *p*-polarized component carries SPR-induced phase variations.

The 2nd harmonic provides a combined response of phase and intensity, enabling:

- High sensitivity to minute RI changes (phase-dominated regime, detection limit: 2.89×10^{-7} RIU).
- Wide dynamic range for larger RI variations (intensity-dominated regime, up to 10^{-2} RIU).

The 3rd harmonic, optimized at a modulation amplitude of $\pi/2$, maximizes sensitivity while maintaining a detectable 2nd harmonic response. This approach achieves a 50-fold improvement in detection limit over conventional intensity-based SPR, with a demonstrated resolution of 5.5 10^{-7} RIU.

Figures 2-5(B) depict the integrated signals of the 3rd harmonics, along with their respective phase and intensity components, as functions of the refractive index [13].

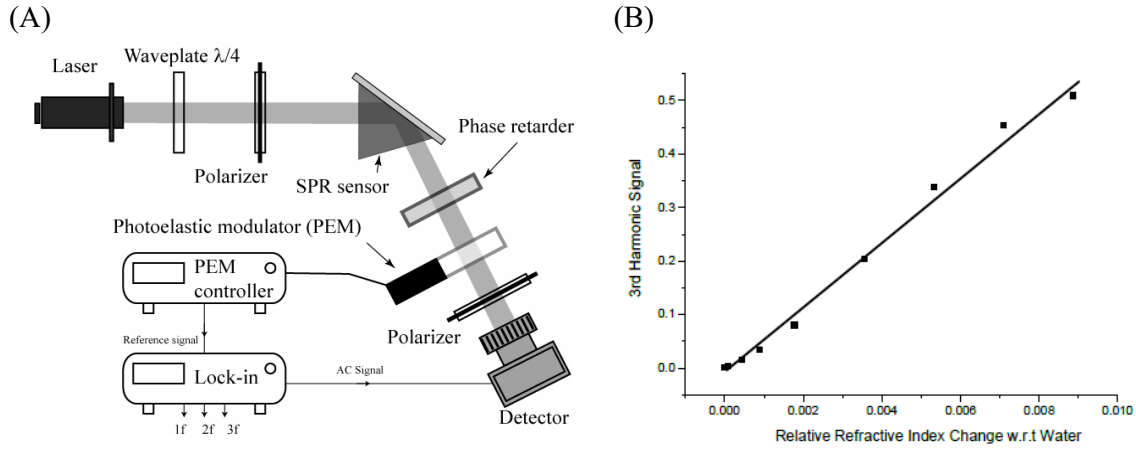

Figure 2-5 (A) Schematic diagram of the experimental setup. (B) Third harmonic generation response versus refractive index variation. Adapted from [13].

To demonstrate the effect of attenuation bands on sensitivity, a study compared the sensitivity of two configurations through experimentation [14], diffraction grating-based and prism-based couplers. Both setups use a thin gold (~50 nm) film to excite plasmons, and a laser source measures the reflected light intensity to detect resonance shifts caused by changes in the refractive index of a liquid. The diffraction grating-based sensor's sensitivity is comparable to the prism-based one but has distinct angular characteristics. Figure 2-6 shows that the sensitivity of the grating-based sensor increases with wavelength and depends on the grating pitch and diffraction order. Specifically, higher-order diffraction modes show greater sensitivity. The study concludes that while the prism-based sensor is a well-established method, the grating-based sensor offers potential for miniaturization [14].

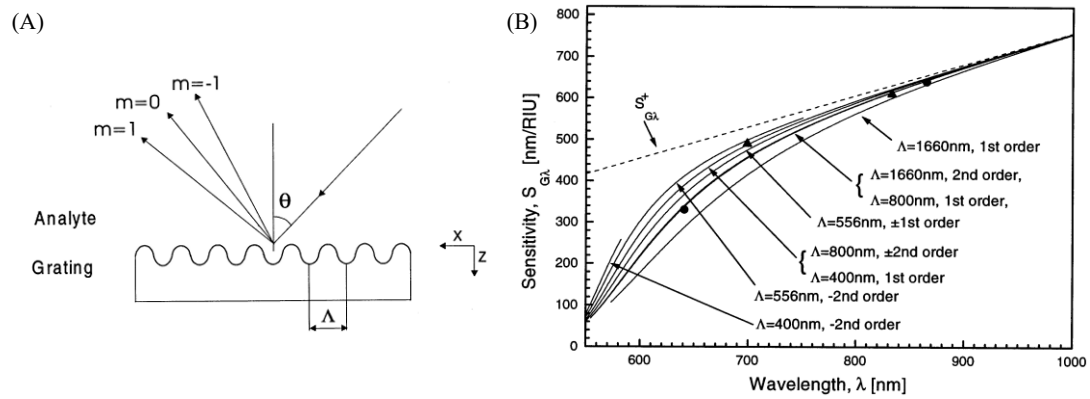

Figure 2-6.(A) Schematic of diffraction of light at the surface of a diffraction grating. (B) The spectral sensitivity is analyzed for a gold-coated diffraction grating with four different pitches, assuming an analyte refractive index of n = 1.32. The exact sensitivity values were calculated numerically using rigorous coupled-wave analysis (RCWA), Circles (○) represent the first diffraction order. Triangles (△) represent the second diffraction order. Adapted from [14].

Hitoshi Suzuki et al. [15] investigated how gold film thickness affects the performance of a multimode optical fiber-based SPR sensor. The study found that as the gold layer thickness increases, the resonance dip in the transmission spectrum shifts toward longer wavelengths. This behavior, shown in Figure 2-7 (A), is due to changes in plasmonic coupling efficiency. The research also found that sensitivity varies with film thickness. Figure 2-7 (B) demonstrates that while thinner films are more sensitive, there's an optimal intermediate thickness that balances sensitivity and spectral quality.

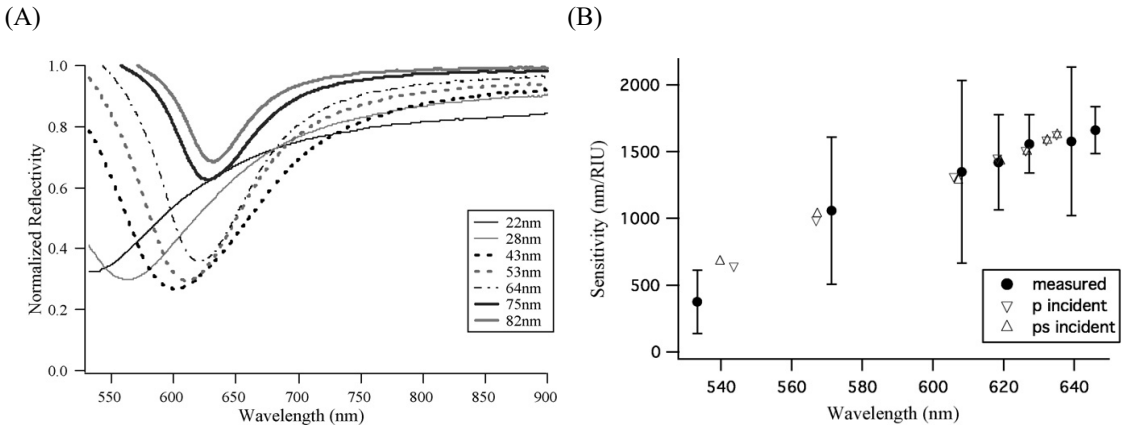

Figure 2-7 (A) Typical SPR spectra for distilled water. The resonance wavelength shifts toward longer wavelengths as the gold thickness increases. (B) Sensitivity dependence on wavelength. The wavelength for each gold thickness corresponds to the midpoint between the resonance wavelength for distilled water and that for a 20 wt.% ethanol solution. Adapted from [15].

Yagmur Yildizhan et al. [16] developed a fiber-optic SPR biosensor to detect breast cancer-specific extracellular vesicles (EVs). The sensor, coated with a ~50 nm gold film, uses specific antibodies to capture EVs, achieving a detection limit of 1.2×10^6 EVs/mL and a specificity of 92.5%. Within 10 minutes, the sensor observed a 3.8 nm resonance wavelength shift in cancer-derived EVs. The sensor is 3-fold more sensitive than ELISA and requires 40% less sample volume. Figure 2-8 (A) illustrates the FO-SPR EV detection sandwich bioassay protocol, which uses capture antibodies and AuNPs to

amplify the signal. Figure 2-8 (B) shows the results of this bioassay, and Figure 2-8 (C) presents a linear regression fit demonstrating the sensor's performance.

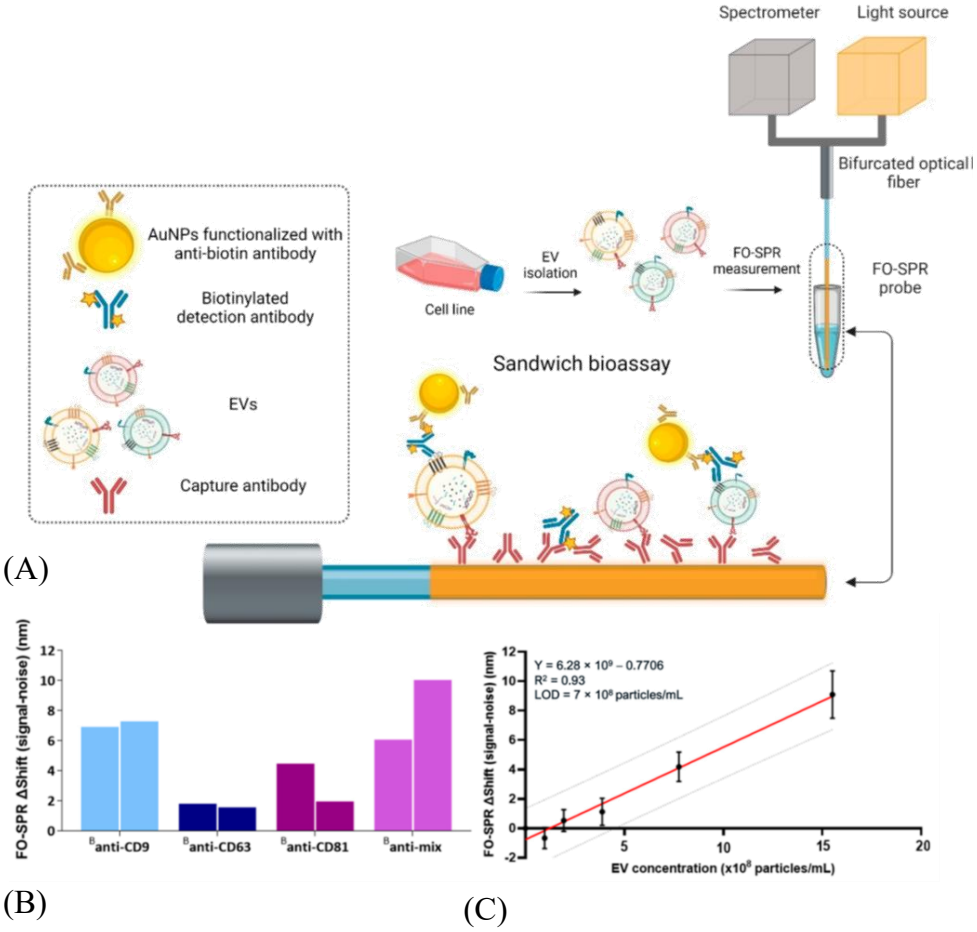

Figure 2-8. (A) Schematic illustrating the key steps in the FO-SPR EV detection sandwich bioassay. (B) FO-SPR sandwich bioassay utilizing distinct antibody combinations for detection. (C) Data were analyzed using simple linear regression. Adapted from [16].

In another work, Sarika Singh et al. [17] developed a SPR fiber optic biosensor for detecting phenolic compounds in water. The sensor was made by coating an optical fiber with a silver film and then immobilizing the enzyme tyrosinase (PPO) using a gel entrapment method. The sensor's response was measured using a wavelength interrogation technique. Experimental results showed a red shift in the resonance wavelength as the concentration of phenolic compounds increased.

In Ref [18] introduced another investigation, Jeroen Pollet et al. introduced a reusable, and label-free fiber optic SPR sensor for detecting DNA hybridization and DNA-protein interactions. The fiber was coated with a 50 nm gold layer, followed by a protein-repulsive self-assembled monolayer of mixed polyethylene glycol (PEG) and streptavidin, which was used to attach biotinylated ssDNA. The sensor was first tested for DNA hybridization using a 37-mer ssDNA with a 15-nucleotide overlap, showing a linear response in the 0.5-5 µM range. In a second assay, the sensor was functionalized with ssDNA aptamers to detect human immunoglobulin E (hIgE), achieving a LOD of 2 nM and a limit of

quantification (LOQ) of 6 nM. The dissociation constant between the aptamer and hIgE was determined to be 30.9 ± 2.9 nM, and the sensor was also easily regenerated.

In a recent investigation, Sonia Akter et al. [19] have proposed a gold-coated optical fiber biosensor that uses SPR to non-invasively detect pregnancy by analyzing urine samples. The sensor was designed to differentiate between the RI of normal urine, which is 1.335 and 1.34, and pregnant urine, which is 1.342 and 1.343. The sensor features a 50 nm thick gold layer and operates in the wavelength range of 1.1 µm to 2.0 µm. Through finite element method (FEM) simulations, the sensor demonstrated a high wavelength sensitivity of 8535.18 nm/RIU at an RI of 1.335, a figure of merit (FOM) of 56.52 RIU^{-1}, and a LOD of 93.88 nm. Other performance metrics include a maximum birefringence of 1.24×10^{-2}, a coupling length of 769.88 µm, a transmittance of -23.47 dB, and a power spectrum shift of 1 dBm^{-1}.

In other job, Wenjia Wang et al. [20] proposed and demonstrated a highly sensitive, label-free fiber optic biosensor for detecting C-reactive protein (CRP). The researchers used dopamine as a cross-linking agent to immobilize anti-CRP monoclonal antibodies. This modified sensor successfully and specifically detected CRP, showing a linear response ($R^2 = 0.97$) for concentrations ranging from 0.01 to 20 µg/ml. The highest sensitivity was 1.17 nm per lg (µg/ml).

As another example, Jiangli Dong et al. [21] proposed and demonstrated a few-mode fiber (FMF) based SPR biosensor. The sensor was created by side-polishing a few-mode fiber and coating it with a thin layer of gold film. The researchers optimized the fiber's geometry, gold film thickness, and mode selection using the finite element method. They tested three sensors with different residual fiber thicknesses and achieved a maximum SRI sensitivity of 4903 nm/RIU and a FOM of 46.1 RIU^{-1} in the SRI range of 1.333 to 1.404. For solutions, the sensor showed an average sensitivity of 6328 nm/RIU for SRI and 1.17 nm/(mg/ml) for concentration. The study also included a schematic of the sensor in Figure 2-9. (A) and a cross-section in Figure 2-9. (B).

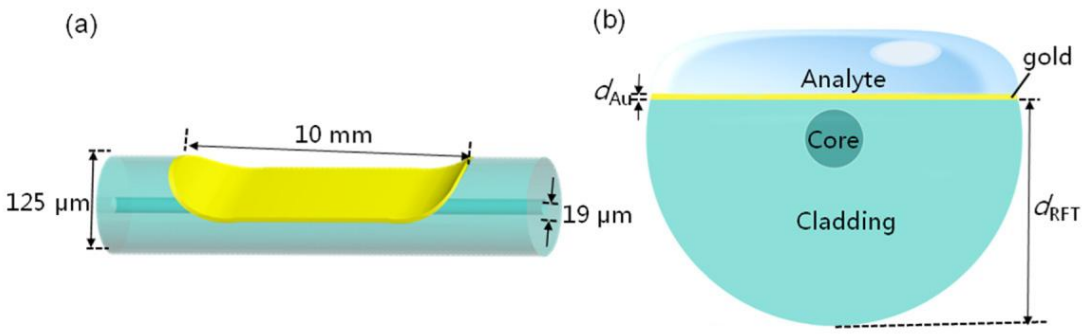

Figure 2-9. (A) Schematic of the FMF-SPR sensor. (B) Cross section of the FMF-SPR sensor. Adapted from [21].

Jitendra Narayan Dash et al. [22] proposed a D-shaped photonic crystal fiber (PCF) sensor that uses SPR for detecting the refractive index of an analyte and the thickness of a biolayer. The sensor incorporates a graphene layer over silver, which both helps adsorb biomolecules and prevents the

oxidation of the silver. Numerical simulations showed the sensor's amplitude sensitivity for chemical analytes to be 216 RIU^{-1}, with a resolution of 4.6×10^{-5} RIU. Wavelength sensitivity was found to be as high as 3700 nm RIU^{-1}, with a resolution of 2.7×10^{-5} RIU. The sensor can also measure biolayer thickness with an amplitude sensitivity of 0.26 nm^{-1} and a resolution of 39 pm, or a wavelength sensitivity of 2 nm nm^{-1} and a resolution of 50 pm.

2.4. Theoretical principles of LSPR

LSPR refers to the interaction between electrons in metallic nanostructures and the electromagnetic field of incident light [23]. This phenomenon occurs due to the scattering behavior of small conductive particles when exposed to an oscillating electromagnetic field. As shown in Figure 0-10, when light excites these particles, electron and ion clusters form on their curved surfaces. These clusters generate a restoring force, leading to resonance and an amplified electromagnetic field both inside and outside the metal particles an effect known as **LSPR**.

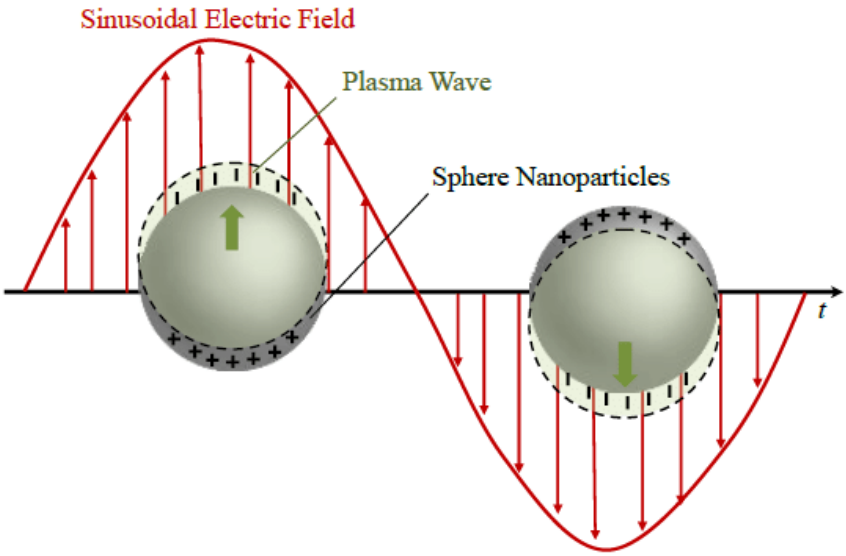

Figure 2-10 Schematic illustration of LSPR. Adapted from [24].

LSPR can be induced by direct light interaction, allowing various light sources to be used in LSPR-based sensing systems. Noble metals like gold and silver exhibit resonance wavelengths within the visible spectrum, which is why their colloidal solutions display vivid colors [25]. This behavior stems from the scattering and absorption properties of small metal particles, a concept theoretically explained by Gustav Mie (1869–1957). His 1908 paper applied Maxwell's electromagnetic equations to describe this phenomenon [26], establishing a crucial framework for analyzing and predicting the properties of nanostructures beyond just spherical particles. Below, we discuss some fundamental theories related to this.

2.4.1. Mie Theory

Mie conducted extensive calculations on light scattering by small spherical particles using Maxwell's equations from electromagnetic theory. Through this approach, he successfully accounted for the ruby-red color of gold colloidal solutions by applying principles of absorption and scattering. However, it was only in the 1950s that research on colloids gained significant attention. Since then, numerous studies have expanded on Mie's original theory, adapting it for particles of different compositions, sizes, and shapes, including non-spherical particles, spheres in absorbing media, and coated, distorted, magnetic, chiral, and anisotropic spheres, ranging from a few nanometers to 10 micrometers in diameter [25].

To analyze Maxwell's equations for spherical particles in a non-absorbing medium, Mie derived key formulas for scattering, absorption, and extinction cross-sections. While detailed mathematical derivations can be found in specialized textbooks [27], [28], this thesis presents only the final relevant equations as follows [27], [28]:

$$\sigma_{sca} = \frac{2\pi}{|k|^2}\sum_{L=1}^{\infty}(2L+1)(|a_L|^2 + |b_L|^2) \tag{2-6}$$

$$\sigma_{ext} = \frac{2\pi}{|k|^2}\sum_{L=1}^{\infty}(2L+1)[Re(|a_L| + |b_L|)] \tag{2-7}$$

$$\sigma_{abs} = \sigma_{sca} - \sigma_{ext} \tag{2-8}$$

In these equations, k represents the wavevector of the incident light, while L denotes integer values corresponding to different multipole moments of scattering (such as dipole (L=1), quadrupole (L=2), and higher-order terms). The coefficients a_l and b_l are defined using Ricatti-Bessel functions (Ψ_L and χ_L), which describe the scattering behavior of spherical particles.

$$a_L = \frac{m\Psi_L(mx)\Psi_L'(x) - \Psi_L'(mx)\Psi_L(x)}{m\Psi_L(mx)\chi_L'(x) - \Psi_L'(mx)\chi_L(x)} \tag{2-9}$$

$$b_L = \frac{\Psi_L(mx)\Psi_L'(x) - m\Psi_L'(mx)\Psi_L(x)}{\Psi_L(mx)\chi_L'(x) - m\Psi_L'(mx)\chi_L(x)} \tag{2-10}$$

The parameter m is defined as the ratio of complex refractive indices, where $m = \tilde{n}/n_m$. Here, $\tilde{n} = n_R + in_I$ represents the complex refractive index of the metallic material (with n_R and n_I being its real and imaginary components, respectively), while n_m denotes the refractive index of the surrounding dielectric medium. This formulation:

$$m = \frac{\tilde{n}}{n_m} = \frac{\tilde{n} = n_R + in_I}{n_m} \tag{2-11}$$

$$\chi = k_m r = \frac{2\pi}{\lambda_m} r \tag{2-12}$$

With k_m is the wavenumber in the medium.

Equations (2-6)-(2-12) represent generalized formulations applicable to particles of various sizes and morphologies. However, under specific conditions, these expressions can be significantly simplified to provide more intuitive physical insights. A notable case occurs when analyzing spherical nanoparticles with diameters substantially smaller than the excitation wavelength ($2\pi r \ll \lambda$, or equivalently, $x \ll 1$). In this regime the higher-order multipole terms (a_L and b_L for $L \geq 2$) become negligible. Equations (2-9) and (2-10) reduce to the simplified forms presented in (2-13) and (2-14). This approximation effectively considers only dipole contributions while ignoring quadrupole and higher-order effects.

$$a_1 \approx -\frac{i2x^3}{3}\frac{m^2-1}{m^2+2} \tag{2-13}$$

$$b_1 \approx 0 \tag{2-14}$$

Substitute m in Equation (2-12) into Equation (2-13), then:

$$a_1 \approx -\frac{i2x^3}{3}\frac{n_R^2 - n_I^2 + 2in_Rn_I - n_m^2}{n_R^2 - n_I^2 + 2in_Rn_I + 2n_m^2} \tag{2-15}$$

When accounting for the complex dielectric function of metals, we can express:

$$\tilde{\varepsilon} = \varepsilon_1 + i\varepsilon_2 \tag{2-16}$$

$$\varepsilon_1 = n_R^2 - n_I^2 \tag{2-17}$$

$$\varepsilon_2 = 2n_Rn_I \tag{2-18}$$

$$\varepsilon_m = n_m^2 \tag{2-19}$$

Eequation (2-15) can be modified to be

$$a_1 \approx \frac{i2x^3}{3}\frac{-i\varepsilon_1^2 - i\varepsilon_1\varepsilon_m + 3\varepsilon_2\varepsilon_m - i\varepsilon_2^2 + 2i\varepsilon_m^2}{(\varepsilon_1 + 2\varepsilon_m)^2 + \varepsilon_2^2} \tag{2-20}$$

By substituting the complex dielectric function into Equation (2-6) and (2-7), we obtain explicit expressions for the scattering (σ_{sca}) and extinction (σ_{ext}) coefficients

$$\sigma_{sca} = \frac{32\pi^4\varepsilon_m^2V^2}{\lambda^4}\frac{(\varepsilon_1 - \varepsilon_m)^2 + \varepsilon_2^2}{(\varepsilon_1 + 2\varepsilon_m)^2 + \varepsilon_2^2} \tag{2-21}$$

$$\sigma_{ext} = \frac{18\pi\varepsilon_m^{3/2}V}{\lambda}\frac{\varepsilon_2(\lambda)}{(\varepsilon_1(\lambda) + 2\varepsilon_m)^2 + \left(\varepsilon_2(\lambda)\right)^2} \tag{2-22}$$

Equation (2-22) serves as a fundamental tool for modeling the extinction spectra of small nanoparticles under optical excitation. The extinction cross-section (σ_{ext}) depends critically on three

parameters: the particle size through its volume V (which scales with the radius r as $V \propto r^3$), the material's complex dielectric function components $\varepsilon_1(\lambda)$ and $\varepsilon_2(\lambda)$, and the permittivity of the surrounding medium ε_m. The extinction reaches its maximum when the denominator$[\varepsilon_1(\lambda) + 2\varepsilon_m]^2 + \varepsilon_2(\lambda)^2$ is minimized, a condition that is optimally satisfied when $\varepsilon_1(\lambda) \approx -2\varepsilon_m$, known as the Fröhlich resonance condition [23].

For noble metals such as gold (Au) and silver (Ag), this theoretical framework allows precise calculation of σ_{ext}, as demonstrated in previous studies [27], [29], [30]. Notably, the model shows excellent agreement between theoretical predictions and experimental measurements, particularly for small nanoparticles (<50 nm) where the dipole approximation remains valid. This agreement underscores the model's reliability for predicting the optical response of plasmonic nanostructures [29], [31], [32].

The resonance condition $\varepsilon_1(\lambda) \approx -2\varepsilon_m$, not only explains the strong extinction peaks observed in gold and silver nanoparticles but also accounts for the vivid color variations in their colloidal solutions. These colors arise from the wavelength-dependent scattering and absorption characteristics dictated by the nanoparticles' plasmonic properties. Furthermore, this theoretical approach provides quantitative design rules for optimizing plasmonic nanoparticles in sensing applications, where maximizing the extinction efficiency is often crucial.

The success of this model in matching experimental data confirms its utility in predicting and interpreting the optical behavior of metallic nanoparticles. However, its accuracy is highest for particles small enough to neglect higher-order multipole contributions, typically below 50 nm in diameter. For larger particles, additional effects such as quadrupole resonances and radiation damping must be considered, requiring more advanced theoretical treatments. Nevertheless, for many practical applications involving small gold and silver nanoparticles, Equation (2-22) remains a powerful and widely used tool for understanding and designing plasmonic systems.

Table 2-1Values of dielectric constants of different metals. Adapted from [33].

Metal	**Dielectric constant** $(\boldsymbol{\varepsilon_1 + i\varepsilon_2})$	$\boldsymbol{\varepsilon_1/\varepsilon_2}$
Gold (Au)	-10.92 + 1.49i	7.33
Copper (Cu)	-14.67 + 0.72i	20.4
Silver (Ag)	-18.22 + 0.48i	38.0
Aluminium (Al)	-42.00 + 16.40i	2.56

Table 2.1 presents the dielectric constants of some common metals, enabling the calculation and comparison of their extinction spectra using the equations discussed previously. The theoretical results

for gold and silver are shown in Figure 2-11, where distinct differences in their optical properties become evident.

Figure 0-11(A) displays the real part (ε_1) of the dielectric functions for gold (yellow line) and silver (gray line), revealing that ε_1(Au) > ε_1 (Ag) across the examined spectral range. This difference influences their respective plasmonic responses, particularly in terms of resonance energy and field enhancement. Figure 0-11 (B) plots the imaginary part (ε_2) of the dielectric functions, which plays a crucial role in plasmon resonance damping and peak broadening. The lower ε_2 values for silver compared to gold indicate reduced losses, leading to sharper resonance peaks in silver nanostructures.

This theoretical prediction is further supported by experimental observations. Figure 0-11(C) shows the absorption spectrum of a gold and silver colloid solution, where broader resonance peaks are observed due to higher intrinsic losses in gold. In contrast, silver exhibits narrower resonances, consistent with its lower ε_2 values. The sharper plasmonic peaks in silver make it particularly attractive for applications requiring high field confinement and spectral precision, such as sensing and nanophotonics [34], [35]. These findings highlight the importance of material selection in plasmonic system design, where trade-offs between resonance quality, loss, and spectral tunability must be carefully considered.

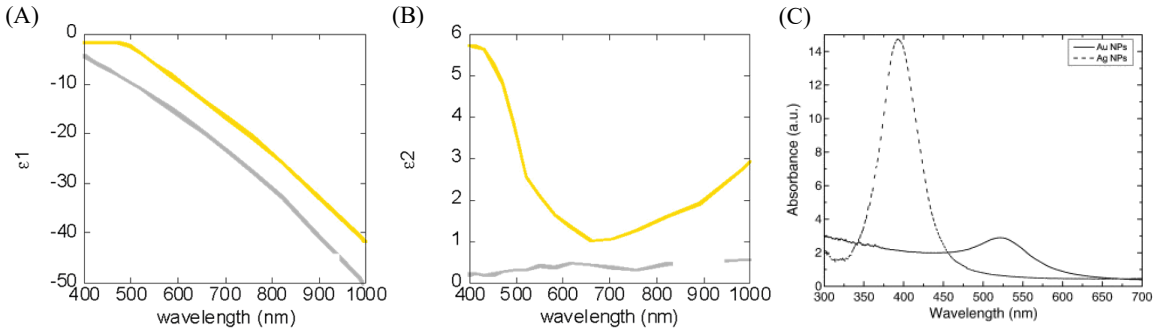

Figure 2-11 (A) Real and (B) Imaginary part of extinction spectra from gold (yellow line) and silver (grey line) [36]. (C) Normalized UV–vis spectra of 10 nm gold (continuous line) and silver (dashed line) colloidal NPs. Each spectrum is normalized by the corresponding NPs concentration. Adapted from [35].

2.4.2. Discrete Dipole Approximation (DDA) calculations

While the original Mie theory provides a rigorous framework for analyzing light scattering by spherical nanoparticles, its applicability becomes limited when dealing with real-world nanostructures that often exhibit deviations from perfect sphericity. To address this challenge, E.M. Purcell and C.R. Pennypacker [37] pioneered a numerical approach that extends beyond the constraints of classical Mie theory, enabling the analysis of nonspherical particles. This methodological advancement has been further developed in comprehensive treatments, such as Enguehard's book chapter [38] and subsequent studies, which detail the complex computational procedures involved [39], [40], [41], [42], [43].

A particularly useful synthesis of contemporary modeling techniques was presented by Zhao et al. [30], who systematically compared various approaches for characterizing nanoparticle optical properties, including scattering and absorption spectra. Their work notably highlighted the DDA method, which has emerged as a powerful computational tool for analyzing arbitrarily shaped nanostructures. The DDA method, first introduced in this context, represents a significant advancement over traditional Mie theory by discretizing particles into arrays of interacting dipoles, thereby accommodating diverse morphologies encountered in experimental systems.

These developments in theoretical modeling have been crucial for bridging the gap between idealized spherical systems and practical nanostructures, enabling more accurate predictions of optical properties for real-world NPs samples with complex geometries and compositions. The evolution from Mie's analytical solutions to modern numerical approaches reflects the growing sophistication required to address the challenges posed by nanomaterial characterization in cutting-edge plasmonic research.

In DDA calculations, a NPs is typically represented by a three-dimensional array of dipole elements arranged within a cubic grid. Each element possesses a polarizability $\alpha_i (i: 1 \rightarrow N)$, which is determined by the dielectric function of the NP. The dipole moment P_i of each element is given by $P_i = \alpha_i E_{loc,i}$, where $E_{loc,i}$ represents the local electric field. This field is the combined effect of the incident field and the retarded fields from the remaining N−1 dipole elements, as described by Equation 2-21.

$$E_{loc,i} = E_{inc,i} + E_{dipole,i} = E^0 e^{ik \cdot r_i} - \sum_{\substack{j=1 \\ j \neq i}}^{N} A_{ij} \cdot P_j \qquad (2\text{-}23)$$

where E^0 is the amplitude of incident wavelength, and $k = 2\pi/\lambda$ is the wave vector and A_{ij} is the matrix of dipole interaction and is given by:

$$A_{ij} = k^2 e^{ikr_{ij}} \frac{r_{ij} \times (r_{ij} \times P_j)}{r_{ij}^3} + e^{ikr_{ij}} (1 - ikr_{ij}) \frac{[r_{ij}^3 P_j - 3r_{ij}(r_{ij} \cdot P_j)]}{r_{ij}^5} \qquad (2\text{-}24)$$

With r_{ij} is the vector from element i to element j. After having solved these equations, the final conclusion for extinction cross-section is given by:

$$C_{ext} = \frac{4\pi k}{\left|\vec{E}^{inc}\right|^2} \sum_{j=1}^{N} Im\left[\vec{E}_j^{inc,*}\right] \cdot \vec{P}_j \qquad (2\text{-}25)$$

The DDA method has become a well-established and widely utilized computational approach for simulating diverse nanostructures, including nanotriangles, nanodisks, nanocubes, core-shell particles, and hollow particles, with sizes ranging from a few nanometers to several hundred nanometers. This method has been particularly valuable in the work of the El-Sayed group, who have successfully applied DDA calculations to investigate various metallic nanostructures, such as gold-silver alloys with different composition ratios and sizes, gold nanorods, gold nanocages, and coupled nanoparticle systems[44], [45], [46], [47]. Their computational results have demonstrated excellent agreement with

experimental observations, establishing DDA as a powerful predictive tool for plasmonic applications. Notably, these simulations have contributed significantly to sensing technologies, including the development of gold nanoframes with enhanced refractive index sensitivity [48].

Beyond Mie theory and DDA, numerous other numerical methods have been developed for nanoparticle characterization. Thomas Wriedt's 1998 review comprehensively examined various computational approaches, including the point matching method, T-matrix method, generalized multipole technique (GMT), and several volume-based methods such as finite difference time domain (FDTD), transmission line matrix (TLM), volume integral equation (VIE), and FEM [41]. Myroshnychenko [49] and colleagues later provided a comparative analysis of popular techniques like DDA, FDTD, and boundary element method (BEM), highlighting their respective strengths and limitations. A.R. Jones further contributed to this field with an extensive review of light scattering characterization methods [50].

The continuous advancement of computational technology, marked by increasing processing power and improved algorithmic efficiency, has dramatically enhanced the capability of these numerical methods. This progress has enabled researchers to investigate increasingly complex nanostructures with greater accuracy, opening new possibilities for tailored nanomaterial design across various applications. These computational tools have become indispensable for both fundamental studies of light-matter interactions at the nanoscale and the development of practical plasmonic devices, bridging the gap between theoretical predictions and experimental realization in nanophotonics research.

2.5. Effect of attenuation band in LSPR in sensitivity

As in previous section discussed, the resonance condition for LSPR emerges from the quasi-static approximation, which applies when NPs are significantly smaller than the excitation wavelength (typically $d < \lambda/10$). This condition is mathematically expressed as [51]:

$$\varepsilon_1(\lambda) \approx -2\varepsilon_m \qquad (2\text{-}26)$$

Where $\varepsilon_1(\lambda)$ is the real part of the permittivity of the metal, and ε_m is the dielectric constant of the surrounding medium, which is related to its refractive index. The LSPR peak frequency is related to the plasma frequency of the metal as:

$$\omega_{LSPR} = \frac{\omega_p}{\sqrt{1 + 2\varepsilon_m}} \qquad (2\text{-}27)$$

Where metal plasma frequency (ω_p) is the natural angular frequency at which the free conduction electrons in a metal collectively oscillate in response to an external electromagnetic field, assuming the positive ion lattice remains stationary. It is a fundamental material parameter determined by the free

electron density and their effective mass, and it sets the upper frequency limit for which the metal exhibits negative real permittivity and supports plasmonic resonances, formally, it is given by:

$$\omega_p = \sqrt{\frac{n_e e^2}{\varepsilon_0 m^*}} \tag{2-28}$$

Where n_e is the free electron density, e is the elementary charge, ε_0 is the vacuum permittivity and m^* is the effective electron mass. What this really means is that $\omega_p$defines the intrinsic timescale of electron response in a metal.

To express this in terms of wavelength, we use $\lambda_{max} = \frac{2\pi c}{\omega_{max}}$ and $\varepsilon_d = n_d^2$, n_d refractive index of the dielectric medium surrounding, Substituting ω_{max}:

$$\lambda_{LSPR} = \lambda_P \sqrt{1 + 2n_d^2} \tag{2-29}$$

The sensitivity of an LSPR sensor is defined as the shift in resonance wavelength $\partial\lambda_{LSPR}$ per unit change in refractive index (∂n_d):

$$S = \frac{\partial \lambda_{LSPR}}{\partial n_d} = \frac{2\lambda_P n_d}{\sqrt{1 + 2n_d^2}} \tag{2-30}$$

The sensitivity of LSPR-based sensors is intrinsically linked to the resonance band position, which is determined by the nanoparticle's material, size, shape, and surrounding dielectric environment. By tuning the LSPR resonance band, through careful selection of metal (e.g., Au, Ag), nanostructure geometry (e.g., spheres, rods, or stars), and dielectric medium, we can effectively control the SRI sensitivity. Shifting the resonance toward longer wavelengths (e.g., near-infrared) typically enhances sensitivity due to the stronger field confinement and increased interaction volume with the surrounding medium. This tunability allows for the optimization of LSPR sensors for specific applications, such as biosensing or chemical detection, where high sensitivity to small SRI changes is crucial [52], [53], [54], [55].

Moreover, the derived relationship between sensitivity and the LSPR resonance condition highlights the importance of plasmonic material properties, particularly the plasma wavelength (λ_P).Additionally, nanostructures with sharp edges or tips exhibit enhanced localized fields, further boosting sensitivity. These insights provide a foundation for designing advanced LSPR sensors with tailored performance, enabling precise detection in fields ranging from medical diagnostics to environmental monitoring. By strategically engineering the LSPR resonance band, researchers can achieve the desired balance between sensitivity, selectivity, and practical applicability in real-world sensing scenarios [30], [36], [56], [57].

2.6. Dependency of LSPR on nanostructure shape

As an example for the attenuation band in LSPR in sensitivity, Rabbani et al. [58] investigated the effect of the LSPR attenuation band on the refractive index sensitivity of plasmonic biosensors by combining quasistatic and effective medium theories, showing that the local sensitivity scales linearly with the LSPR resonant wavelength. Their analysis demonstrated that the spectral position of the LSPR peak, which defines the attenuation band in the extinction spectrum, directly governs the magnitude of sensitivity to surrounding refractive index variations. A red-shift in the attenuation band corresponds to a proportional increase in sensitivity, particularly when the analyte layer thickness expands the effective sensing volume.

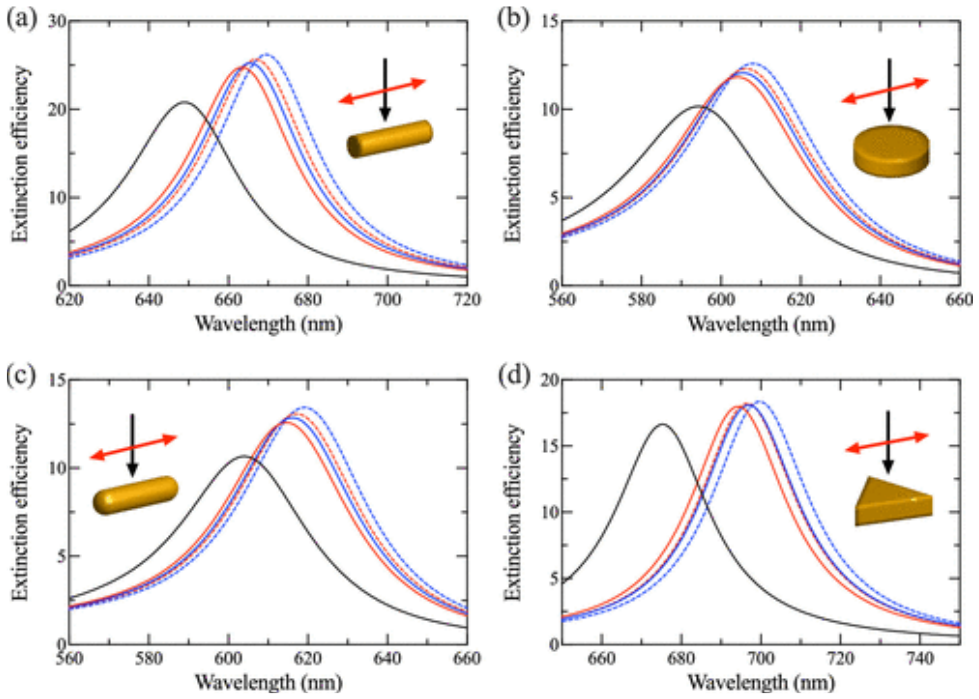

Figure 2-12. Extinction spectra in two-layer system of (a) 40 nm × 20 nm nanocylinder, (b) 40 nm × 12 nm nanodisk, (c) 40 nm × 20 nm nanorod, and (d) 40 nm × 10 nm nanotriangle. In all spectra, the analyte layer has a thickness t = 10 nm (solid) and t = 20 nm (dashed) and an analyte layer RI n = 1.40 (red) and n = 1.41 (blue). For comparison, the extinction spectrum of the nanoparticles without an analyte layer is also shown (black). The inset in each panel shows a schematic of the nanoparticle, as well as the directions of the incident light (black arrow) and its electric field (red arrow). Adapted from [58].

Figure 2-12 clearly illustrates how the extinction spectra of different nanoparticle geometries respond to changes in analyte layer refractive index and thickness. The red-shift of the LSPR peak is more pronounced with thicker layers, confirming that both the attenuation band position and the electromagnetic field confinement around the nanoparticle critically enhance sensitivity. This figure emphasizes that nanocylinders and nanotriangles exhibit sharper and stronger spectral shifts compared to disks and rods, underlining the importance of geometry in modulating the attenuation band and, consequently, the sensing performance.

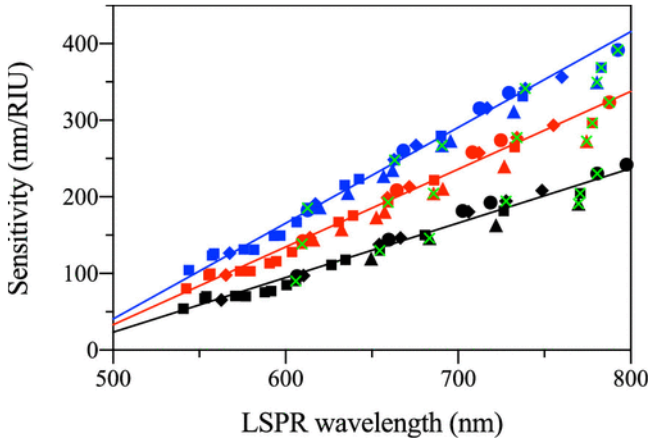

Figure 2-13. Dependence of the local RI sensitivity on LSPR wavelength. Adapted from [58].

Similarly, Figure 2-13 provides a unifying perspective by plotting the SRI sensitivity as a function of LSPR wavelength for various nanoparticle geometries. The results follow a nearly linear trend, verifying the theoretical prediction that sensitivity is intrinsically linked to the position of the attenuation band. Importantly, this figure shows that irrespective of nanoparticle shape, when normalized to characteristic length and analyte layer thickness, the sensitivities align along the linear model. This reinforces that the attenuation band wavelength is not just a spectral feature but the principal determinant of the biosensor's refractive index sensitivity.

2.7. Selected studies of LSPR fiber optic sensors

Several different fiber optic configurations can generate evanescent waves and excite LSPR. These include U-shaped fibers, D-shaped fibers, tapered fibers, and tip-modified fibers, each offering unique advantages for sensing applications. Below, we discuss examples of each configuration and their respective properties.

2.7.1. U-shape fiber

Li et al. [59] introduced and investigated a LSPR biosensor based on a U-shaped multi-mode fiber (U-MMF). The sensor, which they termed n*(Au/G)@U-MMF, was modified with a three-dimensional (3D) complex of gold nanoparticles and multilayer graphene as a spacer. The number of gold-nanoparticle layers (n) was found to be crucial for sensor performance. The sensor demonstrated a high sensitivity of 1251.44 nm/RIU, along with excellent stability and repeatability. It performed well in detecting time- and concentration-dependent DNA hybridization kinetics, with detection concentrations ranging from 0.1 nM to 100 nM, showing great potential for medical diagnostics. The study includes a schematic of the sensor's preparation procedure and experimental setup in Figure 2-14 (A) and (B).

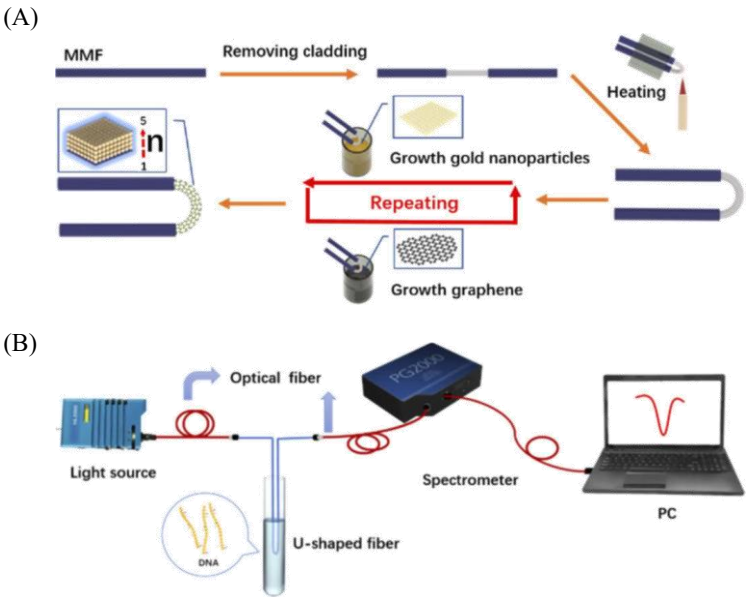

Figure 2-14 (A) Schematic of the preparation procedure of n*(Au/G)@U-MMF. (B) Schematic of the experimental set-up used for the U-MMF LSPR sensor. Adapted from [59].

In Ref [60], Sachin K et al. created the first fiber optic glucose sensor using the localized surface plasmon resonance of metal nanoparticles. The sensor was fashioned into a U-shaped probe with a bending radius of ~0.982 mm to improve sensitivity. The probe was prepared by first attaching gold nanoparticles to the fiber core and then immobilizing glucose oxidase on top. The sensor works by an intensity modulation scheme. When glucose is present, it reacts with the glucose oxidase, altering the local refractive index and causing changes in the absorbance of the gold nanoparticles.

Aoxiang Xiao et al. [61] presented a label-free biosensor for the detection of glial fibrillary acidic protein (GFAP), a biomarker for traumatic brain injury (TBI), by means of optical microfiber. They used various gold nanoparticle interfaces to enhance the evanescent field. The sensor with a gold nanostar interface was the most sensitive, achieving a LOD of 0.09 aM in PBS solution. This sensor can detect GFAP at concentrations from 1 aM to 0.1 nM, capable of single-molecule level detection. When tested in body fluids, the LODs were 0.21 aM in serum and 0.1 aM in artificial cerebrospinal fluid (CSF). A schematic of the sensor is provided in Figure 2-15.

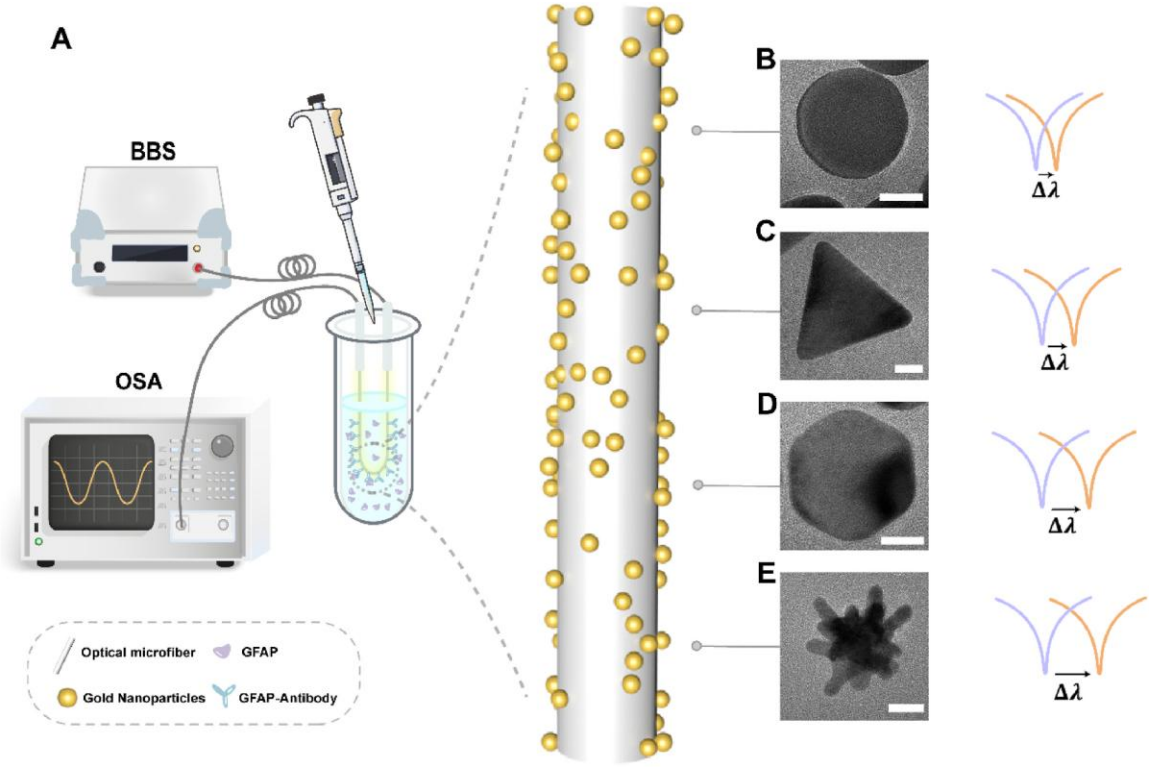

Figure 2-15. A. Scheme of the different morphologies of gold nanoparticle interface-functionalized optical microfiber for the detection of the cancer cell protein biomarker GFAP. Transmission electron microscope (TEM) images of B. gold nanodisk, C. gold nanotriangle, D. gold nanohexagonal, E. gold nanostar. (scale bar: 20 nm).

Zewei Luo et al. [62] developed a U-shaped fiber optic LSPR sensor for the label-free detection of N-glycan expression on cell surfaces, which is crucial for understanding cancer progression . Under optimal conditions, the sensor achieved an ultra-low LOD of 30 cells/mL with a linear range from 1×102 to 1×106 cells/mL. This performance represents a 29-times lower LOD compared to straight fiber sensors. The U-shaped sensor also demonstrated reproducibility, anti-interference, and selectivity, and was used to evaluate N-glycan expression on six different cancer cell lines.

2.7.2. D-Shape fiber

In this section, several representative studies employing D-shaped fiber structures are reviewed and discussed. First, in Ref [63], dos Santos and colleagues proposed a D-shape fiber optic with golden thin file and deposited by using high aspect-ratio colloidal core-shell Ag@Au nanorods (NRs). These NRs operate at telecommunication wavelengths and show SRI of 1720 nm/RIU at 1350 nm (O-band) and 2325 nm/RIU at 1550 nm (L-band), a five-fold improvement over similar gold NRs. The nanorods combine the optical performance of silver with the chemical stability of gold. When used in a side-polished optical fiber to detect glyphosate, the detection limit improved from 724 mg/L to 85 mg/L by shifting from the O to the C/L optical bands. The experimental setup shown in Figure 2-16 uses a broadband light source and an optical spectrum analyzer for real-time monitoring of these spectral changes.

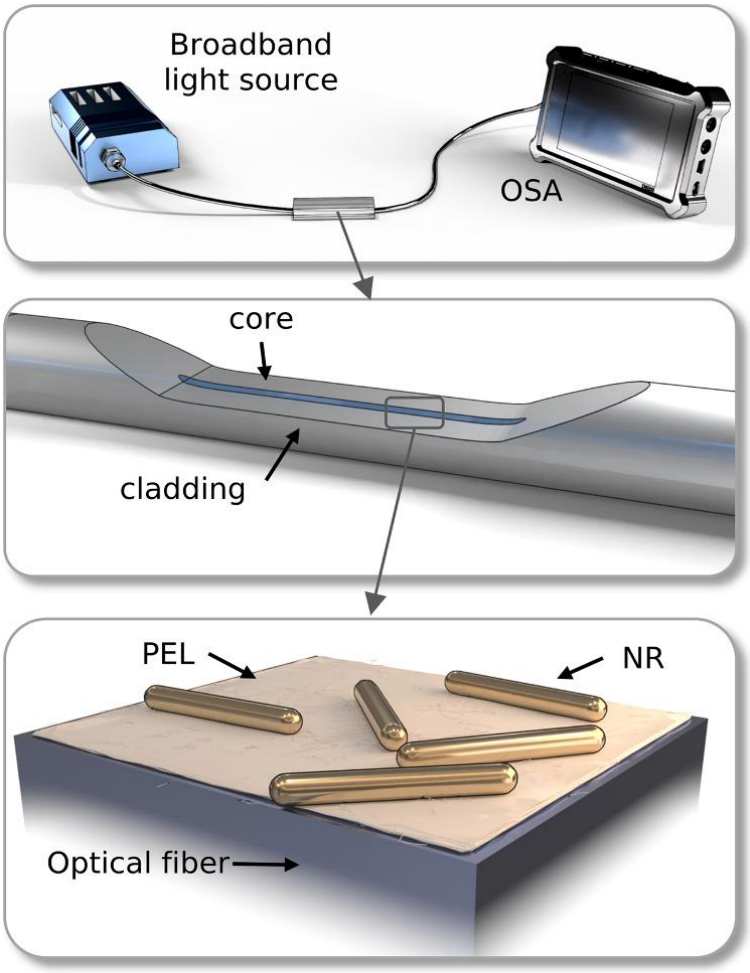

Figure 2-16 Experimental setup for the monitorization of the optical response. On the bottom inset is shown the NR immobilized over the polyelectrolyte layers. Adapted from [63].

In the other work, Kaur Virk et al. [64] developed a photonic sensing platform using D-shaped fiber optic probes for refractive index sensing. They first established the sensitivity of a bare probe using sucrose solutions, finding a linear relationship between the probe's sensing area and its SRI sensitivity. These probes were then functionalized with amine groups and used as a LSPR monitoring platform by immobilizing AuNPs. They demonstrated the LSPR probe's biosensing capability by detecting an Immunoglobulin antibody (HIgG), observing an exponential bimolecular binding kinetic. The limit of detection for the antigen (GaHIgG) was found to be 0.6 µg/mL.

Xun Wu and et al. developed a fiber-optic biosensor that uses SPR for the early detection of breast cancer. The sensor detects the human epidermal growth factor receptor 2 (HER2) protein by immobilizing an HER2 aptamer on a gold-coated, D-shaped polymer optical fiber. The fiber, with a core/cladding diameter of 120/490 µm and a residual thickness of 245 µm, was coated with a 50 nm thick gold layer. In pure water, the initial resonance wavelength was around 1200 nm. For low concentrations of the HER2 protein, the sensor showed a wavelength shift of ~1.37 nm at a concentration of 1 µg/mL (5.5 nM), with a LOD of ~5.28 nM.

2.7.3. Tapered fiber

Yang and et al article [65]. developed a selective and sensitive biosensor for glucose detection using a tapered optical fiber and the LSPR technique by AuNPs with a size of ~10 nm. They also used the enzyme glucose oxidase to improve the sensor's selectivity against other analytes found in serum, such as cholesterol, urea, L-cysteine, ascorbic acid, and galactose. The sensor's performance, as shown in Figure 2-17(B), revealed a clear redshift in the resonance wavelength as glucose concentration increased. It showed good linearity in the 5–30 mM glucose range, which is relevant for clinical diagnostics. The linear relationship between peak wavelength and glucose concentration is further illustrated in Figure 2-17(C), confirming the sensor's stability and reliability. The reusability of the sensor makes it a promising tool for continuous glucose monitoring.

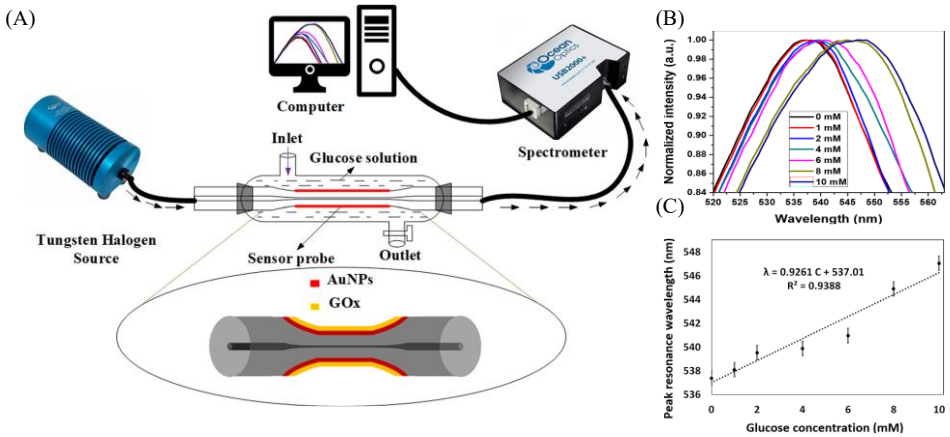

Figure 2-17 (A) Experimental setup for LSPR spectra measurement through a tapered fiber sensor probe. (B) LSPR spectra with different glucose concentrations. (C) Plot of peak absorbance wavelength vs. glucose concentrations. Adapted from [65].

In other job, Xianchao Yang and et al. [66] developed an optical fiber long-range surface plasmon resonance (LRSPR) biosensor with AuNP amplification to overcome the limited penetration depth of conventional and localized SPR sensors. The sensor was created by tapering a single-mode fiber between two multimode fibers to enhance the evanescent field. It was then coated with Al_2O_3-Ag-Au multilayers to stimulate LRSPR, which provides a micron-scale penetration depth. The sensor was modified with a BSA antibody to specifically detect BSA. Introducing AuNPs after the antigen-antibody combination improved the sensitivity 5.6-fold and reduced the minimum detectable BSA concentration by 4 orders of magnitude. The sensor demonstrated a good log-linear spectral response for BSA concentrations ranging from 1 ng/mL to 10 mg/mL, with a high sensitivity of 19.46 nm/log(ng/mL) and a low LOD of 0.3 ng/mL. This sensor also exhibited high specificity, good stability, and a fast response time.

Guo Zhu et al. [67] developed a sensor for detecting ascorbic acid (AA), a biomarker for various diseases. The sensor uses a tapered single-mode optical fiber with LSPR by immobilizing a combination of AuNPs and zinc oxide nanoparticles (ZnO-NPs). The absorbance peak wavelengths for the AuNPs and ZnO-NPs were 519 nm and 370 nm, respectively. Two sensor probes were created: Probe I, which

was immobilized with only AuNPs, and Probe II, which was coated with both AuNPs and an additional layer of ZnO-NPs. To enhance selectivity, the probes were functionalized with ascorbate oxidase, an enzyme that oxidizes AA. The probes' performance was validated by testing AA samples in a concentration range from 500 nM to 1 mM, which covers the normal range in the human body (40 µM–120 µM). The study also confirmed the stability of AA in a PBS solution.

Zhenpeng Men et al. [67] developed a label-free biosensor for detecting paraoxon compounds using a seven-core tapered optical fiber. The sensor leverages the LSPR effect, enhanced by a unique circle-M-circle (CMC) structure that amplifies the evanescent field. The optimized tapered shape also increases its sensitivity to low concentrations of paraoxon residues. The sensor's surface is modified with AuNPs, tungsten disulfide (WS_2) thin layers, and zinc oxide (ZnO) nanowires (NWs) to improve its LSPR effect, stability, and biocompatibility. The experimental results show a sensitivity for paraoxon residues in agricultural products at 33.8 ng/mL, with a detection limit of 6.83 µg/mL.

Zhi Wang and et al. [68] developed a, LSPR biosensor for detecting alanine aminotransferase (ALT), a biomarker for liver injury, at concentrations from 0 to 1000 Units per liter (U/L). The sensor's sensing region was immobilized with AuNPs to promote the LSPR effect, and molybdenum disulfide nanoparticles (MoS_2-NPs) and cerium oxide nanoparticles (CeO_2-NPs) to increase biocompatibility and stability. The probe was then functionalized with glutamate oxidase (GluOx) to improve selectivity. The biosensor showed an excellent linear relationship with ALT concentration and its performance, including reusability, reproducibility, and stability, was evaluated for clinical use in liver injury diagnosis.

Ailing Zhang and et al. [69] proposed an optical fiber biosensor that combines SPR and LSPR by using a tapered noncore fiber (NCF). The sensor is made of two multimode fibers spliced with a tapered NCF in the middle. The tapered waist, with a diameter of 40 µm, is coated with a 50 nm thick gold film, and AuNPs are immobilized on it using polydopamine (PDA). By reducing the NCF diameter and leveraging electric field coupling between the gold film and AuNPs, the sensor's sensitivity was significantly enhanced. It achieved a refractive index sensitivity of 3558 nm/RIU in the detection range of 1.335–1.365, which is about 1.8 times higher than a sensor without these modifications. For detecting rabbit IgG, the sensor demonstrated a sensitivity of 1.16 nm/(µg/ml) and a LOD of 0.017 µg/ml. The biosensor's low cost and high sensitivity make it promising for detecting low concentrations of biomolecules.

Liyanage and et al. [70] designed a tapered optical fiber plasmonic biosensor for detecting a panel of microRNAs. The biosensor integrates three types of metallic nanoparticles: gold spherical nanoparticles (AuNPs), gold nanorods (AuNRs), and gold triangular nanoprisms (AuTNPs). The AuTNPs showed the highest refractive index sensitivity, so they were used for the microRNA assays. Single-stranded DNA (ssDNA) probes were self-assembled on the AuTNPs to bind with the target microRNAs. By measuring the spectral shifts, the sensor achieved a LOD between 103 aM to 261 aM. It also showed an extended dynamic range of 1 fM – 100 nM. When used in human serum, clinically

relevant concentrations of microRNAs were detected with a LOD between 1.097 fM to 1.220 fM. This is the first study to show a TOF plasmonic biosensor's ability to detect a panel of microRNAs, demonstrating a scalable, high-throughput approach.

2.7.4. Fiber tip

This configuration is explain with other example, that done by Chou and et al [71] developed a reflected-type LSPR optical fiber biosensor. The sensor probe was created by sequentially modifying the fiber surface with AuNPs and graphene oxide (GO) using a self-assembly method. The addition of GO significantly improved the sensor's performance. The refractive index sensitivity increased from 29.6 nm/RIU to 79 nm/RIU in the refractive index range of 1.33 to 1.38. After immobilizing anti-mouse IgG, the GO/AuNPs probe demonstrated a quicker response and a larger wavelength shift compared to a probe with only AuNPs. It also showed sensitivity (150.4 nm/μg mL^{-1}), linearity (R^2 = 0.998), and a LOD (4.3 ng/mL) for detecting mouse IgG. This highlights the potential of GO in future biosensing applications. The fabrication process is illustrated in Figure 2-18.

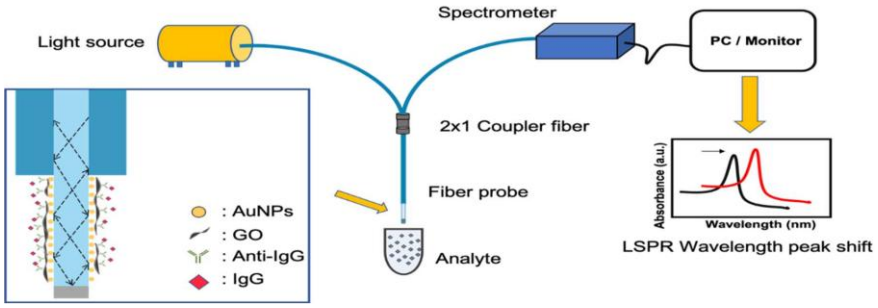

Figure 2-18 Schematic illustration of the setup for optical fiber biosensor system, including the light source, the spectrometer, the 2 × 1 coupler fiber. Adapted from [71].

Sanders et al. [72] reported a miniaturized, LSPR-coupled fiber-optic nanoprobe for the label-free and sensitive detection of free prostate specific antigen (f-PSA), a cancer biomarker. The biosensor uses a reusable, dielectric-metallic hybrid interface with a robust gold nano-disk array fabricated directly onto the fiber end facet using EBL and metal lift-off. The sensor detected f-PSA using a mouse anti-human PSA monoclonal antibody linked to a self-assembled monolayer on the LSPR-FO facet. The nanoprobe demonstrated a near-field SRI sensitivity of ~226 nm/RIU and an LOD of 100 fg/mL (~3 fM) for f-PSA in PBS solutions. Control experiments confirmed the sensor's specificity and selectivity.

Sciacca et al. [73] developed a dip biosensor by depositing metallic nanoparticles onto the tip of a cleaved optical fiber. The sensor works by analyzing the light scattered back into the fiber after interacting with LSPR at the tip. By using a combination of gold and silver nanospheres, the researchers created a multiplexed biosensor that can simultaneously detect two different gastric cancer biomarkers in about 10 minutes.

Yangxi Zhang and et al. [74] developed a biosensor by directly printing plasmonic AuNPs onto the end face of a standard multimode optical fiber. The AuNPs were printed using a precision

photoreduction technology to form micropatterns of a controlled size. The sensor utilizes the LSPR of the AuNPs to provide a distinct spectral signal for label-free bio-detection. This optical fiber-tip biosensor can detect both antibodies and SARS-CoV-2 mimetic DNA sequences at concentrations as low as 0.8 pM. The technology is promising for various applications, including point-of-care testing and in vivo diagnostics.

Hong Lei et al. [75] developed a biosensor for detecting the mycotoxin Fumonisin B1 (FB1). The sensor is based on LSPR and uses the tip of an optical fiber modified with $–NH_2$, AuNPs, and an aptamer. The biosensor showed a linear relationship ($R^2 = 0.9817$) between the LSPR peak shifts and the logarithmic concentration of FB1 in the range of 0.8–200.0 ng/mL. It achieved a low LOD of 0.17 ng/mL, with high selectivity, recovery rates from 96.08% to 112.23%, and a repeatability relative standard deviation (RSD) of 3.37%. The sensor's performance was validated using corn samples.

Santosh Kumar and et al. [76] developed LSPR biosensor for the accurate and selective measurement of cholesterol, a crucial factor in diagnosing cardiovascular and other diseases. The sensor uses a tapered optical fiber probe functionalized with AuNPs and cholesterol oxidase (ChOx) to enhance its sensitivity and selectivity. The synthesized AuNPs were characterized by UV-visible spectrophotometry, TEM, and EDS, while SEM confirmed their successful coating on the fiber. The biosensor successfully detects cholesterol within a clinically relevant range of 0 to 10 mM, achieving a low limit of detection of 53.1 nM.

Yichao Xu et al. [77] developed a optical fiber-based biosensor for detection of zearalenone (ZEN), a food contaminant. The sensor was created by coating the end of an optical fiber with synthesized AuNPs of about 25 nm and then modifying it with a ZEN nucleic acid aptamer. The biosensor showed a relationship between ZEN concentrations and the redshifts of the LSPR peak in the range of 1 to 480 ng/mL, with a limit of detection of 0.102 ng/mL. The sensing interface can be easily regenerated by cutting and polishing the fiber end, making the sensor reusable. It also demonstrated selectivity for ZEN and recovery and repeatability.

Hyeong-Min Kim et al. [78] developed a micro-electro-mechanical systems (MEMS)-based LSPR sensor with a uniformly distributed noble metal nanostructure array on a silicon microtip. This design addresses the lack of reproducibility and reliability in conventional LSPR sensors caused by irregular, rearranged nanoparticles. Their novel fabrication process uses a single photolithography mask and a self-aligned etching process to create gold nanoparticles at the tip. They confirmed the sensor's improved reproducibility through reliability tests and verified its feasibility by measuring LSPR signals in media with varying refractive indices. A schematic of the sensor is shown in Figure 2-19.

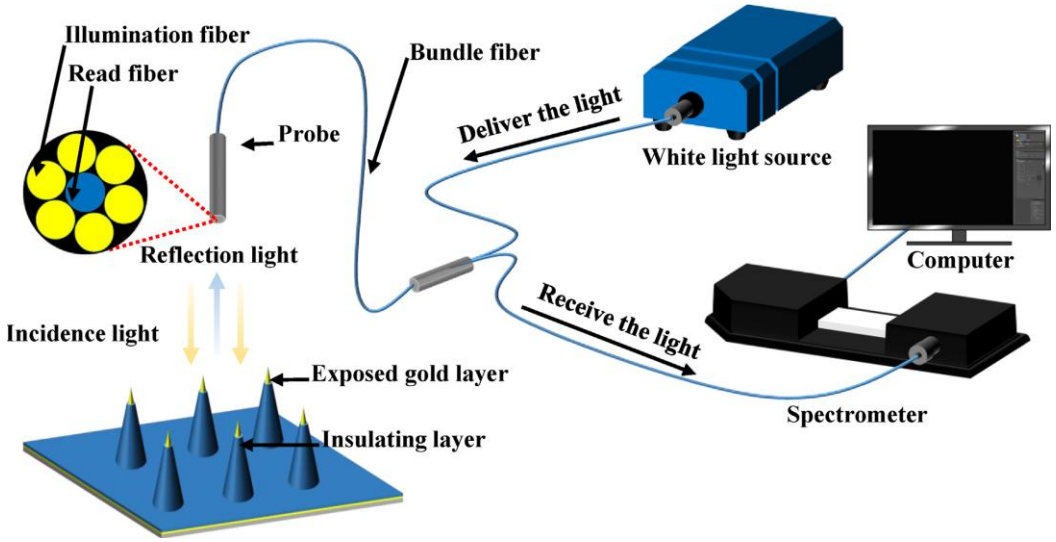

Figure 2-19. Schematic diagram of the optical measurement system with the LSPR sensor chip: The white light source and the spectrometer are connected to two ends of a bundle fiber. The opposite end illuminates the fabricated LSPR sensor using the six illumination fibers. Reflected light from the LSPR sensor is collected by the spectrometer through the read fiber. Adapted from [78].

Based on this section, the performance of these devices is heavily dictated by the nanostructure morphology, which influences both the electric field confinement and the spectral position of the attenuation band. Comparative analysis reveals that anisotropic geometries generally outperform standard nanospheres due to their superior surface-to-volume ratios and ability to create localized "hotspots" with amplified electric fields. Specifically, NS have demonstrated an exceptional LOD of 0.09 aM for GFAP, significantly surpassing simpler structures like nanodisks, nanohexagonals, and nanotriangles [61]. AuNRs also offer significant advantages over spheres because their longitudinal plasmon band can be tuned by modulating their aspect ratio, providing a five-fold improvement in sensing glyphosate (LOD: 85 mg/L) when operating in the C/L optical bands [63]. Furthermore, complex configurations like the 3D AuNP/multilayer graphene composite on U-shaped fibers achieve sensitivities as high as 1251.44 nm/RIU. Even among faceted particles, nanotriangles exhibit higher refractive index sensitivity than spherical AuNPs, leading to a LOD between 103 aM and 261 aM for microRNA detection [70]. These results underscore that strategically engineering the nanoparticle shape, transitioning from nanospheres to sharp-edged stars, triangles, or rods, is the principal determinant for achieving the high sensitivity and low detection limits required for real-world clinical and environmental biosensing.

2.8. Conclusions

This chapter has provided a comprehensive examination of the fundamental principles and practical implementations of SPR and LSPR. By exploring the theoretical foundations, from the strict momentum-matching conditions of propagating surface plasmons to the Mie Theory and DDA for

localized oscillations, the distinct physical mechanisms of these two phenomena were elucidated. A critical finding discussed herein is the intrinsic relationship between the attenuation band and sensor performance; specifically, the sensitivity of both SPR and LSPR platforms is governed by the spectral position of the resonance peak, where a shift toward longer wavelengths typically yields enhanced refractive index sensitivity.

The technological evolution from bulky prism-based systems (Kretschmann and Otto configurations) to compact fiber-optic architectures highlights a significant shift toward portable, real-time biosensing. Various fiber geometries, including U-shaped, D-shaped, tapered, and tip-modified fibers, have been shown to offer unique advantages in evanescent field manipulation and sensitivity enhancement. Furthermore, the comparison of nanostructure morphologies demonstrates that anisotropic shapes, such as nanostars and nanotriangles, provide superior detection limits (as low as 0.09 aM for GFAP) and higher field confinement compared to traditional spherical nanoparticles. Ultimately, the strategic selection of materials (e.g., gold and silver), geometric configurations, and interrogation methods (wavelength, angle, or intensity modulation) provides a robust framework for designing high-performance plasmonic sensors tailored for medical diagnostics and environmental monitoring

The following chapter presents numerical simulations of various nanostructure configurations within the region of interest for the experimental part of this research.

2.9. References

[1] R. W. Wood, "XLII. On a remarkable case of uneven distribution of light in a diffraction grating spectrum," The London, Edinburgh, and Dublin Philosophical Magazine and Journal of Science, vol. 4, no. 21, pp. 396–402, Sep. 1902, doi: 10.1080/14786440209462857.

[2] N. J. de Mol and M. J. E. Fischer, "Surface plasmon resonance: a general introduction," in Surface plasmon resonance: methods and protocols, Springer, 2010, pp. 1–14.

[3] R. Al Mahmud, R. H. Sagor, and M. Z. M. Khan, "Surface plasmon refractive index biosensors: A review of optical fiber, multilayer 2D material and gratings, and MIM configurations," Opt Laser Technol, vol. 159, p. 108939, Apr. 2023, doi: 10.1016/j.optlastec.2022.108939.

[4] M. Piliarik, H. Vaisocherová, and J. Homola, "Surface Plasmon Resonance Biosensing," 2009, pp. 65–88. doi: 10.1007/978-1-60327-567-5_5.

[5] X. Tong et al., "High-Sensitivity Angle Modulation Biosensor Based on Surface Plasmon Resonance of Metasurface," IEEE Photonics J, vol. 14, no. 6, pp. 1–5, Dec. 2022, doi: 10.1109/JPHOT.2022.3215195.

[6] J. Homola, "On the sensitivity of surface plasmon resonance sensors with spectral interrogation," Sens Actuators B Chem, vol. 41, no. 1–3, pp. 207–211, Jun. 1997, doi: 10.1016/S0925-4005(97)80297-3.

[7] E. Klantsataya, P. Jia, H. Ebendorff-Heidepriem, T. Monro, and A. François, "Plasmonic Fiber Optic Refractometric Sensors: From Conventional Architectures to Recent Design Trends," Sensors, vol. 17, no. 1, p. 12, Dec. 2016, doi: 10.3390/s17010012.

[8] R. Tabassum and R. Kant, "Recent trends in surface plasmon resonance based fiber–optic gas sensors utilizing metal oxides and carbon nanomaterials as functional entities," Sens Actuators B Chem, vol. 310, p. 127813, May 2020, doi: 10.1016/j.snb.2020.127813.

[9] L. Liu, J. Yang, Z. Yang, X. Wan, N. Hu, and X. Zheng, "Theoretical Analysis of the Optical Propagation Characteristics in a Fiber-Optic Surface Plasmon Resonance Sensor," Sensors, vol. 13, no. 6, pp. 7443–7453, Jun. 2013, doi: 10.3390/s130607443.

[10] G. Meng, N. Luan, H. He, F. Lei, and J. Liu, "Side-Opened Hollow Fiber-Based SPR Sensor for High Refractive Index Detection," Sensors, vol. 24, no. 13, p. 4335, Jul. 2024, doi: 10.3390/s24134335.

[11] L. Li et al., "Wedged Fiber Optic Surface Plasmon Resonance Sensor for High-Sensitivity Refractive Index and Temperature Measurements," Sensors, vol. 22, no. 23, p. 9099, Nov. 2022, doi: 10.3390/s22239099.

[12] Y. Zeng et al., "Wavelength-Scanning SPR Imaging Sensors Based on an Acousto-Optic Tunable Filter and a White Light Laser," Sensors, vol. 17, no. 1, p. 90, Jan. 2017, doi: 10.3390/s17010090.

[13] P. P. Markowicz, W. C. Law, A. Baev, P. N. Prasad, S. Patskovsky, and A. Kabashin, "Phase-sensitive time-modulated surface plasmon resonance polarimetry for wide dynamic range biosensing," Opt Express, vol. 15, no. 4, p. 1745, Feb. 2007, doi: 10.1364/OE.15.001745.

[14] J. Homola, I. Koudela, and S. S. Yee, "Surface plasmon resonance sensors based on diffraction gratings and prism couplers: sensitivity comparison," Sens Actuators B Chem, vol. 54, no. 1–2, pp. 16–24, Jan. 1999, doi: 10.1016/S0925-4005(98)00322-0.

[15] H. Suzuki, M. Sugimoto, Y. Matsui, and J. Kondoh, "Effects of gold film thickness on spectrum profile and sensitivity of a multimode-optical-fiber SPR sensor," Sens Actuators B Chem, vol. 132, no. 1, pp. 26–33, May 2008, doi: 10.1016/j.snb.2008.01.003.

[16] Y. Yildizhan et al., "Detection of Breast Cancer-Specific Extracellular Vesicles with Fiber-Optic SPR Biosensor," Int J Mol Sci, vol. 24, no. 4, p. 3764, Feb. 2023, doi: 10.3390/ijms24043764.

[17] S. Singh, S. K. Mishra, and B. D. Gupta, "SPR based fibre optic biosensor for phenolic compounds using immobilization of tyrosinase in polyacrylamide gel," Sens Actuators B Chem, vol. 186, pp. 388–395, Sep. 2013, doi: 10.1016/j.snb.2013.06.034.

[18] J. Pollet et al., "Fiber optic SPR biosensing of DNA hybridization and DNA–protein interactions," Biosens Bioelectron, vol. 25, no. 4, pp. 864–869, Dec. 2009, doi: 10.1016/j.bios.2009.08.045.

[19] S. Akter and H. Abdullah, “Development and Optimization of an SPR-Based Fiber Optic Biosensor for Non-Invasive Pregnancy Detection,” Plasmonics, Jul. 2025, doi: 10.1007/s11468-025-03149-3.
[20] W. Wang et al., “A label-free fiber optic SPR biosensor for specific detection of C-reactive protein,” Sci Rep, vol. 7, no. 1, p. 16904, Dec. 2017, doi: 10.1038/s41598-017-17276-3.
[21] J. Dong et al., “Side-polished few-mode fiber based surface plasmon resonance biosensor,” Opt Express, vol. 27, no. 8, pp. 11348–11360, 2019.
[22] J. N. Dash and R. Jha, “On the Performance of Graphene-Based D-Shaped Photonic Crystal Fibre Biosensor Using Surface Plasmon Resonance,” Plasmonics, vol. 10, no. 5, pp. 1123–1131, Oct. 2015, doi: 10.1007/s11468-015-9912-7.
[23] S. A. Maier, Plasmonics: fundamentals and applications, vol. 1. Springer, 2007.
[24] Y. Zhang, W. An, C. Zhao, and Q. Dong, “Radiation induced plasmonic nanobubbles: fundamentals, applications and prospects,” AIMS Energy, vol. 9, no. 4, pp. 676-713·, 2021, doi: 10.3934/energy.2021032.
[25] H. Yockell-Lelièvre, F. Lussier, and J.-F. Masson, “Influence of the Particle Shape and Density of Self-Assembled Gold Nanoparticle Sensors on LSPR and SERS,” The Journal of Physical Chemistry C, vol. 119, no. 51, pp. 28577–28585, Dec. 2015, doi: 10.1021/acs.jpcc.5b09570.
[26] G. Mie, “Beiträge zur Optik trüber Medien, speziell kolloidaler Metallösungen,” Ann Phys, vol. 330, no. 3, pp. 377–445, Jan. 1908, doi: 10.1002/andp.19083300302.
[27] U. Kreibig and M. Vollmer, Optical properties of metal clusters, vol. 25. Springer Science & Business Media, 2013.
[28] C. F. Bohren and D. R. Huffman, Absorption and scattering of light by small particles. John Wiley & Sons, 2008.
[29] W. Haiss, N. T. K. Thanh, J. Aveyard, and D. G. Fernig, “Determination of Size and Concentration of Gold Nanoparticles from UV−Vis Spectra,” Anal Chem, vol. 79, no. 11, pp. 4215–4221, Jun. 2007, doi: 10.1021/ac0702084.
[30] J. Zhao et al., “Methods for Describing the Electromagnetic Properties of Silver and Gold Nanoparticles,” Acc Chem Res, vol. 41, no. 12, pp. 1710–1720, Dec. 2008, doi: 10.1021/ar800028j.
[31] J. J. Mock, M. Barbic, D. R. Smith, D. A. Schultz, and S. Schultz, “Shape effects in plasmon resonance of individual colloidal silver nanoparticles,” J Chem Phys, vol. 116, no. 15, pp. 6755–6759, Apr. 2002, doi: 10.1063/1.1462610.
[32] K. L. Kelly, E. Coronado, L. L. Zhao, and G. C. Schatz, “The optical properties of metal nanoparticles: the influence of size, shape, and dielectric environment,” 2003, ACS Publications.
[33] B. D. Gupta and R. K. Verma, “Surface Plasmon Resonance-Based Fiber Optic Sensors: Principle, Probe Designs, and Some Applications,” J Sens, vol. 2009, no. 1, Jan. 2009, doi: 10.1155/2009/979761.
[34] K. M. Mayer and J. H. Hafner, “Localized Surface Plasmon Resonance Sensors,” Chem Rev, vol. 111, no. 6, pp. 3828–3857, Jun. 2011, doi: 10.1021/cr100313v.
[35] M. Lismont and L. Dreesen, “Comparative study of Ag and Au nanoparticles biosensors based on surface plasmon resonance phenomenon,” Materials Science and Engineering: C, vol. 32, no. 6, pp. 1437–1442, Aug. 2012, doi: 10.1016/j.msec.2012.04.023.
[36] K. M. Mayer and J. H. Hafner, “Localized Surface Plasmon Resonance Sensors,” Chem Rev, vol. 111, no. 6, pp. 3828–3857, Jun. 2011, doi: 10.1021/cr100313v.
[37] E. M. Purcell and C. R. Pennypacker, “Scattering and absorption of light by nonspherical dielectric grains,” Astrophysical Journal, Vol. 186, pp. 705-714 (1973), vol. 186, pp. 705–714, 1973.
[38] F. Enguehard, “Mie theory and the discrete dipole approximation. calculating radiative properties of particulate media, with application to nanostructured materials,” in Thermal Nanosystems and Nanomaterials, Springer, 2009, pp. 151–212.
[39] C. Noguez, “Surface plasmons on metal nanoparticles: the influence of shape and physical environment,” The Journal of Physical Chemistry C, vol. 111, no. 10, pp. 3806–3819, 2007.
[40] G. V Hartland, “Optical studies of dynamics in noble metal nanostructures,” Chem Rev, vol. 111, no. 6, pp. 3858–3887, 2011.

[41] T. Wriedt, “A review of elastic light scattering theories,” Part Part Syst Charact, vol. 15, no. 2, pp. 67–74, 1998.
[42] S. K. Ghosh and T. Pal, “Interparticle coupling effect on the surface plasmon resonance of gold nanoparticles: from theory to applications,” Chem Rev, vol. 107, no. 11, pp. 4797–4862, 2007.
[43] B. T. Draine and P. J. Flatau, “Discrete-dipole approximation for scattering calculations,” Journal of the Optical Society of America A, vol. 11, no. 4, pp. 1491–1499, 1994.
[44] P. K. Jain and M. A. El-Sayed, “Plasmonic coupling in noble metal nanostructures,” Chem Phys Lett, vol. 487, no. 4–6, pp. 153–164, 2010.
[45] M. A. Mahmoud, B. Snyder, and M. A. El-Sayed, “Surface plasmon fields and coupling in the hollow gold nanoparticles and surface-enhanced Raman spectroscopy. Theory and experiment,” The Journal of Physical Chemistry C, vol. 114, no. 16, pp. 7436–7443, 2010.
[46] K.-S. Lee and M. A. El-Sayed, “Dependence of the enhanced optical scattering efficiency relative to that of absorption for gold metal nanorods on aspect ratio, size, end-cap shape, and medium refractive index,” J Phys Chem B, vol. 109, no. 43, pp. 20331–20338, 2005.
[47] K.-S. Lee and M. A. El-Sayed, “Gold and silver nanoparticles in sensing and imaging: sensitivity of plasmon response to size, shape, and metal composition,” J Phys Chem B, vol. 110, no. 39, pp. 19220–19225, 2006.
[48] M. A. Mahmoud and M. A. El-Sayed, “Gold nanoframes: very high surface plasmon fields and excellent near-infrared sensors,” J Am Chem Soc, vol. 132, no. 36, pp. 12704–12710, 2010.
[49] V. Myroshnychenko et al., “Modelling the optical response of gold nanoparticles,” Chem Soc Rev, vol. 37, no. 9, pp. 1792–1805, 2008.
[50] A. R. Jones, “Light scattering for particle characterization,” Prog Energy Combust Sci, vol. 25, no. 1, pp. 1–53, 1999.
[51] R. B. M. Schasfoort, Handbook of surface plasmon resonance. Royal Society of Chemistry, 2017.
[52] H. Bin Jeon, P. V. Tsalu, and J. W. Ha, “Shape Effect on the Refractive Index Sensitivity at Localized Surface Plasmon Resonance Inflection Points of Single Gold Nanocubes with Vertices,” Sci Rep, vol. 9, no. 1, p. 13635, Sep. 2019, doi: 10.1038/s41598-019-50032-3.
[53] A. Rabbani, R. Rudacille, and K. Hasegawa, “Local Refractive Index Sensitivity of Localized Surface Plasmon Resonance Biosensors,” The Journal of Physical Chemistry C, vol. 128, no. 45, pp. 19210–19221, Nov. 2024, doi: 10.1021/acs.jpcc.4c03456.
[54] V. P. Zhdanov, “Basics of the LSPR Sensors for Soft Matter at Interfaces,” Plasmonics, vol. 18, no. 3, pp. 971–982, Jun. 2023, doi: 10.1007/s11468-023-01812-1.
[55] S. J. Zalyubovskiy et al., “Theoretical limit of localized surface plasmon resonance sensitivity to local refractive index change and its comparison to conventional surface plasmon resonance sensor,” Journal of the Optical Society of America A, vol. 29, no. 6, p. 994, Jun. 2012, doi: 10.1364/JOSAA.29.000994.
[56] K. A. Willets and R. P. Van Duyne, “Localized Surface Plasmon Resonance Spectroscopy and Sensing,” Annu Rev Phys Chem, vol. 58, no. 1, pp. 267–297, May 2007, doi: 10.1146/annurev.physchem.58.032806.104607.
[57] L. J. Sherry, R. Jin, C. A. Mirkin, G. C. Schatz, and R. P. Van Duyne, “Localized Surface Plasmon Resonance Spectroscopy of Single Silver Triangular Nanoprisms,” Nano Lett, vol. 6, no. 9, pp. 2060–2065, Sep. 2006, doi: 10.1021/nl061286u.
[58] A. Rabbani, R. Rudacille, and K. Hasegawa, “Local Refractive Index Sensitivity of Localized Surface Plasmon Resonance Biosensors,” The Journal of Physical Chemistry C, vol. 128, no. 45, pp. 19210–19221, Nov. 2024, doi: 10.1021/acs.jpcc.4c03456.
[59] C. Li et al., “LSPR optical fiber biosensor based on a 3D composite structure of gold nanoparticles and multilayer graphene films,” Opt Express, vol. 28, no. 5, p. 6071, Mar. 2020, doi: 10.1364/OE.385128.
[60] S. K. Srivastava, V. Arora, S. Sapra, and B. D. Gupta, “Localized Surface Plasmon Resonance-Based Fiber Optic U-Shaped Biosensor for the Detection of Blood Glucose,” Plasmonics, vol. 7, no. 2, pp. 261–268, Jun. 2012, doi: 10.1007/s11468-011-9302-8.
[61] A. Xiao, X. Wu, J. Zheng, Y. Huang, A. Xu, and B.-O. Guan, “Sensitivity evaluation of an optical microfiber featuring interfaces with various gold nanoparticle morphologies: Application

to the GFAP detection," Biosens Bioelectron, vol. 268, p. 116901, Jan. 2025, doi: 10.1016/j.bios.2024.116901.
[62] Z. Luo et al., "Ultrasensitive U-shaped fiber optic LSPR cytosensing for label-free and in situ evaluation of cell surface N-glycan expression," Sens Actuators B Chem, vol. 284, pp. 582–588, Apr. 2019, doi: 10.1016/j.snb.2019.01.015.
[63] P. S. S. dos Santos, J. P. Mendes, I. Pastoriza-Santos, J.-P. Juste, J. M. M. M. de Almeida, and L. C. C. Coelho, "Gold-coated silver nanorods on side-polished singlemode optical fibers for remote sensing at optical telecommunication wavelengths," Sens Actuators B Chem, vol. 425, p. 136936, Feb. 2025, doi: 10.1016/j.snb.2024.136936.
[64] J. Kaur Virk, S. Das, R. S. Kaler, H. Singh, and T. Kundu, "D-shape optical fiber probe dimension optimization for LSPR based bio-sensor," Optical Fiber Technology, vol. 71, p. 102930, Jul. 2022, doi: 10.1016/j.yofte.2022.102930.
[65] Q. Yang et al., "Development of Glucose Sensor Using Gold Nanoparticles and Glucose-Oxidase Functionalized Tapered Fiber Structure," Plasmonics, vol. 15, no. 3, pp. 841–848, Jun. 2020, doi: 10.1007/s11468-019-01104-7.
[66] X. Yang et al., "Tapered optical fiber LRSPR biosensor based on gold nanoparticle amplification for label-free BSA detection," Sens Actuators B Chem, vol. 426, p. 136986, Mar. 2025, doi: 10.1016/j.snb.2024.136986.
[67] G. Zhu et al., "Tapered Optical Fiber-Based LSPR Biosensor for Ascorbic Acid Detection," Photonic Sensors, vol. 11, no. 4, pp. 418–434, Dec. 2021, doi: 10.1007/s13320-020-0605-2.
[68] Z. Wang, R. Singh, C. Marques, R. Jha, B. Zhang, and S. Kumar, "Taper-in-taper fiber structure-based LSPR sensor for alanine aminotransferase detection," Opt Express, vol. 29, no. 26, p. 43793, Dec. 2021, doi: 10.1364/OE.447202.
[69] A. Zhang, Z. Li, P. Chang, Y. Shi, and Z. Wang, "High sensitivity rabbit IgG biosensor co-enhanced by tapered noncore fiber and coupling effect between SPR and LSPR," Appl Phys Lett, vol. 125, no. 19, Nov. 2024, doi: 10.1063/5.0228265.
[70] T. Liyanage, M. Lai, and G. Slaughter, "Label-free tapered optical fiber plasmonic biosensor," Anal Chim Acta, vol. 1169, p. 338629, Jul. 2021, doi: 10.1016/j.aca.2021.338629.
[71] H.-T. Chou, Y.-S. Liao, T.-M. Wu, S.-H. Wang, K.-H. Chiang, and W.-C. Su, "Development of Localized Surface Plasmon Resonance-Based Optical Fiber Biosensor for Immunoassay Using Gold Nanoparticles and Graphene Oxide Nanocomposite Film," IEEE Sens J, vol. 22, no. 7, pp. 6593–6600, Apr. 2022, doi: 10.1109/JSEN.2022.3148285.
[72] M. Sanders, Y. Lin, J. Wei, T. Bono, and R. G. Lindquist, "An enhanced LSPR fiber-optic nanoprobe for ultrasensitive detection of protein biomarkers," Biosens Bioelectron, vol. 61, pp. 95–101, Nov. 2014, doi: 10.1016/j.bios.2014.05.009.
[73] B. Sciacca and T. M. Monro, "Dip Biosensor Based on Localized Surface Plasmon Resonance at the Tip of an Optical Fiber," Langmuir, vol. 30, no. 3, pp. 946–954, Jan. 2014, doi: 10.1021/la403667q.
[74] Y. Zhang et al., "Ultraminiature optical fiber-tip directly-printed plasmonic biosensors for label-free biodetection," Biosens Bioelectron, vol. 218, p. 114761, Dec. 2022, doi: 10.1016/j.bios.2022.114761.
[75] H. Lei, C. Chen, and H. Yan, "A Portable Optical Fiber Tip Facet LSPR Aptasensor for Detection of Fumonisin B1," IEEE Sens J, vol. 22, no. 18, pp. 17838–17844, Sep. 2022, doi: 10.1109/JSEN.2022.3195457.
[76] S. Kumar et al., "LSPR-based cholesterol biosensor using a tapered optical fiber structure," Biomed Opt Express, vol. 10, no. 5, p. 2150, May 2019, doi: 10.1364/BOE.10.002150.
[77] Y. Xu, M. Xiong, and H. Yan, "A portable optical fiber biosensor for the detection of zearalenone based on the localized surface plasmon resonance," Sens Actuators B Chem, vol. 336, p. 129752, Jun. 2021, doi: 10.1016/j.snb.2021.129752.
[78] H.-M. Kim, K.-T. Nam, S.-K. Lee, and J.-H. Park, "Fabrication and measurement of microtip-array-based LSPR sensor using bundle fiber," Sens Actuators A Phys, vol. 271, pp. 146–152, Mar. 2018, doi: 10.1016/j.sna.2018.01.021.

3. Chapter 3
Numerical simulations

This chapter first examines established modeling approaches for plasmonic systems, encompassing theoretical, analytical, and numerical methodologies. Subsequently, the discussion focuses on the model developed in this thesis using Finite Element Method (FEM). Specifically, first are considered isolated nanoparticle (NP) and aggregated structures before advancing to the nanostar (NS)-based surface configuration. Furthermore, the implications of system approximations and constraints are evaluated, and the model's validity is assessed through comparisons with existing simulations and prior experimental data .

The proposed model enables the simulation of idealized or highly controlled systems, such as NS aspect ratios in free space, scenarios impractical to replicate experimentally. Additionally, it facilitates the study of extreme surface geometries, including high-aspect-ratio NS configurations and the influence of illumination direction on NP aggregates. By exploring these simplified and boundary-case systems, the model provides critical insights into the optical and plasmonic properties of the nanostructures under investigation. The results presented in this chapter have been used for the design and evaluation of the LSPR-based sensors reported in the next chapters.

3.1. Nanostructure Modelling Methods

A modeling technique must reliably predict the optical response of the simulated configurations. Modeling methods are broadly categorized as theoretical, analytical, or numerical. Theoretical models yield precise solutions for idealized systems but fail when applied to non-ideal or variable conditions. Analytical methods employ mathematical formulations to describe system behavior,

frequently incorporating approximations to simplify complexity. Numerical methods, while often perceived as less elegant due to their reliance on computational power and iterative calculations, excel in handling intricate, real-world plasmonic systems that defy theoretical or analytical treatment.

This section evaluates the most widely used plasmonic modeling techniques, highlighting their respective strengths and limitations in predicting optical and plasmonic phenomena.

3.1.1. Mie Theory

As discussed in Chapter 2, Mie theory offers a rigorous framework for calculating the absorption and scattering properties of spherical nanoparticles within an isotropic, homogeneous medium [1], [2]. Extensions of this theory have been developed to approximate the optical response of other simple geometries, such as infinite cylinders and ellipsoids [3].

In Ref. [4]. , Mie scattering profiles for nanospheres were computed using PyMieLab_V1 software [5], which implements the BHMIE algorithm for precise calculations Additionally, scattering behavior for ellipsoidal structures was evaluated using the Mie-Gans approximation, as outlined in Chapter 2. Despite its utility, Mie theory exhibits several key limitations, including geometric constraints, which means it cannot accurately predict resonant behavior in complex nanostructures (e.g., nanorods, nanoholes, or nanostars). And environmental simplifications, that means the theory assumes isolated nanostructures in homogeneous media, neglecting effects such as particle density or substrate interactions.

Nevertheless, Mie theory remains invaluable for modeling well-defined, simple systems with high accuracy, providing a foundational tool for understanding plasmonic phenomena in idealized scenarios [6].

3.1.2. Discrete Dipole Approximation

The Discrete Dipole Approximation (DDA), commonly referred to as the coupled dipole method, provides a powerful framework for calculating electromagnetic wave absorption and scattering by arbitrarily shaped nanoparticles. Originally developed by Purcell and Pennypacker to model light scattering from interstellar dust grains, this approach represents complex nanostructures as arrays of interacting point dipoles arranged on a cubic lattice [1], [7], [8]. The fundamental principle involves solving for the induced dipole moments generated by the interaction between this dipole array and the local electromagnetic field, from which the particle's optical properties can be derived. This method has become particularly valuable in plasmonic research due to its ability to handle geometries that defy analytical solutions [9], [10], [11].

For practical implementation, researchers can utilize several open-source DDA software packages, with DDSCAT developed by Draine and Flatau emerging as the most widely adopted solution [11]. This versatile computational tool enables simulation of diverse nanostructures including nanospheres, rectangular prisms, ellipsoids, and cylinders in homogeneous media, allowing direct comparison with

results obtained through Mie-Gans approximations. The accuracy of DDA simulations depends critically on appropriate dipole discretization, with optimal results achieved when the number of dipoles remains substantially smaller than the incident wavelength in the medium. A well-established guideline recommends using at least ten dipoles per wavelength to ensure reliable results, though this must be balanced against computational constraints. It's important to note that the cubic lattice foundation of DDA introduces inherent limitations for certain geometries, particularly for structures that deviate significantly from cubic symmetry or feature highly curved surfaces like perfect spheres, where the approximation may lead to increased numerical errors. Despite these constraints, DDA remains an indispensable tool in computational plasmonic, offering a unique combination of flexibility and computational efficiency for modeling complex nanostructures that lie beyond the reach of purely analytical methods which led to huge throwback of this method that is demanding significant computation time and power due to the large number of dipoles required to model the setup.

3.1.3. Effective Medium Approximation

In this approach, the light scattering properties of the nanoparticle array can be approximated by treating the nanoparticles as homogeneous inclusions within a host matrix. The system is then modeled as an effective medium, combining the optical properties of both the inclusions and the surrounding matrix. The effective dielectric constant of the medium is calculated using a mixing formula, with the Bruggeman and Maxwell-Garnett methods being the most widely used. However, these methods have notable limitations: the Maxwell-Garnett approach is unsuitable for high inclusion volume fractions, while the Bruggeman formula does not account for the inclusion geometry [12], [13], [14], [15], [16]. Given that the nanostructure inclusions occupied a relatively small volume fraction compared to the host medium, the Maxwell-Garnett equation was selected to compute the effective dielectric constant of the nanostructure -based medium. A detailed discussion of this approximation, including its governing equations, is provided in Chapter 2.

3.1.4. Finite Element Method

The Finite Element Method (FEM) is a powerful numerical modeling technique that simulates the physical behavior of complex systems by discretizing the computational domain into smaller, manageable elements [17]. By solving simplified governing equations over these finite elements, typically triangular or tetrahedral in shape, FEM provides a flexible framework for analyzing diverse geometries and material properties. The accuracy of the simulation heavily depends on mesh refinement, where smaller elements yield higher precision, particularly at boundaries or regions with strong field gradients.

While FEM is widely applicable, alternative numerical methods such as the Finite-Difference Time-Domain (FDTD) and Boundary Element Method (BEM) offer different advantages. FDTD employs a structured grid of square elements, making it efficient for wave propagation problems but less adaptable

to irregular geometries. In contrast, BEM focuses on discretizing only the boundaries of the system, reducing computational load for problems with well-defined interfaces but struggling with inhomogeneous media [18].

In this thesis, FEM was employed to simulate nanostructured systems. FEM was chosen over FDTD and BEM due to its superior adaptability in modeling complex, non-spherical, and coupled nanostructures, where other methods may fail to converge or produce inaccurate results. However, this flexibility comes at a computational cost: as model complexity increases, so do the demands on memory and processing time. For instance, refining the mesh to improve accuracy can extend simulation times to over a day, even on high-performance systems [15], [16].

To optimize efficiency, strategic constraints were implemented, balancing mesh resolution, boundary conditions, and solver settings to achieve reliable results without excessive computational overhead. This approach ensured an effective trade-off between numerical accuracy and practical feasibility, enabling robust simulations of nanostructured surfaces while maintaining computational tractability.

3.2. Numerical simulations of Nanostructures

This study begins by examining the electromagnetic response of an isolated nanoparticle, including **its** SRI sensitivity. Subsequently, the effects of particle aggregation and cluster formation will be systematically analyzed to evaluate their influence on optical properties. Finally, NS geometries will be simulated to investigate how morphological variations impact attenuation bands and further enhance SRI sensitivity. Through this stepwise approach, the relationship between nanostructure design and performance metrics will be rigorously explored. The model was developed using COMSOL Multiphysics 6.1a commercially available FEM-based software.

3.2.1. Isolated nanoparticle

In the initial simulation phase, we focus on a single nanoparticle system implemented with a carefully designed computational domain. The gold NP is surrounded by a 200 nm thick dielectric layer (refractive index n = 1.33, simulating aqueous environment), which itself is enclosed by an additional 200 nm perfectly matched layer (PML). This multilayer architecture, illustrated in Figure 3-1, serves dual purposes: (1) the inner dielectric layer provides physical separation for near-field analysis, while (2) the outer PML effectively simulates an infinite dielectric medium while minimizing artificial boundary reflections.

In Figure 3-1(A), the mesh distribution of the entire simulation environment is shown, while Figure 3-1(B) focuses on the NP. As previously explained, mesh size is a critical parameter in simulations, and its importance is highly area-dependent. As illustrated in this figure, the mesh size around the NP, the

primary region of interest, is significantly smaller compared to that in the PML. Specifically, for the NP, the mesh size is set to be less than one-tenth of the wavelength [6], [15].

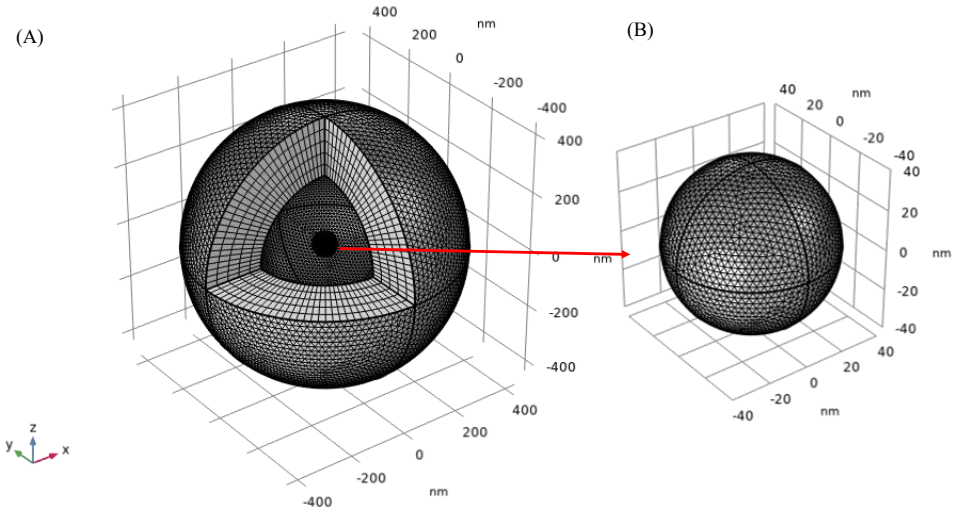

Figure 3-1. Mesh distribution in (A) whole environment, (B) in NP.

The electromagnetic excitation consists of a plane wave propagating along the z-axis (from -z to +z directions) with x-polarization and constant power density of 1 W/m² across all simulations. Figure 3-2 (A) and (B) presents the computed electric field distribution at the NP surface for excitation wavelength $\lambda = 480$ nm [19], [20], revealing characteristic dipolar plasmon resonance patterns. Through comprehensive FEM analysis, we quantify both near-field enhancements and far-field responses, particularly focusing on wavelength-dependent heat dissipation (absorption spectrum shown as red curve in Figure 3-3 (A). For a 50 nm gold NP in aqueous medium (n = 1.33), we observe a dominant absorption peak at $\lambda = 535$ nm, consistent with both experimental literature [21], [22] and our reference data in Figure 3-3 (A). This resonance exhibits the expected size dependence [15], [23], [24].

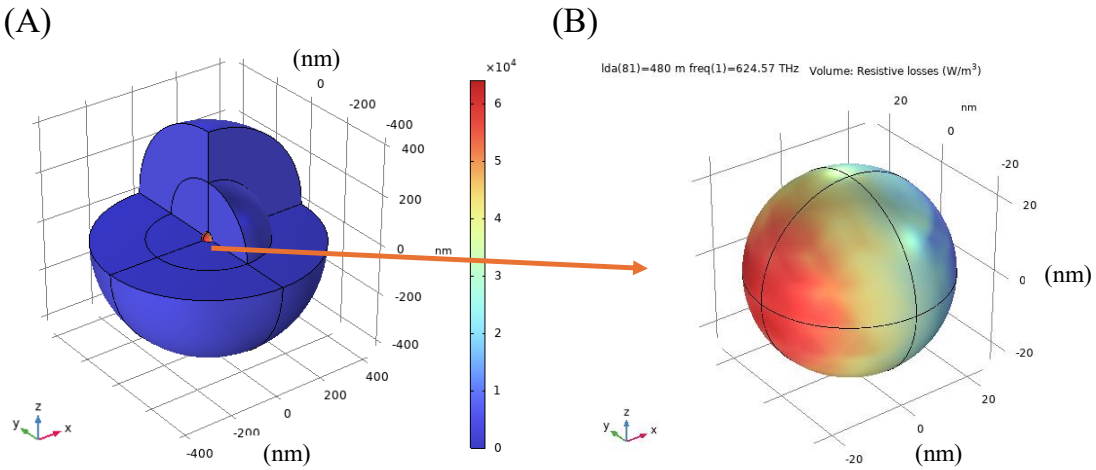

Figure 3-2 Schematic of the simulation environment: (A) Several layers including the gold structure, dielectric layers, and the PML; (B) The distribution of the electric field surrounding each gold nanoparticle.

The surrounding refractive index sensitivity is systematically evaluated by varying the surrounding medium's refractive index (SRI) from 1.33 to 1.38. As shown in Figure 3-3, each SRI change induces a characteristic redshift in the absorption maximum, with sensitivity quantified through linear regression of resonance wavelength versus SRI. Our simulations reveal that 50 nm diameter NP achieve optimal sensitivity (130 nm/RIU in the SRI = 1.33-1.38 range), in agreement with prior theoretical and experimental studies [24], [25], [26]. This size represents a compromise between sufficient electromagnetic field penetration depth and strong plasmonic confinement [15].

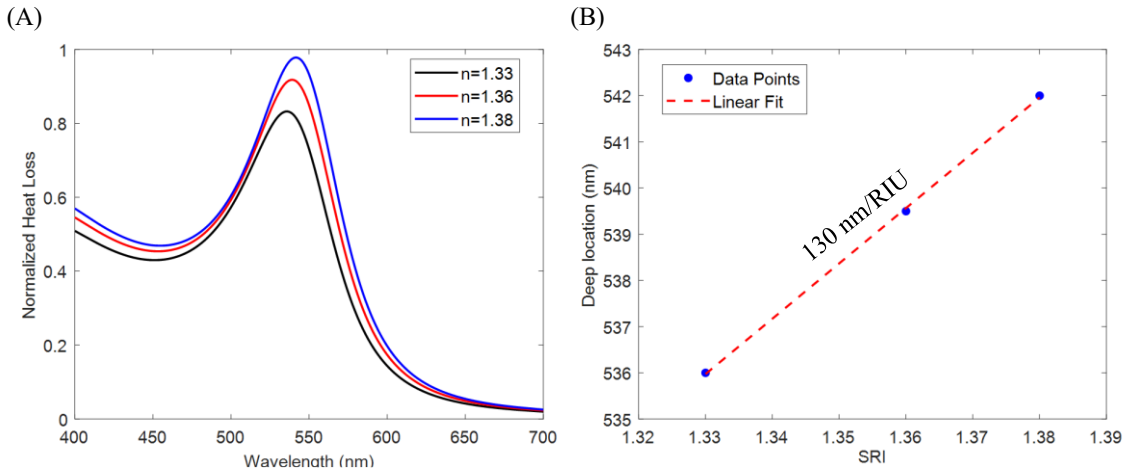

Figure 3-3 (A) The absorption spectra of a single ANP at different surrounding refractive index; (B) Resonance wavelength of the absorption band peak versus surrounding refractive index.

3.2.2. Effect of nanoparticle size

Previous simulations have assumed a fixed NP size of 50 nm. This section investigates the influence of NP size on the absorption spectrum and the SRI sensitivity. This investigation is crucial for two main reasons: firstly, to inform the optimal NP size selection for the experimental phase of this research, and secondly, to understand the required precision in synthesizing NPs, specifically how deviations in size might impact sensitivity, absorption, Full Width at Half Maximum (FWHM) and Figure of Merit (FOM).

FWHM is a measure of the width of a peak in a spectral curve, measured between the two points where the value is half of the maximum amplitude. A smaller FWHM value indicates a sharper, more defined peak, which is crucial for distinguishing between closely spaced signals. In spectroscopy, a narrow FWHM is often a sign of high spectral resolution, allowing for better identification and analysis of different components in a sample.

Figure of Merit (FOM) is a dimensionless metric used to evaluate the performance of a sensor. In the context of plasmonic sensing, it's typically defined as the ratio of the sensor's sensitivity to the FWHM. The formula is often expressed as:

$$FOM = \frac{Sensitivity}{FWHM} \qquad (3\text{-}1)$$

A higher FOM indicates a better performing sensor because it signifies a large change in the sensor's response (high sensitivity) for a given stimulus, combined with a narrow, well-resolved spectral peak (low FWHM). This makes the sensor more effective at detecting small changes in the surrounding environment.

The simulation methodology closely follows the previous approach, with the key modification being the systematic variation of NP diameter from 20 nm to 90 nm in 10 nm increments. Figure 3-4 presents the simulated absorption spectra for NPs of varying sizes in an aqueous environment. For comparative analysis, all spectra in this figure have been normalized to the global maximum absorption value, which was observed for the 90 nm NP. A red-shift in the absorption band is evident with increasing NP size. However, of particular interest are the changes in absorption intensity and FWHM [24], [27].

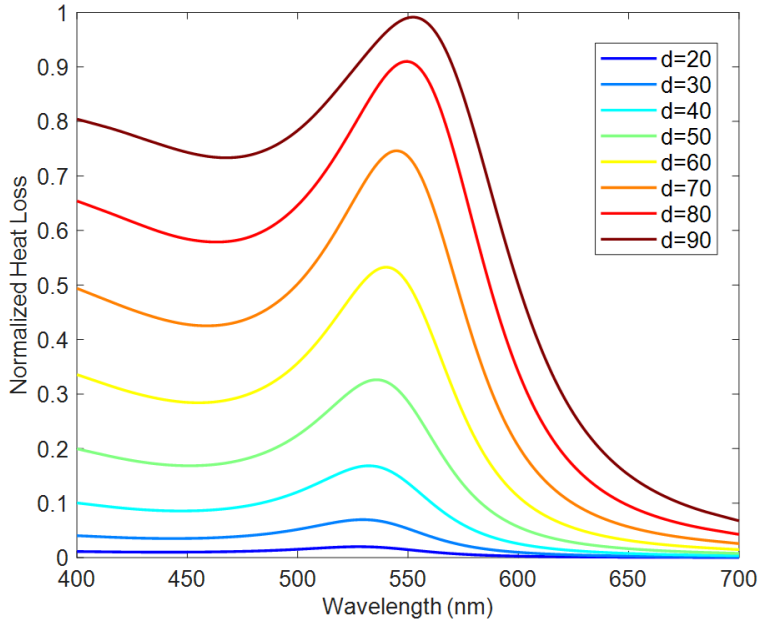

Figure 3-4. Absorption spectrum of different sized nanoparticles (20-90 nm) in an aqueous environment.

Figure 3-5(A) shows the resonance band changes by increasing the NP size, a red-shift of the absorption peak are clearly evident as NP size increases, a trend further emphasized in this Figure. For larger NPs, the absorption peak becomes flatter due to the NP size becoming comparable to the incident wavelength, leading to deviations from ideal Mie scattering behavior [23], [24], [28], [29].

Figure 3-5(B) shows that the normalized absorption band increases with particle size, which indicates that larger nanoparticles scatter more light and may enhance sensitivity [27], [30]. On the other hand, as shown in Figure 3-5(C), larger nanoparticles deviate further from the Mie scattering approximation, leading to an increase in FWHM and a broadening of the attenuation band. This implies that increasing the size involves a trade-off, and an optimal balance point should be determined. In sensing applications, a sharper attenuation band is highly desirable as it enhances accuracy and leads to a better LOD. Consequently, the increased FWHM observed with larger NPs represents a significant drawback for their use in high-precision sensing [28], [31], [32].

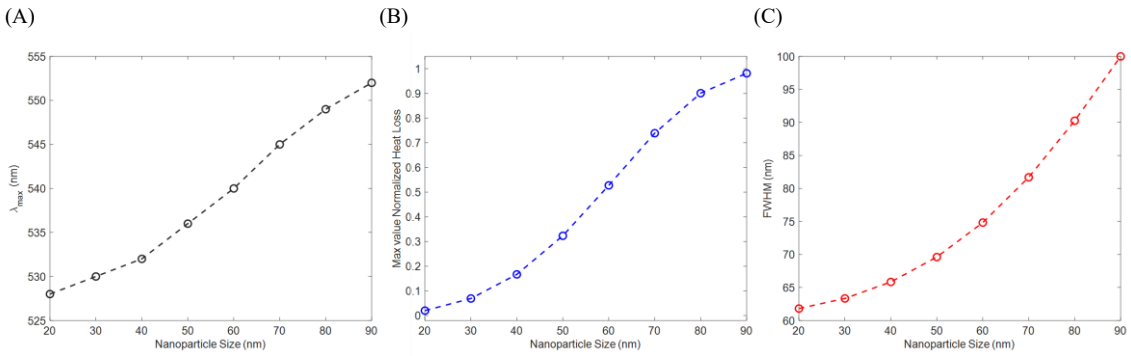

Figure 3-5. (A) Resonance wavelength as a function of NP size. (B) Maximum value normalized absorption versus nanoparticle size. (C) FWHM versus nanoparticle size.

The final stage of this investigation involves the SRI characterization of individual NPs across the previously examined size range. To this aim, in addition to the absorption spectrum for SRI 1.33 (as determined in previous steps), absorption spectra were calculated for each NP size at SRI values of 1.36 and 1.38. Consequently the SRI sensitivity was calculated. Figure 3-6(A) illustrates the relationship between SRI sensitivity and NP size:

SRI sensitivity generally increases with increasing NP size. This increase in sensitivity can be attributed to the increasing absorption coefficient with larger NP sizes, as previously demonstrated in Figure 3-5(B). Furthermore, an increase in resonance wavelength (also shown in Figure 3-5(A)) contributes to higher sensitivity, consistent with the principles discussed in the previous chapter.

However, beyond an NP size of approximately 80 nm, the attenuation spectrum becomes significantly broader. In smaller nanoparticles (much smaller than the wavelength), the electron cloud oscillates coherently, producing sharp dipolar resonances with narrow FWHM. As the particle size increases toward or beyond the resonant wavelength scale, radiative damping, non-uniform polarization, and the excitation of multipolar modes lead to peak broadening and redshifts. This broadening represents a tradeoff: while larger nanoparticles generally exhibit higher refractive index sensitivity due to stronger resonance shifts, the increased linewidth reduces spectral resolution and detection accuracy [33].

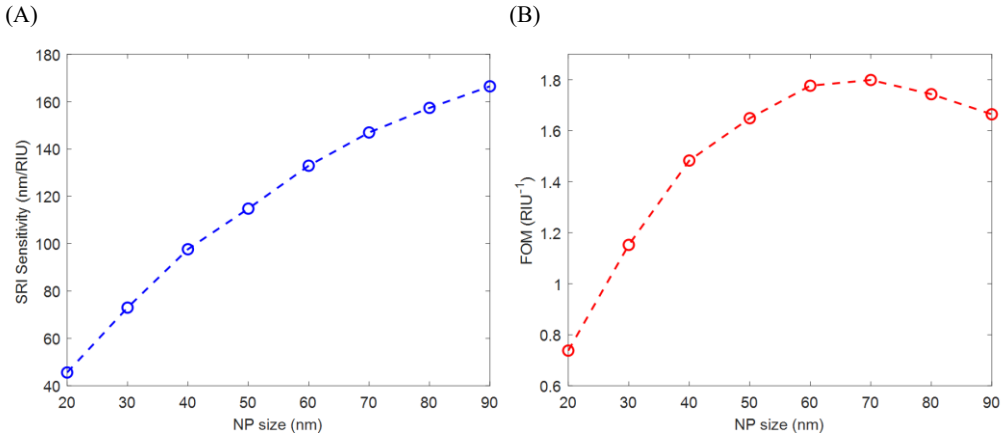

Figure 3-6. (A) SRI sensitivity and (B) FOM for different size of NPs.

Finally the FOM as a function of NP size is plotted in figure 3-6(B): it initially rises as the NP size increases from 20 nm, reaching a maximum value at approximately 60 nm. Any further increase in NP size leads to a rapid and significant decline in the sensor's FOM. This behavior demonstrates that while increasing the size of the NPs can initially improve sensor performance, there is a specific, optimal size at which the sensor's overall quality is maximized [24], [31].

Upon closer examination of both graphs, it becomes evident why the optimal sensor performance occurs at a NPs size of 60 nm. While Figure 3-6(A) shows that the SRI sensitivity remains high between 60 nm and 80 nm, the sharp drop in the FOM after 60 nm indicates that the sensor's resolution must be significantly degrading in this region. This suggests that the 50-60 nm NPs size represents the perfect compromise between achieving a high sensitivity and maintaining a sufficiently narrow resonance bandwidth, in good agreement with results presented in Ref. [24], [31]. Consequently, the 60 nm NP design yields the highest possible FOM, making it the most effective and robust configuration for the sensor. Considering this optimal range, a nanoparticle size of 50 nm will be utilized as an average representative value for subsequent simulations in this study [24].

3.2.3. Aggregated nanoparticles

AuNPs typically exhibit negative surface charges that promote electrostatic repulsion, thereby maintaining colloidal stability by preventing aggregation. However, under realistic conditions, factors such as gradual charge neutralization, environmental contamination, or intentional chemical modifications can lead to partial aggregation, where nanoparticles come into close proximity or direct contact. This section investigates the influence of such aggregation phenomena on the optical properties of AuNPs through computational simulations. To systematically analyze the effects of aggregation, different cluster configurations were modeled, including dimers (2-NP) and trimers (3-NP) of 50 nm diameter NPs in an aqueous environment.

In the case of dimers, Figure 3-2(A) illustrates a configuration where two nanoparticles are aligned along the x-axis within the xy-plane, while light propagates perpendicular to their alignment along the z-axis. The polarization of incident light remains unchanged, simulating a scenario where two nanoparticles aggregate side-by-side in a linear arrangement orthogonal to the propagation direction. The corresponding absorption spectrum, shown in Figure 3-7(B) as a black curve, exhibits a single peak at 560 nm, closely resembling the spectrum of an isolated AuNP, as seen in Figure 3-7(A). Further investigations explore the spectral response under rotational variations of the dimer. Figure 3-7(B) presents absorption spectra for rotation angles of 30°, 45°, 60°, and 90° about the y-axis. As the rotation angle increases, the effective aggregate dimension along the light propagation axis (z-axis) changes, leading to a notable spectral shift. Specifically, two distinct absorption peaks emerge: the shorter-wavelength peak corresponds to the individual NP response, while the longer-wavelength peak arises due to the increased effective size of the dimer along the z-axis upon rotation. Since experimental conditions typically involve an ensemble of randomly oriented aggregates, the angle-averaged

spectrum, represented by the brown curve, is also provided, illustrating the cumulative absorption behavior across multiple incident angles.

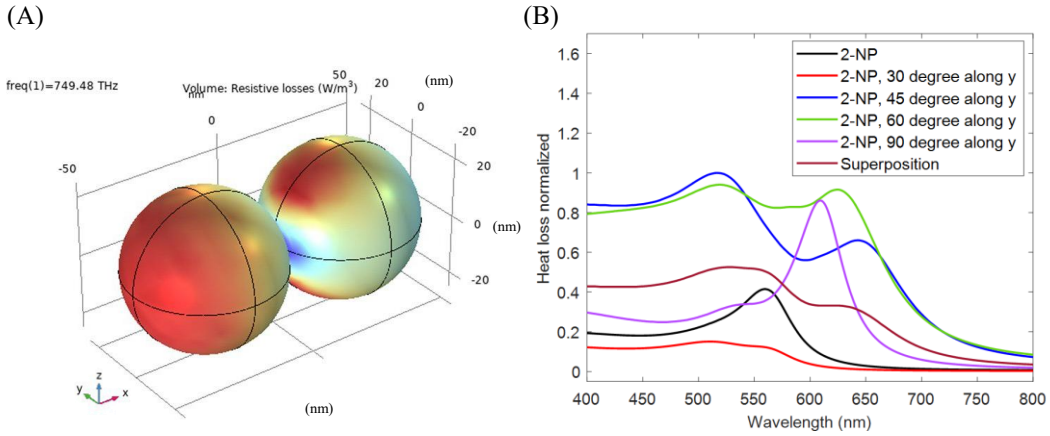

Figure 3-7 Simulation of two nanoparticles: (A) spatial configuration and electric field distribution; and (B) absorption spectra for various configurations and the superposition of these spectra.

The analysis was extended to trimers, where a triangular close-packed arrangement of three NPs in the xy-plane was examined, as depicted in Figure 3-8(A). The absorption spectrum, shown in Figure 3-8(D) as a black curve, initially displays a single peak, analogous to the monomeric case. However, upon rotation, as illustrated in Figure 3-8(B) and (C), the spectra exhibit significant angular dependence. In the configuration shown in Figure 3-8(B), the trimer is rotated such that two NPs remain orthogonal to the light propagation direction, while the third is offset along the z-axis. This results in three distinct absorption peaks, represented by the red curve, corresponding to the response of an individual nanoparticle, the coupled response of the two in-plane NPs, and the combined interaction involving all three NPs. In contrast, the configuration in Figure 3-8(C) features two nanoparticles stacked along the z-axis, with the third positioned laterally, leading to two absorption peaks, as seen in the blue curve. This behavior is similar to that observed in the dimer case at intermediate rotation angles, as shown in Figure 3-7(B) by the blue and green curves.

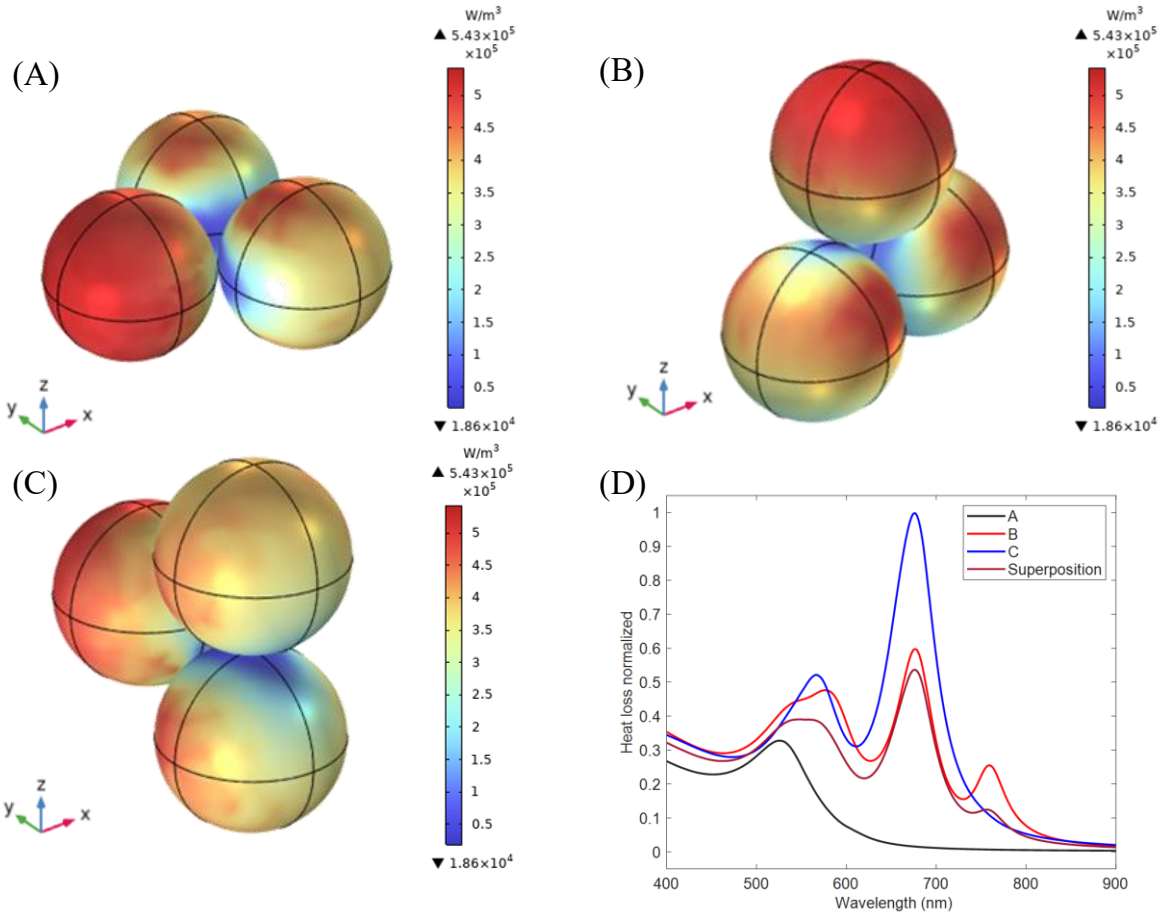

Figure 3-8 Simulation of three nanoparticles: (A), (B), (C) three different spatial configuration and related electric field distributions; (D) absorption spectrum for the various configurations and the superposition of these spectra.

The number and position of absorption peaks are strongly influenced by the geometric arrangement of NPs relative to the incident light. A key observation is the consistent appearance of the primary peak around 560 nm across all configurations, corresponding to the intrinsic plasmonic response of an individual NP. Additional peaks emerge due to interparticle coupling, with their spectral positions dependent on the aggregate's effective size along the light propagation axis. Rotational variations introduce spectral broadening and peak splitting, reflecting the anisotropic optical response of non-spherical aggregates. These results highlight the critical role of NP organization in determining plasmonic properties, with significant implications for applications such as sensing, catalysis, and photothermal therapy, where controlled aggregation is essential for optimizing performance. The findings underscore the importance of considering both individual and collective nanoparticle behavior in the design and interpretation of plasmonic systems.

In real-world applications, such as colloidal AuNP solutions or AuNP layers deposited on transducer surfaces, the observed absorption spectrum is a complex combination of contributions from various nanoparticle arrangements—from isolated single nanoparticles to multi-layered aggregates.

To simplify this complex scenario, various solutions have been simulated, each containing a specific ratio of single nanoparticles, dimers (clusters of two), and trimers (clusters of three) (as detailed in Table

3-1). The absorption spectra for these configurations were calculated by incorporating participation weights from Table 3-1, allowing us to understand how different levels of aggregation contribute to the overall spectral response [15].

Table 3-1. Properties of the calculated solutions.

aggregation state	S1	S2	S3	S4
single nanoparticle	33.33 %	50 %	25 %	25 %
superposition of 2 NPs	33.33 %	25 %	50 %	25 %
superposition of 3 NPs	33.33 %	25 %	25 %	50 %

As illustrated in Figure 3-9 the superposition of these diverse aggregation states leads to the emergence of two primary absorption peaks. Given our previous observations from Figure 3-7 and Figure 3-8, where individual NPs consistently appeared in all simulated solutions, it's clear that the first prominent peak in the absorption spectrum is largely attributed to the behavior of these single NPs.

Crucially, the final simulated spectrum represents an average of all these contributing behaviors. This averaging effect is what ultimately gives rise to the presence of two distinct absorption bands. We observed a notable trend: as the participation weight of higher aggregation level clusters increases, the second absorption peak becomes more prominent and exhibits greater redshift. This redshift is a direct consequence of the enhanced plasmonic coupling occurring within larger aggregates, leading to a shift of the resonance to longer wavelengths [15], [25], [27], [31].

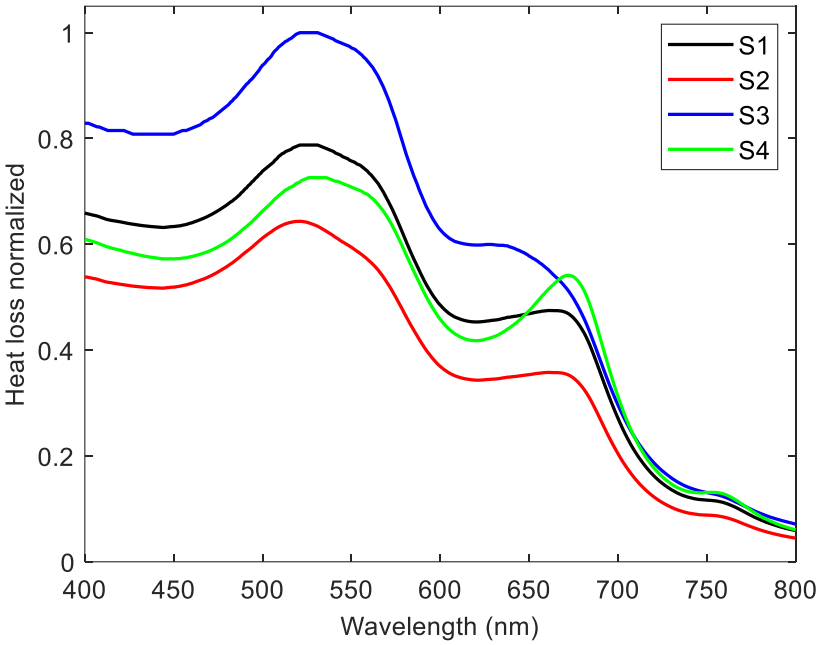

Figure 3-9. Numerical absorption spectra related to four distinct combinations of single, two, and three nanoparticles. Details of the solutions are reported in Table 1.

While this analysis considers a limited number of aggregation states and orientations, it provides a fundamental understanding necessary for interpreting the experimental spectra discussed in the subsequent section. This systematic approach allows us to deconvolute the complex spectral signatures observed experimentally, linking macroscopic optical properties to the underlying microscopic arrangement of nanoparticles [15].

3.2.4. Nanostars

The simplest metallic nanostar can be described as a solid spherical core surrounded by multiple branches that interact with the surrounding medium. The number of branches, their shape, height, aspect ratio, and spatial distribution are parameters that can vary over a wide range and play a crucial role in determining the LSPR properties. These morphological features act as effective tuning mechanisms for controlling the optical response.

In this section, the focus is placed on a specific case study in which certain structural aspects were selected to reproduce the experimental conditions while maintaining geometric symmetry during simulation. This approach allows for a simplification of the numerical analysis without compromising the physical relevance of the model. Nevertheless, it is believed that several general design criteria can also be derived from this study.

In our study case, the NS structure comprises a spherical gold (Au) core surrounded by multiple silver (Ag) branches: specifically it consists of a 40 nm Au spherical core and 14 symmetrically arranged Ag branches The number of branches was chosen to maintain structural symmetry during simulation. Each branch has a conical shape with a smoothed tip (curvature radius = 0.5 nm) to avoid sharp discontinuities. To maintain a consistent outer diameter of 60 nm, the branch height was fixed at 10 nm, while the base width was varied between 4 nm and 16.7 nm, resulting in branch height-to-width aspect ratio (BAR) values ranging from 0.6 to 2.5.

Figure 3-10 shows the morphology of simulated NSs, Figure 3-10(A) shows the whole simulation medium, and Figure 3-10(B) and (C) illustrate two representative cases: a high-BAR (2.5) NS with narrow, elongated branches and a low-BAR (1.2) NS with wider branches, respectively. Notably, as the BAR decreases (i.e., branch width increases), the Ag coverage over the Au core becomes more extensive. For BAR < 1, the gold core is entirely enveloped by the silver branches [25], [26].

Figure 3-10(D) illustrates the mesh distribution for the NS with a BRA of 1.2. The mesh size is intentionally smaller at the tips of the branches, which are the sharpest morphological features. The diameter of these branched tips is 1 nm, and the minimum mesh size within the NS itself is approximately 0.25 nm. In the surrounding environment, the mesh size expands to a maximum of 31 nm, which is still smaller than the common rule of thumb of $\lambda/10$ for accurate simulation.

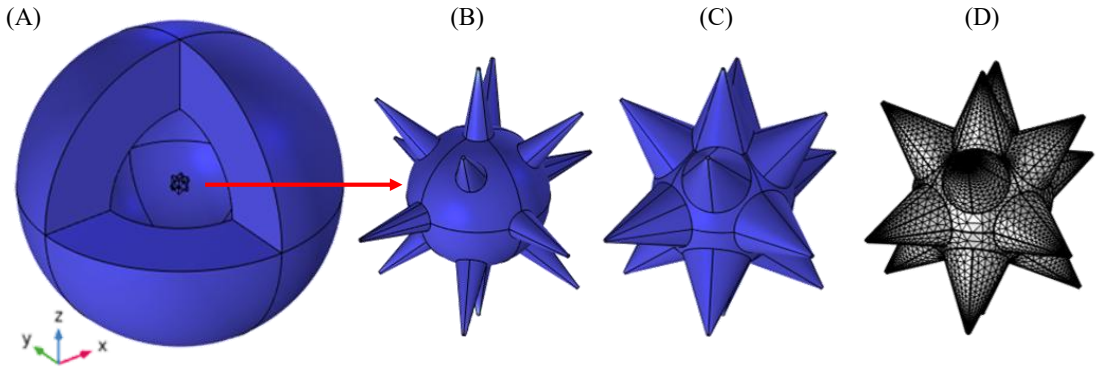

Figure 3-10. The simulation geometry: (A) the whole simulation medium; (B) the NS with a BAR of 2.5; and (C) BAR = 1.2. (D) BAR=1.2 with meshing.

Figure 3-11 presents the simulated absorption spectra of the NS across different BAR values (0.6–2.5), where as previously mentioned the base width decreases from 16.7 nm to 4 nm while keeping the height constant at 10 nm. For comparison, the absorption spectra of a 40 nm pure AuNP (black curve) and a 40 nm AuNP coated with a 10 nm Ag shell (grey curve) are also included. The pure AuNP exhibits a characteristic absorption peak at 532 nm, whereas the addition of the Ag shell induces a blue shift to 442 nm, resembling the optical response of a 60 nm Ag nanoparticle.

As the Ag shell transitions into a branched morphology (NS structure), the LSPR behavior changes significantly. At low BAR (0.6), a single absorption peak is observed, but as the BAR increases, this peak splits into two distinct resonances with varying amplitudes and bandwidths [34], [35]. The primary peak red-shifts progressively with increasing BAR, accompanied by notable changes in intensity and spectral width [6], [16], [36], [37], [38].

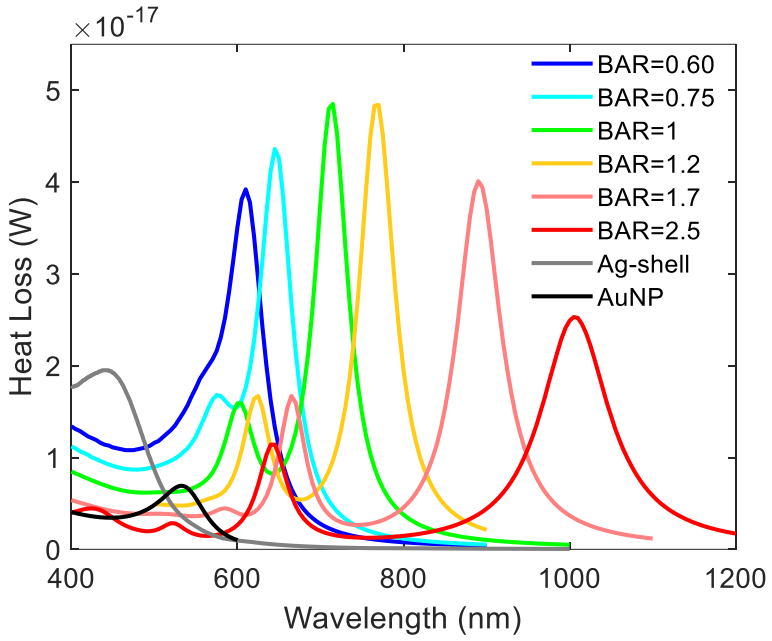

Figure 3-11. Simulated absorption spectrum of NSs with different branch base widths

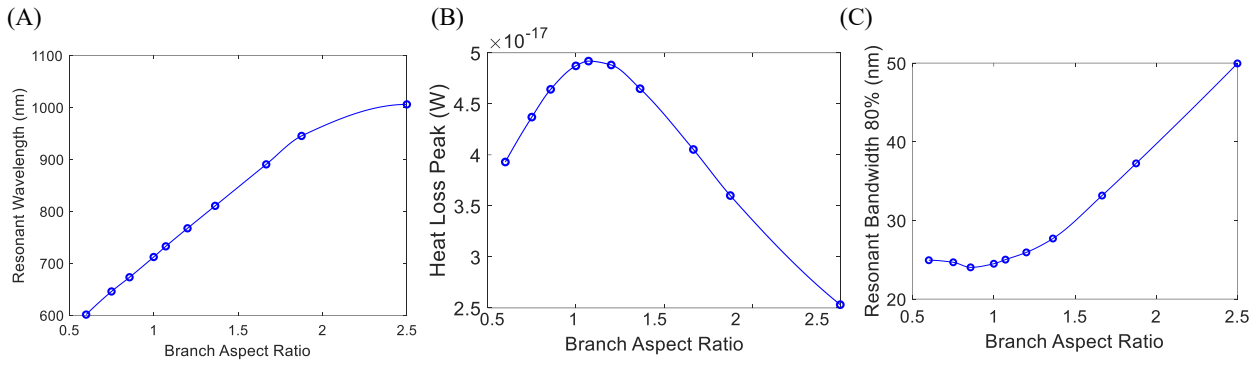

Figure 3-12. (A) Relationship between the resonance wavelength (for SRI = 1.33), (B) heat loss peak and (C) resonance bandwidth with BAR

Figure 3-12(A) demonstrates the linear dependence of the main resonance wavelength on BAR in the range 0.6–2.0, followed by a saturation effect near BAR = 2.5. Overall, this behavior highlights the effectiveness of geometric tuning in controlling LSPR properties.

Additionally, Figure 3-12(B) and Figure 3-12(C) analyze the peak amplitude and bandwidth (measured at 80% of maximum amplitude), respectively. The bandwidth is achieved at BAR ≈ 1, corresponding to a resonance near 650–700 nm. At higher BAR values, the resonance weakens, and the bandwidth broadens, making detection more challenging in practical sensing applications.

The sensitivity to SRI changes (1.33–1.35) was evaluated as a function of BAR (Figure 3-13). The results reveal that sensitivity increases from 200 nm/RIU to ~750 nm/RIU as BAR rises from 0.6 to 2.5 following a nearly linear relationship [16].

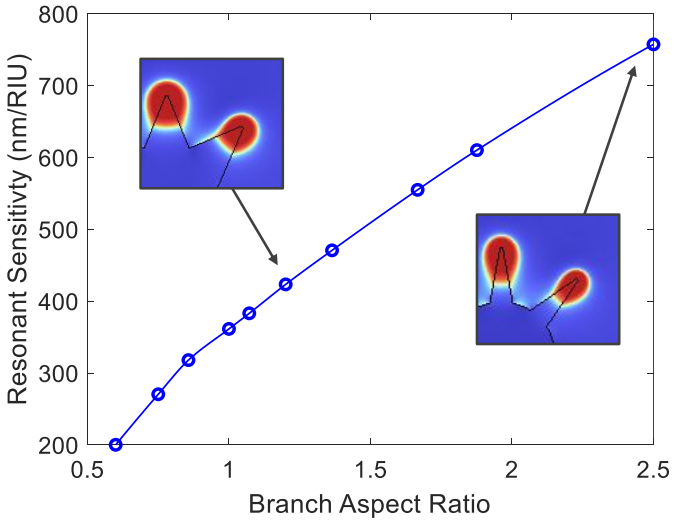

Figure 3-13. Simulated sensitivity of the absorbance peak wavelength to the SRI in range 1.33-1.35 as a function of the BAR. In inset the electromagnetic field distribution around the branches in case of BAR = 1.2 and BAR = 2.5.

To further elucidate the mechanism, electric field distribution maps (insets in Figure 3-13) are provided for two cases: BAR = 1.2 and BAR = 2.5. These simulations demonstrate how the localized

field enhancement around the branches contributes to the improved SRI sensitivity at higher BAR values [16].

In summary, adjusting the branch geometry of the NS not only enables precise LSPR tuning but also enhances refractive index sensitivity, making this structure highly promising for chemical and biosensing applications [35]. The ability to control both the resonance position and sensitivity through simple geometric modifications establishes the NS as a versatile and efficient plasmonic platform [16], [36].

3.2.5. Effect of nanostars size

As established in the theory section and Section 3.2.2, the nanostructure size influences the resonance band, SRI sensitivity, and FWHM. The following analysis will therefore investigate the impact of NS size on these parameters.

Section 3.2.4 defined NS branch height and width as a ratio to the seed size, which was fixed at d=40 nm. In that section, the effect of the BAR on SRI sensitivity was investigated by sweeping the branch size while keeping the seed and branches height fixed.

This section presents a new investigation where the BAR is held constant at 1, while the overall size of the NS is varied. This size change is a sweep from 50% to 400% of the NS studied in the previous section, which is equivalent to varying the seed size d from 20 nm to 80 nm. For clarity, Figure 3-14 (A) and (B) shows the NS with seed sizes of 20 nm and 40 nm, respectively.

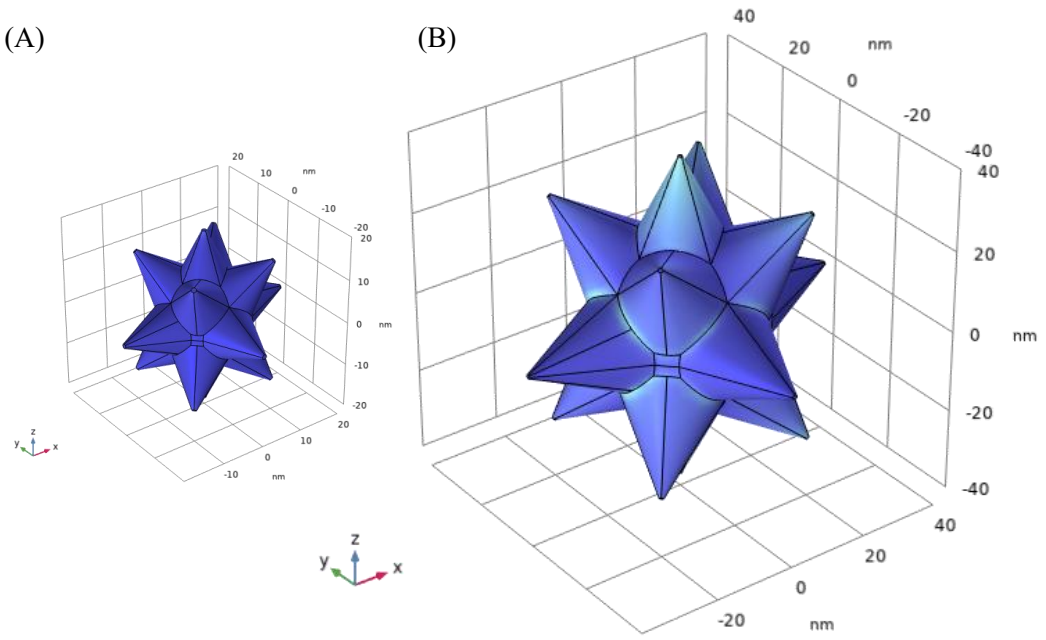

Figure 3-14. NS with BAR=1 with seed sizes of (A) 20 nm (B) 40 nm.

The normalized attenuation spectra of different NS are shown in Figure 3-15. As seen in this figure, increasing the size of the NS leads to an increase in the attenuation spectrum and a noticeable broadening of the attenuation band, a phenomenon also observed in nanoparticles.

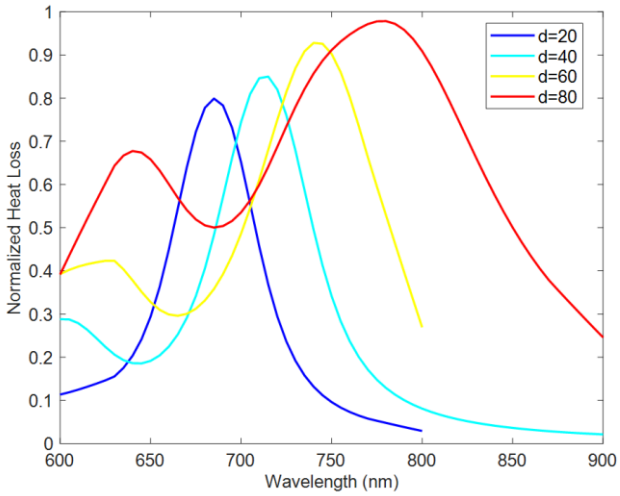

Figure 3-15. Normalized attenuation spectra for different NS.

Resonance wavelength of each spectrum calculated and draw versos NS size in Figure 3-16(A). Increasing the NS size results in a redshift (an increase) of the resonance wavelength, as depicted in Figure 3-16(A). Simultaneously, the attenuation band becomes broader. This broadening effect is similar to what is observed in simpler nanoparticles and occurs because, as the nanostructure size increases, it begins to deviate from the Mie theory approximation. The Mie theory is most accurate for smaller, spherical particles, and as particles become larger and more complex, their optical behavior is no longer perfectly described by the theory, leading to a broadening of the resonance peak.[38], [39], [40]

The SRI sensitivity for each NS was calculated and is shown in Figure 3-16(B). These results indicate that SRI sensitivity increases with increasing the NS size, similar to NPs [41].

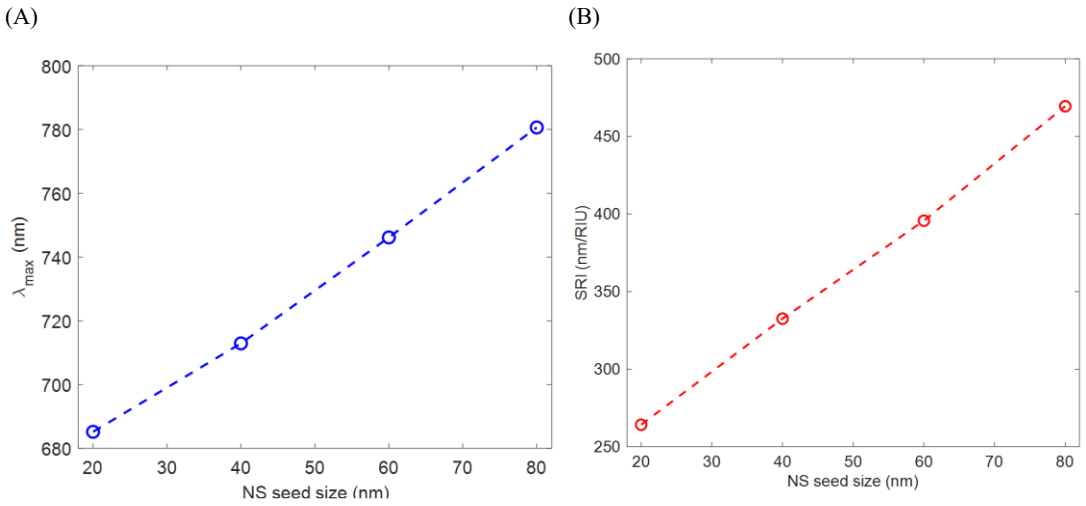

Figure 3-16. (A) Resonance wavelength versus seed size. (B) SRI sensitivity versus NS seed size.

As discussed previously, the FOM can be employed to compare sensor quality. To calculate this parameter, the FWHM for each NS was first calculated, as shown in Figure 3-17(A). Using these

FWHM values and the SRI sensitivity, the FOM for each NS was then calculated and is shown in Figure 3-17(B) [42], [43].

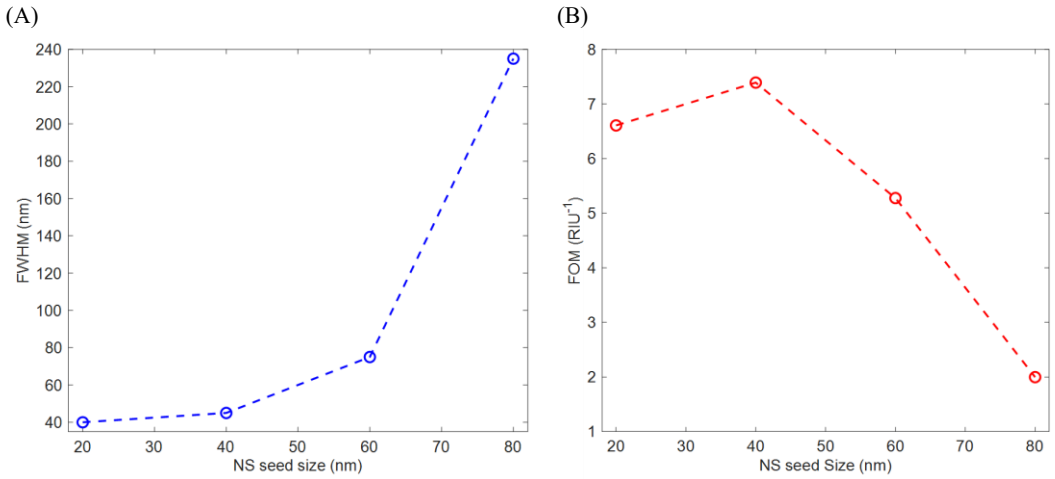

Figure 3-17. (A) FWHM and (B) FOM of NS in different seed size.

The provided data illustrates the crucial relationship between NSs seed size and key sensor performance metrics, namely the FWHM and the FOM. As depicted in Figure 3-17(A), the FWHM shows a steady increase with growing seed size, but this trend becomes particularly pronounced and non-linear as the size is scaled from 40 nm to 80 nm. This broadening of the resonance peak indicates a degradation in the sensor's resolution for larger nanostructures. Concurrently, Figure 3-17(B) reveals a more complex relationship for the FOM, which is a composite metric of sensor quality. The FOM initially rises, reaching a clear maximum value around a seed size of 40 nm, before falling sharply as the seed size is further increased [43].

This analysis highlights a critical trade-off in the sensor's design. The optimal performance is not achieved at the lowest FWHM (at 20 nm) but rather at a point where the balance between sensitivity and resolution is maximized. The increase in FOM from 20 nm to 40 nm suggests that the rise in sensitivity over this range is significant enough to outweigh the slight broadening of the resonance peak. The nanostructure with a 40 nm seed size represents the pinnacle of performance for this system, as it achieves the highest overall FOM [41], [43].

Beyond this optimal point, the sensor's performance deteriorates rapidly. The sharp decline in the FOM for seed sizes larger than 40 nm is primarily driven by the dramatic increase in FWHM, as shown in the first graph. This broadening effect quickly degrades the sensor's resolution, overshadowing any potential gains in sensitivity and leading to a suboptimal design. Therefore, the data strongly supports that a nanostructure with a 40 nm seed size is the most efficient and highest-performing configuration, striking the ideal balance between the competing demands of high sensitivity and high resolution [33].

3.2.6. Effect of substrate

As previous results examined nanostructures in an unlimited aqueous environment, this section specifically explores the effect of a nearby glass surface, since the nanostructures will later be deposited onto glass optical fibers.

The initial simulation configuration involves a single layer of AuNPs deposited on a glass (silica) substrate. To evaluate the absorption spectrum, a precisely constructed square unit cell is employed. This unit cell contains a whole spherical nanoparticle at its center, surrounded by a quarter of a nanoparticle at each of its four corners, effectively simulating a endless NP-layer. This nanoparticle arrangement is placed on top of a silica layer, with water serving as the surrounding medium for the nanoparticles. The flexibility to change the surrounding medium based on experimental needs is a key advantage of this simulation approach.

To accurately represent an infinite, uniform layer of nanoparticles in the xy-plane, periodic boundary conditions are applied along the x and y axes of the unit cell. Furthermore, to prevent unwanted reflections and ensure that the silica and outer medium behave as infinite extensions, PML boundary conditions are implemented at the top and bottom of the unit cell. This ensures that the electric field does not reflect from the boundaries, providing a more realistic simulation environment.

The NPs considered in this study have a diameter of 50 nm, specifically chosen to match the experimental conditions. Initially, these nanoparticles are arranged in the aforementioned square unit cell, where they are in complete contact with each other, as depicted in Figure 3-15(A). The incident light is a plane wave propagating along the z-direction (from -z to +z) and is polarized along the x-direction, with a constant illumination power of 1 W/m².

A crucial aspect of this investigation is the effect of introducing a small gap between the NPs, specifically when they are separated by a distance of $2\sqrt{2}$ nm edge-to-edge. This allows for the study of how inter-particle spacing influences the absorption spectrum.

Additionally, the impact of the silica substrate is thoroughly investigated. The simulation is repeated with the NPs suspended in water on the xy surface (i.e., without the silica layer), maintaining the same setup as the initial simulation. This comparison helps to isolate the specific contribution of the substrate to the overall absorption behavior.

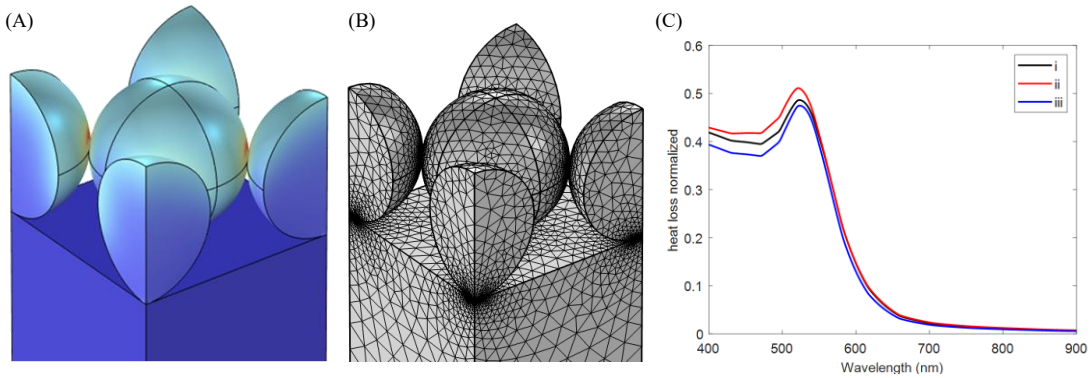

Figure 3-18. (A) Simulation geometry (unit cell) and the distribution of electric fields on the golden nanoparticles at wavelength λ = 525 nm. (B) mesh distribution. (C) The absorption spectrum of different configurations: i) NPs on glass attached; ii) NPs without glass attached; iii) NPs separated by a small gap, arranged on glass in water.

Figure 3-18(A) illustrates the simulation geometry, depicting the electric field distribution around NPs at an excitation wavelength (λ) of 525 nm, specifically for nanoparticles deposited on a silica surface in an aqueous environment. Figure 3-18(B) shows the mesh distribution in the simulation medium. In connection point mesh size decrease and in general mesh size is lower than λ/10.

Figure 3-18(C) compares the absorption spectra for three configurations:

(i) Nanoparticles in direct contact, placed on glass in water.

(ii) Nanoparticles in direct contact, suspended in water without a substrate.

(iii) Nanoparticles separated by a small gap, arranged on glass in water.

All three cases exhibit similar absorption peaks between 520 nm and 523 nm. When NPs are on a silica substrate (cases i and iii), the spectral shape remains nearly identical, regardless of their contact or separation. However, a slight redshift (from 520 nm to 523 nm) occurs for NPs on glass compared to those in pure water. This shift arises because the LSPR is influenced by the refractive index of the surrounding medium. Since glass has a higher refractive index than water, the plasmonic electrons experience a modified dielectric environment, leading to the observed redshift [40], [44], [45].

In real-world scenarios, NPs on a substrate may exist as isolated particles, clusters, or aggregates, contributing to a broader experimental absorption spectrum around 520 nm compared to simulations.

In summary, for a uniform nanoparticle layer orthogonal to light propagation, the simulations suggest minimal impact from interparticle contact or the glass substrate, with only a minor redshift observed. The plasmonic response is predominantly determined by the nanoparticles' intrinsic properties and their collective arrangement, rather than subtle environmental variations. Further investigation is needed to fully elucidate the mechanisms behind this relative insensitivity [46], [47], [48], [49].

3.3. Conclusion

In this chapter, we've explored the electromagnetic behavior of various nanostructures under diverse conditions, focusing on their interaction with light. We've investigated both individual and aggregated

nanoparticles, examining their behavior with and without a glass substrate. Nanostar-based configurations have been also explored. A key aspect of our study has been understanding how to tune the attenuation band by altering nanostructure morphology and how these changes subsequently affect SRI sensitivity. The insights gained from these numerical investigations will form the foundational information for the experimental phase of this project, as reported in next chapters.

3.4. References

[1] F. Enguehard, “Mie theory and the discrete dipole approximation. calculating radiative properties of particulate media, with application to nanostructured materials,” in Thermal Nanosystems and Nanomaterials, Springer, 2009, pp. 151–212.

[2] G. Mie, “Beiträge zur Optik trüber Medien, speziell kolloidaler Metallösungen,” Ann Phys, vol. 330, no. 3, pp. 377–445, Jan. 1908, doi: 10.1002/andp.19083300302.

[3] S. W. Prescott and P. Mulvaney, “Gold nanorod extinction spectra,” J Appl Phys, vol. 99, no. 12, 2006.

[4] C. F. Bohren and D. R. Huffman, Absorption and scattering of light by small particles. John Wiley & Sons, 2008.

[5] D. Ma, P. Tuersun, L. Cheng, Y. Zheng, and R. Abulaiti, “PyMieLab_V1.0: A software for calculating the light scattering and absorption of spherical particles,” Heliyon, vol. 8, no. 11, p. e11469, 2022, doi: https://doi.org/10.1016/j.heliyon.2022.e11469.

[6] J. M. Terrés-Haro, J. Monreal-Trigo, A. Hernández-Montoto, F. J. Ibáñez-Civera, R. Masot-Peris, and R. Martínez-Máñez, “Finite element models of gold nanoparticles and their suspensions for photothermal effect calculation,” Bioengineering, vol. 10, no. 2, p. 232, 2023.

[7] C. Noguez, “Surface plasmons on metal nanoparticles: the influence of shape and physical environment,” The Journal of Physical Chemistry C, vol. 111, no. 10, pp. 3806–3819, 2007.

[8] G. V Hartland, “Optical studies of dynamics in noble metal nanostructures,” Chem Rev, vol. 111, no. 6, pp. 3858–3887, 2011.

[9] E. M. Purcell and C. R. Pennypacker, “Scattering and absorption of light by nonspherical dielectric grains,” Astrophysical Journal, Vol. 186, pp. 705-714 (1973), vol. 186, pp. 705–714, 1973.

[10] S. K. Ghosh and T. Pal, “Interparticle coupling effect on the surface plasmon resonance of gold nanoparticles: from theory to applications,” Chem Rev, vol. 107, no. 11, pp. 4797–4862, 2007.

[11] B. T. Draine and P. J. Flatau, “Discrete-dipole approximation for scattering calculations,” Journal of the Optical Society of America A, vol. 11, no. 4, pp. 1491–1499, 1994.

[12] D. A. G. Bruggeman, “Calculation of different physical constants of heterogen substances I Dielectric constants and conductibility of mixtures from isotrop substances,” Ann. Phys, vol. 416, no. 8, pp. 665–679, 1935.

[13] V. A. Markel, “Introduction to the Maxwell Garnett approximation: tutorial,” Journal of the Optical Society of America A, vol. 33, no. 7, pp. 1244–1256, 2016.

[14] B. A. Belyaev and V. V Tyurnev, “Electrodynamic calculation of effective electromagnetic parameters of a dielectric medium with metallic nanoparticles of a given size,” Journal of Experimental and Theoretical Physics, vol. 127, pp. 608–619, 2018.

[15] A. Moslemi, L. Sansone, F. Esposito, S. Campopiano, M. Giordano, and A. Iadicicco, “Optical fiber probe based on LSPR for the detection of pesticide Thiram,” Opt Laser Technol, vol. 175, p. 110882, Aug. 2024, doi: 10.1016/j.optlastec.2024.110882.

[16] A. Moslemi et al., “Highly sensitive gold nanostar based optical fiber sensor with tunable plasmonic resonance,” Sensors and Actuators Reports, p. 100326, Apr. 2025, doi: 10.1016/j.snr.2025.100326.

[17] O. C. Zienkiewicz, R. L. Taylor, and J. Z. Zhu, “The standard discrete system and origins of the finite element method,” The finite element method: its basis and fundamentals, pp. 1–20, 2013.

[18] N. J. Halas, S. Lal, W.-S. Chang, S. Link, and P. Nordlander, “Plasmons in strongly coupled metallic nanostructures,” Chem Rev, vol. 111, no. 6, pp. 3913–3961, 2011.

[19] Y. Tang, Q. Luo, Y. Chen, and K. Xu, “All-Silicon Photoelectric Biosensor on Chip Based on Silicon Nitride Waveguide with Low Loss,” Nanomaterials, vol. 13, no. 5, p. 914, Mar. 2023, doi: 10.3390/nano13050914.

[20] K. Xu, “Silicon electro-optic micro-modulator fabricated in standard CMOS technology as components for all silicon monolithic integrated optoelectronic systems *,” Journal of Micromechanics and Microengineering, vol. 31, no. 5, p. 054001, May 2021, doi: 10.1088/1361-6439/abf333.
[21] L. Litti and M. Meneghetti, “Predictions on the SERS enhancement factor of gold nanosphere aggregate samples,” Physical Chemistry Chemical Physics, vol. 21, no. 28, pp. 15515–15522, 2019, doi: 10.1039/C9CP02015B.
[22] H. Lei, S. Zhu, C. Liu, W. Zhang, C. Chen, and H. Yan, “Constructing the Au nanoparticle multimer on optical fiber end face to enhance the signal of localized surface plasmon resonance biosensors: A case study for deoxynivalenol detection,” Sens Actuators B Chem, vol. 380, p. 133380, Apr. 2023, doi: 10.1016/j.snb.2023.133380.
[23] P. N. Njoki et al., “Size Correlation of Optical and Spectroscopic Properties for Gold Nanoparticles,” The Journal of Physical Chemistry C, vol. 111, no. 40, pp. 14664–14669, Oct. 2007, doi: 10.1021/jp074902z.
[24] R. K. Saini, A. K. Sharma, A. Agarwal, and R. Prajesh, “Near field FEM simulations of plasmonic gold nanoparticle based SERS substrate with experimental validation,” Mater Chem Phys, vol. 287, p. 126288, 2022.
[25] N. Nath and A. Chilkoti, “Label-Free Biosensing by Surface Plasmon Resonance of Nanoparticles on Glass: Optimization of Nanoparticle Size,” Anal Chem, vol. 76, no. 18, pp. 5370–5378, Sep. 2004, doi: 10.1021/ac049741z.
[26] V. Semwal, O. R. Jensen, O. Bang, and J. Janting, “Investigation of Performance Parameters of Spherical Gold Nanoparticles in Localized Surface Plasmon Resonance Biosensing,” Micromachines (Basel), vol. 14, no. 9, p. 1717, Aug. 2023, doi: 10.3390/mi14091717.
[27] B. M. Ross, J. R. Waldeisen, T. Wang, and L. P. Lee, “Strategies for nanoplasmonic core-satellite biomolecular sensors: Theory-based Design,” Appl Phys Lett, vol. 95, no. 19, 2009.
[28] Y. Q. He, S. P. Liu, L. Kong, and Z. F. Liu, “A study on the sizes and concentrations of gold nanoparticles by spectra of absorption, resonance Rayleigh scattering and resonance non-linear scattering,” Spectrochim Acta A Mol Biomol Spectrosc, vol. 61, no. 13–14, pp. 2861–2866, 2005.
[29] N. M. Saleh and A. A. Aziz, “Simulation of surface plasmon resonance on different size of a single gold nanoparticle,” in Journal of physics: conference series, IOP Publishing, 2018, p. 12041.
[30] E. Gharibshahi and E. Saion, “Influence of Dose on Particle Size and Optical Properties of Colloidal Platinum Nanoparticles,” Int J Mol Sci, vol. 13, no. 11, pp. 14723–14741, Nov. 2012, doi: 10.3390/ijms131114723.
[31] V. Semwal, O. R. Jensen, O. Bang, and J. Janting, “Investigation of Performance Parameters of Spherical Gold Nanoparticles in Localized Surface Plasmon Resonance Biosensing,” Micromachines (Basel), vol. 14, no. 9, p. 1717, Aug. 2023, doi: 10.3390/mi14091717.
[32] M. Zhou and Z. Geng, “Integrated LSPR Biosensing Signal Processing Strategy and Visualization Implementation,” Micromachines (Basel), vol. 15, no. 5, p. 631, 2024.
[33] K. Kolwas and A. Derkachova, “Plasmonic abilities of gold and silver spherical nanoantennas in terms of size dependent multipolar resonance frequencies and plasmon damping rates,” Opto-Electronics Review, vol. 18, no. 4, Jan. 2010, doi: 10.2478/s11772-010-0043-6.
[34] S. K. Dondapati, T. K. Sau, C. Hrelescu, T. A. Klar, F. D. Stefani, and J. Feldmann, “Label-free Biosensing Based on Single Gold Nanostars as Plasmonic Transducers,” ACS Nano, vol. 4, no. 11, pp. 6318–6322, Nov. 2010, doi: 10.1021/nn100760f.
[35] H. Yuan, C. G. Khoury, H. Hwang, C. M. Wilson, G. A. Grant, and T. Vo-Dinh, “Gold nanostars: surfactant-free synthesis, 3D modelling, and two-photon photoluminescence imaging,” Nanotechnology, vol. 23, no. 7, p. 075102, Feb. 2012, doi: 10.1088/0957-4484/23/7/075102.

[36] F. Zhang, L. Xu, Y. Wang, and P. Wang, “Engineering plasmonic Au nanostars: Enhanced plasmonic properties, preparation and biomedical application,” Mater Today Bio, vol. 33, p. 102022, Aug. 2025, doi: 10.1016/j.mtbio.2025.102022.
[37] N. M. Ngo, H.-V. Tran, and T. R. Lee, “Plasmonic nanostars: systematic review of their synthesis and applications,” ACS Appl Nano Mater, vol. 5, no. 10, pp. 14051–14091, 2022.
[38] A. S. De Silva Indrasekara, S. F. Johnson, R. A. Odion, and T. Vo-Dinh, “Manipulation of the geometry and modulation of the optical response of surfactant-free gold nanostars: a systematic bottom-up synthesis,” ACS Omega, vol. 3, no. 2, pp. 2202–2210, 2018.
[39] C. G. Khoury and T. Vo-Dinh, “Gold nanostars for surface-enhanced Raman scattering: synthesis, characterization and optimization,” The Journal of Physical Chemistry C, vol. 112, no. 48, pp. 18849–18859, 2008.
[40] Y. Il Park, H. Im, R. Weissleder, and H. Lee, “Nanostar Clustering Improves the Sensitivity of Plasmonic Assays,” Bioconjug Chem, vol. 26, no. 8, pp. 1470–1474, Aug. 2015, doi: 10.1021/acs.bioconjchem.5b00343.
[41] S. Barbosa et al., “Tuning size and sensing properties in colloidal gold nanostars,” Langmuir, vol. 26, no. 18, pp. 14943–14950, Sep. 2010, doi: 10.1021/la102559e.
[42] M. Sivis, N. Pazos-Perez, R. Yu, R. Alvarez-Puebla, F. J. García de Abajo, and C. Ropers, “Continuous-wave multiphoton photoemission from plasmonic nanostars,” Commun Phys, vol. 1, no. 1, p. 13, 2018.
[43] Y. Il Park, H. Im, R. Weissleder, and H. Lee, “Nanostar Clustering Improves the Sensitivity of Plasmonic Assays,” Bioconjug Chem, vol. 26, no. 8, pp. 1470–1474, Aug. 2015, doi: 10.1021/acs.bioconjchem.5b00343.
[44] C. Wu and Q.-H. Xu, “Stable and Functionable Mesoporous Silica-Coated Gold Nanorods as Sensitive Localized Surface Plasmon Resonance (LSPR) Nanosensors,” Langmuir, vol. 25, no. 16, pp. 9441–9446, Aug. 2009, doi: 10.1021/la900646n.
[45] K. Grochowska et al., “Engineering Au nanoparticle arrays on SiO2 glass by pulsed UV laser irradiation,” Plasmonics, vol. 8, no. 1, pp. 105–113, 2013.
[46] T. Leelawattananon and S. Chittayasothorn, “Simulation Effects on the Optical Response of Gold Nanoparticles.,” in SIMULTECH, 2019, pp. 360–367.
[47] T. Bora et al., “Modeling nanomaterial physical properties: theory and simulation,” Int J Smart Nano Mater, 2019.
[48] A. G. Nikitin, T. Nguyen, and H. Dallaporta, “Narrow plasmon resonances in diffractive arrays of gold nanoparticles in asymmetric environment: Experimental studies,” Appl Phys Lett, vol. 102, no. 22, 2013.
[49] N. Thomas, P. Sreekeerthi, and P. Swaminathan, “Combined experimental and simulation study of self-assembly of colloidal gold nanoparticles on silanized glass,” Physical Chemistry Chemical Physics, vol. 24, no. 40, pp. 25025–25035, 2022.

4. Chapter 4
Fabrication and characterization of LSPR fiber optic probes

This chapter presents the experimental achievements related to the fabrication of LSPR fiber-optic devices obtained during the three years of the Ph.D. program. The first set of results concerns the development of fiber-optic transducers functionalized with spherical gold nanoparticles, primarily achieved during the first and part of the second year of the doctoral work. These results have also been published in [1]. Subsequently, the optimization of the sensing device is presented, highlighting the improvements achieved through the introduction of gold nanostars as plasmonic elements. These enhancements include increased sensitivity and improved spectral tunability of the optical response. The corresponding results were obtained during the final phase of the Ph.D. work and published in [2]. In this chapter, the main results are comparatively presented and discussed.

Finally, a case study involving the detection of the agricultural pesticide Thiram is reported to evaluate and compare the performance of the developed devices. In the following two chapters, the results obtained from the application of NP- and NS-coated fiber devices for the biosensing of OTA and cortisol, respectively, will be presented and discussed.

4.1. Sensors Design

The design of the sensor probe in this work was developed to achieve the following goals:

- Obtain a miniaturized device;
- Enable operation in a single-end configuration (sensor probe);

- Minimize optical power losses (intrinsic configuration);
- Enhance the interaction between the light guided in the fiber and the gold nanostructures to efficiently excite the LSPR.

To meet all these requirements, gold nanostructures, comprising both spherical NPs and NSs, were deposited onto the surface of an etched optical fiber. As shown in Figure 4-1, the interaction of light propagating through the fiber with these nanostructures excites LSPR, which creates a distinct attenuation band in the reflection spectrum. The central objective is to demonstrate that by controlling the morphology of the nanostructures, we can precisely tune the LSPR wavelength, thereby optimizing the transducer's sensitivity for specific sensing applications.

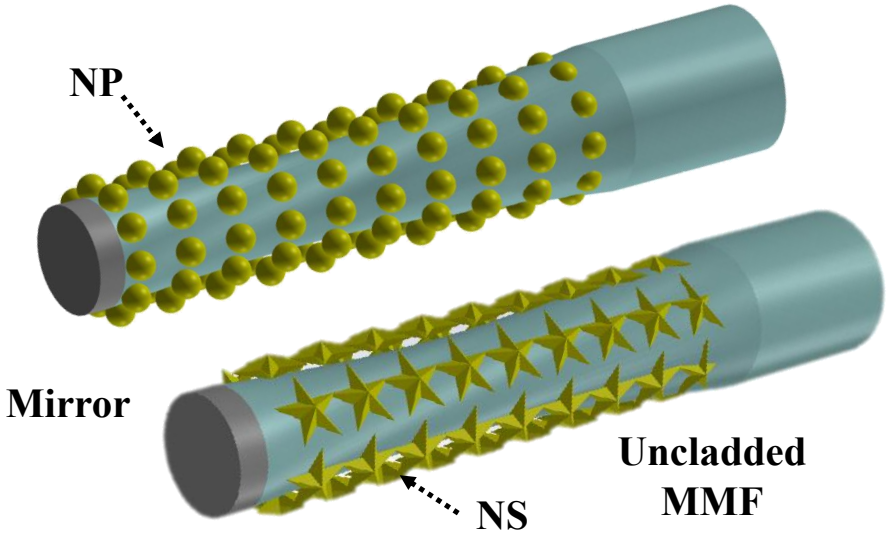

Figure 4-1. Schematic of transducer with NP and NS deposition.

4.2. Fiber Optic selection

The initial and critical step in fabricating the proposed transducer involves the judicious selection of an appropriate optical fiber. This choice necessitates careful consideration of several key requirements. Foremost among these is the guiding spectrum; as previously discussed, LSPR is excited in the visible range. Consequently, the chosen optical fiber must efficiently guide light within the 400 to 1000 nm range with minimal optical loss.

Another crucial aspect is core accessibility, specifically the need to maximize the excitation of evanescent waves. To achieve this, a portion of the fiber's cladding must be completely removed. This requirement presents a significant challenge when considering single-mode fibers (SMF). While SMFs, typically characterized by very small core diameters (e.g., around 5 µm) and standard cladding sizes (e.g., 125 µm), could potentially offer a high evanescent field ratio if unclad, their extreme fragility makes them exceedingly difficult to handle and integrate into a practical sensor.

Given that mode interference is not a critical factor in this project and the primary function of the fiber is efficient power delivery, there are no limitations precluding the use of multimode fibers (MMF). Multimode fibers offer superior robustness and ease of handling compared to their single-mode counterparts, making them highly suitable for power delivery applications. A wide array of MMF options are available, varying in cladding and core sizes. Among the various MMF silica fibers, those with differing core sizes, such as 50 µm and 105 µm, are commonly available.

Ultimately, the Thorlabs FG105LCA multimode fiber (105 µm core / 125 µm cladding) was selected. This choice was predicated on its ability to support the required guiding spectrum and its favorable structural properties for evanescent wave excitation. By removing a mere 10 µm layer of cladding (reducing the overall diameter from 125 µm to 105 µm), the core becomes readily accessible, facilitating the generation of strong evanescent waves, all while maintaining a more robust and manageable fiber structure compared to unclad single-mode alternatives. This specific fiber also aligns well with the "Silica Multimode (High OH)" category outlined in the comparative table, confirming its suitability for visible light applications.

4.3. Read out setup

The chosen readout configuration for this setup is a reflection-based scheme. This configuration offers significant practical advantages, primarily facilitating the vertical and strain-free positioning of the optical fiber, which is crucial for optimal sensor performance. Furthermore, for subsequent experimental stages, this setup allows for the direct use of simple laboratory counting, such as well plates (e.g., Falcon plates), rather than complicated flow channels and baths. This transition significantly streamlines the experimental workflow, minimizing potential contamination and physical damage to the sensor.

As depicted in Figure Figure 4-2. Schematic of the optoelectronic readout setup. The setup comprises a broadband light source (Avantes AvaLight-HAL-S-Mini), which provides incident light across the visible spectrum. This incident light is coupled into one input port of a 50:50 MMF coupler (105/125 µm core/cladding). The light exiting the coupler's opposite port is then directed towards the sensing area. Upon interaction with the sensor, the reflected light is guided back through the same fiber path to the coupler. Finally, the reflected signal emerges from the second output port on the first side of the coupler, reaching a spectrometer (Ocean Optics HR2000+). The spectral data acquired by the spectrometer is then transmitted to a personal computer for real-time display, storage, and subsequent analysis.

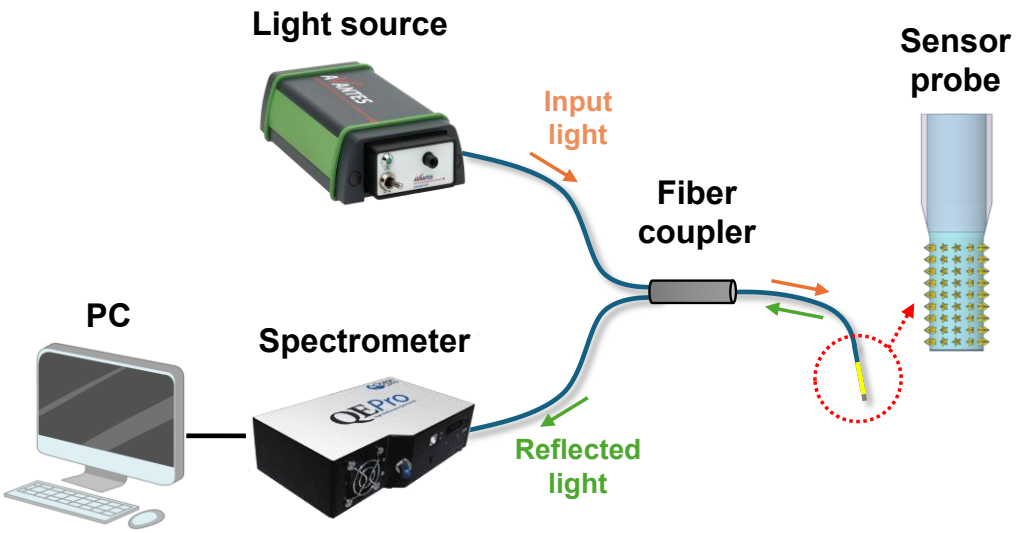

Figure 4-2. Schematic of the optoelectronic readout setup.

4.4. Nanostructure synthesis

In this investigation, two primary nanostructures were utilized: NPs and NSs. The synthesis procedures for each of these will be explained in the following sections and were carried out in cooperation with the IPCB-CNR institute which developed the protocols.

4.4.1. NPs synthesis

This protocol outlines the comprehensive, step-by-step procedure for the synthesis of NPs using the classical citrate reduction method, commonly known as the Turkevich method [3]. This widely adopted chemical synthesis approach relies on the reduction of a gold salt precursor, specifically sodium tetrachloroaurate ($NaAuCl_4$), by a mild reducing agent, sodium citrate, under controlled heating conditions. The precision of each step is critical for obtaining uniformly sized and stable nanoparticles.

To commence the synthesis, meticulous preparation of the stock solutions is essential. First, a highly concentrated stock solution of sodium citrate ($Na_3C_6H_5O_7$) is prepared at a precise concentration of 10 mg/mL. Simultaneously, a stock solution of sodium tetrachloroaurate (III) dihydrate ($NaAuCl_4$) is prepared at a concentration of 0.125 mol/L. It is imperative that all reagents utilized in this protocol are of analytical purity to prevent impurities from affecting the reaction outcome. Furthermore, the deionized water employed for all solution preparations must be highly purified, ideally demonstrating a resistivity of 18.2 MΩ cm at 25 °C, typically achieved through a Millipore Milli-Q system.

Once the stock solutions are ready, the initial reaction mixture is prepared. A precise volume of 420 µL of the prepared $NaAuCl_4$ stock solution is carefully dispensed into 94.6 mL of the deionized water within a suitable reaction vessel, typically a round-bottom flask equipped with a stirring mechanism. This diluted gold precursor solution is then subjected to constant agitation while being heated. The temperature is gradually increased until it reaches a precise 90 °C. Maintaining constant agitation

throughout the heating phase ensures uniform temperature distribution and prevents localized overheating, which could lead to inconsistent nucleation.

Upon achieving the target temperature of 90 ˚C, the reducing agent is introduced. A rapid addition of 5 mL of the sodium citrate stock solution into the vigorously stirring hot gold precursor solution is performed. The swift addition is crucial as it promotes a burst nucleation event, leading to the formation of a more uniform population of gold nanoparticles. Following the addition of sodium citrate, the reaction mixture continues to be agitated and heated consistently at 90 ˚C for an additional 20 minutes. This duration allows for the complete reduction of the gold ions and the subsequent growth of the gold nanoparticles.

During this critical reaction phase, a distinctive and observable color change occurs in the suspension, serving as a visual indicator of successful golden NPs formation. The solution will progressively transition from an initial light yellow hue, characteristic of the gold salt, to a transient greyish color, and finally stabilize into a characteristic vibrant red. The final red color is indicative of the formation of stable, dispersed spherical gold nanoparticles, whose LSPR typically absorbs strongly in the visible red region of the electromagnetic spectrum. After the 20-minute reaction period, the hot NPs suspension is allowed to cool slowly to room temperature under continued mild agitation to prevent aggregation. For long-term preservation and stability, the synthesized gold nanoparticle suspension is then stored under refrigerated conditions, specifically maintained at 4 ˚C. The entire synthetic process, from reagent mixing to final cooling, is also schematically illustrated in Figure 4-3 of the original research article, providing a visual guide to the experimental steps [1], [4].

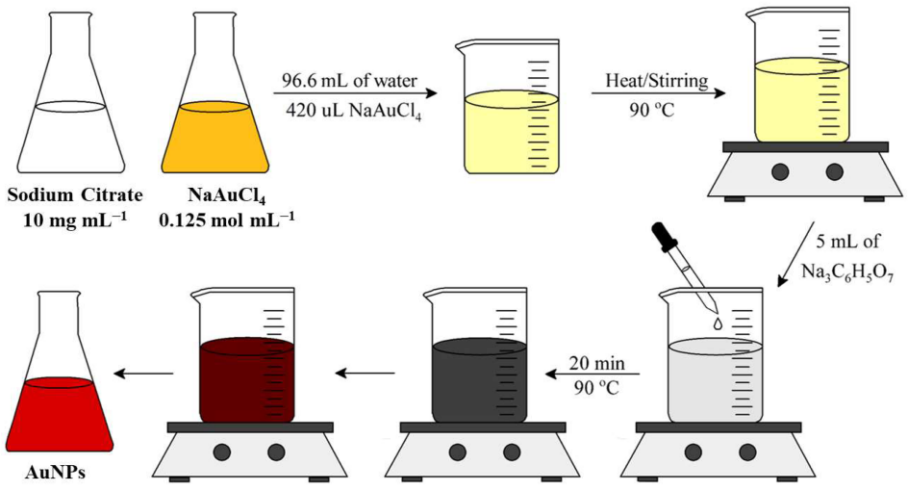

Figure 4-3. Schematic diagram showing the steps for NPs synthesis. Adapted from [4].

4.4.2. NSs synthesis

The synthesis of NSs is initiated by preparing a seed solution. This is accomplished by adding 15 mL of a 1% citrate solution to 100 mL of a boiling 1 mM $HAuCl_4$ solution under vigorous stirring. The mixture is then allowed to boil for 15 minutes, ensuring the solution volume remains stable throughout

this period. Following the boiling phase, the solution is cooled and subsequently filtered using a 0.22 µm nitrocellulose membrane. The filtered seed solution is then stored at 4 ˚C for long-term preservation. The as-prepared citrate-stabilized seed solution typically exhibits a diameter of 12 ± 0.7 nm and an absorbance (A520) of 2.81.

For the actual NSs synthesis, 100 µL of the aforementioned citrate-stabilized seed solution is added to 10 mL of a 0.25 mM auric chloride ($HAuCl_4$) solution in a 20 mL glass vial at room temperature. This mixture is maintained under moderate stirring at approximately 700 rpm. Crucially, 10 µL of 1 M HCl is also added to the HAuCl4 solution to lower the pH, a factor known to promote more red-shifted plasmons in the resulting NSs. Immediately following the addition of the seed solution, 100 µL of silver nitrate ($AgNO_3$) and 50 µL of ascorbic acid (AA; 100 mM) are added simultaneously. The silver nitrate concentration is a critical parameter for tuning the NSs geometry and LSPR band. For this investigation, specific $AgNO_3$ concentrations of 0.8 mM (NS-1), 1.5 mM (NS-2), 2.0 mM (NS-3), and 3.0 mM (NS-4) were used to synthesize NSs with varying plasmonic properties. Rapid addition of the ascorbic acid is essential, as drop-wise addition can lead to the formation of NPs instead of NSs. The solution is then stirred for a brief 30 seconds, during which its color rapidly transitions from light red to blue or greenish-black, indicating the initiation of NSs formation.

To halt further nucleation and control the growth, one centrifugal wash is performed immediately after the 30-second stirring period. This wash is conducted at 3000-5000 relative centrifugal force for 15 minutes in a 15 mL tube. After centrifugation, the NSs solution is redispersed in deionized water, filtered using a 0.22 µm nitrocellulose membrane, and subsequently stored at 4 ˚C for long-term stability. Careful control of parameters such as pH, stirring speed, and concentration ratios of $AgNO_3$, ascorbic acid, $HAuCl_4$, and seed solution allows for the synthesis of NSs with tunable geometries and plasmon bands, ranging from approximately 600 nm to 1000 nm [2], [5].

4.4.3. Nanostructures characterization

The precise characterization of synthesized NSs and NPs in the liquid phase is paramount to confirming their structural integrity, size, morphology, and optical properties. In this investigation, two primary techniques were employed for liquid-phase characterization: Transmission Electron Microscopy (TEM) and Ultraviolet-Visible (UV-Vis) Spectroscopy. These methods provide complementary insights into the physical and optical characteristics of the synthesized nanostructures.

TEM was utilized to meticulously examine the morphology and size distribution of the NPs and NS. The TEM images were acquired using a TEM FEI Tecnai G12 Spirit Twin, equipped with a LaB6 emission source operating at 120 kV, and a CCD camera Fei Eagle 4 K (Japan). For the NPs, as illustrated in Figure 4-4 and Figure 4-5(A), an average diameter of 43 ± 8 nm was determined from Dynamic Light Scattering (DLS) analysis, indicating a relatively monodisperse population.

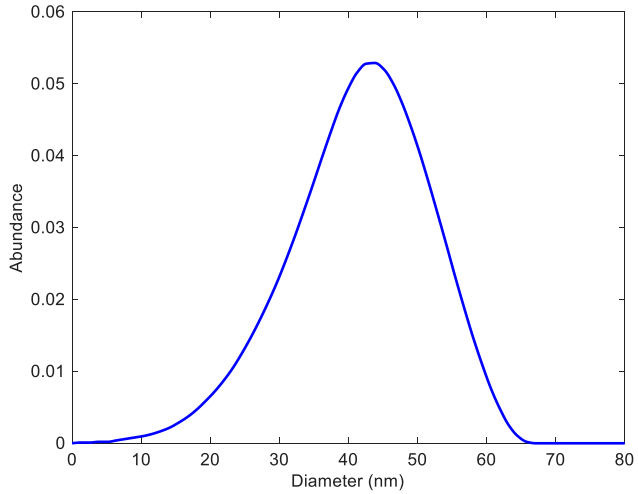

Figure 4-4. Size distribution of AuNPs, in inset a representative TEM image of AuNPs.

In the case of the NSs, despite their inherently irregular overall shape, the characteristic morphology featuring multiple sharp branches extending radially from a central core was clearly observable. The overall diameter of the synthesized NSs ranged from 30 nm to 55 nm. Furthermore, the number of branches exhibited variability, ranging from 10 to 15 for NS-1 and NS-4, as depicted in Figure 4-5(B) and 4-5(C), respectively. A distinct morphological difference was also noted: the branches of NS-1 appeared less sharp compared to those of NS-4, suggesting the influence of synthesis parameters on tip sharpness.

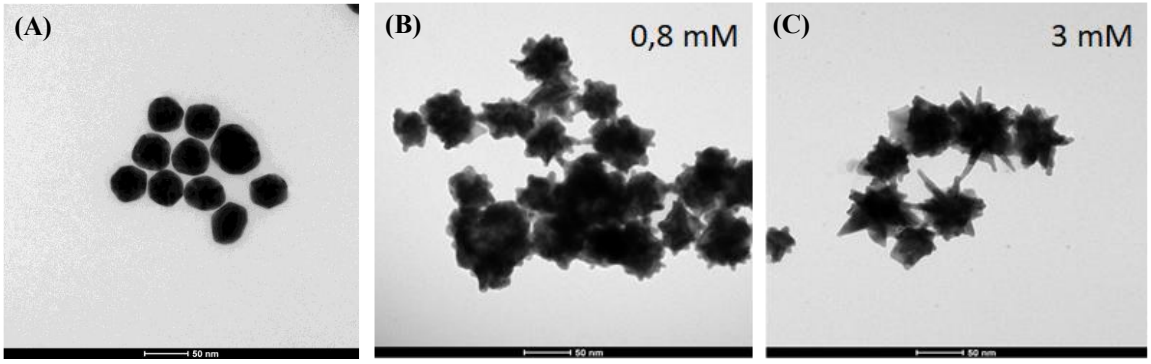

Figure 4-5. TEM images of: (A) NP, (B) NSs sample NS-1 and (C) sample NS-4.

UV-Visible Spectroscopy was employed to characterize the optical properties of the nanostructures, primarily focusing on their LSPR peaks. The UV-Vis spectra were recorded using an Agilent Cary 60 UV/Vis spectrophotometer with standard quartz cuvettes. Figure 4-4 presents the UV-Vis spectra of four types of NSs samples—namely NS-1, NS-2, NS-3, and NS-4 all measured in aqueous solution. For comparative analysis, the UV-Vis spectrum of the NP was also included. The results clearly demonstrate that the UV-Vis spectra of NSs are highly dependent on the concentration of silver nitrate used during their synthesis. Specifically, as the silver nitrate concentration increases from 0.8 mM to 3 mM, a pronounced red shift of the absorbance peak is observed within the 500–850 nm range, as further illustrated in Figure 4-6 and according to literature [5], [6]. Quantitatively, the resonance wavelengths

for NS-1, NS-2, NS-3, and NS-4 were determined to be 545 nm, 570 nm, 685 nm, and 820 nm, respectively. In contrast, the NP exhibited a characteristic LSPR peak at 531 nm.

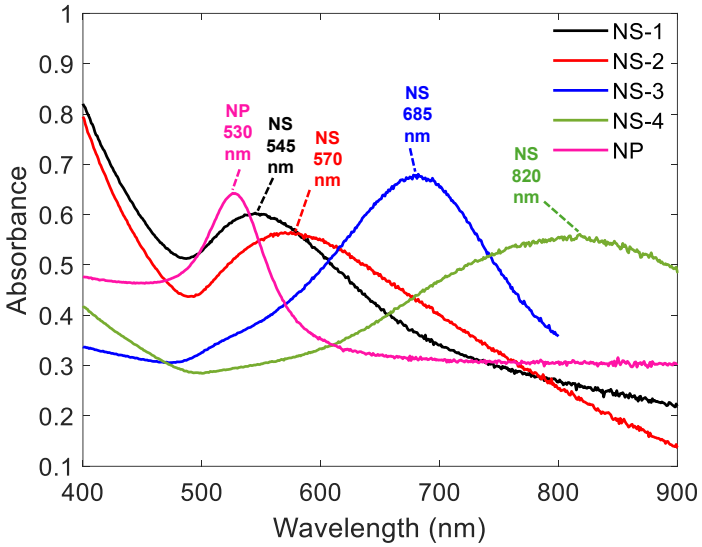

Figure 4-6. Absorbance spectra of different investigated NPs and NSs in water solution. Labels indicate the resonance wavelengths.

4.5. Immobilization Steps for Gold Nanoparticles on Functionalized Silica Surfaces

Gold nanostructure immobilization on solid surfaces is a critical step for many applications in biosensing, surface-enhanced spectroscopy, and nanostructured materials. A variety of immobilization strategies have been developed to control nanoparticle density, distribution, and adhesion. These strategies rely on modifying the glass surface with specific chemical groups that interact with the nanostructure either through electrostatic attraction or covalent bonding [7], [8]. In this section, two immobilization strategies are described and results are compared in detail: the use of (3-aminopropyl) triethoxysilane (APTES) and (3-mercaptopropyl) trimethoxysilane (MPTES).

4.5.1. Surface chemistry

The first method involves functionalizing the MMF surface with APTES in acetone (5 % w/w). This compound contains three hydrolyzable ethoxy groups that covalently anchor to surface silanols, forming a robust siloxane network. The terminal $–NH_2$ group of the APTES remains available for interaction with NPs, primarily via electrostatic attraction with citrate-capped NPs. The process begins by cleaning the silica fiber using a sequence of piranha solution treatment for 1 hour, and solvent rinsing. The cleaned substrate is then immersed in a 10 mM solution of APTES in anhydrous toluene 2 hours. After silanization, the surface is rinsed, sonicated briefly in toluene to remove weakly attached silanes, dried overnight to complete cross-linking. This method results in a dense amine-terminated layer suitable for nanoparticle immobilization.

In the second method, the terminal chemistry is altered to thiol groups using (MPTES). Similar to APTES, MPTES is grafted onto the cleaned silica surface under identical conditions, immersion in toluene 5 hours followed by post-processing. However, in this case, the terminal –SH group provides a strong affinity to gold surfaces through covalent-like Au–S bonding. While this method is theoretically robust, experimental results showed that MPTES functionalization leads to lower nanoparticle coverage.

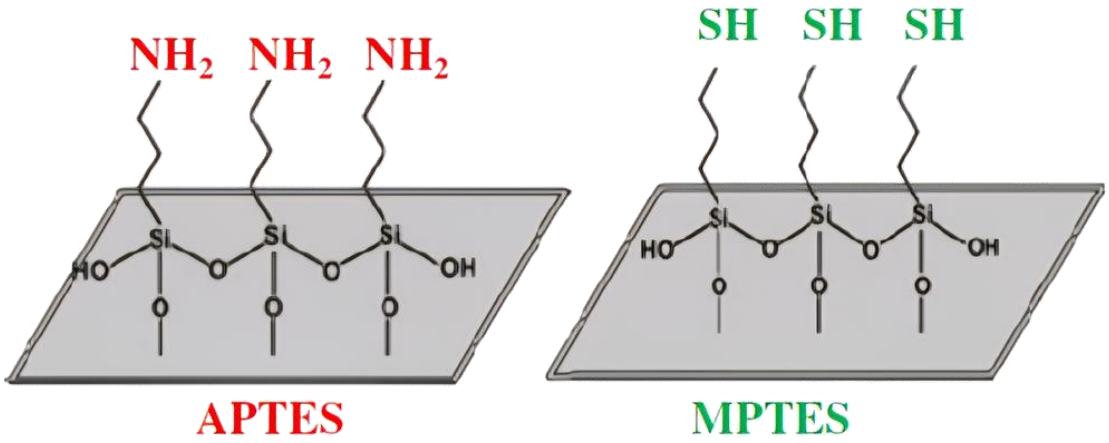

Figure 4-7. Schematic description of the two functionalized surfaces. Adapted from [7].

4.5.2. Gold Nanoparticles Deposition and Characterization

Once the silica fiber surfaces were functionalized, NPs were deposited by immersing the substrates in a freshly prepared citrate-stabilized gold colloid. This colloid, synthesized by the Turkevich-Frens method which was explained previously, yielded ~43 nm diameter nanoparticles with a strong LSPR at 530 nm. Deposition was carried out either under gentle agitation or in a sonication bath for five hours to improve particle dispersion and limit aggregation. Post-deposition, the samples were rinsed and dried overnight.

Surface characterization through SEM images in Figure 4-10 reveal the morphological distribution of NPs on the two surfaces. All surfaces showed particle clustering, but the APTES surface exhibited higher coverage (Figures. 4-10(A) and (B)), the NPs dispersion improved significantly for APTES surfaces, with the latter showing the best distribution with a predominance of isolated particles. MPTES surfaces showed lower NP deposition respect to APTES (Figures. 4-10(C) and (D)) reinforcing the hypothesis of poor silane coverage.

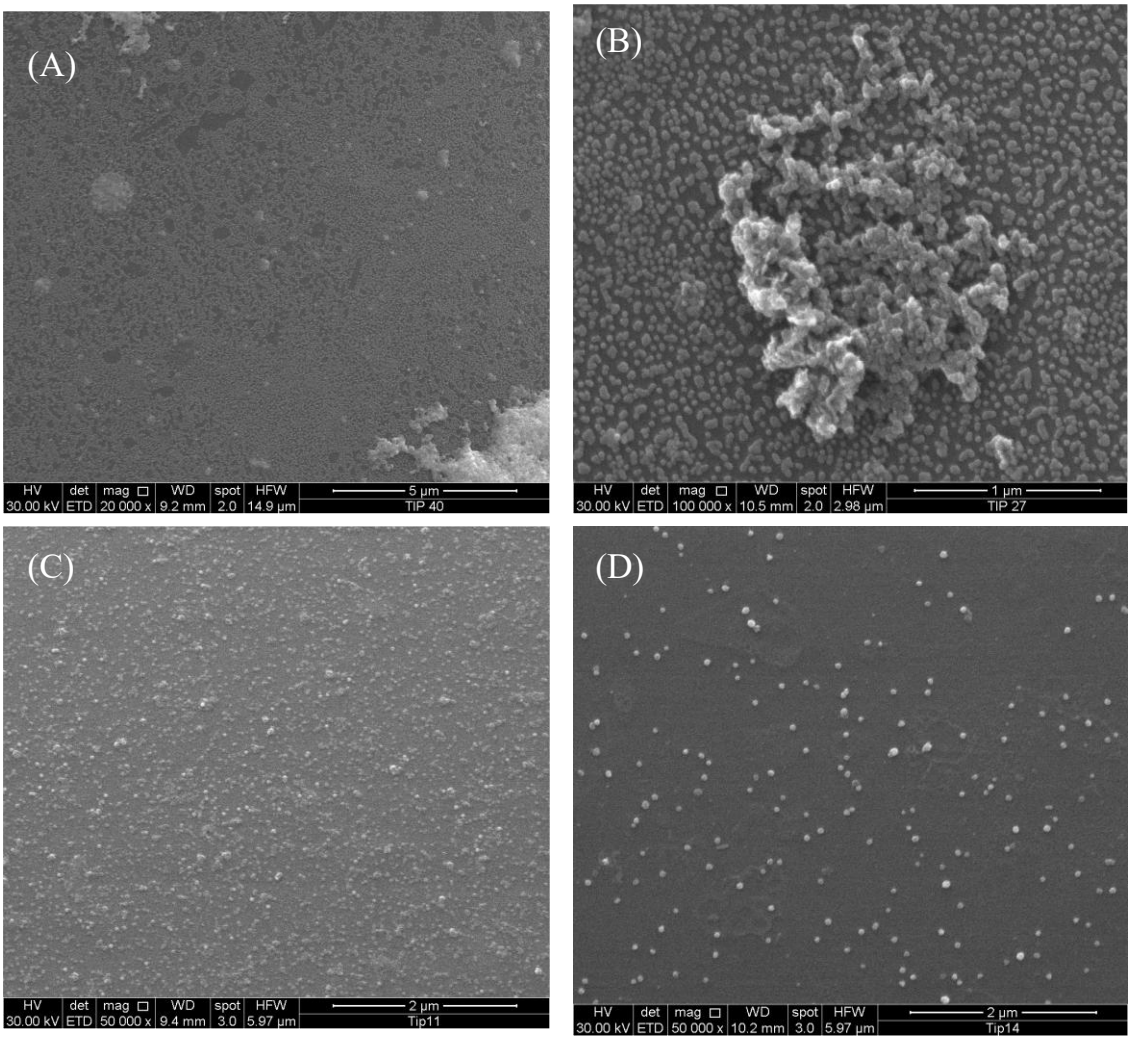

Figure 4-8. SEM images of fiber surface after NPs deposition with (A) and (B) APTES functionalization and (C) and (D) after MPTES functionalization surfaces.

Through investigation and comparative analysis, the APTES method emerged as the superior strategy for immobilizing golden nanostructures on fiber surfaces. Its optimal balance of surface coverage, particle dispersion, and stability makes it highly effective. Therefore, for our study, we selected the APTES functionalization route to immobilize gold structures, ensuring a reliable and reproducible platform for future biosensing applications.

4.6. Transducer fabrication

The development of LSPR-based optical fiber sensors begins with the fabrication of etched and chemically functionalized fiber probes. A segment of multimode silica optical fiber (core/cladding: 105/125 µm) is first prepared by stripping off its protective polymer jacket. The fiber is then chemically etched to expose the core and reduce its diameter, enhancing the evanescent field interaction with the external environment. The etching process is performed using hydrofluoric acid (HF, 24% concentration), into which the fiber is immersed for 25 minutes. This etching step reduces the fiber

diameter to approximately 95 µm, exposing the evanescent field while maintaining sufficient mechanical integrity. In Figure 4-9 the comparison of MMF before and after etching is showing.

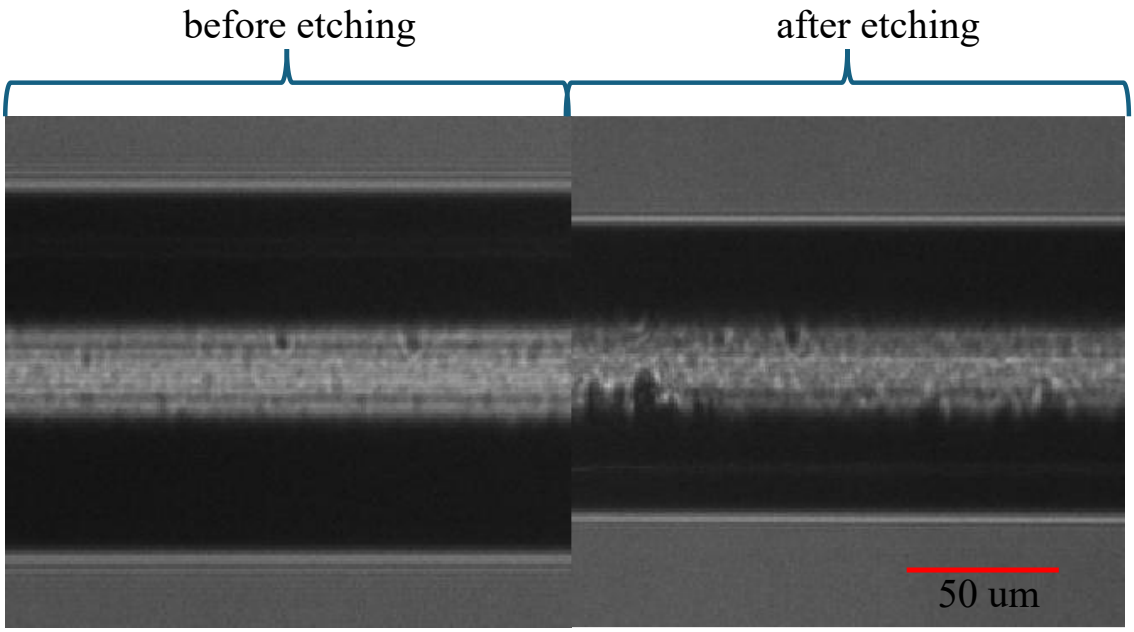

Figure 4-9. Effect of etching on MMF

Following etching, the silica surface must be chemically activated to support the stable attachment of metallic nanostructures. For this step, we adapted the method described in Section 4.5 to meet the specific requirements of the current project. This is achieved through a two-step silanization protocol. First, the etched fiber is cleaned and hydroxylated by immersion in freshly prepared piranha solution (a 7:3 mixture of sulfuric acid and hydrogen peroxide) for 1 hour. This step removes organic contaminants and introduces hydroxyl groups (–OH) on the silica surface, which are necessary for subsequent silane coupling. After extensive rinsing with deionized water, the fiber is immersed in a 5% (w/w) solution of APTES in acetone for 2 hours at room temperature. This silanization step grafts amine-terminated silane molecules onto the hydroxylated silica, rendering the surface positively charged. The fiber is then rinsed with acetone and dried in air overnight, yielding a functionalized surface suitable for nanostructure deposition.

To enable reflectometric sensing, the tip of the fiber is cleaved and subsequently coated with a thin silver mirror layer. This reflective coating is essential for collecting the backward-propagating light that interacts with the LSPR-active region along the fiber surface. For the silver mirror coating on the fiber tip, a chemical reduction method was employed using a Tollens' reagent-based approach. The process involved the in-situ formation of silver from silver nitrate through reduction by dextrose in alkaline conditions, allowing a reflective silver layer to deposit on the fiber tip surface. To prepare the mirror solution, silver nitrate ($AgNO_3$) was first prepared at a concentration of 0.1 M by dissolving 0.085 g of $AgNO_3$ in 5 mL of distilled water (D.W.). Separately, potassium hydroxide (KOH) was prepared at 0.8 M by dissolving 0.45 g in 10 mL of D.W. For each coating reaction, two portions of 320 µL of the silver

nitrate solution were measured using a micropipette or Gilson, followed by the addition of two 220 µL portions of the KOH solution, with immediate shaking to form a brown precipitate of silver oxide. Subsequently, one drop of 30% ammonia solution was added to dissolve the precipitate, turning the solution clear and indicating the formation of the soluble diamminesilver(I) complex. After this, two 16 µL portions of 0.5 M dextrose (prepared by dissolving 0.9 g in 10 mL D.W.) were added as the reducing agent, followed by further shaking. The reduction of silver ions by dextrose under these alkaline conditions facilitated the deposition of a uniform metallic silver layer on the fiber tip, forming a mirror-like surface suitable for optical applications.

After the fiber is functionalized and mirrored, it's immersed in colloidal solutions containing metallic nanostructures, either NPs or NSs. This immersion lasts for approximately five hours for NPs and overnight for NSs. NSs solutions require a longer deposition time due to their lower concentration compared to NPs, allowing for greater surface coverage on the fiber and a LSPR deep. Figure 4-10(A) illustrates the reflection spectrum of the transducer at each key fabrication step. Initially, the spectrum of a bare, non-etched, cleaved fiber was set as the reference. After etching, the fiber was spliced to a reference fiber. The spectrum was then updated as a new reference after mirroring and functionalization with APTES to isolate the spectral changes caused only by the subsequent gold deposition. Figure 4-10(B) and (C) shows the evolution of the transducer's reflection spectrum over time during the NPs and NSs deposition process. Initially, the changes in the spectrum are very rapid. However, after approximately five hours, the spectrum stabilizes, indicating that the fiber is fully covered with a layer of nanoparticles. At this point, the fiber can be removed from the solution.

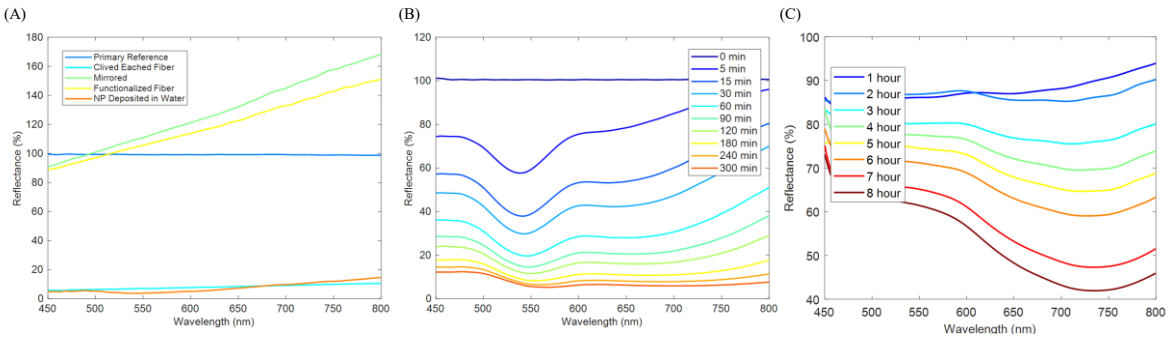

Figure 4-10. (A) Transducer fabrication steps. (B) Reflection spectrum evolution during NPs deposition. (C) Reflection spectrum evolution during NSs deposition.

These nanostructures were synthesized separately using either the Turkevich method (for NPs) or a seed-mediated growth approach (for NSs) which were explained before. Electrostatic interaction between the negatively charged citrate-stabilized nanoparticles and the positively charged APTES-functionalized surface facilitates stable adsorption. Following deposition, the fibers are rinsed five times with water to remove loosely bound particles and dried overnight. In Figure 4-1 schematic of transducer after NSs deposition is shown.

The optical performance of the fabricated sensors was evaluated by measuring reflectance spectrum. Figure 4-11(A) and (B) displays the normalized reflectance spectra of various sensor samples, both in

air and water. The spectra exhibit clear attenuation bands characteristic of LSPR excitation. In water, the NP-coated probe displays a resonance at approximately 562 nm, while NS-coated samples S1, S2, and S3 exhibit red-shifted bands at 549 nm, 580 nm, and 810 nm, respectively. These shifts confirm that by modulating nanostar morphology through synthesis, specifically, by varying the silver nitrate concentration and controlling the aspect ratio of the nanostar branches, LSPR wavelength and sensitivity can be tuned. Sample S4 exhibits an LSPR band outside the detection range, which is likely due to excessive redshift and indicates the need for optimizing branch sharpness. As illustrated in Figure 4-11(B), the attenuation bands observed for transducers featuring various nanostructures in an aqueous environment exhibit a noticeable red shift. This shift is relative to the UV-Vis spectrum attenuation bands of the same nanostructures when analyzed in solution (Figure 4-6). This observed red shift suggests an increase in the effective refractive index of the medium surrounding the nanostructures once they are deposited onto the glass substrate, as compared to their state in solution[9], [10], [11]. Furthermore, the attenuation band of S-1 was too spectrally close to that of the NP sample, leading to its exclusion from further analysis. Therefore, for the ongoing analysis, our focus will be solely on samples NP, S-2, and S-3.

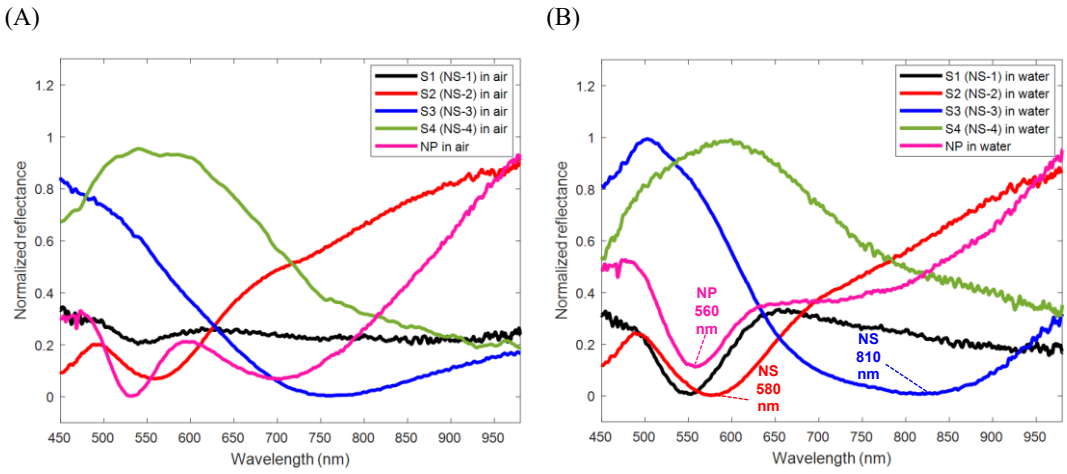

Figure 4-11. Normalized reflection spectra of the transducers with different NS and NP deposition when the surrounding medium is (A) air and (B) water.

Figure 4-12 presents high-magnification SEM images of the nanostructure-coated fiber surfaces were performed to verify the effectiveness of the fabrication procedures using Quanta 200 FEG (FEI, USA). The NP-decorated fiber (Fig. 4-12(A)) shows a uniform monolayer of spherical nanoparticles with minimal aggregation, reflecting high deposition quality. In contrast, the NS-coated sample S3 (Figs. 4-12(B) and (C)) reveals the presence of both isolated NSs and clusters, indicating slightly lower deposition uniformity. Nonetheless, the morphological distribution remains suitable for effective plasmonic coupling and sensing applications.

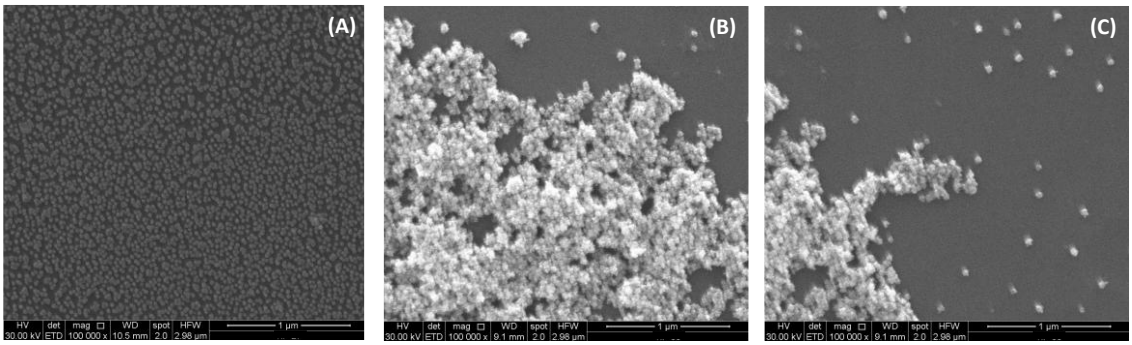

Figure 4-12. SEM images of optical fiber samples at 100,000x magnification: (A) NP-based sample; (B)-(C) S3.

4.7. SRI Characterization

The SRI sensitivity is a critical parameter in evaluating the performance of plasmonic optical fiber sensors, as it directly reflects the sensor's ability to detect small variations in the surrounding medium. To investigate the SRI response of the fabricated probes, sensors functionalized with different types of NPs and NSs, were tested using aqueous glycerol solutions with varying refractive indices. The solutions were prepared to cover a range from 1.330 to 1.400, simulating biologically and chemically relevant environments. The refractive index of each solution was measured using an Abbe refractometer, with the resolution of 2×10^{-4}.

The sensors were interrogated using a broadband light source and a reflectance measurement setup which explain in section 4.3. As the refractive index of the surrounding medium increased, a redshift in LSPR band was observed. This shift occurs due to the increase in the effective dielectric constant near the metal nanostructures surface, which modifies the resonance condition of the collective electron oscillation.

Figure 4-13 illustrates the resonance wavelength evolution as a function of the surrounding refractive index for three representative sensor types: one functionalized with NPs, and two others with NSs derived from sample conditions S2 and S3.

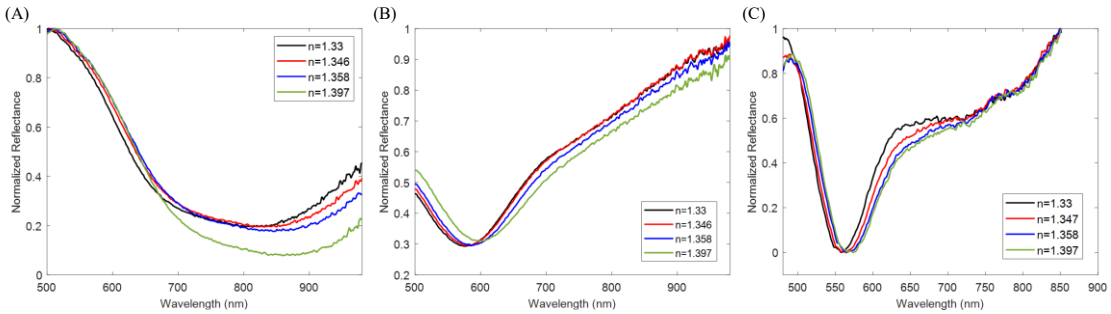

Figure 4-13. Reflection spectrum in different SRI within n = 1.33–1.40 for transducer: (A) S3, (B) S2, and (C) NP.

Figure 4-14 illustrates the wavelength shift as a function of the SRI for each sample. For calculating the resonance wavelength, first it is needed to find the wavelength corresponding to the minimum value

in the spectrum. This is done by selecting the region of interest around the minimum and fitting a polynomial curve of degree 2, 3, or more, choosing the degree that provides the best fit. At this stage, the wavelength resolution of the fitted curve is the same as the original data. To improve the wavelength resolution and more accurately find the minimum, an interpolation function can be used on the fitted curve. For this purpose, it will insert a desired number of points (e.g., 100 points) between each pair of original data points on the fitted curve. The values for these new points are predicted using the polynomial's equation. This method improves the wavelength resolution by a factor of hundred, allowing for a more precise determination of the minimum point, which is the resonance wavelength. This method applied on all spectrums to find resonance wavelengths and then for each transducer resonance wavelength shift respect to resonance wavelength in water were calculated.

A linear fit was applied to the data, and the SRI sensitivity was determined from the slope of the fitting line for each sample. The NP-based sensor displayed a relatively modest response, with a total shift of 9 nm across the entire SRI range and a sensitivity of approximately 128 nm/RIU. In contrast, the NS-based probes exhibited significantly enhanced sensitivity. The sensor functionalized with S2-type NSs showed a resonance shift of 31 nm, corresponding to a sensitivity of 437 nm/RIU. Most notably, the S3-type NSs-coated fiber demonstrated a resonance shift of nearly 39 nm over the same SRI range, resulting in a calculated sensitivity of 561 nm/RIU.

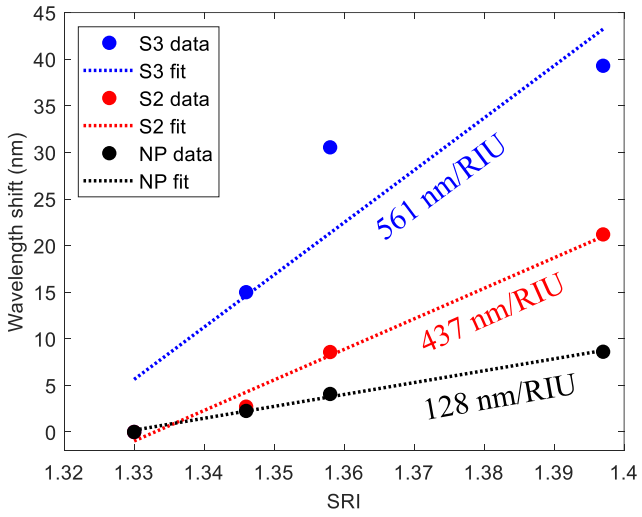

Figure 4-14. Wavelength shift as a function of the SRI for S3, S2, and NP.

These differences in performance are directly linked to the morphological features of the nanoparticles. The NSs used in samples S2 and S3 possess sharp, elongated branches, which intensify the local electromagnetic field at their tips. This field enhancement increases the interaction of the LSPR with changes in the surrounding medium, thereby amplifying the sensor's spectral response to refractive index variations. Moreover, the greater tunability of nanostar geometry allows the resonance band to be positioned at longer wavelengths, where the sensitivity to dielectric changes is inherently higher.

The experimentally obtained sensitivity values align well with theoretical expectations and numerical simulations reported earlier in the study in chapter 3. This confirms that optimizing nanostructure morphology, specifically by increasing the BAR, is an effective strategy to maximize SRI sensitivity. Additionally, the reproducibility and stability of the resonance shifts across repeated measurements indicate a robust nanoparticle immobilization process and a stable sensor platform.

In conclusion, the SRI characterization demonstrates the superior performance of nanostar-functionalized optical fiber sensors over their spherical nanoparticle counterparts. Among the tested configurations, the S3 NS-based sensor offers the highest sensitivity and therefore represents the most suitable candidate for applications requiring precise detection of minute refractive index changes, such as in biosensing or environmental monitoring.

4.8. Stability and temperature cross-sensitivity

The long-term stability of the sensor's response was assessed by immersing the S3-based fiber in water and continuously monitoring the LSPR wavelength shift over a 48-hour period. The results, shown in Figure 4-15(A), demonstrate excellent stability: the wavelength fluctuations remained within ±1.5 nm throughout the test. This confirms that the sensor maintains consistent performance over extended durations, making it suitable for applications requiring prolonged monitoring. A temperature trace recorded simultaneously using an FBG reference is shown in Figure 4-16(B). The comparison indicates that minor signal drifts observed in the sensor may be largely attributed to ambient temperature fluctuations rather than degradation of the sensing layer itself.

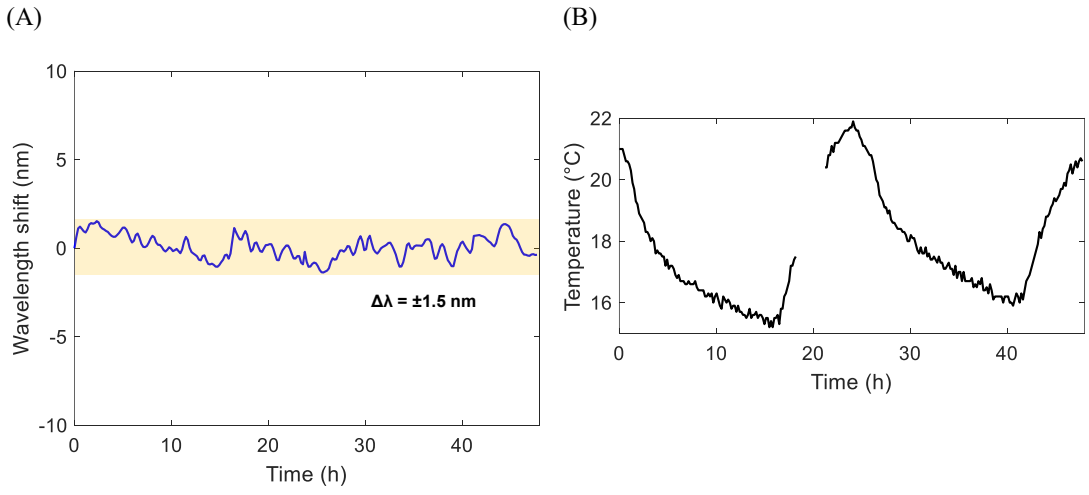

Figure 4-15. Stability of the response as a function of the time over 48 h when the sensor is placed in water environment at controlled thermal conditions: (A) wavelength shift of the sensor; (B) temperature trend during the experiment.

To explicitly assess the temperature cross-sensitivity, the sensor was placed in a controlled thermal environment using a tubular oven, with an integrated FBG used as a temperature reference. The temperature was incrementally increased from 20 °C to 50 °C, and the corresponding LSPR resonance

wavelength shifts were recorded. These results are plotted in Figure 4-16, which displays the average wavelength shifts, calculated from five repeated measurements, relative to the baseline at 20 ˚C. The sensor's spectral response to temperature followed a linear trend, with a slope of approximately 0.13 nm/˚C, indicated by the dashed line in the figure 4-16. This low temperature sensitivity is either comparable to or better than values reported in the literature, confirming that the sensor exhibits minimal cross-sensitivity to thermal effects. Such thermal stability is a significant advantage for accurate sensing in environments where temperature fluctuations are unavoidable.

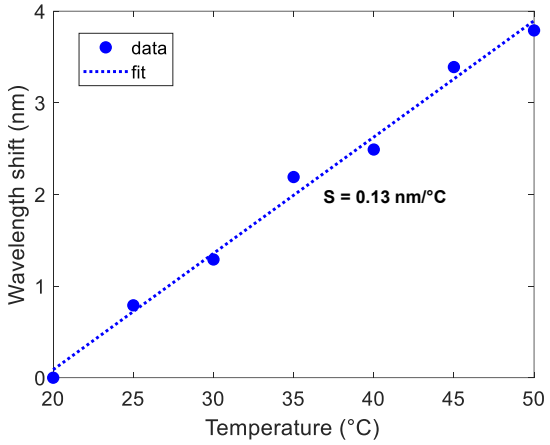

Figure 4-16. Wavelength shift as a function of the temperature for NS-based sensor.

In summary, the nanostar-based optical fiber sensor demonstrates strong signal stability over multiple days, and a low degree of temperature-induced interference. These characteristics collectively validate the sensor's robustness and suitability for practical chemical and biosensing applications.

4.9. Chemical-sensitivity: Thiram test

In this section, a target is selected as a case study to evaluate the transducer under simplified conditions. This allows for the estimation of bio-sensitivity overall selectivity of the transducer. The results provide a foundational understanding that will guide future sensor development for more complex and specific targets.

To assess the biosensing capabilities of the developed plasmonic optical fiber sensor, the fungicidal compound thiram was chosen as a model analyte. Thiram is ideal for this proof-of-concept study due to its inherent chemical affinity for gold surfaces. Its sulfur-containing functional groups strongly bind to gold nanostructures through robust Au–S interactions [12], [13]. This direct binding eliminates the need for a biological recognition element (e.g., an antibody or aptamer), simplifying the sensing mechanism and determination of thiram using golden nanostructures LSPR effect. Consequently, thiram serves as a clean model system for evaluating the sensor's bio-responsiveness. This foundational approach is crucial for future development, enabling the later incorporation of molecular recognition layers for specific biological targets. By evaluating the sensor's response to thiram, we can determine

its sensitivity limits in the absence of biological amplification, thereby guiding the selection and design of future bispecific interfaces.

Tetramethyl thiuram disulfide (Thiram) is a widely used agricultural fungicide and was also selected since it poses significant health risks, including skin and mucosal irritation and organ damage, due to its overuse. Therefore, accurate detection of thiram residues in the environment is critical. Traditional detection methods, such as ion mobility spectrometry and high-pressure liquid chromatography, are often expensive and require complex equipment [13], [14]. While colorimetric detection methods utilizing noble metal nanoparticles have emerged [15], [16], many struggle with achieving satisfactory LODs or involve overly complex preparation procedures. These methods leverage the distinctive LSPR effect of chemically modified gold, silver, and copper nanoparticles to determine thiram concentration. For instance, Ke Lui et al. [17] achieved a remarkable LOD of 0.04 μM for thiram using the LSPR effect of aggregated gold nanoparticles in a UV–VIS spectrometer. Similarly, Jigneshkumar V. Rohit et al. [18] reported a LOD of 2.81 μM with silver nanoparticles using the same technique [19], [20]. Furthermore, SERS has been employed for thiram detection, with Lili Kong et al. [21] demonstrating a detection limit of 2 ppm. Another study by Grégory Barbillon et al. [22] utilized assembled Au/ZnO nano-urchins as SERS substrates, achieving an impressive LOD of 10 pM. Despite these advancements in achieving low LODs, most of these methods are limited to laboratory settings due to their reliance on cumbersome and expensive equipment.

The sensing mechanism relies on the LSPR shift induced by the binding of thiram molecules to the surface of NPs or gold NSs immobilized on the etched fiber. As thiram molecules attach to the metallic nanostructures, they alter the local dielectric environment surrounding the plasmonic surface, leading to a measurable redshift in the resonance wavelength. This shift is monitored using the same reflectometric setup described in previous sections.

A solution of Thiram in deionized water has been prepared as a stock solution of 10^{-5} M and different concentrations have been prepared by serial dilution techniques (within 10 pM- 100 μM range).

The experiment was designed to evaluate the fiber sensor's response to increasing concentrations of thiram in water. The sensors used in this study were fabricated as previously described, with surfaces functionalized by either NPs or NSs synthesized under two different conditions (samples S2 and S3).

Each transducer was immersed in thiram solution starting from the lowest concentration and allowed to stabilize for approximately 30 minutes to ensure spectral stability and proper incubation of thiram molecules with the nanostructures. After stabilization, the sensor was sequentially exposed to higher concentrations. Purified deionized water was used both as the solvent for thiram and as the zero-concentration baseline.

Reflectance spectra were recorded automatically every 30 seconds throughout the experiment. Additionally, the RI of all thiram solutions was verified using an Abbe refractometer. No measurable RI change was detected, as the difference was below the refractometer's resolution (2×10^{-4}).

The LSPR attenuation band wavelength shift over time (sensorgram) for the investigated samples are plotted in Fig. 4-17. A concentration-dependent LSPR redshift was observed, indicating binding events between thiram molecules and gold nanostructures. This response provides valuable kinetic and concentration-dependent information.

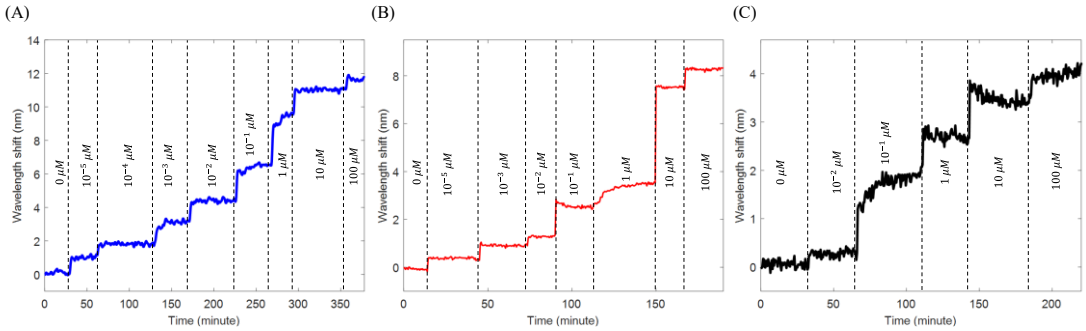

Figure 4-17. Real-time response as a function of Thiram concentration for (A) S3, (B) S2, and (C) NP. The vertical red lines indicate the time the solutions were changed.

Notably, the magnitude of the wavelength shift varied significantly between samples: nanostructures with LSPR tuned at higher initial wavelengths exhibited larger thiram-induced shifts. At first glance, sample S3 (with ~12 nm redshift) appears significantly more sensitive than sample S2 (~8 nm shift) and the NP-functionalized sample (~4 nm shift). These results confirm that nanostar morphology significantly enhances the sensor's responsiveness due to stronger plasmonic field confinement at the sharp nanostar tips. The higher surface sensitivity of the S3 NS-coated sensor is clearly reflected in the more pronounced shift, even at lower thiram concentrations.

4.9.1. Limit of Detection

The Limit of Detection (LOD) is a critical parameter in sensor performance, representing the lowest concentration of an analyte that can be reliably distinguished from the background noise with a defined level of confidence. It reflects the sensor's sensitivity and ability to detect trace amounts of a target substance. In practical terms, the LOD is often estimated as three times the standard deviation (SD) from the baseline region on a fitted curve trend of the sensor response. This approach accounts for the natural fluctuations in the baseline signal, ensuring that the detected response is significantly above the noise level. A lower LOD indicates a more sensitive detection system, which is particularly important in applications requiring early-stage detection or monitoring of very low analyte concentrations [23].

From the sensorgrams, the average and standard deviation of the wavelength shift for each concentration were calculated after stabilization, using a minimum of 10 data points. To quantitatively model the dose-response behavior, the experimental data were fitted using a sigmoidal function, as expressed in Equation (4-1) [23], [24].

$$\Delta\lambda = \Delta\lambda_{max} \cdot \left[\frac{\left(\frac{x}{x_0}\right)^p}{1 + \left(\frac{x}{x_0}\right)^p} \right] \qquad (4\text{-}1)$$

In this formula $\Delta\lambda$ is the observed wavelength shift representing the sensor response, $\Delta\lambda_{max}$ is the maximum shift in resonance wavelength, where the sensor has been saturated, x is the thiram concentration (in µM), x_0 represents the half-maximal concentration (the inflection point of the curve), and p is the exponent that determines the steepness of the transition from the initial rise to the plateau. This model is widely used in chemical and biosensing to describe Langmuir-type or cooperative binding behaviors. Figure 4-19 presents the wavelength shift (nm) versus thiram concentration (µM) plotted on a semi-logarithmic scale for all samples, with the data fitted using Equation (4-1). The fitting parameters for all the samples are thus summarized in Table 4-1.

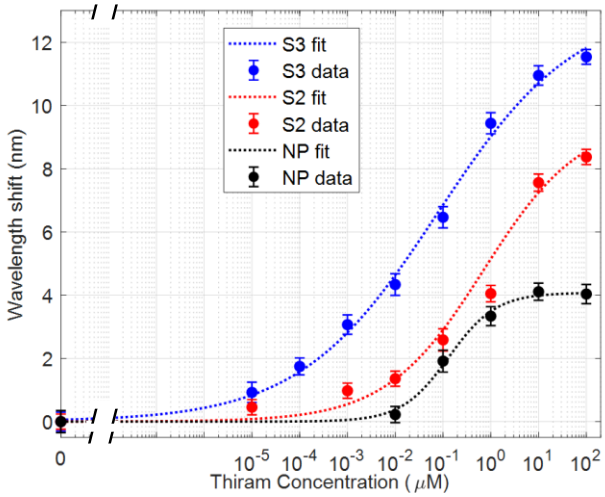

Figure 4-18. Semi-log calibration curve of the sensor S3, S2 and NP.

Table 4-1. Logistic fitting parameters and LOD for all the samples.

$Sample$	$\Delta\lambda_{max}\ [nm]$	$x_0\ [\mu M]$	p	LOD
$S3$	13.20	0.077	0.30	$0.3\ pM$
$S2$	9.60	0.71	0.43	$0.2\ nM$
NP	4.08	0.13	0.87	$7\ nM$

From the Figure 4-18, It can be observed a clear concentration-dependent redshift in the resonance wavelength, indicating a successful interaction between Thiram molecules and the sensing surface. The NP sample, shown in black, exhibits the lowest wavelength shifts across the concentration range, with a maximum shift around 4 nm. This suggests that the NP structure, while capable of detecting Thiram, has relatively lower sensitivity compared to the other two configurations. The red curve corresponds to the S2 sample, which demonstrates an improved response with a higher wavelength shift across nearly the entire concentration range. Its maximum shift reaches approximately 8.5 nm, indicating a stronger

plasmonic coupling or enhanced surface interaction, likely due to improved nanoparticle distribution or morphology.

The highest sensitivity is observed in the S3 configuration (blue data), which displays the largest wavelength shifts, reaching nearly 13 nm at the highest Thiram concentration. This superior performance is also evident from the leftward shift of its response curve, indicating a lower x_0, which translates into earlier and more pronounced spectral changes even at lower analyte concentrations. The S3 curve is also steeper, suggesting a sharper transition in its response, a desirable characteristic for biosensing applications aiming at rapid detection.

Additional key observations can be made from Figure 4-18. While all sensors detect thiram with wavelength shifts proportional to concentration, those incorporating NSs S3 and S2 demonstrate significantly higher sensitivity compared to the NP-based devices. Notably, sensor S3 exhibits the greatest sensitivity, consistent with its enhanced SRI response, achieved by tuning the absorbance peak to a longer wavelength. The $\Delta\lambda_{max}$ ratio between S3 and S2 (1.37) closely aligns with their SRI sensitivity ratio (1.28), further supporting this trend. Additionally, the p parameter for NS-based samples is markedly lower than that of the NP sample, resulting in smoother dose-response curves and broader effective detection range for thiram concentrations.

The LOD values for sensors S3, S2, and NP were determined to be 0.3 pM, 0.2 nM, and 7 nM, respectively, also these numbers can be found in Table 4-1. The findings indicate that by modifying the NSs to tune the transducer's resonance band, the sensitivity of the SRI improved, particularly at longer wavelengths of the attenuation band.

Table 4-2 compares the sensor's performance with existing Thiram detection methods reported in the literature. The results show that all tested samples exhibit a lower LOD than UV-VIS-based techniques. Moreover, sensors S3 and S2 demonstrate even better detection limits than those achieved by SERS methods. This approach not only provides a wider dynamic range but also surpasses other techniques in terms of detection sensitivity [1], [15], [25], [26], [27], [28], [29], [30], [31], [32]. Additionally, this method offers practical advantages, including lower cost and greater portability, making it suitable for real-world sensing applications.

Table 4-2.Comparison of the sensor performance with existing literature.

Configuration	Range	LOD	Ref.
UV–Vis	2.5–20 μM	40 nM	[31]
LC-MS	0.01–0.1 mg/kg	5 nM	[29]
SERS	1 nM-10 μM	1 nM	[32]
AuNPs-CTAB spectrophotometry	0.2–10 μM	170 nM	[15]
Etched MMF with AuNPs	0.1–100 μM	5 nM	[1]
Etched MMF with AuNSs	10 pM-100 μM	0.3 pM	This work

4.9.2. Selectivity tests

This section examines selectivity performance of the sensor. This characteristic is essential for ensuring reliable operation in real-world biosensing applications. The discussion focuses primarily on the sensor functionalized with NS from sample S3, as this configuration demonstrated the highest sensitivity to both changes in the surrounding refractive index and to thiram detection.

To evaluate the selectivity of the sensor, its response to another common agrochemical, glyphosate, was tested. Unlike thiram, glyphosate (Merck Life Science) lacks thiol-containing functional groups, which significantly reduces its affinity for gold surfaces [1], [33]. The sensor was exposed to a 0.1 µM aqueous solution of glyphosate, and the resulting LSPR shift was recorded. A modest wavelength change of approximately 0.7 nm was observed. For comparison, under identical conditions, thiram at the same concentration induced a substantially larger shift of around 6.5 nm, as illustrated in Figure 4-19. This contrast clearly highlights the sensor's enhanced responsiveness to molecules that contain thiol groups, which bind strongly to gold nanostructures. These results also underscore the potential to further tailor sensor selectivity by modifying the gold surface with biological recognition elements, such as antibodies, aptamers, or molecularly imprinted polymers, depending on the desired target analyte.

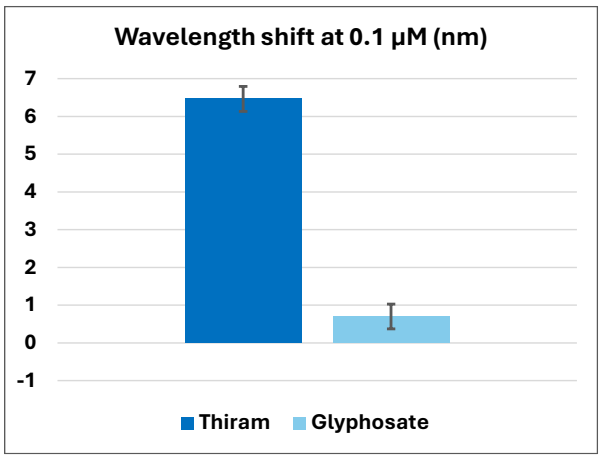

Figure 4-19. Selectivity test using interfering substance (glyphosate) and the analyte (Thiram) at 0.1 µM.

4.10. Conclusion

In this chapter, we have presented a comprehensive investigation into the design and development of highly sensitive LSPR-based optical fiber sensors. The work began with the synthesis of gold nanostructures, including both NPs and NSs, followed by detailed discussion of the readout setup, fiber transducer fabrication, and nanoparticle immobilization. The deposition of nanostructures onto chemically functionalized uncladded multimode silica fibers was optimized to ensure strong plasmonic coupling. The fabricated structures were extensively characterized using techniques such as SEM and TEM for morphological validation, and SRI measurements to quantify the refractive index sensitivity.

By varying the silver nitrate concentration during nanostar synthesis, from 0.8 mM to 3 mM, we were able to precisely tune the morphology of the NSs, leading to adjustable LSPR absorption peaks between 545 nm and 810 nm. The sensor with the longest resonance wavelength (~810 nm in water) demonstrated the highest refractive index sensitivity, reaching up to 560 nm/RIU. These experimental results show excellent agreement with the FEM-based simulations previously reported in Chapter 3, both in terms of LSPR spectral shift and predicted SRI responsiveness. This strong correlation validates the modeling approach and confirms the dominant role of NS morphology in plasmonic enhancement.

Additionally, a bio-sensitivity estimation was conducted using thiram as a model target, selected for its intrinsic affinity toward gold, enabling analyte interaction without biological functionalization. The results demonstrated a detection range spanning from 10 pM to 100 μM, with a LOD as low as 0.3 pM for the NS-based sensor, three orders of magnitude more sensitive than its NP counterpart. These findings also showed agreement between the SRI sensitivity and biosensing response, confirming that enhancements in bulk refractive index detection directly translate to improvements in trace-level molecular sensing.

The tunable performance, directly attributable to the controlled NSs geometry, provides distinct advantages not only in refractive index sensing but also in the detection of biologically relevant molecules. Compared to conventional detection techniques such as UV–Vis absorption or SERS, the developed LSPR-based optical fiber sensor offers superior sensitivity, a simpler setup, and cost-effective fabrication.

In summary, this chapter has demonstrated a versatile and powerful sensing platform with strong potential for deployment in environmental monitoring, digital agriculture, and chemical biosensing. In the next chapters the platform will be applied for the detection of biologically relevant compounds, such as Ochratoxin A and Cortisol, using antibodies as biologically recognition elements to enhance the sensitivity and selectivity of the sensors.

4.11. References

[1] A. Moslemi, L. Sansone, F. Esposito, S. Campopiano, M. Giordano, and A. Iadicicco, "Optical fiber probe based on LSPR for the detection of pesticide Thiram," *Opt Laser Technol*, vol. 175, p. 110882, Aug. 2024, doi: 10.1016/j.optlastec.2024.110882.

[2] A. Moslemi *et al.*, "Highly sensitive gold nanostar based optical fiber sensor with tunable plasmonic resonance," *Sensors and Actuators Reports*, p. 100326, Apr. 2025, doi: 10.1016/j.snr.2025.100326.

[3] W. Zhang, R. Singh, F.-Z. Liu, C. Marques, B. Zhang, and S. Kumar, "WaveFlex Biosensor: A Flexible-Shaped Plasmonic Optical Fiber Sensor for Histamine Detection," *IEEE Sens J*, vol. 23, no. 19, pp. 22533–22542, Oct. 2023, doi: 10.1109/JSEN.2023.3305464.

[4] A. E. F. Oliveira, A. C. Pereira, M. A. C. Resende, and L. F. Ferreira, "Gold Nanoparticles: A Didactic Step-by-Step of the Synthesis Using the Turkevich Method, Mechanisms, and Characterizations," *Analytica*, vol. 4, no. 2, pp. 250–263, Jun. 2023, doi: 10.3390/analytica4020020.

[5] H. Yuan, C. G. Khoury, H. Hwang, C. M. Wilson, G. A. Grant, and T. Vo-Dinh, "Gold nanostars: surfactant-free synthesis, 3D modelling, and two-photon photoluminescence imaging," *Nanotechnology*, vol. 23, no. 7, p. 075102, Feb. 2012, doi: 10.1088/0957-4484/23/7/075102.

[6] T. V Tsoulos *et al.*, "Colloidal plasmonic nanostar antennas with wide range resonance tunability," *Nanoscale*, vol. 11, no. 40, pp. 18662–18671, 2019.

[7] M. Ben Haddada *et al.*, "Optimizing the immobilization of gold nanoparticles on functionalized silicon surfaces: amine- vs thiol-terminated silane," *Gold Bull*, vol. 46, no. 4, pp. 335–341, Dec. 2013, doi: 10.1007/s13404-013-0120-y.

[8] Y. Chaikin, O. Kedem, J. Raz, A. Vaskevich, and I. Rubinstein, "Stabilization of Metal Nanoparticle Films on Glass Surfaces Using Ultrathin Silica Coating," *Anal Chem*, vol. 85, no. 21, pp. 10022–10027, Nov. 2013, doi: 10.1021/ac402020u.

[9] K. Ueno, S. Juodkazis, M. Mino, V. Mizeikis, and H. Misawa, "Spectral Sensitivity of Uniform Arrays of Gold Nanorods to Dielectric Environment," *The Journal of Physical Chemistry C*, vol. 111, no. 11, pp. 4180–4184, Mar. 2007, doi: 10.1021/jp068243m.

[10] C. Zhuang, Y. Xu, N. Xu, J. Wen, H. Chen, and S. Deng, "Plasmonic Sensing Characteristics of Gold Nanorods with Large Aspect Ratios," *Sensors*, vol. 18, no. 10, p. 3458, Oct. 2018, doi: 10.3390/s18103458.

[11] S. Rodal-Cedeira *et al.*, "Plasmonic Au@Pd Nanorods with Boosted Refractive Index Susceptibility and SERS Efficiency: A Multifunctional Platform for Hydrogen Sensing and Monitoring of Catalytic Reactions," *Chemistry of Materials*, vol. 28, no. 24, pp. 9169–9180, Dec. 2016, doi: 10.1021/acs.chemmater.6b04941.

[12] H. Parham, N. Pourreza, and F. Marahel, "Determination of thiram using gold nanoparticles and Resonance Rayleigh scattering method," *Talanta*, vol. 141, pp. 143–149, Aug. 2015, doi: 10.1016/j.talanta.2015.03.061.

[13] N. Alizadeh, H. Kalhor, and A. Karimi, "Determination of thiram residues in canola seeds, water and soil samples using solid-phase microextraction with polypyrrole film followed by ion mobility spectrometer," *Int J Environ Anal Chem*, vol. 95, no. 1, pp. 57–66, Jan. 2015, doi: 10.1080/03067319.2014.983496.

[14] S. Walia, R. K. Sharma, and B. S. Parmar, "Isolation and Simultaneous LC Analysis of Thiram and Its Less Toxic Transformation Product in DS Formulation," *Bull Environ Contam Toxicol*, vol. 83, no. 3, pp. 363–368, Sep. 2009, doi: 10.1007/s00128-009-9754-0.

[15] S. Rastegarzadeh and Sh. Abdali, "Colorimetric determination of thiram based on formation of gold nanoparticles using ascorbic acid," *Talanta*, vol. 104, pp. 22–26, Jan. 2013, doi: 10.1016/j.talanta.2012.11.023.

[16] K. M. Giannoulis, D. L. Giokas, G. Z. Tsogas, and A. G. Vlessidis, "Ligand-free gold nanoparticles as colorimetric probes for the non-destructive determination of total dithiocarbamate pesticides after solid phase extraction," *Talanta*, vol. 119, pp. 276–283, Feb. 2014, doi: 10.1016/j.talanta.2013.10.063.

[17] B. Kaur, S. Kumar, J. Nedoma, R. Martinek, and C. Marques, “Advancements in optical biosensing techniques: From fundamentals to future prospects,” *APL Photonics*, vol. 9, no. 9, Sep. 2024, doi: 10.1063/5.0216621.
[18] X. Liu *et al.*, “Advanced fiber optic sensors for quantitative nitrite detection: Comparative analysis of plasmonic tilted fiber Bragg gratings and fiber optic tips with ion-imprinted polymers,” *Sensors and Actuators Reports*, vol. 8, p. 100233, Dec. 2024, doi: 10.1016/j.snr.2024.100233.
[19] A. Urrutia, J. Goicoechea, and F. J. Arregui, “Optical Fiber Sensors Based on Nanoparticle-Embedded Coatings,” *J Sens*, vol. 2015, pp. 1–18, 2015, doi: 10.1155/2015/805053.
[20] J. Chen *et al.*, “Optimization and Application of Reflective LSPR Optical Fiber Biosensors Based on Silver Nanoparticles,” *Sensors*, vol. 15, no. 6, pp. 12205–12217, May 2015, doi: 10.3390/s150612205.
[21] N. Cennamo *et al.*, “Localized Surface Plasmon Resonance with Five-Branched Gold Nanostars in a Plastic Optical Fiber for Bio-Chemical Sensor Implementation,” *Sensors*, vol. 13, no. 11, pp. 14676–14686, Oct. 2013, doi: 10.3390/s131114676.
[22] N. Cennamo *et al.*, “Sensitive detection of 2,4,6-trinitrotoluene by tridimensional monitoring of molecularly imprinted polymer with optical fiber and five-branched gold nanostars,” *Sens Actuators B Chem*, vol. 208, pp. 291–298, Mar. 2015, doi: 10.1016/j.snb.2014.10.079.
[23] Á. Lavín *et al.*, “On the Determination of Uncertainty and Limit of Detection in Label-Free Biosensors,” *Sensors*, vol. 18, no. 7, p. 2038, Jun. 2018, doi: 10.3390/s18072038.
[24] F. Esposito *et al.*, “Long period grating in double cladding fiber coated with graphene oxide as high-performance optical platform for biosensing,” *Biosens Bioelectron*, vol. 172, p. 112747, Jan. 2021, doi: 10.1016/j.bios.2020.112747.
[25] B. N. Khlebtsov, V. A. Khanadeev, E. V. Panfilova, D. N. Bratashov, and N. G. Khlebtsov, “Gold Nanoisland Films as Reproducible SERS Substrates for Highly Sensitive Detection of Fungicides,” *ACS Appl Mater Interfaces*, vol. 7, no. 12, pp. 6518–6529, Apr. 2015, doi: 10.1021/acsami.5b01652.
[26] Y. Yu *et al.*, “Gold-Nanorod-Coated Capillaries for the SERS-Based Detection of Thiram,” *ACS Appl Nano Mater*, vol. 2, no. 1, pp. 598–606, Jan. 2019, doi: 10.1021/acsanm.8b02075.
[27] S. Asgari *et al.*, “Nanofibrillar cellulose/Au@Ag nanoparticle nanocomposite as a SERS substrate for detection of paraquat and thiram in lettuce,” *Microchimica Acta*, vol. 187, no. 7, p. 390, Jul. 2020, doi: 10.1007/s00604-020-04358-9.
[28] X. He, S. Yang, T. Xu, Y. Song, and X. Zhang, “Microdroplet-captured tapes for rapid sampling and SERS detection of food contaminants,” *Biosens Bioelectron*, vol. 152, p. 112013, Mar. 2020, doi: 10.1016/j.bios.2020.112013.
[29] A. Peruga, S. Grimalt, F. J. López, J. V. Sancho, and F. Hernández, “Optimisation and validation of a specific analytical method for the determination of thiram residues in fruits and vegetables by LC–MS/MS,” *Food Chem*, vol. 135, no. 1, pp. 186–192, Nov. 2012, doi: 10.1016/j.foodchem.2012.04.064.
[30] V. Tran *et al.*, “Probing the SERS brightness of individual Au nanoparticles, hollow Au/Ag nanoshells, Au nanostars and Au core/Au satellite particles: single-particle experiments and computer simulations,” *Nanoscale*, vol. 10, no. 46, pp. 21721–21731, 2018, doi: 10.1039/C8NR06028B.
[31] J. V. Rohit and S. K. Kailasa, “Cyclen dithiocarbamate-functionalized silver nanoparticles as a probe for colorimetric sensing of thiram and paraquat pesticides via host–guest chemistry,” *Journal of Nanoparticle Research*, vol. 16, no. 11, p. 2585, Nov. 2014, doi: 10.1007/s11051-014-2585-x.
[32] R. K. Saini, A. K. Sharma, A. Agarwal, and R. Prajesh, “Label-free detection of Thiram pesticide on flexible SERS-active substrate,” *Mater Chem Phys*, vol. 295, p. 127088, Feb. 2023, doi: 10.1016/j.matchemphys.2022.127088.
[33] Q. Duan, Y. Liu, S. Chang, H. Chen, and J. Chen, “Surface Plasmonic Sensors: Sensing Mechanism and Recent Applications,” *Sensors*, vol. 21, no. 16, p. 5262, Aug. 2021, doi: 10.3390/s21165262.

5. Chapter 5
Ochratoxin A detection with gold nanoparticles

After presenting the fabrication and characterization of LSPR transducers based on NP and NS depositions in chapter 4, this chapter reports on the detection of mycotoxins, specifically Ochratoxin A (OTA). This work was carried out during my exchange period at the University of Aveiro in Portugal. The focus is on the simple configuration based on NPs. The chapter first details fabrication, refractometric characterization, and morphological analysis. Subsequently, the process of bio-functionalizing the spherical nanoparticle-deposited fiber-optic transducer is discussed. In particular, OTA antibodies were attached to the surface of the transducer. Finally, the detection of OTA is presented, demonstrating a significant advancement toward practical biosensing applications.

5.1. Introduction

OTA is a highly concerning mycotoxin, a toxic secondary metabolite primarily produced by fungi from the genera Aspergillus and Penicillium. Its widespread presence in common food items such as cereals, coffee, and wine has made it a significant global health concern. The primary danger of OTA lies in its severe and multifaceted harmful effects on human and animal health. It is particularly known for its nephrotoxic and hepatotoxic properties, meaning it can cause significant damage to the kidneys and liver, respectively. Due to these effects and its potential to cause tumors, the International Agency for Research on Cancer (IARC) has classified OTA as a possible human carcinogen. The underlying

mechanism of its toxicity is related to its structural similarity to the amino acid phenylalanine, which allows it to interfere with protein synthesis by competing with the phenylalanine-tRNA synthetase enzyme. Beyond its primary toxic effects, OTA has also been shown to act as an endocrine disruptor, an immunosuppressant, and a modulator of protein synthesis and apoptosis. Its long half-life in the body, approximately 35 days, contributes to its prolonged harmful impact [1], [2], [3], [4].

Given these significant health risks, regulatory bodies worldwide have established strict maximum limits for OTA in food. For example, the European Commission has set specific standards to protect consumers, including a maximum limit of 5 µg/kg for roasted coffee beans and 10 µg/kg for instant coffee. A more recent study also cites a maximum limit of 5×10^{-3} mg/kg for instant coffee. The high environmental stability of OTA, which allows it to withstand high temperatures and acidic conditions during food processing, makes these strict limits and effective detection methods critical for ensuring food safety [5], [6], [7], [8], [9].

There are several methods for detecting OTA, each with its own trade-offs in terms of sensitivity, cost, and practicality. The choice of method often depends on the specific application, whether it's for high-precision quantification or rapid screening.

One of the most widely used and reliable methods is High-Performance Liquid Chromatography with Fluorescence Detection (HPLC-FLD). This technique is frequently combined with an immunoaffinity column clean-up step, which selectively extracts and concentrates OTA from the sample before analysis. The combination of these techniques provides high sensitivity and accurate quantitative results, making it the most commonly reported method for OTA analysis in coffee. As an example, Albani L. Gonzalez et al. [10], offers a viable alternative. This method uses second-order multivariate calibration and excitation-emission fluorescence matrix (EEFM) data to quantify OTA. This technique, particularly when using the MCR-ALS algorithm, provided limits of detection between 0.2 and 0.3 ng mL^{-1} and recoveries ranging from 92% to 110%. Notably, the results obtained from this method were in agreement with those from the reference HPLC-FLD method. The new method is also considered more environmentally friendly, as it significantly reduces the use of organic solvents and the amount of waste generated.

For faster and more cost-effective screening of OTA, Thin-Layer Chromatography (TLC) and Enzyme-Linked Immunosorbent Assay (ELISA) are frequently used. TLC is a simple and quick method that involves extracting and separating the sample on a plate, followed by visualization under a UV lamp at 366 nm. This technique is particularly well-suited for settings with limited resources, such as in coffee-producing countries. ELISA, an immunoassay, uses antibodies to quickly screen multiple samples, though it is generally less precise than chromatographic methods like HPLC. For example, Alain Pittet et al. [11] developed and validated a TLC screening method for OTA in green coffee with a control level of 10 µg/kg. The method, which involves extraction with phosphoric acid and dichloromethane and purification by liquid-liquid partition, demonstrated excellent agreement with a quantitative immunoaffinity/HPLC method. It was successfully tested on both spiked samples (5, 10,

and 20 µg/kg) and naturally contaminated ones (from 0.2 to 136.7 µg/kg), with no false positive or false negative results recorded. This validates the method as a rapid, simple, and cost-effective screening tool.

More advanced and sensitive techniques are also available for detecting OTA. Electrochemical sensors offer a practical and affordable option for routine monitoring by using modified electrodes for selective detection. However, for the highest level of specificity and confirmation, Liquid Chromatography Tandem Mass Spectrometry (LC-MS/MS) is considered the gold standard. This method combines the separation power of liquid chromatography with the precise identification capabilities of mass spectrometry, which provides structural information and significantly reduces the risk of false positives. For example, a method developed by Bandeira et al. [12] used LC-MS/MS with a matrix-matched calibration curve to determine OTA in green coffee. The method was validated with a linearity range of 3.0 to 23.0 ng g^{-1}. It achieved high mean recoveries between 90.45% and 108.81% and low limits of detection and quantification (1.2 ng g^{-1} and 3.0 ng g^{-1}, respectively). The authors concluded that their method was suitable for mycotoxin analysis and would be used in the future to produce a Certified Reference Material (CRM) for OTA in coffee.

In this context, several biosensors based on LSPR and SPR on optical fibers have been developed to detect OTA. These fiber optic sensors offer several benefits, including a lower SNR and LOD, as well as being cheaper and faster than traditional laboratory methods.

Several SPR biosensors have been developed for highly sensitive OTA detection. Such label-free biosensor uses a change in refractive index to detect OTA when its aptamer binds to it, achieving detection limits in the picogram per milliliter range and showing promise for portable devices. For example, de Andrade Silva et al. reported using a spoon-shaped waveguide immunosensor to detect OTA in coffee samples. The biosensor's surface was coated with a 60 nm gold layer to enable the SPR phenomenon. The measurements showed a linear relationship between the change in SPR values and OTA concentrations from 0.2 ppt to 5 ppt. This device was highly selective, avoided matrix interference, and is a promising portable, simple, and suitable analytical tool for on-site detection of OTA in coffee.

In addition to SPR sensors, LSPR sensors on optical fibers have also been shown to be effective for OTA detection. These sensors are valued for their simplicity, high sensitivity, and low cost [13], [14]. For example, Bobin Lee et al. [9] proposed an optical fiber-based LSPR sensor to overcome challenges like nanoparticle instability and difficult sample loading. The sensor, made of an optical fiber coated with aptamer-modified gold nanorods (GNRs), is simply dipped into a solution. It quantifies OTA by measuring the spectral red shift of the GNRs' LSPR peak upon binding. This method showed a linear response from 10 pM to 100 nM with a limit of detection of 12.0 pM. The sensor also demonstrated high selectivity for OTA over other mycotoxins and was successfully used to detect OTA in real grape juice samples.

5.2. Design of the biosensor

Based on the mentioned importance of detecting OTA, this chapter introduces a novel FOS for its ultrasensitive detection. The sensor leverages LSPR of gold NPs. A key innovation of this study is the specificity and repeatability for the target based on bio-functionalization. A schematic design of the transducer and established biological architecture and read out setup is reported in Figure 5-1.

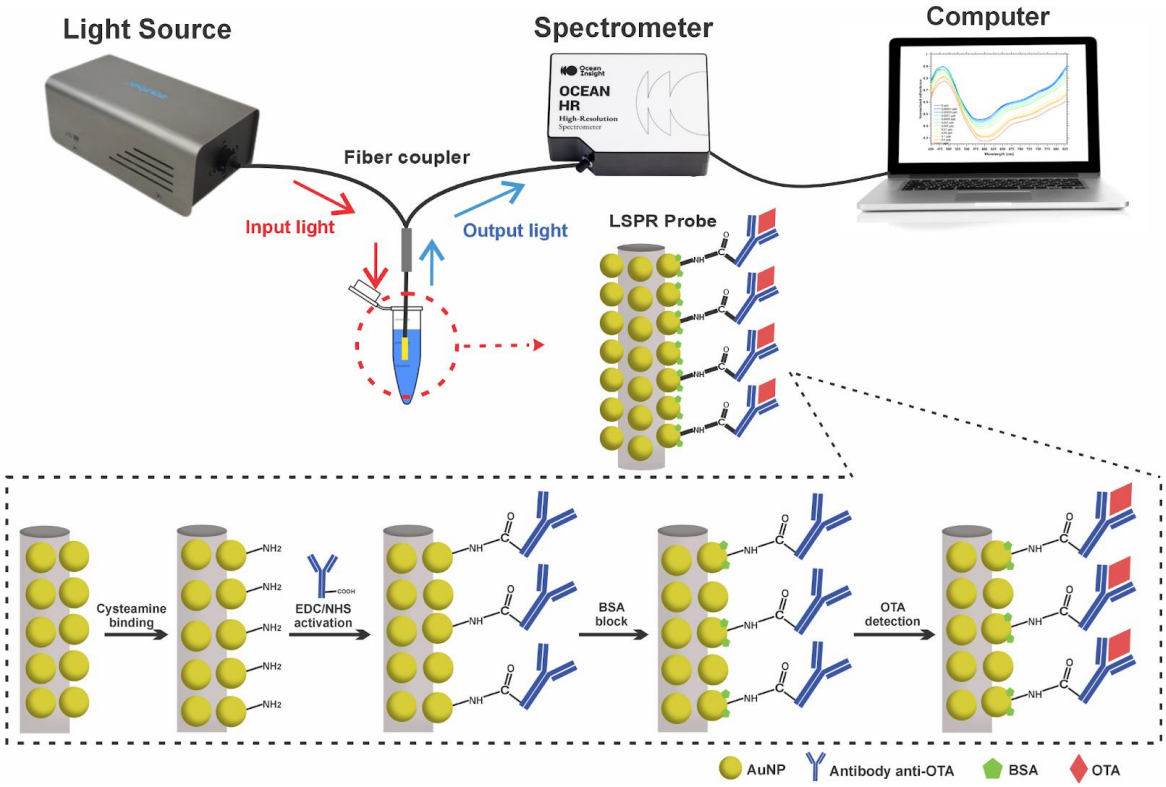

Figure 5-1. Schematic representation of setup configuration and the steps of construction of LSPR-based fiber-optic Biosensor.

The fabrication steps and read-out setup for the transducer were detailed in Chapter 4. The following sections focus on the characterization of the NPs, presenting their corresponding spectra and the transducer's performance, as well as the testing with biological compounds.

5.3. Characterization of nanoparticles

The synthesis of NPs, as described in chapter 4, was confirmed to be successful through several analyses. The UV-Vis spectrum showed a characteristic plasmon resonance peak at 522 nm (Figure 5-2A). The chemical composition was analyzed by XRD, which revealed four distinct peaks at 38°, 44°, 64°, and 77° (Figure 5-2B). Further analysis using DLS (Figure 5-2C) showed that the hydrated AuNPs had an average hydrodynamic size of 35 nm. This size is larger than their actual diameter due to the presence of a hydrated layer on their surface. The particles exhibited a Zeta Potential (ZP) of -40.89

mV, indicating good stability. Finally, TEM images (Figure 5-2D and 5-2E) confirmed that the particles had a hexahedral shape with an average size of 13.67 ± 1.53 nm (n=500) and were well-dispersed (Figure 5-2F).

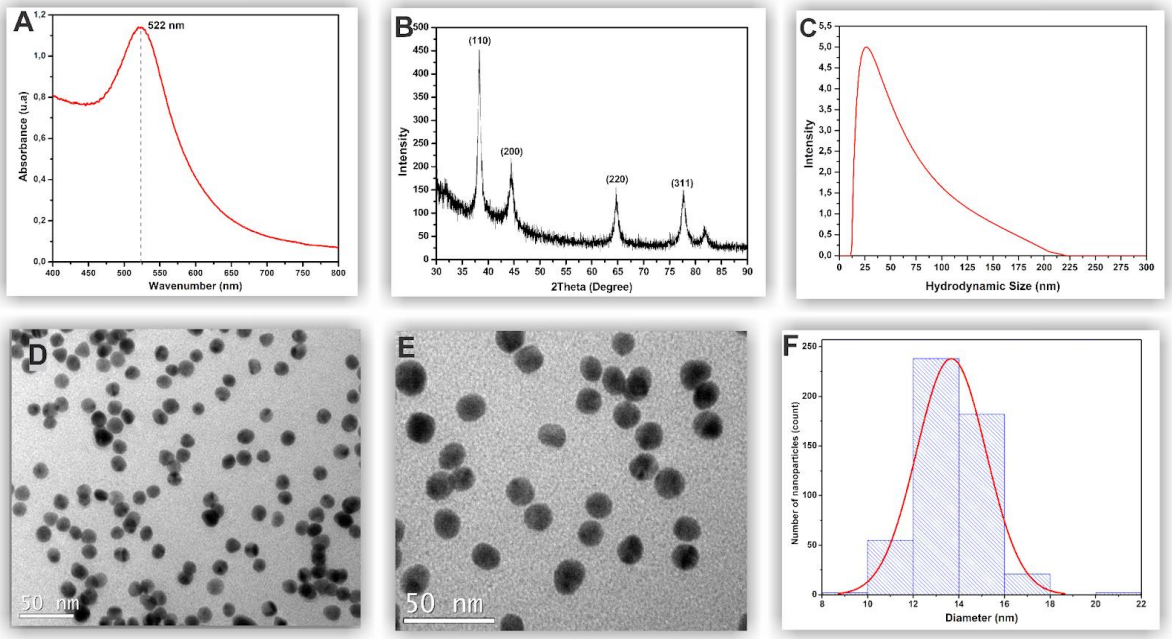

Figure 5-2. (A) UV-Vis of gold nanoparticles; (B) X-ray diffraction of AuNPs; (C) Dynamic Light Scattering of AuNPs; (D, E) TEM images of AuNPs and (F) histogram of the distribution of 500 nanoparticles.

5.4. Fabrication and characterization of the transducer

Building on the methods detailed in Chapter 4, we successfully fabricated several different transducers. Using the NPs characterized in previous section, we deposited them onto the surface of an

optical fiber core. The successful APTES ligand-mediated functionalization was visually confirmed by the color change of the fiber (Figure 5-3A and 5-3B).

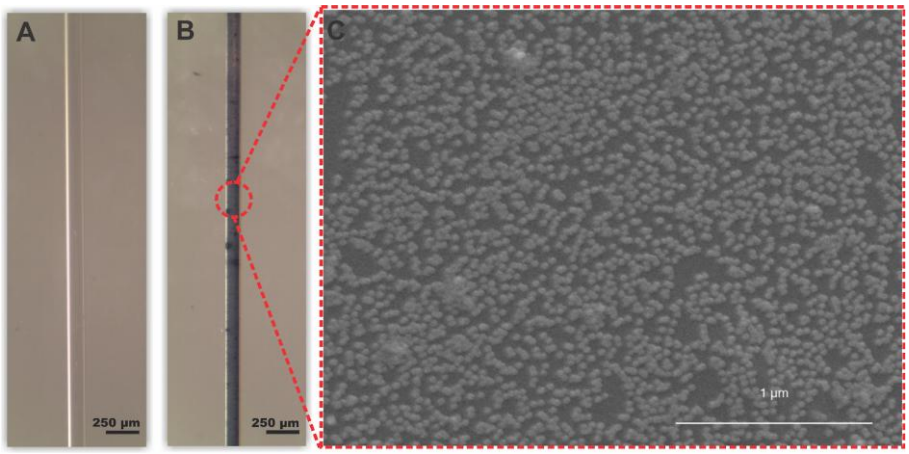

Figure 5-3. Stereo images of fiber-optic before (A) and after (B) NPs deposition; (C) SEM image of fiber surface with NPs.

The SEM image (Figure 5-3C) further confirmed that the NPs were deposited uniformly on the fiber surface with a high density. This uniformity is crucial for ensuring the accurate immobilization of antibodies and for reproducibility of LSPR signal.

Reflection spectrum and SRI sensitivity of one of samples as example is shown in Figure 5-4 (A) and (B) respectively. The calculated SRI sensitivity was measured to be 160 ± 10 nm/RIU for all samples.

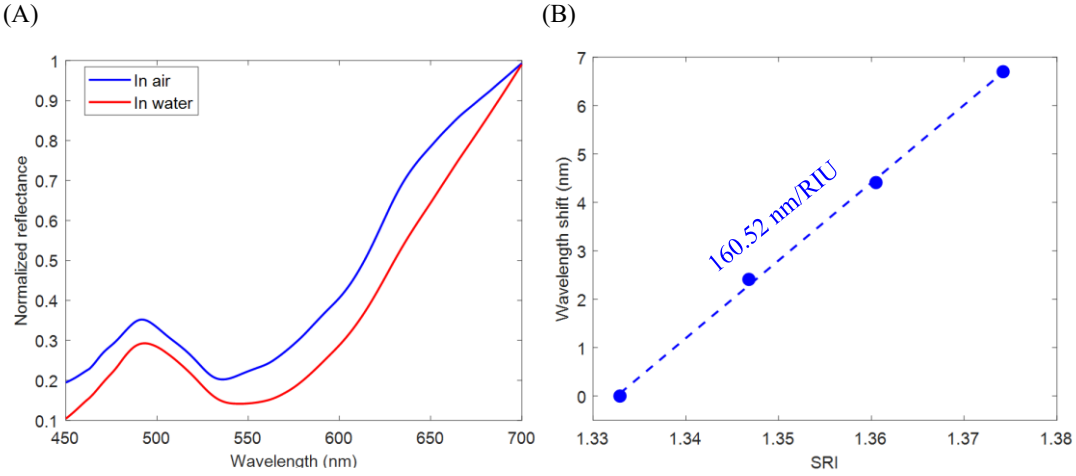

Figure 5-4(A). Reflection spectrum of transducer in air and water. (B) SRI sensitivity.

5.5. Bio-functionalization

The process of bio-functionalization is a critical step in creating a biosensor. As shown in Figure 5-1, the procedure begins by immersing the transducer in a 20 mM cysteamine solution for 18 hours to

modify the surface of the NPs with amine (-NH_2) groups. This is a crucial first step for proper antibody immobilization. The transducer is then thoroughly rinsed with deionized water.

Following this, Anti-OTA antibodies (RayBiotech, DS-PB-01496), are immobilized using an Ethyl-Di-Carbodiimide (EDC) (Sigma Aldrich, 03449)- N-Hydroxysuccinimide (NHS) (Sigma Aldrich, 130672), covalent coupling system. A solution containing 100 µg/mL of antibodies is first activated with 8 mM EDC and 5 mM NHS for one hour. The activated antibody solution is then incubated with the transducer for two hours to allow for covalent binding. The sensor is washed with Phosphate-Buffered Saline (PBS) to remove any unbound antibodies. To prevent non-specific binding, the biosensor is then blocked by incubating it in a 0.5% bovine serum albumin (BSA) solution for 30 minutes, followed by a final rinse with PBS. This conjugation process ensures the proper orientation of the antibodies and preserves their binding affinity with OTA (Sigma-Aldrich, 01877) [12].

The effectiveness of these surface modifications was confirmed by monitoring the reflection spectra in PBS after each functionalization step (Figure 5-5(A)) and antibody deposition sensorgram (Figure 5-5(B)). The presence of the AuNPs on the optical fiber core introduces a characteristic absorption peak in the visible region (~520–600 nm), which is highly sensitive to variations in the local refractive index. Both the cysteamine immobilization and antibody conjugation induced redshifts in the LSPR spectra, confirming the successful surface modifications. Functionalization with cysteamine induced a shift of ~13 nm, and the antibody immobilization resulted in an additional shift of 2 nm. Moreover, to investigate the effect of cysteamine, one sample was bio-functionalized without it to compare with the other samples.

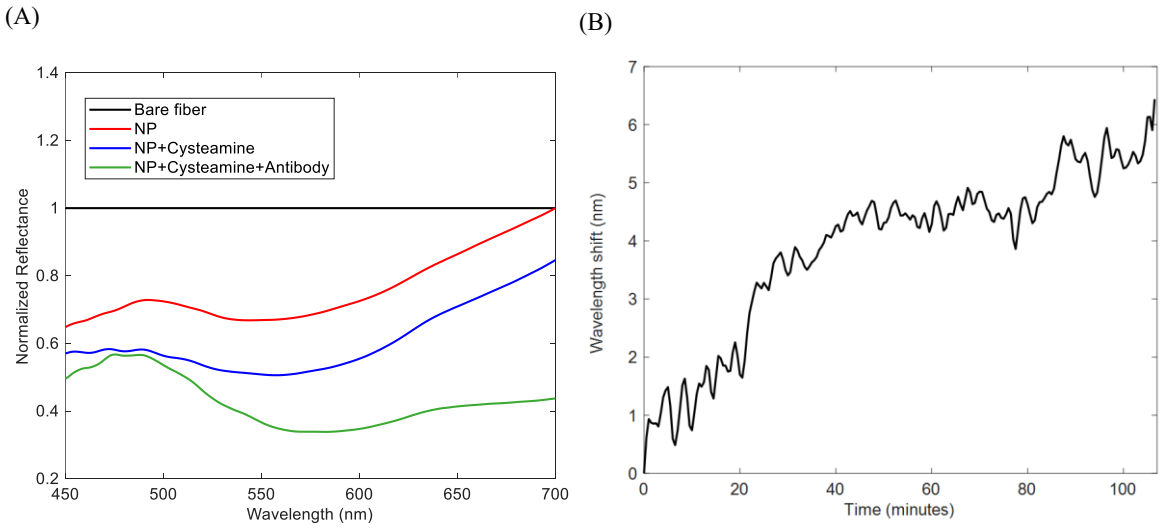

Figure 5-5. (A) Reflected spectra for sensor: bare fiber (black), optical fiber with AuNPs (red), after cysteamine functionalization (blue), and after antibody conjugate (green). (B) Antibody deposition sensorgram.

5.6. Testing with OTA

To detect Ochratoxin A, the sensor was immersed in solutions with concentrations ranging from 1×10^{-5} to 1 ppb ($2.48 \times 10^{-8}\ to\ 0.00248\ \mu M$). After a 30-minute incubation, the sensor was washed with PBS for 5 minutes to remove non-specific residues. The reflection spectra were monitored every 30 seconds. The experiment consisted of three independent tests with three sensors prepared in the same way (S1, S2, S3) and a fourth sensor (S4) prepared intentionally different without cysteamine in the process.

Figure 5-6 (A) and (B) show the effect of the OTA solutions on two samples: one that was bio-functionalized with cysteamine and one without, respectively. In both cases, a gradual shift of the plasmonic resonance peak was observed as the OTA concentration increased, indicating a specific interaction between the analyte and the immobilized antibodies. However, the resonance wavelength shift was clearly greater for the sample that included cysteamine in its bio-functionalization.

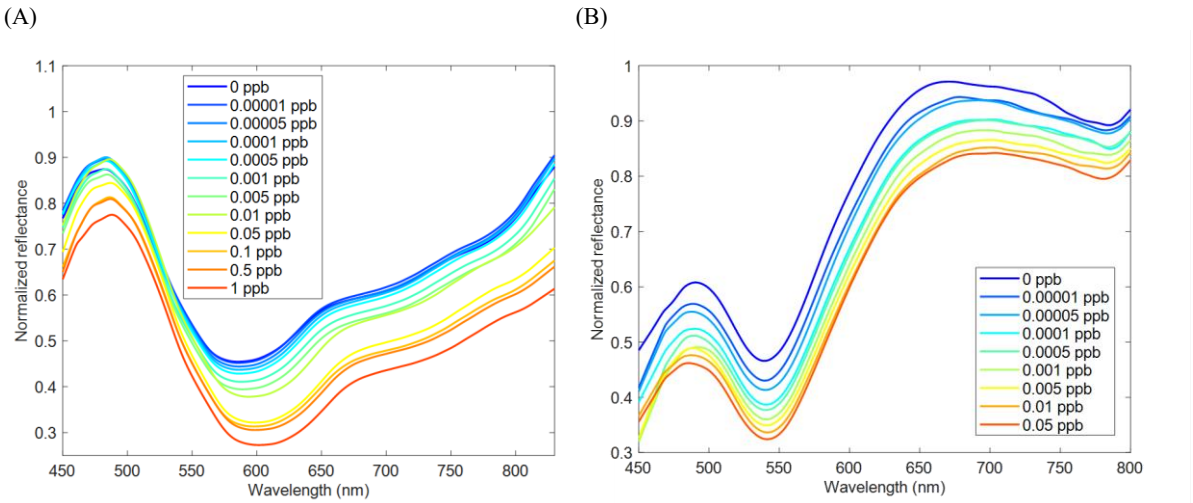

Figure 5-6. Spectra at different concentrations for samples (A) with and (B) without cysteamine in bio-functionalization process.

Figure 5-7(A) shows the time-dependent wavelength shift of the resonance peak from the baseline (zero concentration) for one of the sensors with cysteamine as an exemplary. In this process, after each incubation step with a specific target concentration, the transducer was immersed in PBS to remove unbound molecules. This step is crucial because it allows for monitoring the wavelength shift caused only by the specifically bonded targets, as evidenced by a slight blue shift observed during these PBS washing steps.

The experiment was repeated three times and for each concentration the $\Delta\lambda$ value is calculated by taking the difference between the wavelength measured in PBS after each incubation and the reference wavelength obtained in pure PBS. Consequently, each data point shown in the graph represents the mean value, and the associated error bars correspond to the SD obtained from the three repeated experiments for each concentration. The average and SD of were used to plot the calibration curve in a

semi-logarithmic scale, as shown in Figure 5-7(B). This curve, which is fitted with equation (4-1), plots the change in the plasmonic resonance wavelength ($\Delta\lambda$) as a function of the OTA concentration. This dose-response relationship demonstrates the system's sensitivity and reproducibility for detecting OTA, even at ultra-low concentrations.

As evidenced by Figure 5-7(B) and Table 5-1, the inclusion of cysteamine in the bio-functionalization process significantly enhances the sensor's performance. While samples S1, S2, and S3, which were functionalized with cysteamine, showed an average wavelength shift of approximately 17.56 nm, sample S4, without cysteamine, exhibited a minimal shift of only about 3 nm. This improvement is a direct result of cysteamine's function in forming a robust and well-organized self-assembled monolayer (SAM) on the gold surface. By providing both a thiol group to bind to the gold and an amine group for subsequent antibody attachment, cysteamine ensures the proper orientation and creates a dense layer of antibodies. This dense and uniform layer allows for more efficient and abundant binding of OTA, which in turn produces a much larger and more sensitive LSPR signal. This enhanced signal directly translates to an improved sensitivity and a lower LOD for the biosensor. Additionally, because of the cysteamine treatment, more antibodies are active on the gold surface, which also increases the transducer's saturation point. According to Figure 5-6(B), samples S1 to S3 saturate at approximately 1 ppb, while sample S4 saturates at about 10^{-3} ppb. This demonstrates that the inclusion of cysteamine effectively increased the dynamic range of the sensor [15].

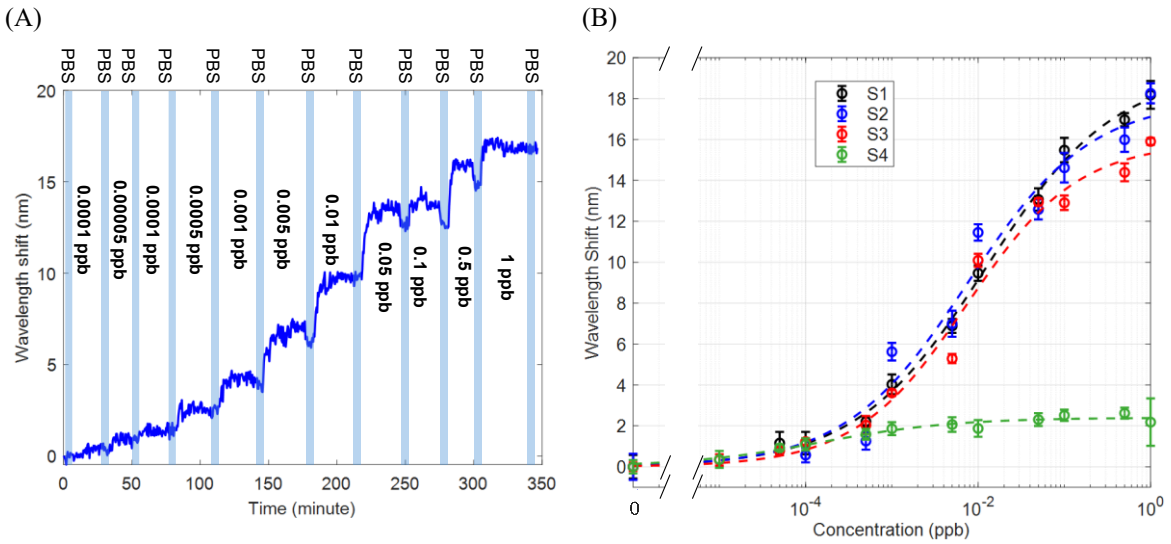

Figure 5-7. (A) Sensorgram of S2 and (B) calibration curves of the biosensors for OTA detection.

According to the method described in Chapter 4, the LOD was calculated as the mean value of the blank signal (PBS) plus three times its standard deviation (3σ). The standard deviation was obtained from three independent experiments. Based on these measurements, the resulting LOD was 0.0003 ppb ($0.743\ pM$), indicating high sensor Table 5-1 presents the parameters for the biosensor's performance, based on three independent tests. . As LOD exceeded the lowest concentration initially tested, the dynamic working range of the sensor was adjusted. The corrected range spans from the LOD to the

saturation point, specifically 0.0003 ppb to 1 ppb ($0.743\ pM\ to\ 0.00248\ \mu M$) which demonstrates excellent sensitivity and a wide dynamic range.

Table 5-1. Logistic fitting parameters for biosensor calibration curves.

Sample	$\Delta\lambda_{MAX}$ [nm]	x_0 [ng/mL]	P
S1	19.09	1.15×10^{-2}	0.61
S2	17.96	7.53×10^{-3}	0.61
S3	15.88	7.41×10^{-3}	0.67
S4	2.42	1.53×10^{-4}	0.52

A comparison of the biosensors performance with other optical devices for OTA detection from the recent literature is presented in Table 5-2. The key distinction of this work is that it is the only one to date that employs the fiber-optic-based LSPR effect with the specificity of antibodies as the recognition element. The simple configuration, high sensitivity, rapid response time of less than 30 minutes, and the potential for miniaturization position this technology as a promising analytical tool for real-time monitoring within the food production chain.

Table 5-2. Comparative analysis between different plasmonic sensors for OTA detection.

Transducer	Method	Bioreceptor	Detection range (ppb)	LOD (ppb)	Selectivity	Ref
TIP Fiber	**LSPR- NRs**	**Aptamer**	4×10^{-9} - 4×10^{-5}	4.8	**Zearalenone, Ochratoxin B**	[9]
Waveguides	**Gold film - SPR**	**Antibody**	0.0002 - 0.005	0.0002	**Ochratoxin B**	[8]
Au-AgNPs	**LSPR**	**Antibody**	0.050 - 0.20	0.007	**-**	[13]
Gold Electrode	**EIS**	**Antibody**	0.5 - 100	0.15	**Ochratoxin B**	[7]
Fiber - AuNPs	**LSPR**	**Antibody**	1×10^{-4} - 1	1.85×10^{-5}	**Ochratoxin B**	**This work**

5.7. Selectivity

For the selectivity studies, ochratoxin B (OTB) (Supelco, 32411) [14], a structurally similar mycotoxin, was used as a key interferent. OTB is a relevant choice because it is often found alongside OTA in matrices like coffee, wine, and cereals. As shown in Figure 5-8, the biosensor's response to an equimolar concentration of OTB was significantly different from its response to OTA ($p < 0.05$, Student's t-test). The wavelength shift ($\Delta\lambda$) for OTB was less than 5% of the shift observed for OTA at the same concentration (1 ppb each). This finding confirms the high specificity of the immobilized antibodies, which is particularly important for practical applications where both contaminants may be present simultaneously. The results demonstrate the robustness and selective performance of the developed system even in complex environments.

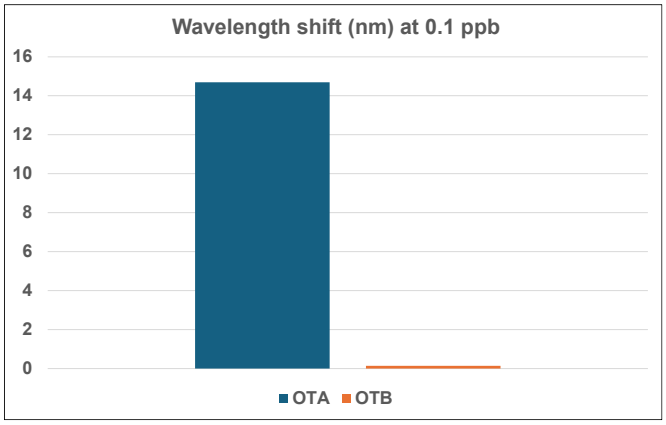

Figure 5-8. Selectivity test comparing the wavelength shift of biosensors for a 0.01 pbb concentration of OTA and OTB.

5.8. Conclusion

This chapter describes the development of a portable optical biosensor based on the LSPR effect in an optical fiber for the ultrasensitive and selective detection of OTA. The sensor's surface was functionalized with AuNPs and anti-OTA antibodies, which allowed for an exceptionally low LOD of 0.0003 ppb ($0.743\ pM$), and a working range of 0.0003to 1 ppb ($0.743\ pM\ to\ 0.00248\ \mu M$). The study also investigated the significant effect of cysteamine on both the LOD and the dynamic range for OTA detection. The biosensor's high selectivity for OTA over OTB, combined with a rapid analysis time of less than 30 minutes, makes it a promising analytical tool for on-site monitoring in the food production chain.

5.9. References

[1] F. Malir, V. Ostry, A. Pfohl-Leszkowicz, and E. Novotna, "Ochratoxin A: Developmental and Reproductive Toxicity—An Overview," Birth Defects Res B Dev Reprod Toxicol, vol. 98, no. 6, pp. 493–502, Dec. 2013, doi: 10.1002/bdrb.21091.

[2] E. E. Creppy, F. C. Størmer, D. Kern, R. Röschenthaler, and G. Dirheimer, "Effects of ochratoxin a metabolites on yeast phenylalanyl-tRNA synthetase and on the growth and in vivo protein synthesis of hepatoma cells," Chem Biol Interact, vol. 47, no. 2, pp. 239–247, Nov. 1983, doi: 10.1016/0009-2797(83)90160-6.

[3] H. Assaf, H. Azouri, and M. Pallardy, "Ochratoxin A Induces Apoptosis in Human Lymphocytes through Down Regulation of Bcl-xL," Toxicological Sciences, vol. 79, no. 2, pp. 335–344, Jun. 2004, doi: 10.1093/toxsci/kfh123.

[4] G. Müller, B. Burkert, H. Rosner, and H. Köhler, "Effects of the mycotoxin ochratoxin A and some of its metabolites on human kidney cell lines," Toxicology in Vitro, vol. 17, no. 4, pp. 441–448, Aug. 2003, doi: 10.1016/S0887-2333(03)00053-5.

[5] A. A. Nuhu, "Occurrence, harmful effects and analytical determination of Ochratoxin A in coffee," J Appl Pharm Sci, pp. 120–127, 2015, doi: 10.7324/JAPS.2015.50121.

[6] G. A. Guadalupe, D. E. Grandez-Yoplac, E. Arellanos, and E. Doménech, "Probabilistic Risk Assessment of Metals, Acrylamide and Ochratoxin A in Instant Coffee from Brazil, Colombia, Mexico and Peru," Foods, vol. 13, no. 5, p. 726, Feb. 2024, doi: 10.3390/foods13050726.

[7] J. P. de Oliveira, F. Burgos-Flórez, I. Sampaio, P. Villalba, and V. Zucolotto, "Label-free electrochemical immunosensor for Ochratoxin a detection in coffee samples," Talanta, vol. 260, p. 124586, Aug. 2023, doi: 10.1016/j.talanta.2023.124586.

[8] T. de Andrade Silva et al., "Plasmonic immunosensors based on spoon-shaped waveguides for fast and on-site ultra-low detection of ochratoxin A in coffee samples," Talanta, vol. 271, p. 125648, May 2024, doi: 10.1016/j.talanta.2024.125648.

[9] B. Lee, J.-H. Park, J.-Y. Byun, J. H. Kim, and M.-G. Kim, "An optical fiber-based LSPR aptasensor for simple and rapid in-situ detection of ochratoxin A," Biosens Bioelectron, vol. 102, pp. 504–509, Apr. 2018, doi: 10.1016/j.bios.2017.11.062.

[10] A. L. Gonzalez, V. A. Lozano, G. M. Escandar, and M. A. Bravo, "Determination of ochratoxin A in coffee and tea samples by coupling second-order multivariate calibration and fluorescence spectroscopy," Talanta, vol. 219, p. 121288, Nov. 2020, doi: 10.1016/j.talanta.2020.121288.

[11] A. Pittet and D. Royer, "Rapid, Low Cost Thin-Layer Chromatographic Screening Method for the Detection of Ochratoxin A in Green Coffee at a Control Level of 10 μg/kg," J Agric Food Chem, vol. 50, no. 2, pp. 243–247, Jan. 2002, doi: 10.1021/jf010867w.

[12] R. D. da C. C. Bandeira et al., "Development and validation of a method for detection and quantification of ochratoxin A in green coffee using liquid chromatography coupled to mass spectrometry," Food Science and Technology, vol. 32, no. 4, pp. 775–782, Nov. 2012, doi: 10.1590/S0101-20612012005000120.

[13] D. I. Meira, A. I. Barbosa, J. Borges, R. L. Reis, V. M. Correlo, and F. Vaz, "Label-free localized surface plasmon resonance (LSPR) biosensor, based on Au-Ag NPs embedded in TiO2 matrix, for detection of Ochratoxin-A (OTA) in wine," Talanta, vol. 284, p. 127238, Mar. 2025, doi: 10.1016/j.talanta.2024.127238.

[14] W. Xu et al., "Trident-Shaped WaveFlex Fiber-Optic Biosensor for Ochratoxin A Detection in Real Cereal Products," IEEE Sens J, vol. 24, no. 9, pp. 14101–14108, May 2024, doi: 10.1109/JSEN.2024.3370863.

[15] R. E. Ionescu, "Use of Cysteamine and Glutaraldehyde Chemicals for Robust Functionalization of Substrates with Protein Biomarkers—An Overview on the Construction of Biosensors with Different Transductions," Biosensors (Basel), vol. 12, no. 8, p. 581, Jul. 2022, doi: 10.3390/bios12080581.

6. Chapter 6
Cortisol detection with gold nanostars

This chapter presents another demonstration of LSPR-based fiber biosensors for the ultra-sensitive detection of the cortisol hormone. In particular, the study transitions from spherical gold NPs to NSs. By optimizing the synthesis parameters of NSs, the LSPR band was shifted toward higher wavelengths, resulting in an enhanced bulk refractometric sensitivity. The transducers were further biofunctionalized by attaching anti-cortisol antibodies, ensuring selective binding and detection of the target analyte, cortisol. This work represents a significant advancement toward practical biosensing applications. Most of the experimental activity was carried out during my exchange period at the University of Aveiro in Portugal and results have been published in Photonics Research journal [1].

6.1. Introduction

Cortisol is a steroid hormone ($C_{21}H_{30}O_5$) synthesized by the adrenal cortex under the control of the hypothalamic–pituitary–adrenal (HPA) axis. It plays a central role in regulating the body's stress response, metabolic balance, immune activity, cardiovascular function, and homeostasis. In response to stressor, corticotropin-releasing hormone (CRH) from the hypothalamus stimulates the pituitary gland to secrete adrenocorticotropic hormone (ACTH), which then triggers cortisol release from the adrenal glands. Acute cortisol release enhances energy availability, increases heart rate, and suppresses non-essential processes (e.g., digestion, certain immune functions) to support a "fight-or-flight" state. However, chronic dysregulation, either sustained elevation or suppression, can have harmful effects,

including immune suppression, digestive inhibition, obesity, bone fragility, cardiovascular disease, hypertension, mood disorders, and metabolic imbalances. Low cortisol levels are linked to conditions such as Addison's disease, characterized by hypotension, fatigue, and weight loss.

In healthy individuals, cortisol secretion follows a circadian rhythm, peaking in the early morning and gradually declining throughout the day. In occupational settings, however, this pattern can be disrupted by persistent exposure to high workloads, psychological stress, shift work, or hazardous environments. Such dysregulation has been associated with fatigue, reduced cognitive performance, impaired decision-making, and long-term health deterioration. Studies on occupational stress have shown measurable correlations between perceived stress events and salivary cortisol fluctuations, especially in high-demand professions like healthcare, where emotional strain, irregular schedules, and high responsibility can cause repeated acute spikes.

Given its strong correlation with physiological and psychological stress, cortisol is recognized as a primary biomarker for stress assessment. Monitoring its levels is crucial for diagnosing stress-related disorders, guiding treatment, and implementing preventive measures in both clinical and occupational contexts. The COVID-19 pandemic further underscored the need for such monitoring, as many professions experienced intensified workloads and emotional stressors, leading to more frequent cortisol dysregulation [2], [3].

Saliva is a non-invasive method that reflects free, biologically active cortisol, making it useful for monitoring daily rhythms, though it requires sensitive assays due to low concentrations. Hair analysis provides a long-term record of cortisol exposure over several months, which is ideal for assessing chronic stress, but it cannot detect short-term changes. While sweat is promising for wearable sensors, its correlation with blood and salivary levels is still being studied. Blood is the clinical gold standard because it measures both bound and free cortisol, but it's invasive and not practical for continuous monitoring. Urine offers a measure of cumulative cortisol over a 24-hour period, which is useful for long-term load assessment but not for real-time tracking. Lastly, interstitial fluid offers potential for continuous, minimally invasive monitoring via microneedle sensors, although this method is still in its early stages of development.

In current practice, most cortisol detection is performed in laboratories using techniques such as enzyme-linked immunosorbent assays (ELISA), radioimmunoassays (RIA), chemiluminescence assays, or liquid chromatography–mass spectrometry (LC-MS). While these methods are accurate, they are time-consuming, costly, and unsuitable for point-of-care or real-time applications.

Emerging connected health technologies, including plasmonic biosensors, electrochemical immunosensors, and wearable devices, are addressing this gap. These platforms aim to provide rapid, sensitive, and repeatable cortisol detection in ambulatory settings, enabling continuous stress monitoring and personalized health management. In occupational health, integrating such systems could facilitate early intervention, improve workplace safety, and sustain productivity by identifying stress patterns before they manifest as chronic conditions [2], [4].

Concerning the detection of cortisol using fiber optic sensors (FOS), several significant works have been reported in the literature. For instance, Leitão et al. explored a method for detecting cortisol using fiber optic sensors. In one approach, they developed a plasmonic tilted fiber Bragg grating (TFBG) sensor. The TFBG was fabricated by inscribing a tilted grating into a single-mode optical fiber, which couples light from the fiber core into the surrounding cladding. The surface of this sensor was then functionalized with anti-cortisol antibodies. The detection mechanism relies on the principle that the binding of cortisol to these antibodies on the sensor's surface alters the effective refractive index of the cladding modes. This change results in a measurable shift in the TFBG's plasmonic resonance wavelength, with the magnitude of the shift being directly proportional to the cortisol concentration. This sensor achieved a sensitivity of 0.275 ± 0.028 nm/(ng/mL) within a detection range of 0.1–10 ng/mL [5].

In a separate study, Leitão et al. employed a different technique utilizing a SPR-based sensor with an unclad plastic optical fiber (POF). A section of the POF's cladding was removed, and the exposed core was coated with a thin film of a gold-palladium (AuPd) alloy. This metallic layer is essential for the generation of surface plasmons. Similar to the previous method, the AuPd surface was functionalized with anti-cortisol antibodies to ensure specific binding. The SPR phenomenon occurs when light propagating through the fiber excites plasmons in the metal film at a specific angle and wavelength. The binding of cortisol molecules to the antibodies on the surface causes a change in the local refractive index, which in turn leads to a shift in the SPR curve's resonance angle or wavelength. This sensor was characterized for cortisol concentrations between 0.005 and 10 ng/mL, demonstrating a very low LOD of 1 pg/mL [6].

Soares et al. introduced a different approach using a long period grating (LPG) inscribed in a double-clad optical fiber (DCF). This grating couples light from the fiber core into the co-propagating cladding modes, creating distinct attenuation bands in the transmission spectrum. To enhance the sensor's performance, the surface was coated with graphene oxide (GO) before immobilizing the anti-cortisol antibodies. This GO layer provides a high surface area for antibody attachment. The sensor was integrated into a microfluidic channel, allowing for precise control of the sample. The binding of cortisol to the antibodies on the GO-coated surface induced a shift in the LPG's attenuation bands. By monitoring this shift, the cortisol concentration was determined. This method was specifically tuned to the mode transition region to maximize sensitivity and achieved a wide dynamic detection range of 0.01–100 ng/mL with a LOD of 0.06 ng/mL [7].

6.2. Design of the biosensor

Based on the mentioned importance of detecting cortisol, this chapter introduces a novel FOS for its ultrasensitive detection. The sensor leverages LSPR and an engineered nanostructure morphology. A key innovation of this study is the strategic morphological transition from NPs to NSs. This design

choice allows for the precise tuning of the LSPR attenuation band and significantly enhances both the SRI sensitivity and the LOD. A schematic design of the transducer and established biological architecture is reported in Figure 6-1.

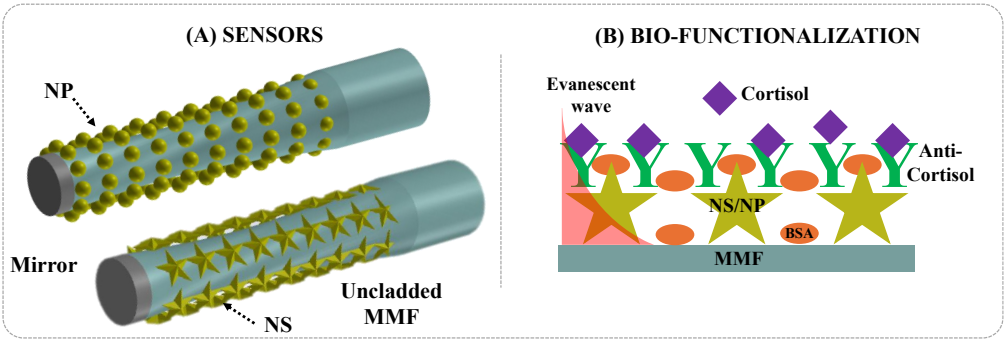

Figure 6-1. Scheme of the sensor: (A) LSPR fiber optic transducer; (B) Biofunctionalized fiber surface.

The fabrication steps and read-out setup for the transducer were detailed in Chapter 4. The following sections focus on the characterization of the nanostructures, presenting their corresponding spectra and the transducer's performance, as well as the testing with biological compounds.

6.3. Characterization of nanostructures

While the comprehensive synthesis steps for both NPs and NSs were detailed in Chapter 4, it is important to note that a silver nitrate concentration of 2 mM was specifically used for the synthesis of the NSs in this investigation. The successful morphological transition from NPs to NSs was confirmed by UV-Vis spectroscopy. The synthesized NPs showed LSPR peak at 525 nm, which red-shifted to 665 nm for the NSs (Figure 6-2). This result clearly demonstrates that the LSPR wavelength can be tuned by altering the nanostructure morphology [8].

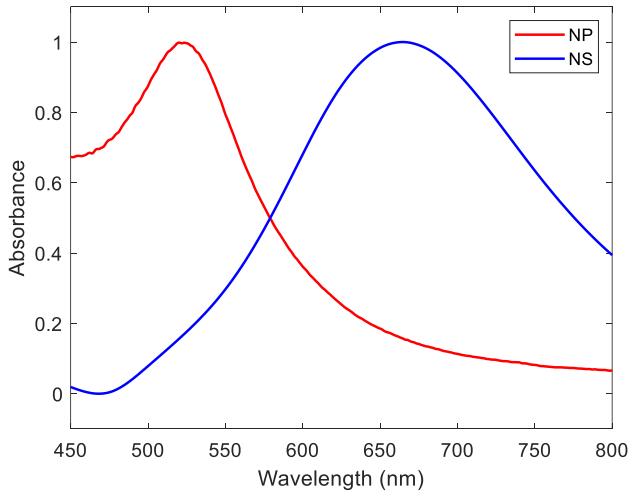

Figure 6-2. UV-Vis spectra of NPs and NSs in solution.

TEM was used to characterize the morphology and size of the synthesized particles. The TEM images of the NPs [Fig 6-3(A)] confirmed their spherical nature, with a mean diameter of 15.84 ± 1.57 nm (n = 400) [Fig 6-3(B)]. In contrast, the NSs [Fig 6-2(D)] displayed a star-like morphology with multiple projections and an average size of 78 ± 15 nm (n = 120) [Fig 6-2(E). Both synthesis processes successfully yielded highly monodisperse samples.

Further characterization with dynamic light scattering (DLS) [Fig 6-3(C,F)] provided insight into the hydrodynamic diameter of the particles in solution. The mean hydrodynamic dimension for the hydrated NPs was 351 ± 122 nm, while for the NSs it was 825 ± 15 nm. These values are significantly larger than the physical diameters measured by TEM due to the presence of adsorbed hydrated layers. The pronounced discrepancy between the TEM and DLS size ratios for the NSs is likely associated with their complex morphology and the resulting interaction with the surrounding hydrated layer.

Furthermore, zeta potential (ZP) analysis was performed to assess particle stability. The NPs exhibited a ZP of –40.89 mV, confirming their high colloidal stability. Conversely, the NSs had a ZP of –11.2 mV, which suggests a lower degree of stability relative to the NPs.

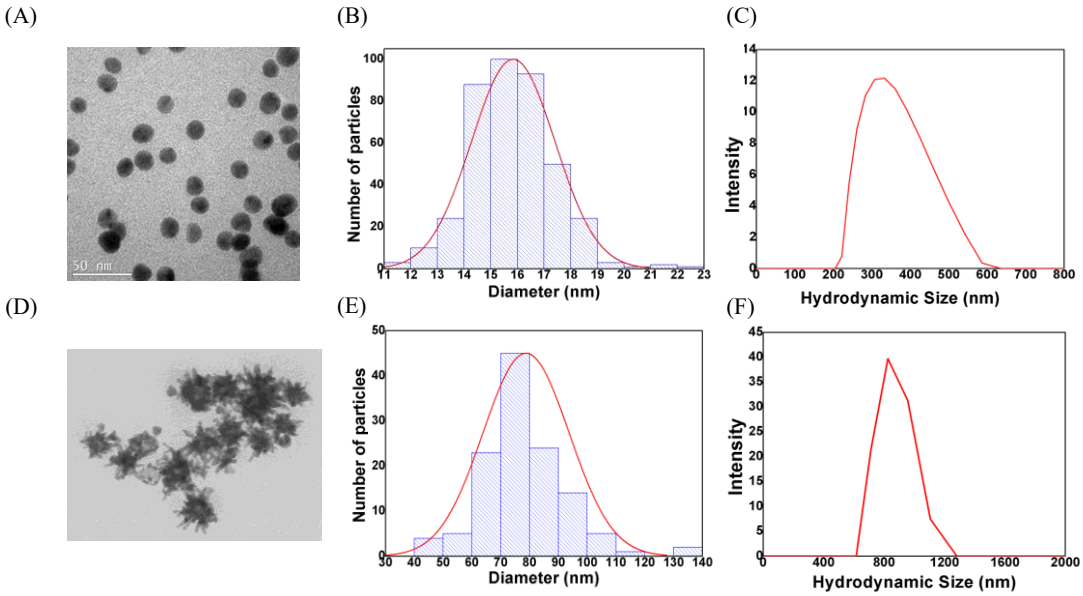

Figure 6-3. Images of (a) NPs and (d) NSs obtained by TEM. Size histogram of (b) NPs and (e) NSs obtained by TEM images. Hydrodynamic size histogram of (c) NPs and (f) NS obtained by DLS.

6.4. Fabrication and characterization of the transducer

Building on the methods detailed in Chapter 4, different transducers were fabricated using the NPs and NSs synthesized as described in Section 4.2.2. The reflection spectra of these transducers, measured in both air and water, are shown in Figure 6-4.

In air, the attenuation bands for the NP-based and NS-based transducers were observed at approximately 535 nm and 615 nm, respectively. When immersed in water, these bands shifted to 545 nm and 665 nm. This corresponds to a spectral red-shift of approximately 10 nm for the NP-based sensor and a much larger shift of 50 nm for the NS-based sensor. These results conclusively demonstrate that manipulating the nanostructure morphology allows for the precise tuning of the spectral position of the attenuation band. More importantly, it significantly enhances the sensitivity to changes in the surrounding environment, as evidenced by the much larger red-shift observed in the NS-based transducer [8], [9], [10], [11].

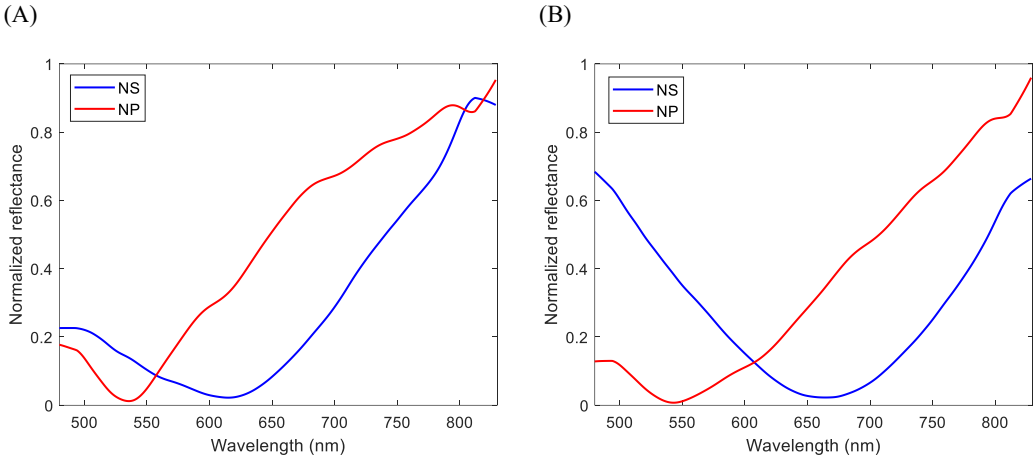

Figure 6-4. Reflected spectra of NS- and NP-based transducers when they are surrounded by (A) air and (B) water.

SEM analysis was conducted on the fabricated samples to assess the quality of the nanostructure deposition. As shown in Figure 6-5(A), the NP-based transducer displays a highly uniform single layer of gold nanoparticles at 200,000x magnification. In comparison, the SEM image of the NS-based transducer (Figure 6-5(B)) reveals a less uniform distribution characterized by clusters of nanostructures. Despite the reduced uniformity of the NS-based device, the clear attenuation bands observed in the corresponding reflection spectra (Figure 6-3) confirmed that the fabrication was successful for our experimental goals.

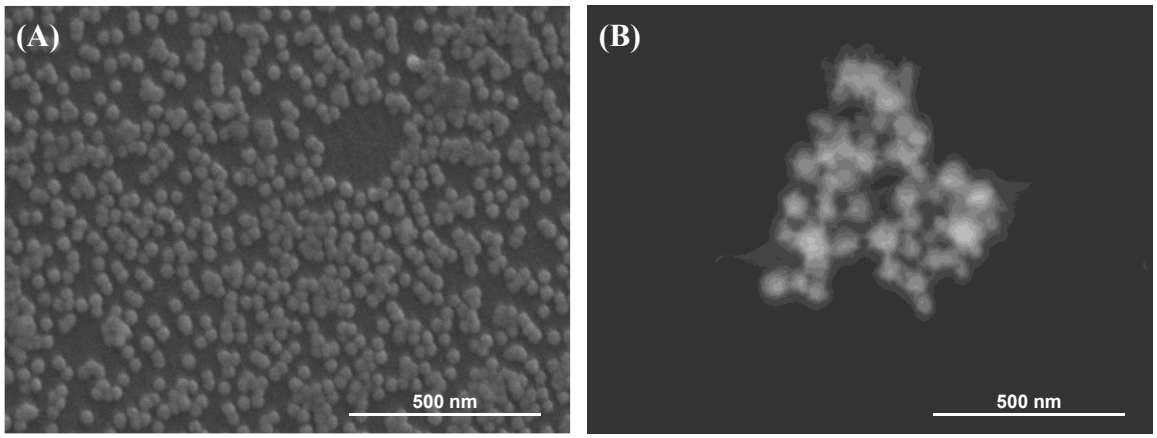

Figure 6-5. Images of (A) NPs and (B) NSs deposited on optical fiber transducer obtained by SEM.

For our comparative analysis, we evaluated the SRI sensitivity of transducers fabricated with NPs and NSs. To do this, we prepared solutions with varying refractive indices, ranging from n = 1.33 to 1.40, by diluting glucose in deionized water. We then sequentially exposed each transducer to these solutions. The SRI sensitivity was determined by tracking the attenuation band and measuring its wavelength shift as the refractive index of the solution changed.

The experimental data, shown by markers in Figure 6-6, are represented by a linear fit with dashed lines. The results demonstrated a clear impact of nanostructure morphology on sensing performance. The NS-based transducer achieved a high sensitivity of 402 nm/RIU, which is significantly greater than the 156 nm/RIU sensitivity of the NP-based transducer. These findings indicate that setting the LSPR to a higher wavelength, a characteristic of the NS-based design, substantially enhances the SRI sensitivity [8], [12], [13]. Furthermore, our achieved sensitivity of 402 nm/RIU is notably superior to other reported fiber optic sensors, such as the 100 nm/RIU sensitivity of a POF sensor and the 193 nm/RIU of a nanodot-based sensor [8], [14].

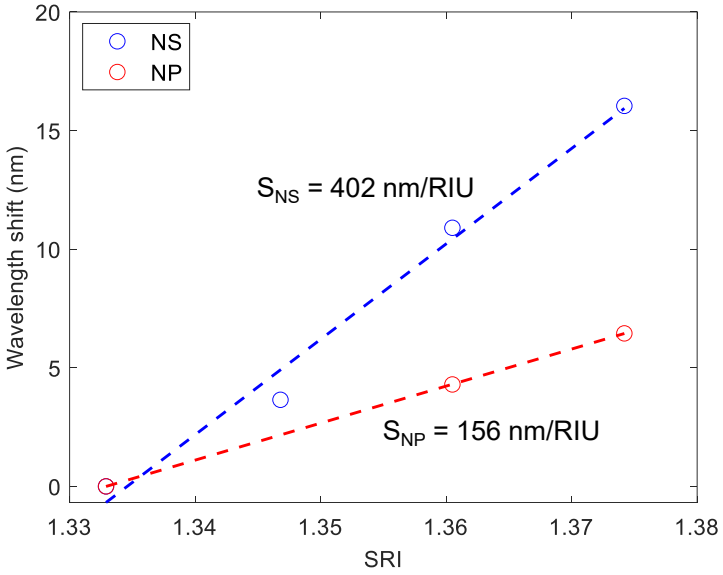

Figure 6-6. Resonance wavelength shift versus the SRI for NS- and NP-based transducers.

6.5. Bio-functionalization

The effect of biofunctionalization process on the sensors is depicted schematically in Figure 6-7(A) and (B). To immobilize anti-cortisol antibodies (Thermo Fisher Scientific, PA1-85347). on the NPs and NSs surfaces, a protocol adapted from Oliveira et al. was used [15]. This procedure involved activating a 100 µg/mL antibody solution with EDC (Sigma Aldrich, 03449) and NHS (Sigma Aldrich, 130672 , followed by a two-hour incubation with the sensor. After a washing and blocking step with Bovine Serum Albumin (BSA), the sensor was ready for testing.

The successful immobilization of antibodies was confirmed by a red shift in the reflection spectra. Specifically, a shift of 0.5 nm was observed for the NP-based device and 1.8 nm for the NS-based device. This difference in spectral shift is consistent with the higher SRI sensitivity of the NS transducer.

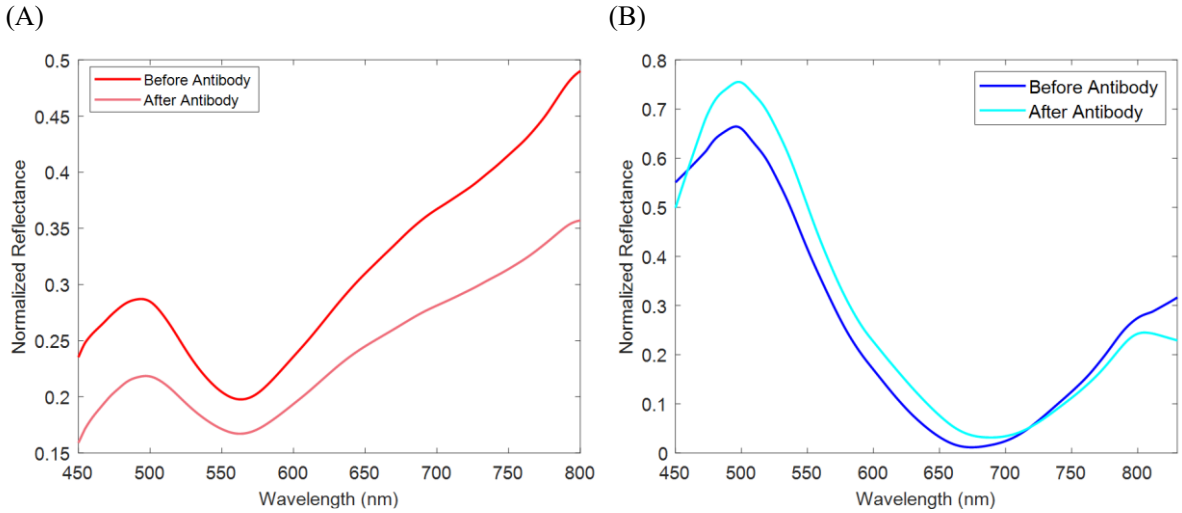

Figure 6-7. Reflected spectra for (A) NP- and (B) NS-based transducer, before and after antibody deposition

6.6. Testing with cortisol

For cortisol testing, each transducer was sequentially immersed in a series of cortisol solutions (Sigma Aldrich, H400) in PBS, with concentrations ranging from 10^{-3} ng/mL to 10^{5} ng/mL (2.76 pM to 0.29 µM). The transducers were incubated in each solution for approximately 20 minutes, followed by a 5-minute rinse in PBS to remove any unbound molecules. Throughout this process, the reflection spectrum was continuously recorded every 30 seconds.

Figures 6-8(A) and 6-9(A) present the normalized reflection spectra for the NP- and NS-based biosensors, respectively, after immersion in each cortisol concentration. The results show clear redshift in the attenuation band as the cortisol concentration increases. This spectral shift confirms the successful binding of cortisol to the immobilized antibodies on the transducer surface, demonstrating the functionality of the biosensors

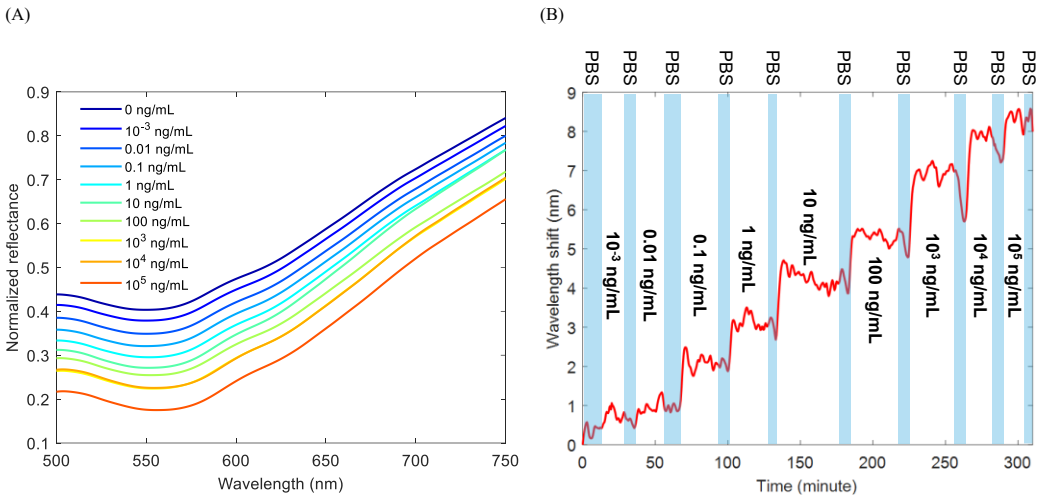

Figure 6-8. Cortisol detection with NP-based biosensor: (A) spectra at different concentration; and (B) sensorgram reporting wavelength shift vs time.

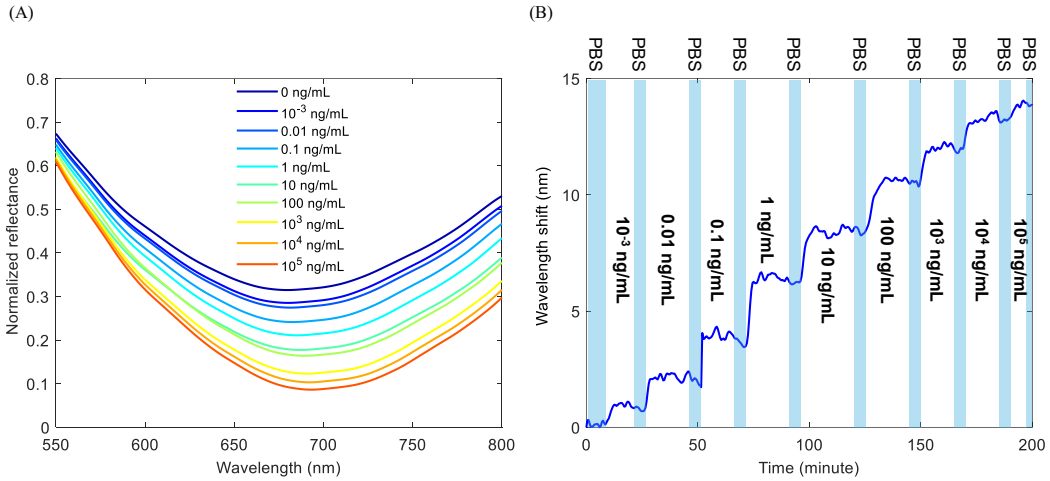

Figure 6-9. Cortisol detection with NS-based biosensor: (A) spectra at different concentration; and (B) sensorgram reporting wavelength shift vs time.

In a more detailed analysis, the real-time wavelength shifts for the NP- and NS-based biosensors are plotted as sensorgrams in Figure 6-8(B) and Figure 6-9(B), respectively. As cortisol molecules bind to the antibodies, the attenuation band in the reflection spectrum shifts towards longer wavelengths. This wavelength shift increases with higher cortisol concentrations due to the greater number of available binding sites. Eventually, the shift begins to stabilize as the antibodies become saturated with cortisol. When the transducer is then washed in PBS to remove unbound molecules, a slight blue-shift occurs, leaving only the signal from the specifically bound cortisol.

While both biosensors exhibit this similar behavior, the NS-based sensor shows a significantly larger shift of approximately 14 nm, whereas the NP-based transducer only shows a shift of about 7.5 nm.

Subsequently, calibration curves for both biosensors were generated and are plotted on a semi-log scale in Figure 6-10, showing the relationship between wavelength shift and cortisol concentration. The baseline for the resonance wavelength was set to the value initially recorded in PBS, representing a zero-analyte concentration.The experiment was repeated twice for transducers functionalized with NP

and NS. For each test, the resonance wavelength shift corresponding to each concentration was calculated by averaging the measured values over approximately 5 minutes of acquisition, yielding about 10 data points per concentration. Each data point shown in the graph represents the mean value, and the associated error bars correspond to the standard deviation obtained from the two repeated experiments for each concentration. To ensure consistent conditions, measurements were taken after the incubation of each concentration in PBS, which eliminated any contributions from the solution's refractive index. The experimental data were fitted using a Logistic function, shown as dotted curves, as described in previous chapters (Equation 4-1) [16].

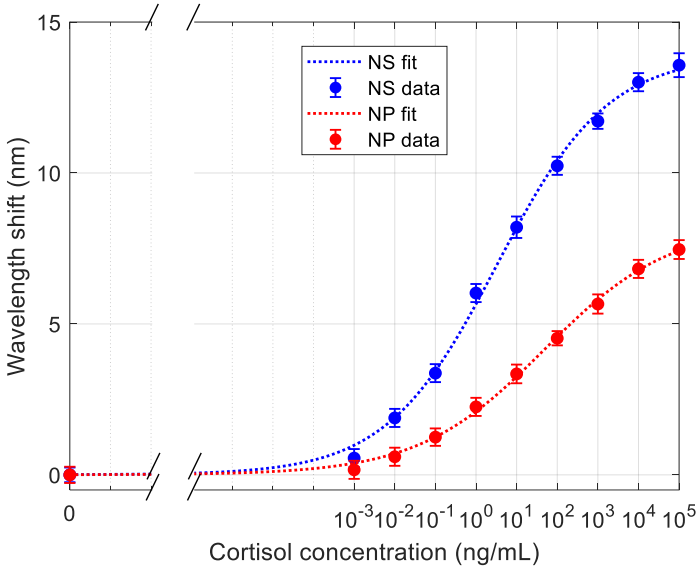

Figure 6-10. Calibration curve of the LSPR biosensors for cortisol measurement. Experimental points are reported with markers while fit with Logistic function are reported with dotted lines.

Table 6-1 summarizes the fitting parameters and the calculated LOD for each transducer. The LOD was determined as mentioned in previous chapter 4, i.e., the target concentration corresponding to the blank measurement response (zero concentration) plus three times its SD. For the NS-based biosensor, the LOD was found to be 0.1 pg/mL (0.276 pM), which is a tenfold improvement over the 1 pg/mL (2.76 pM) LOD of the NP-based biosensor. These results demonstrate that tuning the LSPR band by adjusting the nanostructure morphology not only increases the SRI sensitivity but also, as a direct consequence, reduces the LOD by an order of magnitude.

Table 66-1 Logistic fitting parameters for biosensor calibration curves

Sample	$\Delta\lambda_{MAX}$ [nm]	x_0 [ng/mL]	p	LOD
NP	8.30	48.22	0.2795	1 pg/mL
NS	13.92	3.29	0.3186	0.1 pg/mL

A comparison of the biosensor's performance with other cortisol detection methods is presented in Table 6-2. The LOD for all samples in this study is lower than that of various electrochemical (EC) and other fiber optic sensors [5], [7], [17], [18], [19], [20], [21], [22], [23], [24], [25]. Additionally, this

result demonstrates a larger dynamic range compared to other studies, with a detection range that effectively covers the reference levels for monitoring cortisol in biological fluids. A significant advantage of this configuration is its cost-effectiveness and portability, which makes it a highly promising option for real-world sensing applications in a wide range of scenarios.

Table 6-2. Performance of cortisol biosensors.

Configuration	Range	LOD	Ref.
EC	9.8-49.5 ng/mL	8 ng/mL	[19]
EC	0.03-10^4 ng/mL	10 pg/mL	[21]
Photofuel cell	0.362-362.46 ng/mL	0.318 ng/mL	[20]
LPG+GO	0.01-100 ng/mL	0.06 ng/mL	[7]
LMR	10^{-3}-10^3 ng/mL	25.9 fg/mL	[24]
FBG-SPR	0.1-10 ng/mL	0.1 ng/mL	[5]
SPR	9-250 ng/mL	0.0126 ng/mL	[25]
LSPR-NP	0.01-100 ng/mL	147.9 pg/mL	[17]
LSPR-NP	10^{-3}-10^5 ng/mL	1 pg/mL	Current work
LSPR-NS	10^{-3}-10^5 ng/mL	0.1 pg/mL	Current work

6.7. Selectivity test

The selectivity of the cortisol biosensors was tested against testosterone, a potentially interfering compound, at a concentration of 10 ng/mL [7]. The results, presented in Figure 6-11, show a minimal response to testosterone for both the NS-based transducer (light blue) and the NP-based transducer (light red), with the observed shifts falling largely within the measurement error bars.

In contrast, the wavelength shifts recorded for cortisol (blue for NS-based, red for NP-based) were substantially higher for both transducers. This significant difference in response between the target analyte (cortisol) and the interfering substance (testosterone (Sigma Aldrich, 69240)) confirms the high selectivity of the biosensors for cortisol.

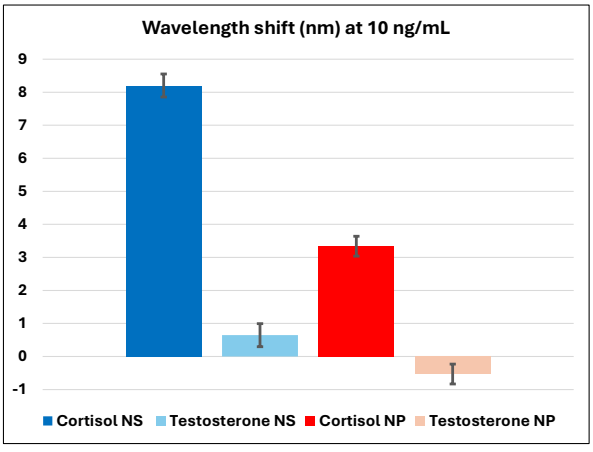

Figure 6-11. Selectivity test comparing the wavelength shift of both NS- and NP-based biosensors for a 10 ng/mL concentration of the target (cortisol) and interfering substance (testosterone).

6.8. Conclusion

In this chapter, we successfully developed and comparatively characterized optical fiber biosensors integrated with golden NPs and NSs for cortisol detection. Building on the transducer design from Chapter 4, which demonstrated tunable SRI and high bio-sensitivity, we applied these principles to a specific target to achieve a lower LOD and a selective sensor, which was tested against testosterone.

Specifically, by transitioning from NPs to NSs, we were able to tune the LSPR resonances wavelength from 545 to 665 nm, resulting in a significant enhancement of the SRI sensitivity from 156 nm/RIU to 420 nm/RIU. Subsequently, the bio-functionalization process, which utilized anti-cortisol antibodies, enabled specific and selective cortisol detection. The resulting biosensors demonstrated excellent performance, with the NS-based device achieving a LOD as low as 0.1 pg/mL (0.276 pM) and a wide dynamic range of 10^{-3}-10^{5} ng/mL (i.e., from 1 pg/mL to 100 µg/mL and 2.76 pM to 0.29 µM), which outperforms many existing methods.

Selectivity tests confirmed minimal interference from substances like testosterone, further highlighting the reliability of the biosensor for practical applications. A notable advantage of this approach is its cost-effectiveness and portability, positioning it as a promising option for real-world sensing applications. The ability to manipulate nanostructure properties to optimize sensor performance opens new avenues for developing highly sensitive and tunable optical biosensors. Future work could focus on further miniaturization and integration of this technology for point-of-care diagnostics and continuous monitoring applications.

6.9. References

[1] A. Moslemi et al., "Cortisol detection via fiber optic biosensor based on localized surface plasmon resonance of gold nanostars," Photonics Res, Oct. 2025, doi: 10.1364/PRJ.571026.

[2] T. Iqbal, A. Elahi, W. Wijns, and A. Shahzad, "Cortisol detection methods for stress monitoring in connected health," Health Sciences Review, vol. 6, p. 100079, Mar. 2023, doi: 10.1016/j.hsr.2023.100079.

[3] T. Gerding and J. Wang, "Stressed at Work: Investigating the Relationship between Occupational Stress and Salivary Cortisol Fluctuations," Int J Environ Res Public Health, vol. 19, no. 19, p. 12311, Sep. 2022, doi: 10.3390/ijerph191912311.

[4] R. Santonocito, R. Puglisi, A. Cavallaro, A. Pappalardo, and G. Trusso Sfrazzetto, "Cortisol sensing by optical sensors," Analyst, vol. 149, no. 4, pp. 989–1001, 2024, doi: 10.1039/D3AN01801F.

[5] C. Leitão et al., "Cortisol In-Fiber Ultrasensitive Plasmonic Immunosensing," IEEE Sens J, vol. 21, no. 3, pp. 3028–3034, 2021, doi: 10.1109/JSEN.2020.3025456.

[6] C. Leitão et al., "Cortisol AuPd plasmonic unclad POF biosensor," Biotechnology Reports, vol. 29, p. e00587, Mar. 2021, doi: 10.1016/j.btre.2021.e00587.

[7] S. Soares et al., "Cortisol detection using a Long Period Fiber Grating Immunosensor coated with Graphene Oxide," Sensors and Actuators Reports, vol. 9, p. 100279, Jun. 2025, doi: 10.1016/j.snr.2024.100279.

[8] A. Moslemi et al., "Highly sensitive gold nanostar based optical fiber sensor with tunable plasmonic resonance," Sensors and Actuators Reports, p. 100326, Apr. 2025, doi: 10.1016/j.snr.2025.100326.

[9] N. Cennamo et al., "Localized Surface Plasmon Resonance with Five-Branched Gold Nanostars in a Plastic Optical Fiber for Bio-Chemical Sensor Implementation," Sensors, vol. 13, no. 11, pp. 14676–14686, Oct. 2013, doi: 10.3390/s131114676.

[10] K. Ueno, S. Juodkazis, M. Mino, V. Mizeikis, and H. Misawa, "Spectral Sensitivity of Uniform Arrays of Gold Nanorods to Dielectric Environment," The Journal of Physical Chemistry C, vol. 111, no. 11, pp. 4180–4184, Mar. 2007, doi: 10.1021/jp068243m.

[11] C. Zhuang, Y. Xu, N. Xu, J. Wen, H. Chen, and S. Deng, "Plasmonic Sensing Characteristics of Gold Nanorods with Large Aspect Ratios," Sensors, vol. 18, no. 10, p. 3458, Oct. 2018, doi: 10.3390/s18103458.

[12] Y. Lin, Y. Zou, Y. Mo, J. Guo, and R. G. Lindquist, "E-Beam Patterned Gold Nanodot Arrays on Optical Fiber Tips for Localized Surface Plasmon Resonance Biochemical Sensing," Sensors, vol. 10, no. 10, pp. 9397–9406, Oct. 2010, doi: 10.3390/s101009397.

[13] Y. Zhang, L. Ding, J. Zhao, X. Jiang, and F. Ma, "Localized Surface Plasmon Resonance- Based Fiber Optic Biosensor for Acetylcholine Detection," IEEE Sens J, vol. 23, no. 21, pp. 25987–25995, Nov. 2023, doi: 10.1109/JSEN.2023.3304619.

[14] Y. Lin, Y. Zou, and R. G. Lindquist, "A reflection-based localized surface plasmon resonance fiber-optic probe for biochemical sensing," Biomed Opt Express, vol. 2, no. 3, p. 478, Mar. 2011, doi: 10.1364/BOE.2.000478.

[15] J. P. de Oliveira, F. Burgos-Flórez, I. Sampaio, P. Villalba, and V. Zucolotto, "Label-free electrochemical immunosensor for Ochratoxin a detection in coffee samples," Talanta, vol. 260, p. 124586, Aug. 2023, doi: 10.1016/j.talanta.2023.124586.

[16] A. Moslemi, L. Sansone, F. Esposito, S. Campopiano, M. Giordano, and A. Iadicicco, "Optical fiber probe based on LSPR for the detection of pesticide Thiram," Opt Laser Technol, vol. 175, p. 110882, Aug. 2024, doi: 10.1016/j.optlastec.2024.110882.

[17] X. Liu et al., "SFFO Cortisol Biosensor: Highly Sensitive S-Flex Fiber Optic Plasmonic Biosensor for Label-Free Cortisol Detection," IEEE Sens J, vol. 24, no. 2, pp. 1494–1501, Jan. 2024, doi: 10.1109/JSEN.2023.3336414.

[18] P. Manickam, S. K. Pasha, S. A. Snipes, and S. Bhansali, "A Reusable Electrochemical Biosensor for Monitoring of Small Molecules (Cortisol) Using Molecularly Imprinted

Polymers," J Electrochem Soc, vol. 164, no. 2, pp. B54–B59, Dec. 2017, doi: 10.1149/2.0781702jes.
[19] S. M. Mugo, W. Lu, and S. Robertson, "A Wearable, Textile-Based Polyacrylate Imprinted Electrochemical Sensor for Cortisol Detection in Sweat," Biosensors (Basel), vol. 12, no. 10, p. 854, Oct. 2022, doi: 10.3390/bios12100854.
[20] Y. Zhu, X. Yao, K. Yan, Y. Chen, and J. Zhang, "A ratiometric self-powered aptasensor for simultaneous detection of cortisol and progesterone based on spatially resolved tri-channel photofuel cell," Biosens Bioelectron, vol. 223, p. 115020, Mar. 2023, doi: 10.1016/j.bios.2022.115020.
[21] B. J. Sanghavi et al., "Aptamer-functionalized nanoparticles for surface immobilization-free electrochemical detection of cortisol in a microfluidic device," Biosens Bioelectron, vol. 78, pp. 244–252, Apr. 2016, doi: 10.1016/j.bios.2015.11.044.
[22] R. E. Fernandez et al., "Disposable aptamer-sensor aided by magnetic nanoparticle enrichment for detection of salivary cortisol variations in obstructive sleep apnea patients," Sci Rep, vol. 7, no. 1, p. 17992, Dec. 2017, doi: 10.1038/s41598-017-17835-8.
[23] G. Karuppaiah, M.-H. Lee, S. Bhansali, and P. Manickam, "Electrochemical sensors for cortisol detection: Principles, designs, fabrication, and characterisation," Biosens Bioelectron, vol. 239, p. 115600, Nov. 2023, doi: 10.1016/j.bios.2023.115600.
[24] S. P. Usha, A. M. Shrivastav, and B. D. Gupta, "A contemporary approach for design and characterization of fiber-optic-cortisol sensor tailoring LMR and ZnO/PPY molecularly imprinted film," Biosens Bioelectron, vol. 87, pp. 178–186, Jan. 2017, doi: 10.1016/j.bios.2016.08.040.
[25] X. Wang, X. Sun, Y. Hu, L. Zeng, and J. Duan, "Plasmonic dual-parameter optical fiber sensor for cortisol and glucose detection," Optik (Stuttg), vol. 284, p. 170933, Aug. 2023, doi: 10.1016/j.ijleo.2023.170933.

7. Chapter 7
Glyphosate detection by TFBG coated with gold nanostructures

This chapter presents another fiber-optic biosensor, but with a transducer different from the previous ones: a tilted fiber Bragg grating (TFBG) inscribed in single-mode fiber. In line with the topics of this thesis, the TFBG was coated with gold nanostructures (NPs and NSs) as a novel approach to enhance sensitivity. The device was further functionalized with specific antibodies and tested for the detection of glyphosate, a harmful herbicide, with significant enhancement on the state-of-the-art. This work was primarily carried out during my exchange period at the University of Aveiro in Portugal.

7.1. Introduction

Glyphosate is a widely used, broad-spectrum systemic herbicide and crop desiccant primarily employed in agriculture to control weeds. Since its introduction in the 1970s, it has become one of the most commonly applied herbicides worldwide due to its efficacy in killing a broad range of plants, its relatively low toxicity to non-target organisms, and its compatibility with genetically modified crops engineered for glyphosate resistance. Chemically, glyphosate is a phosphonomethyl derivative of the amino acid glycine. It functions by inhibiting the enzyme 5-enolpyruvylshikimate-3-phosphate synthase (EPSPS), which is essential in the shikimate pathway responsible for the biosynthesis of aromatic amino acids in plants. Because mammals lack this pathway, glyphosate was initially regarded as having low toxicity. However, concerns about environmental persistence, bioaccumulation, of glyphosate, and its

potential health effects, including carcinogenicity, have prompted extensive research into its detection in environmental and food samples [1], [2].

Detecting glyphosate is challenging due to its high polarity, low volatility, and lack of strong chromophores. Over the years, multiple analytical techniques have been developed to identify and quantify glyphosate residues with sensitivity and selectivity suitable for regulatory, environmental, and health monitoring.

Chromatographic Techniques, methods such as liquid chromatography (LC) and gas chromatography (GC), often coupled with mass spectrometry (MS), are considered gold standards. LC-MS/MS is highly sensitive and selective for glyphosate and its main metabolite AMPA (aminomethylphosphonic acid), offering a limit of detection of approximately 0.076 µg/mL with a dynamic range of 0.1 to 10 µg/mL. GC requires derivatization of glyphosate to increase volatility, which can complicate sample preparation [3].

Enzymatic Inhibition Assays, these bioassays exploit glyphosate's mode of action by measuring the inhibition of EPSPS or related enzymes. Enzymatic assays typically use spectroscopic techniques to detect changes in enzyme activity. These methods are relatively simple and cost-effective for screening. For example, a UV/Vis enzymatic inhibition assay has a limit of detection around 2 mg/L and a dynamic range of 3.4 to 20 mg/L. A fluorimetric version is more sensitive, with a dynamic range of 7 to 1000 µg/L [4].

Immunoassays techniques such as ELISA (enzyme-linked immunosorbent assay) and fluorescent immunoassays use antibodies specific to glyphosate. Immunosensors can achieve low limits of detection and are suitable for field applications due to their portability and rapid response. A typical immunoassay can have a limit of detection of around 0.09 ng/mL with a dynamic range of 0 to 100 ng/mL. An electrochemical impedance immunosensor offers a limit of detection of approximately 0.1 ng/mL with a dynamic range of 0.1 to 72 ng/mL [5].

Electrochemical Biosensors, these sensors utilize biorecognition elements coupled with electrical transducers to detect glyphosate through changes in current, voltage, or impedance. For instance, sensors based on lipopeptides can detect glyphosate at nanomolar levels, with a reported limit of detection around 24 nM and a dynamic range in the nanomolar range. Electrochemical sensors are attractive due to their sensitivity, ease of miniaturization, and potential for real-time monitoring [6].

Fluorescent and Colorimetric Probes, Novel sensors using nanomaterials and dyes modulated by glyphosate binding have been developed. For example, a Cu^{2+}-modulated PDOA fluorescent probe can achieve a limit of detection of approximately 1.8 nM, with a dynamic range in the low nM to µM range. A colorimetric sensor using an aptamer and DNA zyme has a limit of detection of around 13 nM and a dynamic range in the nanomolar range. These methods are promising for rapid and on-site detection [7].

Several recent articles demonstrate the use of fiber-optic sensors for glyphosate detection, leveraging the advantages of optical fiber systems such as immunity to electromagnetic interference, portability,

low cost, and potential for in situ real-time detection. In recent investigations into novel detection methods for glyphosate, a number of innovative sensors have been developed. For example, Zhang et al. [8] created a fiber optic biosensor that leverages LSPR. This unique design was fabricated by fusing seven-core and single-mode fibers and tapering the sensing area. The sensor's performance was further enhanced using gold nanoparticles for LSPR, alongside multi-walled carbon nanotubes (MWCNTs) with cerium oxide nanorods (CeO2-NRs) to increase the surface area and improve enzyme adhesion, resulting in a LOD of 1.94μM.

Based on this, other researchers have explored different approaches. Sasikumar et al. [9], for instance, introduced dissolvable green fluorescent carbon dots (G-CDs) as a fluorometric probe. Their method relies on glyphosate selectively quenching the fluorescence of these G-CDs, demonstrating a low LOD of 7.44μg/L (0.044μM). Similarly, Bai et al. [10] developed a ratiometric fluorescent sensing platform using an enoxacin-embedded Eu(III) metal-organic framework (ENX@EuMOF). This platform provides dual fluorescent signals, with a decrease at 613 nm and an increase at 520 nm in response to glyphosate, achieving a LOD of 0.35mg/L within a sensing range of 5 to 100mg/L.

Optical detection has also been explored through plasmonic sensors. Bombardia et al. [11] developed a plasmonic plastic optical fiber sensor that was enhanced with cysteamine-encapsulated gold nanoparticles. This U-shaped sensor demonstrated an average sensitivity of −0.2nm/μM for glyphosate concentrations up to 50μM, with a resolution of 0.3μM. In a different study, Torul et al. [34, 35] utilized SERS with 4-mercapto-phenylboronic acid-derivatized gold nanorods, achieving a very low LOD of 16.9×10^{-6}μg/L. This SERS substrate was successfully applied to determine glyphosate concentrations in tomato juice samples.

Moving beyond optical methods, Zouaoui et al. [12] developed a highly sensitive impedimetric microsensor. This sensor features a double-layered imprinted polymer film of molecularly imprinted chitosan on an electropolymerized polypyrrole layer doped with cobaltabis (dicarbollide) ions. This innovative design demonstrated a broad detection range from 0.31pg/mL to 50ng/mL and achieved an exceptionally low LOD of 1fg/mL for glyphosate.

7.2. Tilted Fiber Bragg Grating working principle

TFBGs are a special type of fiber grating where the planes of refractive index modulation are inscribed at a small angle relative to the fiber axis. This structural modification distinguishes them from conventional fiber Bragg gratings, which primarily couple the guided core mode to its backward counterpart, resulting in a single narrow Bragg resonance. In a TFBG, the tilt of the grating enables strong and efficient coupling of the core mode into a broad set of backward-propagating cladding modes. Because cladding modes extend to the outer boundary of the fiber and interact with the surrounding medium, their resonances are inherently sensitive to changes in the external refractive

index. This property makes TFBGs particularly attractive for applications in refractometry and biochemical sensing.

The distribution of cladding mode resonances in a TFBG spectrum is governed by a phase-matching condition between the forward core mode and the backward cladding modes. This condition selects a large number of discrete wavelengths where coupling is allowed, which appear as sharp resonances in the transmission spectrum. Unlike long period gratings, where coupling is forward and the resonances are broader, TFBGs provide contra-directional coupling to cladding modes, producing narrow and densely spaced resonances over a wide spectral range. The Bragg resonance itself, which corresponds to core-to-core coupling, remains largely insensitive to changes in the surrounding medium and can be used as a stable reference.

Cladding mode resonances, on the other hand, are highly sensitive to variations in the surrounding refractive index. As the refractive index of the external medium increases, the effective indices of cladding modes change, causing their resonant wavelengths to shift. This shift is particularly pronounced near the cutoff region, where the effective index of a cladding mode approaches that of the surrounding medium. In this regime, small variations in refractive index lead to large spectral shifts, sometimes reaching tens of nanometers per refractive index unit. However, as the mode becomes weakly guided and eventually leaky, its resonance depth decreases and the feature disappears from the spectrum [13], [14], [15].

Experimental studies have quantified the refractometric sensitivity of bare TFBGs. In an investigation of a 10° bare TFBG, Korganbayev and et al. [16] measured sensitivities in the range of 2–12 nm/RIU, depending on the cladding mode order and spectral position. Complementary work on 6° bare TFBGs by Trono et al. [17] confirmed this trend, reporting values of 5–15 nm/RIU when the surrounding refractive index was varied between 1.333 and 1.465. These results consistently show that while bare TFBGs provide measurable refractive index sensitivity, they are limited compared to coated or etched configurations, which can yield sensitivities an order of magnitude higher. Nevertheless, the bare TFBG serves as a robust baseline platform, combining stable Bragg reference peaks with cladding mode resonances that are directly responsive to the environment.

Moreover, when a thin gold layer is deposited on a TFBG, the cladding modes of the grating can efficiently interact with the surrounding medium through the excitation of SPR. This phenomenon occurs when P-polarized light, having its electric field parallel to the metal interface, couples with collective electron oscillations at the gold–dielectric boundary. As a result, the transmission spectrum of the TFBG exhibits spectral features that are related to SPR effect and their demodulation has been the topic of different works in order to enhance the sensitivity. The sensing behavior strongly depends on the thickness and morphology of the gold coating [18], [19], [20], [21]. Miguel Vidal et al. [22] studied how different analysis methods affect the performance of Au coatedTFBGs for detecting the heart failure biomarker NT-proBNP. They found that tracking the lower envelope of the signal provided the lowest detection limits: 0.75 ng/mL for bare TFBGs and 0.19 ng/mL for plasmonic TFBGs. The

research highlights the importance of the analysis method in biosensor performance.In the other example, Ziqiao Ren and et al. [23] proposed a plasmonic TFBG sensor to detect cadmium ions (Cd^{2+}). The sensor, coated with a thin gold film, uses glutathione (GSH) to bind with Cd2+. The researchers enhanced sensitivity by using GSH-modified gold nanoparticles, achieving a limit of detection of ~0.06 nM, which is two orders of magnitude better than previously reported fiber grating-based Cd^{2+} sensors. The sensor also demonstrated a wide dynamic range from 0.01 nM to 1000 nM.: as an example, ultrathin layers (≈5 nm) generate hypersensitive responses due to incomplete coverage and localized plasmonic effects, whereas continuous coatings around 30–35 nm enable efficient SPR excitation with greatly enhanced sensitivity. For instance, gold-sputtered TFBGs with ~35 nm thickness demonstrated an amplitude sensitivity as high as 693 dB/RIU and enabled the detection of cytokeratin 17 at femtomolar concentrations (LOD ≈ 10^{-12} g/mL). These results confirm that coating TFBGs with optimized gold layers transforms them into powerful plasmonic biosensors, where refractometric and biochemical sensitivities are governed by the interplay between cladding mode coupling, polarization effects, and the gold layer configuration [19]. In other example, Wang et al. [18] proposed a GO–SPA co-modified gold-coated TFBG-SPR biosensor for the detection of human IgG. The sensor achieved a sensitivity of 0.096 dB/(μg/mL) with a detection limit of 0.5 μg/mL, outperforming devices modified only with GO or SPA. This approach enabled highly oriented antibody immobilization and efficient antigen–antibody binding in the range of 30–100 μg/mL. In other job, Fang Wang et al. [24] developed a TFBG-SPR DNAzyme biosensor with Au film and GNPs for Pb^{2+} detection. The sensor achieved an ultralow detection limit of ~8.56 pM with a wide dynamic range from 10^{-11} M to 10^{-6} M, showing excellent selectivity against other metal ions. Clinical serum tests further confirmed its practicality for portable and point-of-care applications.

7.3. Fiber optic readout setup

The experimental readout setup is depicted in Figure 7-1. The system is primarily comprised of a Bragg Meter (BSI-108, B-SENS), which serves as both the light source and the spectral analyzer for the light transmitted through the sensor. The Bragg Meter operates within a wavelength range of 1510-1590 nm. For this work, two different channels of the Bragg Meter were employed to inject light and measure the transmitted signal after the TFBG. An in-line polarizer (Thorlabs ILP1550SM) and a polarization controller (Thorlabs FPC562) were also included in the incident light path, as was an isolator on the transmitted light path to prevent signal disturbance from back-reflections. The TFBG itself was secured at one end, while a stable 30 g weight was hung from the other to maintain constant stretching. This measure is critical for preventing any undesirable wavelength shifts that could arise from variations in tension on the fiber.

TFBGs were fabricated in single-mode fiber (Corning SMF-28) using an intense pulsed ultraviolet laser (193 nm) and a phase mask [14]. The grating planes were inscribed at a 10° tilt relative to the fiber normal axis. This tilt angle directs light into the cladding, exciting cladding modes with an effective refractive index close to that of water [25]. In this article, the fiber in this state is referred to as bare fiber. Additionally, TFBG with nanostructure deposition of spherical gold NPs and NSs was also employed in this work according to the description reported in the next section.

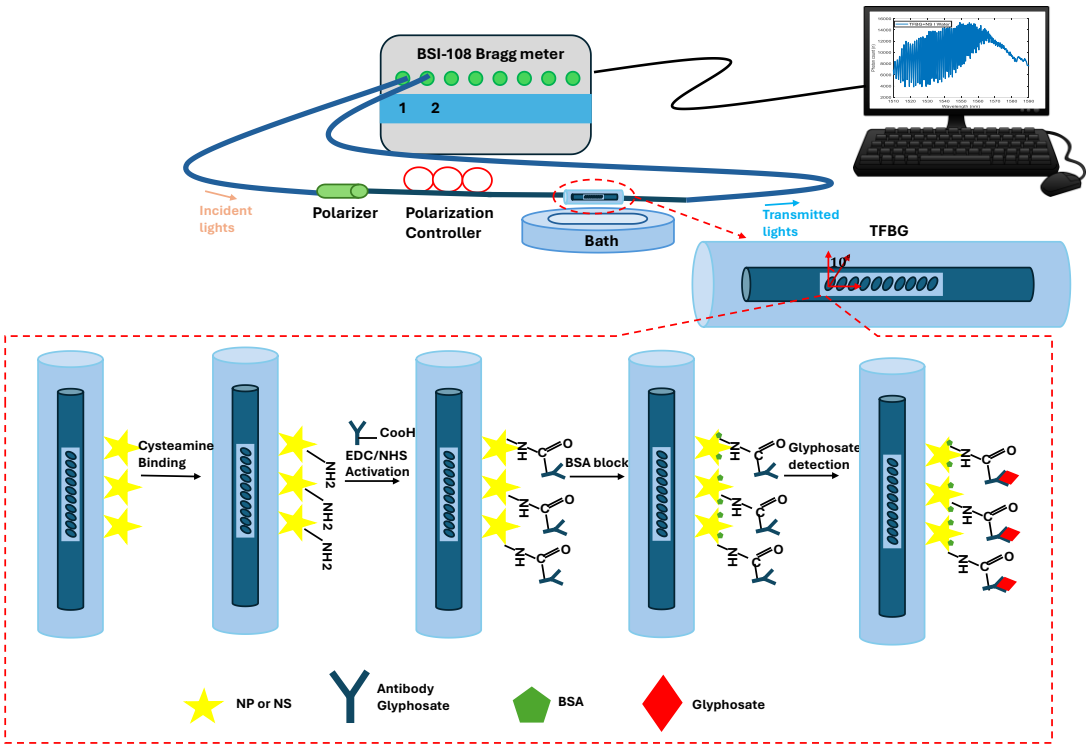

Figure 7-1. Schematic of read-out setup and bio-functionalization and target detection steps on the TBFG.

7.4. Nanostructure synthesis and characterization

While the comprehensive synthesis steps for both NPs and NSs are detailed in Chapter 4, it is important to note that a silver nitrate concentration of 2 mM was specifically utilized for the NS synthesis in this investigation. The successful morphological transition from NPs to NSs was confirmed via UV-Vis spectroscopy. The synthesized NPs exhibited a localized surface plasmon resonance (LSPR) peak at 522 nm, which red-shifted to 680 nm for the NSs (Figure 7-2). This result clearly demonstrates that the LSPR wavelength can be precisely tuned by altering the nanostructure morphology [26].

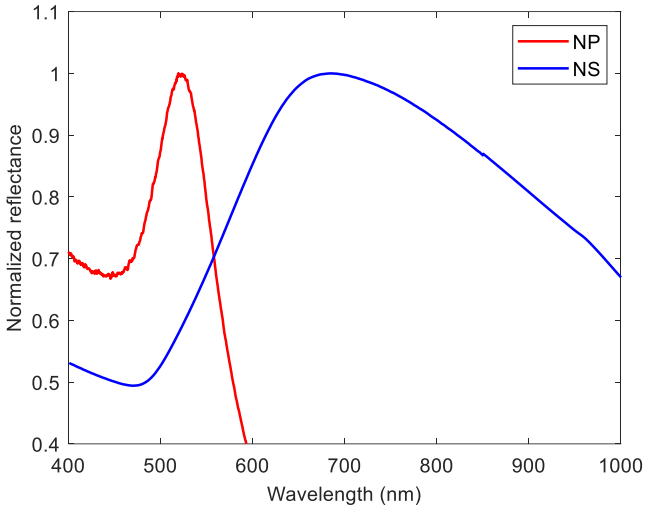

Figure 7-2. Absorbance UV-Vis spectra of different synthesized NPs and NSs in water solution.

7.5. Nanostructure deposition

Following the protocol detailed in Chapter 4 for the deposition of nanostructures on the TFBG, an initial surface salinization is essential, as the silica fiber surface does not naturally attract these nanostructures. The process begins with a 20-minute immersion in piranha solution (3:1 volume ratio H2SO4:H2O2), followed by a deionized water rinse. The fiber is then submerged for two hours in a 5% w/w solution of APTES in acetone. After this, it is washed with acetone and dried overnight. To remove any unbound APTES molecules, the fiber is washed several times with deionized water. Once the salinization is complete, the transducer is immersed in a nanostructure solution for 5 hours, allowing the nanostructures to graft onto the surface via sulfhydryl (SH) groups.

In Figure 7-3, the transmission spectra in a water environment for a bare TFBG, NP-TFBG, and NS-TFBG are presented following the deposition procedure. All spectra exhibit the typical attenuation bands of a TFBG due to power coupling that excites the cladding modes. While the gold NPs and NSs only slightly affect the spectral position of the fringes, the fringe contrast diminishes. This phenomenon occurs because, upon gold deposition, the evanescent wave of the excited cladding modes interacts with the gold nanostructures. The subsequent excitation of plasmonic phenomena results in additional transmission loss and a diminished resonance amplitude for specific modes, as discussed in the relevant literature [27], [28].

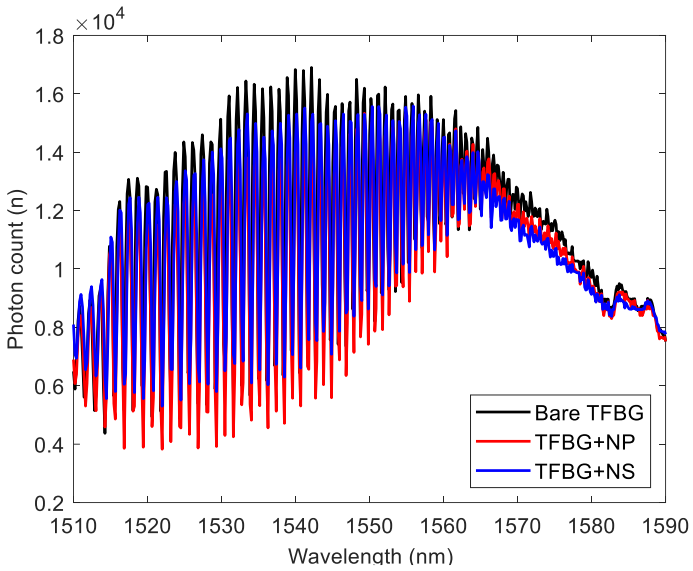

Figure 7-3. Transmission spectra of a TFBG sensor with NS deposition across various surrounding refractive index media.

7.6. SRI characterization

The bulk SRI sensitivity of the optical fiber sensors was investigated as an initial test to evaluate the transducer's performance after fabrication. Measurements were conducted in solutions of varying percentages of deionized water and glucose, which spanned an SRI range of 1.33–1.38. The SRI of these solutions was precisely measured using an Abbe refractometer with a resolution of 2×10^{-4}.

Figure 7-4 illustrates, by way of example, the spectral changes observed in the NS-coated TFBG transducer in response to SRI variations. Two main effects are observable [29]: (i) a slight red shift (on the order of a few picometers) of the cladding mode resonances due to changes in coupling conditions, and (ii) a more evident red shift of the cut-off wavelength of the cladding modes. In the context of biosensing, we primarily focus on the first phenomenon, the shift of a specific cladding mode resonance despite the larger shift of the cut-off region. For this study, we focused on the mode at approximately 1514 nm, which corresponds to the cut-off mode in water. It should be noted that the cut-off condition no longer holds when the SRI changes, as we are referring to the same cladding mode.

The evolution of this resonance with varying SRI is shown in Figure 7-4(a)–(c) for the bare TFBG, NP-coated TFBG, and NS-coated TFBG, respectively. The corresponding sensitivity curves are summarized in Figure 7-4(d), which clearly demonstrates that the deposition of gold nanostructures significantly enhances the SRI sensitivity of this mode. The bare TFBG exhibits a sensitivity of 2041.8 pm/RIU at 1514 nm, which increases to 5499.2 pm/RIU in the NP-coated TFBG and to 7302.2 pm/RIU in the NS-coated TFBG. These results represent sensitivity enhancements of approximately 2.7× and 3.6×, respectively, compared to the bare TFBG.

This improvement is attributed to the increased interaction of the evanescent field with the surrounding medium due to the presence of metallic nanostructures, a phenomenon often described as a plasmonic-like effect. Although the sensor operates at a wavelength far from the typical plasmonic resonance of gold, the nanostructures still enhance the local field, leading to improved sensitivity.

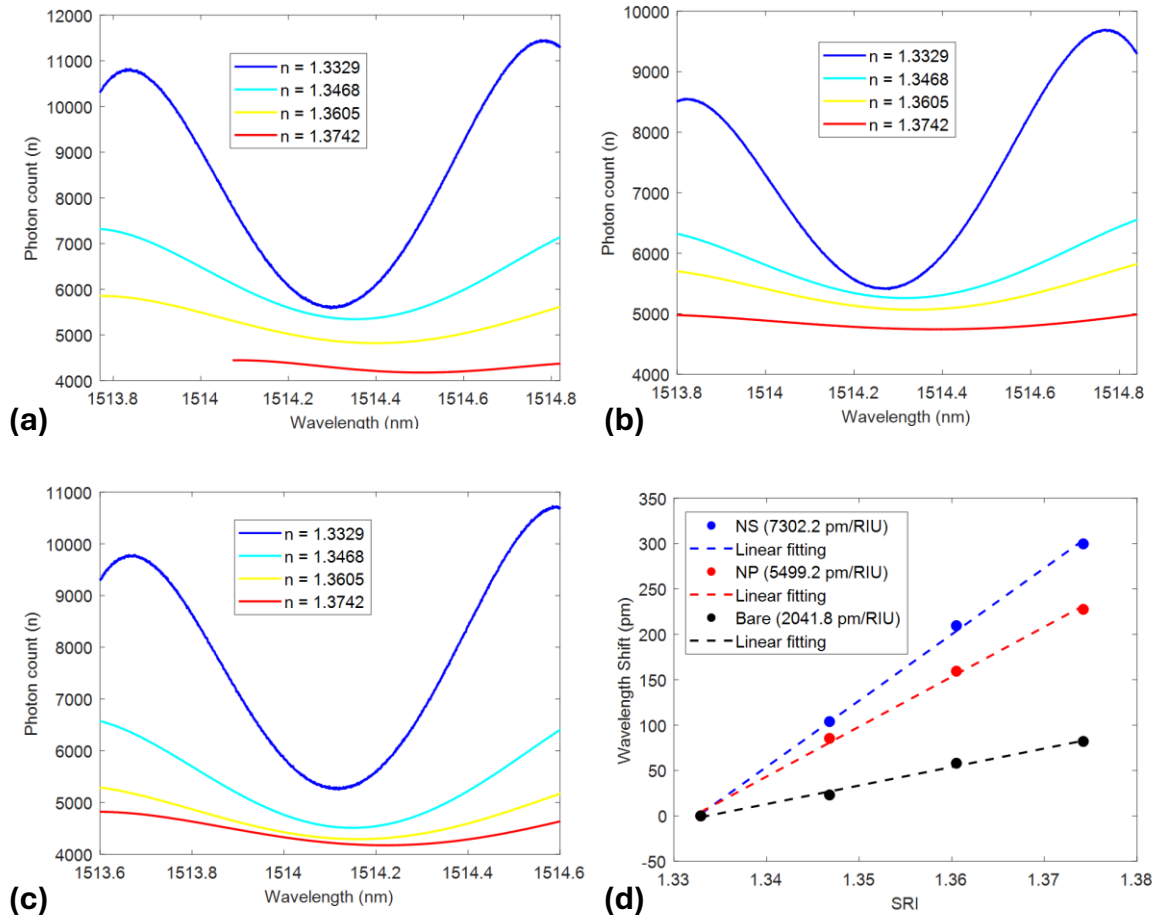

Figure 7-4. The evolution of the 1514 nm mode spectrum with varying SRI for (A) TFBG+NS, (B) TFBG+NP, and (C) a Bare TFBG. (D) The SRI sensitivity for all three samples.

Although not the primary focus of this study, we also investigated the SRI sensitivity of the actual cut-off wavelength. Results indicate that gold nanostructure deposition has a negligible effect in this regard. Specifically, the SRI sensitivities of the cut-off wavelength were measured to be 396.4 nm/RIU for the bare TFBG, 417.5 nm/RIU for the NP-coated TFBG, and 443.2 nm/RIU for the NS-coated TFBG. This corresponds to an increase of only about 12% for the NS-coated sensor compared to the bare fiber [13], [29], [30], [31]. In Figure 7-5(A) Transmission spectrum of TFBG+NS in different SRI is shown as an example and in Figure 7-5(B) SRI sensitivity of TFBG+NS, TFBG+NP and bare TFBG can be seen.

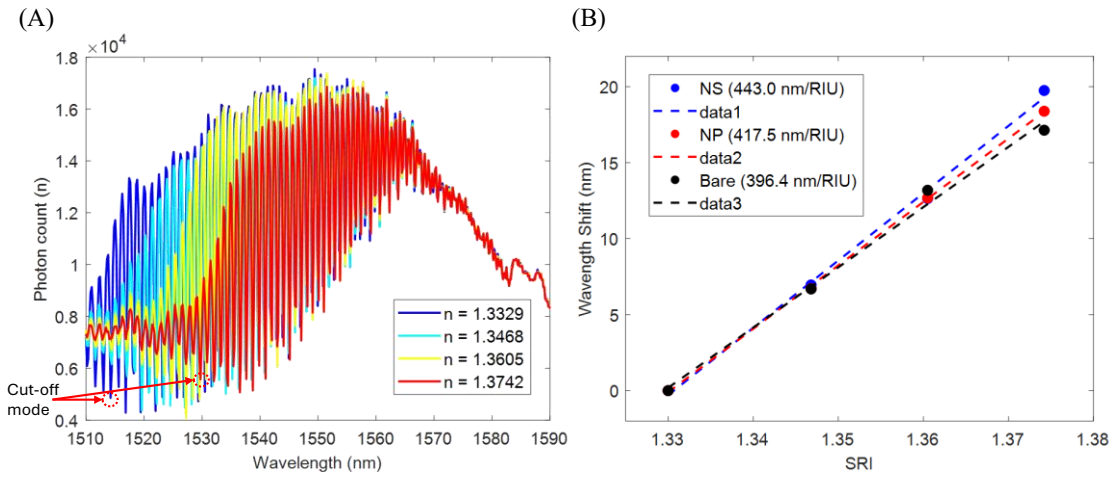

Figure 7-5. (A) Transmission spectrum of TFBG+NS in different SRI. (B) SRI sensitivity of TFBG+NS, TFBG+NP and bare TFBG.

7.7. Bio-functionalization

The process of bio-functionalization is a critical step in creating a biosensor. Following the same protocol as detailed in Chapter 5, and as shown schematically in Figure 7-1, the procedure begins by immersing the transducer in a 20 mM cysteamine solution for 18 hours to modify the surface of the nanoparticles with amine (−NH2) groups. This step is crucial for effective antibody immobilization. The transducer is then thoroughly rinsed with deionized water.

Subsequently, anti-glyphosate antibodies are immobilized using an EDC-NHS covalent coupling system. A solution containing 100 µg/mL of antibodies (AS13 2739, 5 mg/mL) is first activated with 8 mM EDC and 5 mM NHS for one hour. This activated antibody solution is then incubated with the transducer for two hours to allow for covalent binding. To remove any unbound antibodies, the sensor is washed with PBS. To prevent non-specific binding, the biosensor is then blocked by incubating it in a 0.5% BSA solution for 30 minutes, followed by a final rinse with PBS. This conjugation process ensures the proper orientation of the antibodies and preserves their binding affinity with glyphosate (Sigma-Aldrich, Taufkirchen, Germany) [32].

Figures 7-6(A), (B), and (C) provide a zoomed-in view of the mode spectral region at different stages of bio-functionalization for TFBG+NS, TFBG+NP, and bare TFBG samples. The sequential grafting of cysteamine, antibodies, and BSA onto the sensor surface increases the local refractive index, leading to a red shift in the spectrum [15]. This observed shift serves as clear evidence of the successful immobilization of the antibody. The magnitude of the shift is directly related to the refractive index variation at the sensor surface and, consequently, to the amount of grafted biomolecules. Notably, the presence of gold nanostructures, particularly in NP- and NS-coated TFBGs, enhances this effect by providing a greater number of active sites for molecule attachment. This facilitates more effective functionalization and a more pronounced spectral response. The wavelength shift values for

biofunctionalization were highest for the TFBG+NS and lowest for the bare TFBG. This is in agreement with the SRI sensitivities discussed in the previous section.

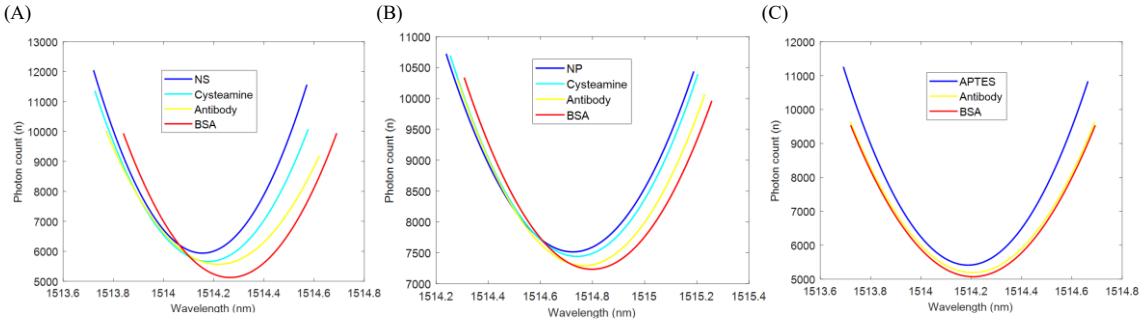

Figure 7-6. Behavior of the spectrum during each functionalization step: (A) TFBG+NS, (B) TFBG+NP, and (C) Bare TFBG.

7.8. Glyphosate detection

For glyphosate detection, a series of solutions with concentrations ranging from 1×10^{-7} to 1 µg/L (equivalent to 0.591 fM to 5.91 nM) were prepared in PBS. Prior to each measurement, the transducer was immersed in a pure PBS solution for 10 minutes to establish a stable baseline.

During the experiment, the transmission spectrum was automatically recorded every 30 seconds. After baseline stabilization, the sensor was exposed to the lowest glyphosate concentration. The sensor was incubated in the solution for approximately 30 minutes to allow for sufficient analyte-receptor interaction, followed by a rinse with PBS to remove any unbound glyphosate molecules. Data was collected during the 5-minute washing step, and the average wavelength shift and standard deviation of the band position were calculated for that specific concentration. This sequential process was repeated for each increasing concentration until no further red shift was observed, indicating sensor saturation where the target molecules occupied all available anti-glyphosate receptors. The experiment was repeated twice for each different transducer to ensure reproducibility.

Figure 7-7 presents the transmission spectra of the NS-coated, NP-coated, and bare TFBGs in a PBS solution after exposure to each glyphosate concentration. A progressive red shift of the attenuation band is observed, which is attributed to the increasing number of glyphosate molecules binding to the antibodies immobilized on the transducer surface.

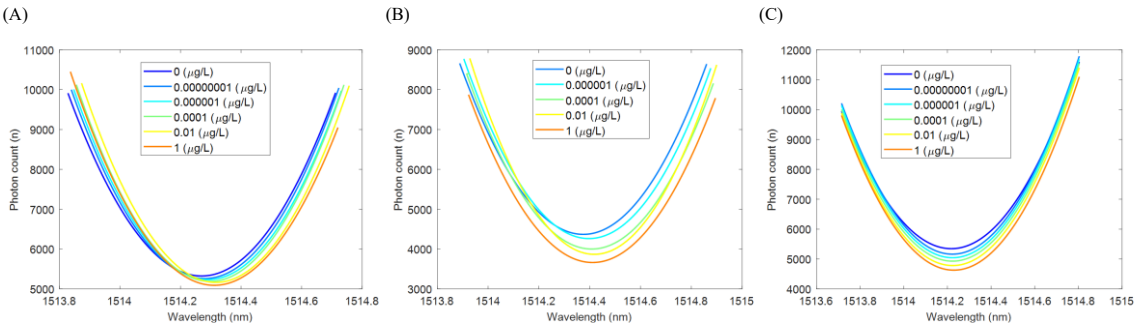

Figure 7-7. Spectrum of samples for each transducer after each concentration of glyphosate: (A) TFBG+NS, (B) TFBG+NP, and (C) Bare TFBG.

Calibration curves for all biosensors were generated and are plotted on a semi-log scale in Figure 7-8, illustrating the relationship between wavelength shift and analyte concentration. The experimental data were fitted using a Logistic function, represented by the dotted curves, as described in previous chapters (Equation 4-1). The baseline for the resonance wavelength was set to the value recorded in pure PBS, which represents a zero-analyte concentration. The experiment was repeated twice for transducers functionalized with NP, NS and bare TFBG. For each test, the resonance wavelength shift corresponding to each concentration was calculated by averaging the measured values over approximately 5 minutes of acquisition, yielding about 10 data points per concentration. Each data point shown in the graph represents the mean value, and the associated error bars correspond to three times the standard deviation obtained from the two repeated experiments for each concentration,. To ensure consistent conditions, measurements were taken after the incubation of each concentration in PBS, which eliminated any contributions from the solution's refractive index.

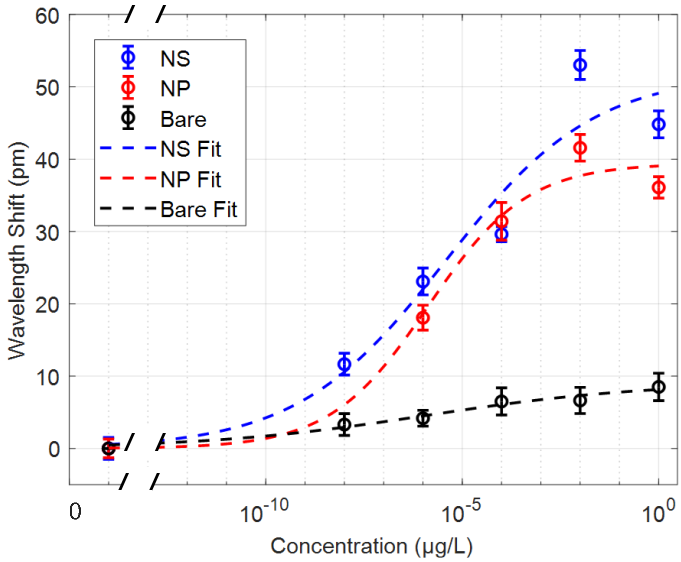

Figure 7-8. Calibration curves for glyphosate detection using TFBG with NS, NP, and bare TFBG. Experimental data points are shown as markers, while the corresponding fits using a logistic function are represented by dotted lines.

Following an initial review of the results, it is clear that the deposition of gold nanostructures significantly increased the wavelength shift. For the bare TFBG, the shift was only 10 pm. This value increased to 50 pm with the NS deposition and 40 pm with the NP deposition, representing a 5-fold and 4-fold improvement, respectively. Table 7-1 summarizes the fitting parameters and the calculated LOD for each transducer. The LOD was determined as the target concentration corresponding to the blank measurement response (zero concentration) plus three times its standard deviation, as detailed in Chapter 5. As shown in Figure 7-8, all sensors reached saturation, indicating that all antibodies were occupied by the target molecules. Notably, the wavelength shift for the TFBG sensors with nanostructure (NS and NP) deposition was about 7 and 5 times higher, respectively, than that of the bare TFBG. Consequently, TFBG sensors with nanostructure deposition exhibit not only higher sensitivity but also a lower LOD, as detailed in Table 7-1. Overall, the NS-coated TFBG sensor demonstrates the best performance in terms of sensitivity, dynamic range, and detection capability, making it the most promising configuration for low-concentration sensing. This enhanced sensitivity is attributed to the interaction of evanescent waves with the nanostructures, leading to a greater portion of light leaking to the fiber surface [15], [29], [30], [33], [34].

Table 7-1. Logistic fitting parameters for biosensor calibration curves and LOD.

Sample	$\Delta\lambda_{MAX}$ [pm]	x_0 [µg/L]	p	LOD [µg/L]
NS	52.8	$5.3 \cdot 10^{-6}$	0.26	10^{-8}
NP	41.2	$2.6 \cdot 10^{-6}$	0.44	10^{-7}
Bare	7.7	$1.2 \cdot 10^{-8}$	0.22	10^{-5}

The achieved LOD of 10^{-8} µg/L (59.1 fM) in the case of the NS-coated TFBG surpasses other reported methods, including those based on FMDH, green fluorescent carbon, radiometric fluorescent approaches, U-shaped fibers, and SERS [8], [9], [10], [11], [12], [35], [36], [37], [38], [39], [40]. A comprehensive comparison of the LOD obtained in this work with previous studies employing different phenomena can be found in Table 7-2.

Table 7-2. Comparison of the sensor performance with existing literature.

Configuration	Other analytical characteristics	Range [µg/L]	LOD [µg/L]	Ref.
Peptide-based probe (FMDH)	dual fluorometric and colorimetric signals	$406 - 1.319$	5.055	[39]
Hump-shaped seven-core fiber	gold NPs	$0 - 100$	328	[41]
U-shaped fiber	gold NPs	$0 - 8500$	50.72	[11]
CS-MIPs/PPy/Au	Recognition	$0.00031 - 50$	$1 \cdot 10^{-6}$	[12]
CuOx@mC/GCE	GLY-Cu(II) complex	$1.7 \cdot 10^{-7} - 1700$	$1.3 \cdot 10^{-7}$	[40]

SERS	gold nanorods	-	$1.7 \cdot 10^{-5}$	[35]
LC–SPE–ESI/MS/MS	AMPA, GLU	-	$5 \cdot 10^{-3}$	[37]
LC–FLD MS/MS	AMPA	$0.1 - 50.0$	0.05	[38]
Fluorometric probe	Green fluorescent carbon dots (G-CDs)	$550 - 850.0$	7.44	[9]
radiometric fluorescent	(ENX@EuMOF)	$5 \cdot 10^{-3} - 0.1$	$3.5 \cdot 10^{-3}$	[42]
TFBG	Bare	$1 \cdot 10^{-7} - 1$	$1 \cdot 10^{-5}$	This work
TFBG	gold NP	$1 \cdot 10^{-7} - 1$	$1 \cdot 10^{-7}$	This work
TFBG	gold NS	$1 \cdot 10^{-7} - 1$	$1 \cdot 10^{-8}$	This work

7.9. Selectivity test

This section explores key factors influencing sensor performance, such as selectivity. The high sensitivity of the NS-coated TFBG sensor to both SRI and glyphosate led us to focus on its performance for these investigations.

To assess the selectivity of the device, its response to glycine was tested, given that its chemical structure is very similar to that of glyphosate. The sensor was immersed in a PBS solution containing 0.01 µg/L of glycine (Sigma-Aldrich, Taufkirchen, Germany), and the resulting wavelength shift of approximately 1.25 pm was recorded [43]. In contrast, exposure to the same concentration of glyphosate induced a significantly larger wavelength shift of approximately 53.2 pm, as shown in Figure 7-9. This marked difference in response demonstrates the superior selectivity of the sensor for glyphosate over glycine.

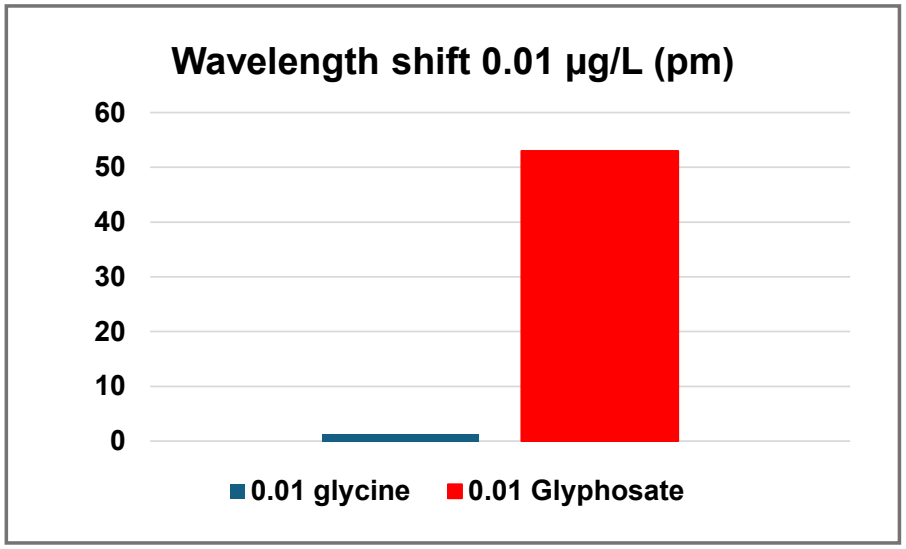

Figure 7-9. Selectivity test using interfering substance (glycine) and the analyte (glyphosate) at 0.01 (µg/L).

7.10. Conclusion

In this chapter, the potential of employing gold nanoparticles on TFBGs for the detection of biological components was successfully investigated. As a compelling case study, the sensor was effectively bio-functionalized for the label-free detection of glyphosate. The LOD for the NS-coated TFBG biosensor was found to be 10^{-8} µg/L (59.1 fM), which represents a three-order-of-magnitude improvement compared to the bare TFBG sensor, which had an LOD of 10^{-5} µg/L. This achieved LOD surpasses other reported methods, including those based on optical fiber configurations as well as techniques such as SERS, FMDH, and green fluorescent approaches. Furthermore, the sensor's selectivity was validated, demonstrating negligible interference from glycine.

7.11. References

[1] D. C. Poudyal, V. N. Dhamu, M. Samson, S. Muthukumar, and S. Prasad, "Portable Pesticide Electrochem-sensor: A Label-Free Detection of Glyphosate in Human Urine," Langmuir, vol. 38, no. 5, pp. 1781–1790, Feb. 2022, doi: 10.1021/acs.langmuir.1c02877.

[2] L. A. Zambrano-Intriago, C. G. Amorim, J. M. Rodríguez-Díaz, A. N. Araújo, and M. C. B. S. M. Montenegro, "Challenges in the design of electrochemical sensor for glyphosate-based on new materials and biological recognition," Science of The Total Environment, vol. 793, p. 148496, Nov. 2021, doi: 10.1016/j.scitotenv.2021.148496.

[3] M. Masci, R. Caproni, and T. Nevigato, "Chromatographic Methods for the Determination of Glyphosate in Cereals Together with a Discussion of Its Occurrence, Accumulation, Fate, Degradation, and Regulatory Status," Methods Protoc, vol. 7, no. 3, p. 38, May 2024, doi: 10.3390/mps7030038.

[4] L. M. E. Ibarra Bouzada, S. R. Hernández, and S. V. Kergaravat, "Glyphosate detection from commercial formulations: comparison of screening analytic methods based on enzymatic inhibition," Int J Environ Anal Chem, vol. 101, no. 13, pp. 1821–1835, Oct. 2021, doi: 10.1080/03067319.2019.1691176.

[5] E. Takács et al., "Utilization of a Novel Immunofluorescence Instrument Prototype for the Determination of the Herbicide Glyphosate," Molecules, vol. 27, no. 19, p. 6514, Oct. 2022, doi: 10.3390/molecules27196514.

[6] P. S. Ferreira et al., "Exploring the Use of a Lipopeptide in Dipalmitoylphosphatidylcholine Monolayers for Enhanced Detection of Glyphosate in Aqueous Environments," Langmuir, vol. 40, no. 26, pp. 13583–13595, Jul. 2024, doi: 10.1021/acs.langmuir.4c01089.

[7] X. Mu, J. Xu, and F. Zeng, "A Novel and Sensitive Fluorescent Probe for Glyphosate Detection Based on Cu2+ Modulated Polydihydroxyphenylalanine Nanoparticles," Biosensors (Basel), vol. 13, no. 5, p. 510, Apr. 2023, doi: 10.3390/bios13050510.

[8] Q. Zhang et al., "Hump-shaped seven-core fiber-based WaveFlex biosensor for rapid detection of glyphosate pesticides in real food samples," Opt Express, vol. 32, no. 15, p. 25789, Jul. 2024, doi: 10.1364/OE.530348.

[9] T. Sasikumar, J. S. Packialakshmi, S. J. Hong, S. Y. Ha, G. H. Shin, and J. T. Kim, "Multifunctional green-emitting fluorescent carbon dots: A versatile fluorometric probe for glyphosate detection and applications in food," J Environ Chem Eng, vol. 12, no. 5, p. 113356, Oct. 2024, doi: 10.1016/j.jece.2024.113356.

[10] L. Bai et al., "Enoxacin-embedded EuMOF-based ratio fluorescent sensing platform integrated with paper-based sensor and skin-attachable hydrogel for glyphosate detection in foods," J Hazard Mater, vol. 489, p. 137658, Jun. 2025, doi: 10.1016/j.jhazmat.2025.137658.

[11] F. M. de Lima Bombardi, M. Muller, and J. L. Fabris, "Plasmonic U-Shaped Optical Fiber Sensor for Glyphosate Detection in Water," in 2021 SBMO/IEEE MTT-S International Microwave and Optoelectronics Conference (IMOC), IEEE, Oct. 2021, pp. 1–3. doi: 10.1109/IMOC53012.2021.9624871.

[12] F. Zouaoui et al., "Experimental Study and Mathematical Modeling of a Glyphosate Impedimetric Microsensor Based on Molecularly Imprinted Chitosan Film," Chemosensors, vol. 8, no. 4, p. 104, Oct. 2020, doi: 10.3390/chemosensors8040104.

[13] D. Harasim and P. Kisała, "Application of Cascaded TFBG for Wavelength-Shift-Based SRI Measurement with Reduced Polarization Cross-Sensitivity," Sensors, vol. 25, no. 6, p. 1831, Mar. 2025, doi: 10.3390/s25061831.

[14] J. Albert, L. Shao, and C. Caucheteur, "Tilted fiber Bragg grating sensors," Laser Photon Rev, vol. 7, no. 1, pp. 83–108, Jan. 2013, doi: 10.1002/lpor.201100039.

[15] K. Tomyshev, E. I. Dolzhenko, A. D. Vasilyeva, L. V. Yurina, and O. V. Butov, "Selective fiber optic TFBG-assisted biosensors featuring functional coatings," Sens Actuators B Chem, vol. 384, p. 133618, Jun. 2023, doi: 10.1016/j.snb.2023.133618.

[16] S. Korganbayev et al., “Optimization of Cladding Diameter for Refractive Index Sensing in Tilted Fiber Bragg Gratings,” Sensors, vol. 22, no. 6, p. 2259, Mar. 2022, doi: 10.3390/s22062259.
[17] S. Cięszczyk, P. Kisała, and J. Mroczka, “New Parameters Extracted from Tilted Fiber Bragg Grating Spectra for the Determination of the Refractive Index and Cut-Off Wavelength,” Sensors, vol. 19, no. 9, p. 1964, Apr. 2019, doi: 10.3390/s19091964.
[18] Q. Wang, J.-Y. Jing, and B.-T. Wang, “Highly Sensitive SPR Biosensor Based on Graphene Oxide and Staphylococcal Protein A Co-Modified TFBG for Human IgG Detection,” IEEE Trans Instrum Meas, vol. 68, no. 9, pp. 3350–3357, Sep. 2019, doi: 10.1109/TIM.2018.2875961.
[19] C. Caucheteur, M. Loyez, Á. González-Vila, and R. Wattiez, “Evaluation of gold layer configuration for plasmonic fiber grating biosensors,” Opt Express, vol. 26, no. 18, p. 24154, Sep. 2018, doi: 10.1364/OE.26.024154.
[20] Q. Duan, Y. Liu, S. Chang, H. Chen, and J. Chen, “Surface Plasmonic Sensors: Sensing Mechanism and Recent Applications,” Sensors, vol. 21, no. 16, p. 5262, Aug. 2021, doi: 10.3390/s21165262.
[21] W. Udos et al., “Spatial frequency spectrum of SPR-TFBG: A simple spectral analysis for in-situ refractometry,” Optik (Stuttg), vol. 219, p. 164970, Oct. 2020, doi: 10.1016/j.ijleo.2020.164970.
[22] M. Vidal et al., “Relevance of the Spectral Analysis Method of Tilted Fiber Bragg Grating-Based Biosensors: A Case-Study for Heart Failure Monitoring,” Sensors, vol. 22, no. 6, p. 2141, Mar. 2022, doi: 10.3390/s22062141.
[23] Z. Ren et al., “Tilted fiber Bragg grating surface plasmon resonance based optical fiber cadmium ion trace detection,” Sens Actuators B Chem, vol. 393, p. 134247, Oct. 2023, doi: 10.1016/j.snb.2023.134247.
[24] F. Wang et al., “Near-infrared band Gold nanoparticles-Au film ‘hot spot’ model based label-free ultratrace lead (II) ions detection via fiber SPR DNAzyme biosensor,” Sens Actuators B Chem, vol. 337, p. 129816, Jun. 2021, doi: 10.1016/j.snb.2021.129816.
[25] T. Guo, F. Liu, B.-O. Guan, and J. Albert, “[INVITED] Tilted fiber grating mechanical and biochemical sensors,” Opt Laser Technol, vol. 78, pp. 19–33, Apr. 2016, doi: 10.1016/j.optlastec.2015.10.007.
[26] A. Moslemi et al., “Highly sensitive gold nanostar based optical fiber sensor with tunable plasmonic resonance,” Sensors and Actuators Reports, p. 100326, Apr. 2025, doi: 10.1016/j.snr.2025.100326.
[27] D. J. Mandia, W. Zhou, J. Albert, and S. T. Barry, “CVD on Optical Fibers: Tilted Fiber Bragg Gratings as Real-time Sensing Platforms,” Chemical Vapor Deposition, vol. 21, no. 1-2–3, pp. 4–20, 2015.
[28] Z. S. Alshaikhli, “A comparative study on polymer and metals coated TFBG temperature sensor: coating thickness impact,” Applied Physics A, vol. 130, no. 2, p. 127, 2024.
[29] S. Lepinay, A. Staff, A. Ianoul, and J. Albert, “Improved detection limits of protein optical fiber biosensors coated with gold nanoparticles,” Biosens Bioelectron, vol. 52, pp. 337–344, Feb. 2014, doi: 10.1016/j.bios.2013.08.058.
[30] M. Morsin, M. Mat Salleh, A. Ali Umar, and M. Sahdan, “Gold Nanoplates for a Localized Surface Plasmon Resonance-Based Boric Acid Sensor,” Sensors, vol. 17, no. 5, p. 947, Apr. 2017, doi: 10.3390/s17050947.
[31] K. Tomyshev, E. I. Dolzhenko, A. D. Vasilyeva, L. V. Yurina, and O. V. Butov, “Selective fiber optic TFBG-assisted biosensors featuring functional coatings,” Sens Actuators B Chem, vol. 384, p. 133618, Jun. 2023, doi: 10.1016/j.snb.2023.133618.
[32] R. D. da C. C. Bandeira et al., “Development and validation of a method for detection and quantification of ochratoxin A in green coffee using liquid chromatography coupled to mass spectrometry,” Food Science and Technology, vol. 32, no. 4, pp. 775–782, Nov. 2012, doi: 10.1590/S0101-20612012005000120.
[33] P. Senthil Kumar, I. Pastoriza-Santos, B. Rodríguez-González, F. Javier García de Abajo, and L. M. Liz-Marzán, “High-yield synthesis and optical response of gold nanostars,”

Nanotechnology, vol. 19, no. 1, p. 015606, Jan. 2008, doi: 10.1088/0957-4484/19/01/015606.
[34] W. Qiu, M. Cheng, R. Chen, H. Lin, and Z. Huang, "Enhancement of evanescent waves in a planar waveguides with an anisotropic metamaterial layer," J Phys Conf Ser, vol. 276, p. 012084, Feb. 2011, doi: 10.1088/1742-6596/276/1/012084.
[35] H. Torul, İ. H. Boyaci, and U. Tamer, "Attomole detection of glyphosate by surface-enhanced Raman spectroscopy using gold nanorods," Fabad J. Pharm. Sci, vol. 35, pp. 179–184, 2010.
[36] A. L. Valle, F. C. C. Mello, R. P. Alves-Balvedi, L. P. Rodrigues, and L. R. Goulart, "Glyphosate detection: methods, needs and challenges," Environ Chem Lett, vol. 17, no. 1, pp. 291–317, Mar. 2019, doi: 10.1007/s10311-018-0789-5.
[37] M. Ibáñez, Ó. J. Pozo, J. V. Sancho, F. J. López, and F. Hernández, "Residue determination of glyphosate, glufosinate and aminomethylphosphonic acid in water and soil samples by liquid chromatography coupled to electrospray tandem mass spectrometry," J Chromatogr A, vol. 1081, no. 2, pp. 145–155, Jul. 2005, doi: 10.1016/j.chroma.2005.05.041.
[38] C. E. Ramirez, S. Bellmund, and P. R. Gardinali, "A simple method for routine monitoring of glyphosate and its main metabolite in surface waters using lyophilization and LC-FLD + MS/MS. Case study: canals with influence on Biscayne National Park," Science of The Total Environment, vol. 496, pp. 389–401, Oct. 2014, doi: 10.1016/j.scitotenv.2014.06.118.
[39] S. Li et al., "A dual-signals fluorometric and colorimetric peptide-based probe for Cu(II) and glyphosate detection and its application for bioimaging and water testing," Science of The Total Environment, vol. 945, p. 174163, Oct. 2024, doi: 10.1016/j.scitotenv.2024.174163.
[40] C. Gu, Q. Wang, L. Zhang, P. Yang, Y. Xie, and J. Fei, "Ultrasensitive non-enzymatic pesticide electrochemical sensor based on HKUST-1-derived copper oxide @ mesoporous carbon composite," Sens Actuators B Chem, vol. 305, p. 127478, Feb. 2020, doi: 10.1016/j.snb.2019.127478.
[41] Q. Zhang et al., "Hump-shaped seven-core fiber-based WaveFlex biosensor for rapid detection of glyphosate pesticides in real food samples," Opt Express, vol. 32, no. 15, p. 25789, Jul. 2024, doi: 10.1364/OE.530348.
[42] L. Bai et al., "Enoxacin-embedded EuMOF-based ratio fluorescent sensing platform integrated with paper-based sensor and skin-attachable hydrogel for glyphosate detection in foods," J Hazard Mater, vol. 489, p. 137658, Jun. 2025, doi: 10.1016/j.jhazmat.2025.137658.
[43] F. Sequeira et al., "Glyphosate Detection Through Piezoelectric and Fiber Optic Sensors Based on Molecular Imprinted Polymers," IEEE Sens J, vol. 24, no. 13, pp. 20331–20342, Jul. 2024, doi: 10.1109/JSEN.2024.3395892.

8. Chapter 8
Conclusion and Future work

This chapter summarizes the key accomplishments obtained through this research work and suggests new possibilities for future investigations.

8.1. Thesis Conclusion

This thesis has focused on the design, fabrication, and characterization of advanced fiber optic biosensors based on the principle of LSPR using gold nanostructures. The work aimed to exploit the strong interaction between light and metallic nanostructures, specifically golden NPs and NSs, to develop highly sensitive and selective platforms for biological and chemical detection.

The theoretical foundation of this research was established through electromagnetic simulations performed in COMSOL Multiphysics, which modeled the interaction between light and plasmonic nanostructures to optimize sensor performance. The influence of nanoparticle shape, size, and distribution on the LSPR resonance band and sensitivity to the SRI was systematically investigated. Results demonstrated that LSPR spectral characteristics can be effectively tuned by controlling geometrical parameters and the local dielectric environment, offering a pathway for precise sensor optimization.

Experimentally, an uncladded multimode optical fiber was employed as the sensing platform to facilitate evanescent wave coupling between the guided light and the surrounding medium. NPs and NSs were synthesized and immobilized on the functionalized fiber surface to form the plasmonic transducer. Optical characterization in reflection mode revealed distinct LSPR bands, which were

correlated with the UV–Vis spectra of nanoparticles in colloidal solution and supported by SEM and TEM imaging for morphology and size verification.

The SRI sensitivity of the developed sensors was carefully evaluated, followed by their application in detecting specific chemical and biological targets, demonstrating sensitivities up to 560 nm/RIU. As a preliminary demonstration, the pesticide Thiram was used as a model analyte due to its natural affinity for gold. The LSPR-based fiber sensor achieved a LOD of 0.3 pM, although not specific it confirmed its remarkable sensitivity for small-molecule detection.

Building upon this, the platform was biofunctionalized with antibodies to enable selective detection of biomolecules. Two biological targets, Cortisol and OTA, were successfully detected with exceptional specificity. The optimized sensors achieved LODs of 0.1 pg/mL for Cortisol and 1.85×10^{-5} ppb for OTA, respectively, demonstrating the system's strong potential for medical and food-safety diagnostics. These experiments were conducted in collaboration with the University of Aveiro during a research exchange period, which provided valuable experience in biosensing surface chemistry and measurement techniques.

In addition to the multimode fiber-based platform, a TFBG configuration was also investigated to further enhance refractive index and biosensing sensitivity. By incorporating gold nanostructures onto the TFBG surface, significant enhancement in spectral response and sensitivity was achieved. The modified TFBG sensor was successfully applied to the detection of glyphosate, achieving an LOD of 10^{-8} µg/L, demonstrating its promise for environmental monitoring applications.

Overall, this thesis provides comprehensive theoretical and experimental insights into the development of plasmonic fiber optic biosensors. By integrating the unique plasmonic properties of gold nanostructures with the optical advantages of fiber platforms, the presented work advances the design of compact, label-free, and highly sensitive sensing devices. The results highlight the potential of these sensors for real-world applications in biomedical diagnostics, environmental monitoring, and food safety, paving the way for future research toward miniaturized, multiplexed, and portable sensing systems.

8.2. Future Work

Several avenues for future research arise from the findings of this thesis, aimed at further improving the performance and applicability of plasmonic fiber optic biosensors. One important direction involves investigating the effect of fiber transducer length on sensing performance. The current sensors are limited to a length of 5 cm, and reducing the fiber length could provide insights into how sensitivity, LOD, and dynamic range are influenced by the transducer dimensions. Shorter sensors could be particularly valuable for applications where space is constrained or compact integration is required.

Another promising approach is the combination of LSPR with conventional SPR by depositing a thin gold layer onto the fiber surface prior to immobilizing nanoparticles. This configuration, referred to as long-range surface plasmon resonance (LRSPR) [1], [2], [3], would allow the resonance band to

be tuned into the near-infrared (NIR) range, expanding the operational wavelength window for fiber-based biosensing. In this context, alternative nanostructures with lower conductivity, such as indium tin oxide (ITO), could also be explored, as they exhibit LSPR in the NIR region [4], [5] and may offer advantages for specific sensing targets.

For practical applications, real-sample testing is essential. For instance, detecting OTA in complex matrices such as coffee would provide a more realistic assessment of sensor performance, addressing industrial needs for fast, reproducible, and low-cost detection at relevant LODs. In addition, further exploration of different nanostructure geometries, including nanocages and nanorods [6], [7], [8], [9], could enhance sensitivity and broaden the range of detectable analytes, as these structures have recently shown significant promise in plasmonic research.

Advancements in fiber geometry also present an exciting opportunity for optimization. Modifications such as polishing, U-shaped and omega-shaped configurations [10], [11], [12], [13], [14], or micromachining the fiber surface could improve evanescent wave excitation, thereby enhancing the interaction between light and plasmonic nanostructures. The use of alternative fiber types, such as photonic crystal fibers, could offer additional control over mode propagation and field confinement, enabling tailored sensing properties. Furthermore, by combining ITO nanostructures and thin films with TFBGs, the optical characteristics of TFBGs can be modified and sensing functionalities can be enhanced using ITO's special properties. This material combines a tunable refractive index, high transparency across the visible and near-infrared spectrum, and notable electrical conductivity, qualities rarely found together in other metal oxides, making it particularly well suited for photonic and optoelectronic sensor development. When ITO coatings are applied to optical fibers, including those with TFBG inscriptions, they interact with the evanescent field of the guided modes, enabling modulation of modal characteristics, effective refractive index, and sensitivity to external refractive index or chemical variations. The incorporation of ITO enhances the overall sensitivity and functionalization of TFBGs by intensifying the interaction between the guided light and the external environment, thereby increasing the evanescent field overlap that is essential for chemical and biosensing applications. Moreover, ITO’s epsilon-near-zero regime and adjustable carrier concentration facilitate unique plasmonic and nonlinear optical effects, as well as efficient electro-optic modulation at the nanoscale. These features contribute to dynamic spectral tuning and improved sensing performance. The optical response of TFBGs coated with ITO can also be finely engineered to achieve broad spectral tunability and multi-parameter sensing, enabling precise discrimination between temperature, strain, and refractive index variations. In addition, ITO’s electrical conductivity introduces the possibility of electrically addressable or actively tunable fiber-optic devices, paving the way for hybrid electro-optic sensor platforms [15], [16], [17], [18], [19].

Overall, these directions not only aim to optimize sensitivity, selectivity, and dynamic range but also to expand the practical applicability of fiber optic plasmonic sensors for real-world biomedical, environmental, and industrial applications. The combination of advanced nanostructures, fiber

engineering, and hybrid plasmonic effects promises to push the limits of label-free optical biosensing in terms of detection capability, speed, and versatility.

8.3. References

[1] J.-Y. Jing, Q. Zhu, Z.-X. Dai, S.-Y. Li, Q. Wang, and W.-M. Zhao, "Sensing self-referenced fiber optic long-range surface plasmon resonance sensor based on electronic coupling between surface plasmon polaritons," Appl Opt, vol. 58, no. 23, p. 6329, Aug. 2019, doi: 10.1364/AO.58.006329.

[2] X. Yang et al., "Tapered optical fiber LRSPR biosensor based on gold nanoparticle amplification for label-free BSA detection," Sens Actuators B Chem, vol. 426, p. 136986, Mar. 2025, doi: 10.1016/j.snb.2024.136986.

[3] X. Li, Q. Zhao, Y.-N. Zhang, Y. Zhao, and X. Zhou, "Porous Gold Nanocubes Particle-Sensitized U-Shaped Fiber-Optic Surface Plasmon Resonance Sensor for Ultra-Sensitive Detection of Virus RNA," IEEE Trans Instrum Meas, vol. 73, pp. 1–8, 2024, doi: 10.1109/TIM.2024.3396836.

[4] B. Han et al., "Modulating Mechanism of the LSPR and SERS in Ag/ITO Film: Carrier Density Effect," J Phys Chem Lett, vol. 12, no. 31, pp. 7612–7618, Aug. 2021, doi: 10.1021/acs.jpclett.1c01727.

[5] J. Zhu, X. Li, W. Zheng, B. Wang, and Y. Tian, "Improved localized surface plasmon resonance index sensitivity based on chemically-synthesized gold nanoparticles on indium tin oxide surfaces," Nanotechnology, vol. 29, no. 5, p. 055701, Feb. 2018, doi: 10.1088/1361-6528/aa9c05.

[6] Y. Yu et al., "Gold-Nanorod-Coated Capillaries for the SERS-Based Detection of Thiram," ACS Appl Nano Mater, vol. 2, no. 1, pp. 598–606, Jan. 2019, doi: 10.1021/acsanm.8b02075.

[7] G. Mushtaq, V. V. R. Sai, and S. Bandyopadhyay, "Chemisorbed gold Nanorods on optical fibers for refractive index sensing," Sens Biosensing Res, vol. 50, p. 100869, Dec. 2025, doi: 10.1016/j.sbsr.2025.100869.

[8] M. Shabaninezhad and G. Ramakrishna, "Theoretical investigation of size, shape, and aspect ratio effect on the LSPR sensitivity of hollow-gold nanoshells," J Chem Phys, vol. 150, no. 14, Apr. 2019, doi: 10.1063/1.5090885.

[9] A. M. Lopatynskyi et al., "Solid and Hollow Gold Nanostructures for Nanomedicine: Comparison of Photothermal Properties," Plasmonics, vol. 13, no. 5, pp. 1659–1669, Oct. 2018, doi: 10.1007/s11468-017-0675-1.

[10] F. M. de Lima Bombardi, M. Muller, and J. L. Fabris, "Plasmonic U-Shaped Optical Fiber Sensor for Glyphosate Detection in Water," in 2021 SBMO/IEEE MTT-S International Microwave and Optoelectronics Conference (IMOC), IEEE, Oct. 2021, pp. 1–3. doi: 10.1109/IMOC53012.2021.9624871.

[11] Z. Luo et al., "Ultrasensitive U-shaped fiber optic LSPR cytosensing for label-free and in situ evaluation of cell surface N-glycan expression," Sens Actuators B Chem, vol. 284, pp. 582–588, Apr. 2019, doi: 10.1016/j.snb.2019.01.015.

[12] P. S. S. dos Santos, J. P. Mendes, I. Pastoriza-Santos, J.-P. Juste, J. M. M. M. de Almeida, and L. C. C. Coelho, "Gold-coated silver nanorods on side-polished singlemode optical fibers for remote sensing at optical telecommunication wavelengths," Sens Actuators B Chem, vol. 425, p. 136936, Feb. 2025, doi: 10.1016/j.snb.2024.136936.

[13] M.-M. Babakhani-Fard, M. I. Zibaii, S. Rostami, and H. Latifi, "Lab on-tip fiber based on dual side hole LSPR for vitamin K1 detection," Sensors and Actuators Reports, p. 100342, May 2025, doi: 10.1016/j.snr.2025.100342.

[14] Z. Luo et al., "Development of a rapid and ultra-sensitive cytosensor: Ω-shaped fiber optic LSPR integrated with suitable AuNPs coverage," Sens Actuators B Chem, vol. 336, p. 129706, Jun. 2021, doi: 10.1016/j.snb.2021.129706.

[15] R. Wang et al., "Mode splitting in ITO-nanocoated tilted fiber Bragg gratings for vector twist measurement," Journal of Lightwave Technology, vol. 39, no. 12, pp. 4151–4157, 2021.

[16] J. J. Imas, J. Albert, I. Del Villar, A. Ozcáriz, C. R. Zamarreño, and I. R. Matías, "Mode Transition During Deposition of Nanoscale ITO Coatings on Tilted Fiber Bragg Gratings," in Optica Advanced Photonics Congress 2022, in Technical Digest Series. Maastricht,Limburg: Optica Publishing Group, 2022, p. BM3A.5. doi: 10.1364/BGPPM.2022.BM3A.5.

[17] J. J. Imas, J. Albert, I. Del Villar, A. Ozcáriz, C. R. Zamarreño, and I. R. Matías, “Mode Transitions and Thickness Measurements During Deposition of Nanoscale TiO_2 Coatings on Tilted Fiber Bragg Gratings,” Journal of Lightwave Technology, vol. 40, no. 17, pp. 6006–6012, 2022.
[18] H. Cheng, L. Wang, R. Xiao, and J. Wang, “Temperature sensing of π-PSFBG with ITO film coated by PLD method,” Optik (Stuttg), vol. 262, p. 169289, 2022.
[19] Z. L. Poole, P. Ohodnicki, R. Chen, Y. Lin, and K. P. Chen, “Engineering metal oxide nanostructures for the fiber optic sensor platform,” Opt Express, vol. 22, no. 3, pp. 2665–2674, 2014.